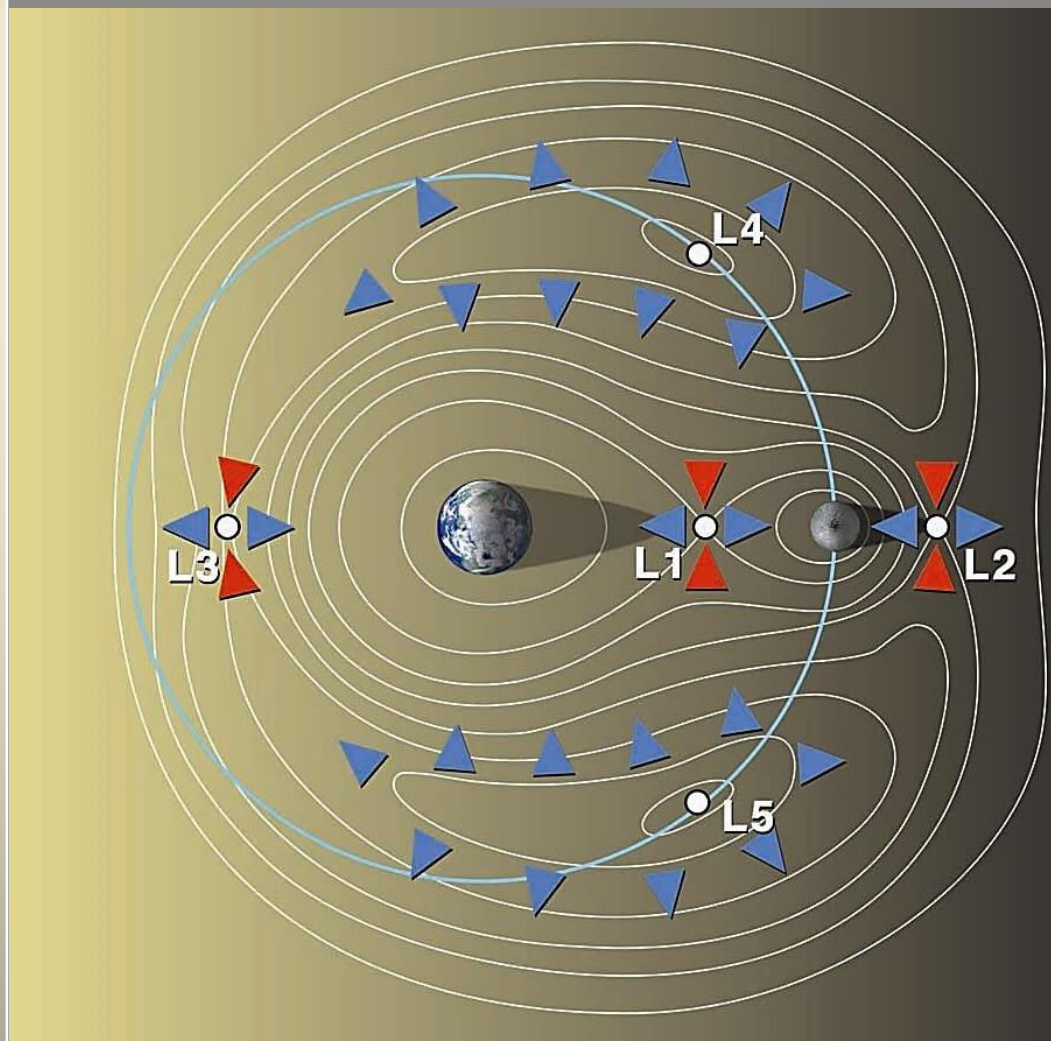


Linear stability and bifurcations of periodic Lagrange orbits in the Elliptic Restricted 3-Body Problem

“An investigation at L1/L2 in the Earth-Moon system”

LOTFI MASSARWEH



@Copyright information:

The image on the front page has been retrieved from <http://i.stack.imgur.com/eXWhr.jpg> by courtesy of the author. It shows the Earth-Moon system with its relative Lagrange points.

Credits: David A. Kring, LPI-JSC Center for Lunar Science and Exploration.

Linear stability and bifurcations of periodic Lagrange orbits in the Elliptic Restricted 3-Body Problem

“An investigation at L1/L2 in the Earth-Moon system”

by

Lotfi Massarweh

in partial fulfilment of the requirements for the degree of

Master of Science
in Aerospace Engineering

at the Delft University of Technology,
to be defended publicly on Wednesday September 21st, 2016 at 10:00 AM.

| | | |
|-------------------|---|----------|
| Student Number: | 4418689 | |
| Project Duration: | January 25 th , 2016 September 6 th , 2016 | |
| Supervisors: | Dr.Ir. E.J.O (Ernst) Schrama | TU Delft |
| | Dr.Ir. W.T. van Horssen | TU Delft |
| Thesis Committee: | Prof. Dr.Ir. Pieter Visser | TU Delft |
| | K.J. (Kevin) Cowan | TU Delft |

An electronic version of this thesis is available at <http://repository.tudelft.nl/>

*"Will you understand what I'm going to tell you?...
No, you're not going to be able to understand it.
...that's because I don't understand it.
Nobody does."*

-Richard P. Feynman

Acknowledgements

Since childhood, we are used to asking questions about the world surrounding us, while we are able of continuously learning from life experiences and from other people. In general, the knowledge of this physical world requires time, not just hours or days, but sometimes even decades and it is built step by step based on the work of many.

And so I am here, one step closer to which is more than a hobby, more than a passion, but a real dream for me. The path for a researcher's career is still long and rather than easy, nonetheless this Master thesis is an important milestone, where all previous efforts are decisively summarized. In this work I have tried to introduce a celestial mechanics problem, studied for centuries and still, a great challenge for engineers and mathematicians. Inspired by so many scientists, my personal objective is here to provide the reader with a work that actually can be used as starting point for future Master students sharing my same passion. A greater effort was therefore necessary to contextualize the problem, e.g. with historical notes, and in this way also including, as far as possible, the most recent literature.

I would like to thank here both my supervisors (Dr.Ir. Schrama and Dr.Ir. Van Horsen) for their time and patience during these past few months, thus allowing me to work in a very calm and friendly environment. I also would like to thank my friends here at TU Delft for giving me plenty of amazing memories and stories to be told in the future. Most important my closest friends of “*El Nuevo Latinoss*” and “*BobbaLaGobba*” for their continuous support until this very last day, as well as for a very special person recently met. However, if I have come this far I owe it to both my two families in Italy and Palestine, while immense has been the affection of my father and my little brother. Last, most of all, the memory of my mother, forever etched in my mind.

Lotfi Massarweh,
Delft, 6th September 2016.

Abstract

The Three Body Problem (3BP) has been one of the main celestial mechanics problems in the past few centuries, for a long time studied by both engineers and mathematicians. Its practical purpose is to describe the motion of three particles only under their mutual gravitational interaction, thus it actually represents a ‘model’ of the real physical world. In fact, it can be seen as an extension of the Two Body Problem (2BP), which solutions are well-known and have been already employed in many space missions since the launch of Sputnik-1 in 1957, first artificial Earth satellite. Alternative formulation is given with the “*restricted problem*”, assuming the mass of the third body as negligible with respect to both principal ones. Under this assumption, justified by the small size of a general spacecraft compared to planets or moons, the ‘unperturbed’ motion of the main masses can be described by a Kepler solution, involving elliptic or circular bounded orbits. It follows the existence of an Elliptic (ER3BP) and a Circular problem (CR3BP), both admitting five equilibrium points (named Lagrange points), where a periodic orbital motion is theoretically possible. In this work three main families of periodic solutions (here called *Lagrange orbits*) have been investigated in a neighbourhood of L1/L2, Lagrange points adopted in the last 40 years for many space missions, e.g. for space observation and exploration purposes. The main objective here is to study these models based on their ‘standard’ formulation, so adopting the Dynamical System Theory for the Circular problem and later extending the entire discussion to the Elliptic one.

In the CR3BP periodic solutions have been found embedded within continuous families, also showing different types of bifurcation. A single shooting method (*Differential Correction algorithm*) and a numerical continuation scheme have been applied, starting with the analytic approximation based on Perturbation Theory (*Linstedt-Poincaré method*). Indeed, the linear stability assessment, through *Variational equations* (studying the so-called Monodromy matrix), has provided large insights into dynamical proprieties of the problem. In some cases, close members within the same family have shown a very different behaviour, in the limit of this linear analysis, but still allowing to well-define principal bifurcations in their continuous parameters. The analysis and all methodologies presented have been tested on a nominal system, here the Earth-Moon-Spacecraft one, while their validity can be trivially extended to several other restricted problems.

The ER3BP has been the second fundamental step of this work, where many additional aspects have been presented, e.g. the loss of continuous families. Nonetheless, non-trivial difficulties arise within the analytic approach, while many insights for the new dynamics can be provided by an analytic approximation of such motion. In support, the numerical approach has been able to tackle the problem, thus improving not only the analysis on linear stability, but most important revealing the so-called “*eccentricity-bifurcation*”. The latter is one of the most peculiar aspects related to the Elliptic problem, which now involves a new time-constraint (nominally the shooting-time), and leads to two branches of solutions (Left/Right family or Peri/Apo group) in agreement with most recent literature. A very different behaviour has been shown between these branches, while only resonance orbits actually survive within the ER3BP, once again highlighting the essentiality of adopting this more complete model for an accurate real space mission design.

Table of Contents

| | |
|---|-----------|
| ABSTRACT | VII |
| LIST OF FIGURES | XIII |
| LIST OF TABLES | XXI |
| NOMENCLATURE | XXV |
| LIST OF ACRONYMS & ABBREVIATIONS..... | XXV |
| LIST OF SYMBOLS..... | XXV |
| 1 INTRODUCTION | 1 |
| 1.1 PROBLEM FORMULATION..... | 2 |
| 1.2 HERITAGE OF PAST MISSIONS..... | 3 |
| 1.3 RESEARCH OBJECTIVES AND TASKS..... | 4 |
| 1.4 CONTENT AND STRUCTURE OF THIS REPORT..... | 5 |
| 2 CR3BP: ANALYSIS AND METHODS | 7 |
| 2.1 INTRODUCTION TO THE CIRCULAR PROBLEM..... | 7 |
| 2.1.1 <i>Dynamical model and reference frame</i> | 8 |
| 2.1.2 <i>Lagrange points and existing symmetries</i> | 10 |
| 2.1.3 <i>TEST-CASE: the Earth-Moon system</i> | 15 |
| 2.2 DYNAMICAL SYSTEM THEORY FOR THE CIRCULAR CASE..... | 19 |
| 2.2.1 <i>Proprieties of “autonomous differential systems”</i> | 19 |
| 2.2.2 <i>The Monodromy matrix and its eigenvalues</i> | 24 |
| 2.2.3 <i>Symplectic form: behaviour of “characteristic multipliers”</i> | 25 |
| 2.2.4 <i>Geometrical meaning of “characteristic multipliers”</i> | 26 |
| 2.2.5 <i>Bifurcation Theory: types and consequences</i> | 28 |
| 2.3 THE ANALYTIC APPROACH..... | 30 |
| 2.3.1 <i>Existence of two mono-parametric Lyapunov families</i> | 31 |
| 2.3.2 <i>Perturbation technique: the Lindstedt-Poincaré method</i> | 32 |
| 2.4 THE NUMERIC APPROACH..... | 38 |
| 2.4.1 <i>Differential Correction algorithm</i> | 38 |
| 2.4.2 <i>Periodicity constraints and numerical validation</i> | 41 |
| 2.4.3 <i>Numerical continuation</i> | 43 |
| 2.4.4 <i>Summary of the numerical algorithm</i> | 45 |
| 3 CR3BP: RESULTS | 47 |
| 3.1 THE HORIZONTAL LYAPUNOV FAMILY AT L1..... | 48 |
| 3.1.1 <i>Proprieties and main bifurcations</i> | 48 |
| 3.1.2 <i>Final comment on the family results</i> | 51 |
| 3.2 THE VERTICAL LYAPUNOV FAMILY AT L1..... | 52 |
| 3.2.1 <i>Proprieties and main bifurcations</i> | 52 |
| 3.2.2 <i>Final comment on the family results</i> | 55 |
| 3.3 THE HALO FAMILY AT L1..... | 56 |
| 3.3.1 <i>Proprieties and main bifurcations</i> | 56 |
| 3.3.2 <i>Final comment on the family results</i> | 59 |

| | | |
|----------|---|------------|
| 3.4 | THE HORIZONTAL LYAPUNOV FAMILY AT L2 | 60 |
| 3.4.1 | <i>Proprieties and main bifurcations</i> | 60 |
| 3.4.2 | <i>Final comment on the family results</i> | 63 |
| 3.5 | THE VERTICAL LYAPUNOV FAMILY AT L2 | 64 |
| 3.5.1 | <i>Proprieties and main bifurcations</i> | 64 |
| 3.5.2 | <i>Final comment on the family results</i> | 67 |
| 3.6 | THE HALO FAMILY AT L2 | 68 |
| 3.6.1 | <i>Proprieties and main bifurcations</i> | 68 |
| 3.6.2 | <i>Final comment on the family results</i> | 71 |
| 3.7 | CONCLUSIVE DISCUSSION ON RESULTS | 72 |
| 4 | ER3BP: ANALYSIS AND METHODS | 75 |
| 4.1 | INTRODUCTION TO THE ELLIPTIC PROBLEM | 75 |
| 4.1.1 | <i>Dynamical model and reference frame</i> | 76 |
| 4.1.2 | <i>Existence of Lagrange points and the new “symmetry constraint”</i> | 81 |
| 4.1.3 | <i>Variation in the symmetry: the shooting-time constraint</i> | 81 |
| 4.1.4 | <i>The non-existence of First Integrals</i> | 83 |
| 4.2 | DYNAMICAL SYSTEM THEORY FOR THE ELLIPTIC CASE | 84 |
| 4.2.1 | <i>Proprieties of “non-autonomous differential system”</i> | 85 |
| 4.2.2 | <i>Floquet Theory for linear stability assessment</i> | 86 |
| 4.2.3 | <i>The loss of continuous families in the ER3BP</i> | 88 |
| 4.3 | THE ANALYTIC APPROACH..... | 90 |
| 4.3.1 | <i>Stability under “elliptic perturbations” using LP-method</i> | 90 |
| 4.3.2 | <i>Extension to a non-linear dynamics and main limitations</i> | 94 |
| 4.4 | THE NUMERIC APPROACH..... | 95 |
| 4.4.1 | <i>Conditions on “MxNy resonance orbits”</i> | 95 |
| 4.4.2 | <i>Modifications in the Differential Correction scheme</i> | 96 |
| 4.4.3 | <i>Numerical Continuation in the eccentricity parameter</i> | 99 |
| 4.4.4 | <i>Summary of the extended numerical algorithm</i> | 101 |
| 5 | ER3BP: RESULTS | 103 |
| 5.1 | FEASIBLE MAIN RESONANCE SOLUTIONS | 103 |
| 5.1.1 | <i>Characteristic multipliers from the CR3BP to the ER3BP</i> | 103 |
| 5.1.2 | <i>Additional note on the Differential Correction algorithm</i> | 105 |
| 5.2 | FIRST EXAMPLE: THE H-LYAPUNOV M1N1 AT L1 | 106 |
| 5.2.1 | <i>Periodicity validation and eigenvalues analysis</i> | 107 |
| 5.3 | SECOND EXAMPLE: THE H-LYAPUNOV M2N1 AT L1 | 108 |
| 5.3.1 | <i>Periodicity validation and eigenvalues analysis</i> | 109 |
| 5.4 | THIRD EXAMPLE: THE V-LYAPUNOV M2N1 AT L1 | 112 |
| 5.5 | ESSENTIAL ASPECTS OF THE “ECCENTRICITY-BIFURCATION”..... | 115 |
| 5.5.1 | <i>Comparison Left/Right families: the Halo “M2N1” at L2</i> | 116 |
| 5.5.2 | <i>Comparison Apo/Peri groups: the Halo “M3N1” at L2</i> | 117 |
| 5.5.3 | <i>Summary of e-bifurcations for the Halo family at L2</i> | 118 |
| 5.6 | LINEAR STABILITY COMPARISON: CIRCULAR VS ELLIPTICAL..... | 121 |
| 5.6.1 | <i>Numerical stability of Peri/Apo-Halo M3N1-resonances at L2</i> | 122 |
| 5.6.2 | <i>Numerical stability due to shooting-phase errors</i> | 124 |
| 6 | CONCLUSIONS | 125 |
| 6.1 | CONCLUSIONS..... | 125 |
| 6.2 | RECOMMENDATIONS FOR FUTURE WORKS..... | 128 |

| | |
|---|------------|
| APPENDICES | 129 |
| A. CONSTANTS AND MAIN PARAMETERS USED..... | 131 |
| PRINCIPAL CONSTANTS FOR THE EARTH-MOON SYSTEM | 131 |
| <i>Comment on the “non-dimensional” system.....</i> | <i>132</i> |
| PARAMETERS ADOPTED FOR ALL MAIN SIMULATIONS..... | 133 |
| B. MATLAB SOFTWARE ENVIRONMENT AND SETTINGS..... | 135 |
| MATLAB ODE SUITE: THE “ODE113”..... | 135 |
| UNSTABLE DYNAMICS OF THE RESTRICTED THREE-BODY PROBLEM | 136 |
| C. OVERVIEW OF MAIN FAMILIES AT L1/L2 IN THE EM-SYSTEM | 141 |
| PRIMARY LYAPUNOV-BIFURCATION: THE HALO FAMILY | 143 |
| <i>Bifurcation shown at L1.....</i> | <i>143</i> |
| <i>Bifurcation shown at L2.....</i> | <i>144</i> |
| SECONDARY LYAPUNOV-BIFURCATION: THE AXIAL FAMILY | 145 |
| BIBLIOGRAPHY | 147 |

List of Figures

| | |
|---|----|
| FIGURE 1: WORKFLOW DIAGRAM OF THE CONTENT AND STRUCTURE OF THIS MASTER THESIS REPORT. IN ORANGE COLOUR THE TWO CHAPTERS RELATED TO THE DESCRIPTION OF MAIN ANALYSES AND METHODOLOGIES FOR BOTH TWO MODELS (CIRCULAR AND ELLIPTICAL). IN GREEN ALL CHAPTERS RELATIVE TO RESULTS AND LAST, IN RED THE FINAL CHAPTER RELATED TO THE CONCLUSIONS. SEE TEXT FOR MORE DETAILS AND INFORMATION. | 5 |
| FIGURE 2: INERTIAL IN RED X_I, Y_I, Z_I AND SYNODIC CO-ROTATING IN MAGENTA x, y, z REFERENCE FRAME FOR THE EARTH-MOON-SATELLITE CIRCULAR RESTRICTED 3-BODY PROBLEM. | 8 |
| FIGURE 3: LOCATION IN THE CO-ROTATING SYNODIC FRAME x, y, z OF ALL FIVE LIBRATION POINTS WITHIN THE xy -PLANE FOR THE EARTH-MOON CIRCULAR PROBLEM. THE SIZE OF MASSES HAS BEEN ENLARGED $[\times 4]$ | 10 |
| FIGURE 4: LOCATION OF ALL FIVE LIBRATION POINTS ON THE xy -PLANE WITH A VARYING μ -PARAMETER BETWEEN 0 AND 1. NOTE THE SYMMETRIC BEHAVIOUR RESPECT TO $\mu = 0.5$, AS EXPLAINED IN THE TEXT. | 11 |
| FIGURE 5: MAIN THREE SYMMETRIES FOR THE EARTH-MOON CIRCULAR RESTRICTED 3-BODY PROBLEM GIVEN IN SYNODIC COORDINATES. THE MASSES' SIZE HAS BEEN ENLARGED $[\times 8]$ FOR GRAPHICAL REASONS. | 14 |
| FIGURE 6: THE GEOMETRY AND THE MOTION OF THE EARTH-MOON SYSTEM IS SHOWN, WITH A SKETCH OF ALL MAIN REFERENCE PLANES INVOLVED (IN PURPLE) AND RELATIVE ANGLES (IN GREEN). | 16 |
| FIGURE 7: GEOMETRY OF THE INCLINED INERTIAL BI-CIRCULAR MODEL BY COURTESY OF (K. HILL ET AL., 2006). FOR THE NOTATION ADOPTED AND MORE DETAILS ON THE MODEL USED, WE REFER TO THEIR PAPER. | 17 |
| FIGURE 8: ILLUSTRATION OF TWO POINCARÉ MAPS (BLUE DIAMONDS) ON A 2-DIMENSIONAL POINCARÉ SECTION (IN VIOLET) FOR PERIODIC/NO-PERIODIC SOLUTIONS (RESPECTIVELY X_{OP} AND X_{ONP} IN DASHED RED). | 23 |
| FIGURE 9: THE THREE POSSIBLE BIFURCATIONS CONSIDERED HERE, LEADING TO THE DESTABILIZATION OF THE 4-DIMENSIONAL SYMPLECTIC MAP AND CONSEQUENTLY INCREASING THE ORDER OF INSTABILITY. | 29 |
| FIGURE 10: ILLUSTRATION ON THE yz -PLANE OF SOME POSSIBLE PERIODIC ORBITS (LEFT) AND LISSAJOUS CURVES (RIGHT) USING A GENERAL UNITARY REFERENCE PULSATION, WITH ω_{xy} AND ω_z RESPECTIVELY HORIZONTAL AND VERTICAL PULSATIONS OF THE DYNAMICS LINEARIZED AROUND L-POINTS. SEE TEXT ABOVE. | 31 |
| FIGURE 11: ILLUSTRATION OF HORIZONTAL AND VERTICAL LYAPUNOV FAMILIES AT L1 (LEFT) AND AT L2 (RIGHT) IN THE EARTH-MOON CR3BP, WHERE THE SIZE OF THE MOON HAS BEEN ENLARGED $\times 2$ | 32 |
| FIGURE 12: ILLUSTRATION OF INVESTIGATED FAMILIES AT L1/L2 IN THE EARTH-MOON SYSTEM: HORIZONTAL LYAPUNOV (RED), VERTICAL LYAPUNOV (GREEN) AND HALO (BLUE) ARE SHOWN AT SAME ENERGY-LEVEL. | 37 |
| FIGURE 13: EXAMPLE OF PERTURBED TRAJECTORY $X(t)$ DEVIATING RESPECT TO THE NOMINAL ONE DEFINED BY $X^*(t)$, WHERE $\delta X(t_0)$ AND $\delta X(t_f)$ ARE RESPECTIVELY THE INITIAL AND THE FINAL DISPLACEMENT. | 38 |
| FIGURE 14: EXAMPLE OF INITIAL GUESS (RED) AND FINAL PATH (BLUE) CORRECTED BY THE DC-ALGORITHM, HAVING THE "ORTHOGONALITY CONDITIONS" AT THE SHOOTING (\diamond) AND AT THE FIRST CROSS (BLUE STAR). | 39 |
| FIGURE 15: EXAMPLE OF "PERIODICITY-VALIDATION" FOR THE HALO FAMILY AT L2 IN THE EARTH-MOON SYSTEM $\mu = 0.012151$. THE COMPLETE DESCRIPTION WILL BE GIVEN IN CHAPTER 3, WITH ALSO RESULTS. | 42 |
| FIGURE 16: EXAMPLE IS GIVEN OF NUMERICAL CONTINUATION BY "NATURAL PARAMETER" (RED) AND "PSEUDO-ARCLENGTH" (GREEN), WHERE WE CONSIDER THE xz -PLANE OF THE EARTH-MOON SYSTEM. IN BLUE BOTH INITIAL SOLUTIONS, WHILE IN DARK YELLOW THE SET OF CORRECTED SHOOTING POSITIONS x_0, z_{0i} | 44 |
| FIGURE 17: GRAPHICAL PLOT OF THE H-LYAPUNOV FAMILY OF PERIODIC ORBITS, EVERY 50 MEMBERS WITH THEIR RELATIVE ORDER OF STABILITY (0-GREEN, 1-BLUE, 2-RED). IT ALSO SHOWS THE MOON (GREY), WITH THE L-POINTS (MAGENTA STAR), SHOOTING CONDITIONS (BLACK DOTS) AND LAST ORBIT (BLACK LINE). | 48 |
| FIGURE 18: GRAPHICAL REPRESENTATION OF ORBITAL ENERGY "J" (TOP-LEFT), WITH ITS ERROR ALONG EACH TRAJECTORY (BOTTOM-LEFT) BASED ON MEAN AND STANDARD DEVIATION. LAST, THE ORBITAL PERIOD "T" (BOTTOM-RIGHT) IS SHOWN ALSO COMPARED WITH THE SAME ORBITAL ENERGY (TOP-RIGHT). | 48 |
| FIGURE 19: ANALYSIS ON THE MONODROMY MATRIX, SHOWING ON THE LEFT THE ORDERS OF INSTABILITY (0-GREEN, 1-BLUE, 2-RED) AND THE ERROR ON THE DETERMINANT, AS DESCRIBED IN SECTION 2.2.4. ON THE RIGHT, THE MODULE OF ALL SIX "CHARACTERISTIC MULTIPLIERS" IS SHOWN, WITH A ZOOM ON THE THRESHOLD VALUE USED FOR CALCULATING THE ORDER-OF-INSTABILITY (RIGHT-BOTTOM). | 49 |
| FIGURE 20: ILLUSTRATION OF SIX EIGENVALUES λ_i AND THREE STABILITY INDICES $v_i = (\lambda_i + \lambda_i^{-1})/2$, GIVEN FOR EACH PAIR OF RECIPROCAL VALUE. MOTION ON COMPLEX PLANE (TOP), RELATIVE PHASE (MIDDLE) AND STABILITY INDEX (BOTTOM) ARE SHOWN, AS THEY WILL BE EXPLAINED IN THE <i>FINAL COMMENT</i> SECTION. | 49 |
| FIGURE 21: ILLUSTRATION OF THE VALIDATION AND VERIFICATION PERFORMED DURING THE NUMERICAL CONTINUATION PROCESS. ALL RELATIVE INFORMATION AND NOTATION CAN BE FOUND IN THE SECTION 2.4.2. | 50 |

FIGURE 22: MAIN RESONANCE ORBITS EXISTING WITHIN THE FAMILY ARE GIVEN USING COMBINATIONS OF M-VALUE (*ORBIT REVOLUTIONS*) AND N-VALUE (*SYSTEM REVOLUTIONS*), WITH $M_{max} = 12$ AND $N_{max} = 4$. THE SYSTEM 2π -PERIOD IS GIVEN BY $N = 1$, WHILE MORE DETAILS CAN BE FOUND LATER IN SECTION 4.4.1. 50

FIGURE 23: SET OF SHOOTING CONDITIONS AT BOTH xz -PLANE CROSSINGS [$t_0 = 0, T_c/2$] WITH THE RELATIVE ORDER OF INSTABILITY. LOOK AT THE LEGEND FOR INFORMATION ON THE COLOUR-NOTATION ADOPTED. 51

FIGURE 24: GRAPHICAL PLOT OF THE V-LYAPUNOV FAMILY OF PERIODIC ORBITS, EVERY 50 MEMBERS WITH THEIR RELATIVE ORDER OF STABILITY (0-GREEN, 1-BLUE, 2-RED). IT ALSO SHOWS THE MOON (GREY), WITH THE L-POINTS (MAGENTA STAR), SHOOTING CONDITIONS (BLACK DOTS) AND LAST ORBIT (BLACK LINE). 52

FIGURE 25: GRAPHICAL REPRESENTATION OF ORBITAL ENERGY “J” (TOP-LEFT), WITH ITS ERROR ALONG EACH TRAJECTORY (BOTTOM-LEFT) BASED ON MEAN AND STANDARD DEVIATION. LAST, THE ORBITAL PERIOD “T” (BOTTOM-RIGHT) IS SHOWN ALSO COMPARED WITH THE SAME ORBITAL ENERGY (TOP-RIGHT). 52

FIGURE 26: ANALYSIS ON THE MONODROMY MATRIX, SHOWING ON THE LEFT THE ORDERS OF INSTABILITY (0-GREEN, 1-BLUE, 2-RED) AND THE ERROR ON THE DETERMINANT, AS DESCRIBED IN SECTION 2.2.4. ON THE RIGHT, THE MODULE OF ALL SIX “CHARACTERISTIC MULTIPLIERS” IS SHOWN, WITH A ZOOM ON THE THRESHOLD VALUE USED FOR CALCULATING THE ORDER-OF-INSTABILITY (RIGHT-BOTTOM). 53

FIGURE 27: ILLUSTRATION OF EIGENVALUES λ_i AND STABILITY INDICES $\nu_i = (\lambda_i + \lambda_i^{-1})/2$, GIVEN FOR EACH PAIR OF RECIPROCAL VALUE. MOTION ON COMPLEX PLANE (TOP), RELATIVE PHASE (MIDDLE) AND STABILITY INDEX (BOTTOM) ARE SHOWN AND THEY WILL BE EXPLAINED IN THE *FINAL COMMENT* SECTION. 53

FIGURE 28: ILLUSTRATION OF THE VALIDATION AND VERIFICATION PERFORMED DURING THE NUMERICAL CONTINUATION PROCESS. ALL RELATIVE INFORMATION AND NOTATION CAN BE FOUND IN THE SECTION 2.4.2 54

FIGURE 29: MAIN RESONANCE ORBITS EXISTING WITHIN THE FAMILY ARE GIVEN USING COMBINATIONS OF M-VALUE (*ORBIT REVOLUTIONS*) AND N-VALUE (*SYSTEM REVOLUTIONS*), WITH $M_{max} = 12$ AND $N_{max} = 4$. THE SYSTEM 2π -PERIOD IS GIVEN BY $N = 1$, WHILE MORE DETAILS CAN BE FOUND LATER IN SECTION 4.4.1. 54

FIGURE 30: SET OF SHOOTING CONDITIONS AT BOTH xz -PLANE CROSSINGS [$t_0 = 0, T_c/2$] WITH THE RELATIVE ORDER OF INSTABILITY. LOOK AT THE LEGEND FOR INFORMATION ON THE COLOUR-NOTATION ADOPTED. 55

FIGURE 31: GRAPHICAL PLOT OF THE HALO FAMILY OF PERIODIC ORBITS, EVERY 50 MEMBERS WITH THEIR RELATIVE ORDER OF STABILITY (0-GREEN, 1-BLUE, 2-RED). IT ALSO SHOWS THE MOON (GREY), THE L-POINTS (MAGENTA STAR), SHOOTING CONDITIONS (BLACK DOTS) AND LAST ORBIT (BLACK LINE). 56

FIGURE 32: GRAPHICAL REPRESENTATION OF ORBITAL ENERGY “J” (TOP-LEFT), WITH ITS ERROR ALONG EACH TRAJECTORY (BOTTOM-LEFT) BASED ON MEAN AND STANDARD DEVIATION. LAST, THE ORBITAL PERIOD “T” (BOTTOM-RIGHT) IS SHOWN ALSO COMPARED WITH THE SAME ORBITAL ENERGY (TOP-RIGHT). 56

FIGURE 33: ANALYSIS ON THE MONODROMY MATRIX, SHOWING ON THE LEFT THE ORDERS OF INSTABILITY (0-GREEN, 1-BLUE, 2-RED) AND THE ERROR ON THE DETERMINANT, AS DESCRIBED IN SECTION 2.2.4. ON THE RIGHT, THE MODULE OF ALL SIX “CHARACTERISTIC MULTIPLIERS” IS SHOWN, WITH A ZOOM ON THE THRESHOLD VALUE USED FOR CALCULATING THE ORDER-OF-INSTABILITY (RIGHT-BOTTOM). 57

FIGURE 34: ILLUSTRATION OF EIGENVALUES λ_i AND STABILITY INDICES $\nu_i = (\lambda_i + \lambda_i^{-1})/2$, GIVEN FOR EACH PAIR OF RECIPROCAL VALUE. MOTION ON COMPLEX PLANE (TOP), RELATIVE PHASE (MIDDLE) AND STABILITY INDEX (BOTTOM) ARE SHOWN AND THEY WILL BE EXPLAINED IN THE *FINAL COMMENT* SECTION. 57

FIGURE 35: ILLUSTRATION OF THE VALIDATION AND VERIFICATION PERFORMED DURING THE NUMERICAL CONTINUATION PROCESS. ALL RELATIVE INFORMATION AND NOTATION CAN BE FOUND IN THE SECTION 2.4.2 58

FIGURE 36: MAIN RESONANCE ORBITS EXISTING WITHIN THE FAMILY ARE GIVEN USING COMBINATIONS OF M-VALUE (*ORBIT REVOLUTIONS*) AND N-VALUE (*SYSTEM REVOLUTIONS*), WITH $M_{max} = 12$ AND $N_{max} = 4$. THE SYSTEM 2π -PERIOD IS GIVEN BY $N = 1$, WHILE MORE DETAILS CAN BE FOUND LATER IN SECTION 4.4.1. 58

FIGURE 37: SET OF SHOOTING CONDITIONS AT BOTH xz -PLANE CROSSINGS [$t_0 = 0, T_c/2$] WITH THE RELATIVE ORDER OF INSTABILITY. LOOK AT THE LEGEND FOR INFORMATION ON THE COLOR-NOTATION ADOPTED. 59

FIGURE 38: GRAPHICAL PLOT OF THE H-LYAPUNOV FAMILY OF PERIODIC ORBITS, EVERY 50 MEMBERS WITH THEIR RELATIVE ORDER OF STABILITY (0-GREEN, 1-BLUE, 2-RED). IT ALSO SHOWS THE MOON (GREY), WITH THE L-POINTS (MAGENTA STAR), SHOOTING CONDITIONS (BLACK DOTS) AND LAST ORBIT (BLACK LINE). 60

FIGURE 39: GRAPHICAL REPRESENTATION OF ORBITAL ENERGY “J” (TOP-LEFT), WITH ITS ERROR ALONG EACH TRAJECTORY (BOTTOM-LEFT) BASED ON MEAN AND STANDARD DEVIATION. LAST, THE ORBITAL PERIOD “T” (BOTTOM-RIGHT) IS SHOWN ALSO COMPARED WITH THE SAME ORBITAL ENERGY (TOP-RIGHT). 60

FIGURE 40: ANALYSIS ON THE MONODROMY MATRIX, SHOWING ON THE LEFT THE ORDERS OF INSTABILITY (0-GREEN, 1-BLUE, 2-RED) AND THE ERROR ON THE DETERMINANT, AS DESCRIBED IN SECTION 2.2.4. ON THE RIGHT, THE MODULE OF ALL SIX “CHARACTERISTIC MULTIPLIERS” IS SHOWN, WITH A ZOOM ON THE THRESHOLD VALUE USED FOR CALCULATING THE ORDER-OF-INSTABILITY (RIGHT-BOTTOM). 61

| | |
|---|----|
| FIGURE 41: ILLUSTRATION OF EIGENVALUES λ_i AND STABILITY INDICES $\nu_i = (\lambda_i + \lambda_i^{-1})/2$, GIVEN FOR EACH PAIR OF RECIPROCAL VALUE. MOTION ON COMPLEX PLANE (TOP), RELATIVE PHASE (MIDDLE) AND STABILITY INDEX (BOTTOM) ARE SHOWN AND THEY WILL BE EXPLAINED IN THE <i>FINAL COMMENT</i> SECTION. | 61 |
| FIGURE 42: ILLUSTRATION OF THE VALIDATION AND VERIFICATION PERFORMED DURING THE NUMERICAL CONTINUATION PROCESS. ALL RELATIVE INFORMATION AND NOTATION CAN BE FOUND IN THE SECTION 2.4.2 | 62 |
| FIGURE 43: MAIN RESONANCE ORBITS EXISTING WITHIN THE FAMILY ARE GIVEN USING COMBINATIONS OF M-VALUE (<i>ORBIT REVOLUTIONS</i>) AND N-VALUE (<i>SYSTEM REVOLUTIONS</i>), WITH $M_{max} = 12$ AND $N_{max} = 4$. THE SYSTEM 2π -PERIOD IS GIVEN BY $N = 1$, WHILE MORE DETAILS CAN BE FOUND LATER IN SECTION 4.4.1. | 62 |
| FIGURE 44: SET OF SHOOTING CONDITIONS AT BOTH xz -PLANE CROSSINGS [$t_0 = 0, T_c/2$] WITH THE RELATIVE ORDER OF INSTABILITY. LOOK AT THE LEGEND FOR INFORMATION ON THE COLOUR-NOTATION ADOPTED. | 63 |
| FIGURE 45: GRAPHICAL PLOT OF THE V-LYAPUNOV FAMILY OF PERIODIC ORBITS, EVERY 50 MEMBERS WITH THEIR RELATIVE ORDER OF STABILITY (0-GREEN, 1-BLUE, 2-RED). IT ALSO SHOWS THE MOON (GREY), WITH THE L-POINTS (MAGENTA STAR), SHOOTING CONDITIONS (BLACK DOTS) AND LAST ORBIT (BLACK LINE). | 64 |
| FIGURE 46: GRAPHICAL REPRESENTATION OF ORBITAL ENERGY “J” (TOP-LEFT), WITH ITS ERROR ALONG EACH TRAJECTORY (BOTTOM-LEFT) BASED ON MEAN AND STANDARD DEVIATION. LAST, THE ORBITAL PERIOD “T” (BOTTOM-RIGHT) IS SHOWN ALSO COMPARED WITH THE SAME ORBITAL ENERGY (TOP-RIGHT). | 64 |
| FIGURE 47: ANALYSIS ON THE MONODROMY MATRIX, SHOWING ON THE LEFT THE ORDERS OF INSTABILITY (0-GREEN, 1-BLUE, 2-RED) AND THE ERROR ON THE DETERMINANT, AS DESCRIBED IN SECTION 2.2.4. ON THE RIGHT, THE MODULE OF ALL SIX “CHARACTERISTIC MULTIPLIERS” IS SHOWN, WITH A ZOOM ON THE THRESHOLD VALUE USED FOR CALCULATING THE ORDER-OF-INSTABILITY (RIGHT-BOTTOM). | 65 |
| FIGURE 48: ILLUSTRATION OF EIGENVALUES λ_i AND STABILITY INDICES $\nu_i = (\lambda_i + \lambda_i^{-1})/2$, GIVEN FOR EACH PAIR OF RECIPROCAL VALUE. MOTION ON COMPLEX PLANE (TOP), RELATIVE PHASE (MIDDLE) AND STABILITY INDEX (BOTTOM) ARE SHOWN AND THEY WILL BE EXPLAINED IN THE <i>FINAL COMMENT</i> SECTION. | 65 |
| FIGURE 49: ILLUSTRATION OF THE VALIDATION AND VERIFICATION PERFORMED DURING THE NUMERICAL CONTINUATION PROCESS. ALL RELATIVE INFORMATION AND NOTATION CAN BE FOUND IN THE SECTION 2.4.2 | 66 |
| FIGURE 50: MAIN RESONANCE ORBITS EXISTING WITHIN THE FAMILY ARE GIVEN USING COMBINATIONS OF M-VALUE (<i>ORBIT REVOLUTIONS</i>) AND N-VALUE (<i>SYSTEM REVOLUTIONS</i>), WITH $M_{max} = 12$ AND $N_{max} = 4$. THE SYSTEM 2π -PERIOD IS GIVEN BY $N = 1$, WHILE MORE DETAILS CAN BE FOUND LATER IN SECTION 4.4.1. | 66 |
| FIGURE 51: SET OF SHOOTING CONDITIONS AT BOTH xz -PLANE CROSSINGS [$t_0 = 0, T_c/2$] WITH THE RELATIVE ORDER OF INSTABILITY. LOOK AT THE LEGEND FOR INFORMATION ON THE COLOR-NOTATION ADOPTED. | 67 |
| FIGURE 52: GRAPHICAL PLOT OF THE HALO FAMILY OF PERIODIC ORBITS, EVERY 50 MEMBERS WITH THEIR RELATIVE ORDER OF STABILITY (0-GREEN, 1-BLUE, 2-RED). IT ALSO SHOWS THE MOON (GREY), THE L-POINTS (MAGENTA STAR), SHOOTING CONDITIONS (BLACK DOTS) AND LAST ORBIT (BLACK LINE). | 68 |
| FIGURE 53: GRAPHICAL REPRESENTATION OF ORBITAL ENERGY “J” (TOP-LEFT), WITH ITS ERROR ALONG EACH TRAJECTORY (BOTTOM-LEFT) BASED ON MEAN AND STANDARD DEVIATION. LAST, THE ORBITAL PERIOD “T” (BOTTOM-RIGHT) IS SHOWN ALSO COMPARED WITH THE SAME ORBITAL ENERGY (TOP-RIGHT). | 68 |
| FIGURE 54: ANALYSIS ON THE MONODROMY MATRIX, SHOWING ON THE LEFT THE ORDERS OF INSTABILITY (0-GREEN, 1-BLUE, 2-RED) AND THE ERROR ON THE DETERMINANT, AS DESCRIBED IN SECTION 2.2.4. ON THE RIGHT, THE MODULE OF ALL SIX “CHARACTERISTIC MULTIPLIERS” IS SHOWN, WITH A ZOOM ON THE THRESHOLD VALUE USED FOR CALCULATING THE ORDER-OF-INSTABILITY (RIGHT-BOTTOM). | 69 |
| FIGURE 55: ILLUSTRATION OF EIGENVALUES λ_i AND STABILITY INDICES $\nu_i = (\lambda_i + \lambda_i^{-1})/2$, GIVEN FOR EACH PAIR OF RECIPROCAL VALUE. MOTION ON COMPLEX PLANE (TOP), RELATIVE PHASE (MIDDLE) AND STABILITY INDEX (BOTTOM) ARE SHOWN AND THEY WILL BE EXPLAINED IN THE <i>FINAL COMMENT</i> SECTION. | 69 |
| FIGURE 56: ILLUSTRATION OF THE VALIDATION AND VERIFICATION PERFORMED DURING THE NUMERICAL CONTINUATION PROCESS. ALL RELATIVE INFORMATION AND NOTATION CAN BE FOUND IN THE SECTION 2.4.2 | 70 |
| FIGURE 57: MAIN RESONANCE ORBITS EXISTING WITHIN THE FAMILY ARE GIVEN USING COMBINATIONS OF M-VALUE (<i>ORBIT REVOLUTIONS</i>) AND N-VALUE (<i>SYSTEM REVOLUTIONS</i>), WITH $M_{max} = 12$ AND $N_{max} = 4$. THE SYSTEM 2π -PERIOD IS GIVEN BY $N = 1$, WHILE MORE DETAILS CAN BE FOUND LATER IN SECTION 4.4.1. | 70 |
| FIGURE 58: SET OF SHOOTING CONDITIONS AT BOTH xz -PLANE CROSSINGS [$t_0 = 0, T_c/2$] WITH THE RELATIVE ORDER OF INSTABILITY. LOOK AT THE LEGEND FOR INFORMATION ON THE COLOR-NOTATION ADOPTED. | 71 |
| FIGURE 59: ILLUSTRATION OF BOTH INERTIAL (RED) AND SYNODIC FRAMES (MAGENTA) FOR THE ELLIPTICAL RESTRICTED 3-BODY PROBLEM, WITH DISTANCES x_1, x_2 REFERRING TO THE POSITION OF M_1, M_2 ALONG THE SYZGY. IN WHITE, THE θ -PHASE IS SHOWN STARTING FROM THE PERI-APSIS, WHILE ALSO $r = r(e, \theta)$ IS SHOWN AS TIME-DEPENDENT RELATIVE DISTANCE BETWEEN BOTH MASSES, AS DESCRIBED IN EQ. (2-1). | 76 |
| FIGURE 60: MAIN THREE SYMMETRIES FOR THE EARTH-MOON ELLIPTICAL RESTRICTED 3-BODY PROBLEM IN PULSATING SYNODIC COORDINATES, WITH $e = 0.1$ AND STARTING AT $\theta_0 = 0$. COMPARE TO FIGURE 5. | 82 |

FIGURE 61: MAIN THREE SYMMETRIES FOR THE EARTH-MOON ELLIPTICAL RESTRICTED 3-BODY PROBLEM IN PULSATING SYNODIC COORDINATES, WITH $e = 0.1$ AND STARTING AT $\theta_0 = \pi/3$. NOTE THE LOSS OF BOTH BACKWARD AND BACKWARD-MIRRORED SYMMETRIES DUE TO THE CONDITION GIVEN IN EQ. (4-19). 83

FIGURE 62: ILLUSTRATION SHOWING TWO POSSIBLE “SEPARATIONS” OF THE TWO REAL UNITARY EIGENVALUES OF A HALO SOLUTION. BRANCH I (GREEN) LEADS TO ADDITIONAL STABLE/UNSTABLE MANIFOLDS, WHILE BRANCH II (RED) LEADS TO COMPLEX CONJUGATE VALUES THAT DO NOT CHANGE THE ORDER OF INSTABILITY. COURTESY OF (S. CAMPAGNOLA ET AL., 2008). 88

FIGURE 63: ILLUSTRATION SHOWING TWO QUASI-PERIODIC FAMILIES AT L₂ IN THE CR₃BP. ON THE LEFT, THE LISSAJOUS ONE EXISTS AT EACH L-POINT AROUND THE VERTICAL LYAPUNOV FAMILY, WHILE ON THE RIGHT THE QUASI-HALO ONE. BOTH ARE CONSEQUENCES OF EXISTING COMPLEX CONJUGATE EIGENVALUES IN THE RELATIVE MONODROMY MATRIX. COURTESY OF (NAGATA ET AL., 2016). 89

FIGURE 64: EXAMPLE SHOWING A SOUTHERN HALO “RESONANCE” ORBIT (M₅N₂) AT L₁, LIBRATION POINT FOR THE EARTH-MOON CR₃BP SYSTEM IN BOTH A ROTATING (LEFT) AND INERTIAL FRAME (RIGHT). 98

FIGURE 65: EXAMPLE OF PERIODICITY ASSESSMENT CONSIDERING M-REVOLUTIONS FOR THE “RESONANCE” SOLUTION ILLUSTRATED IN FIGURE 64. THE MODULUS OF POSITION AND VELOCITY-VARIATIONS (W.R.T. THE INITIAL CONDITION) ARE SHOWN (LEFT-CENTRE) WITH PERIODICITY ERROR (ORANGE CIRCLE). ENERGY ERROR (RIGHT-TOP) AND ABSOLUTE VALUE OF CHARACTERISTIC EXPONENTS (RIGHT-BOTTOM) ARE ALSO GIVEN. 98

FIGURE 66: EXAMPLE SHOWING FOUR EXAMPLES OF RESONANCE ORBITS EXTENDED TO THE ER₃BP WITH $e = 0.1$ WITHIN A NO-PULSATING REFERENCE FRAME: LEFT-HALO “M₂N₁” (TOP-LEFT), RIGHT-HALO “M₂N₁” (TOP-RIGHT), APO-HALO “M₃N₁” (BOTTOM-LEFT) AND PERI-HALO “M₃N₁” (BOTTOM-RIGHT). 100

FIGURE 67: EXAMPLE OF THE ACCURACY VERIFICATION DURING THE PROPAGATION OF A M₂N₁ RESONANCE ORBIT FOR THE H-LYAPUNOV FAMILY (L₁, EARTH-MOON SYSTEM). SEE SECTION 2.4.2 FOR MORE DETAILS. 105

FIGURE 68: EXAMPLE IS SHOWN OF THE STARTING RESONANCE ORBIT (M₁N₁) AT L₁ FOR THE H-LYAPUNOV FAMILY. ON THE LEFT THE 3D-PLOT IS GIVEN IN BOTH CO-ROTATING AND INERTIAL FRAMES, WHILE ON THE RIGHT THE PERIODICITY IS SHOWN TOGETHER WITH ALL SIX CHARACTERISTIC MULTIPLIERS (IN MODULE). 106

FIGURE 69: THE RESONANCE M₁N₁ H-LYAPUNOV ORBIT AT L₁ IS SHOWN IN BOTH NO-PULSATING (TOP) AND PULSATING (BOTTOM) COORDINATES. NOTE THE EXISTENCE OF TWO DIFFERENT GROUPS WHERE THE SHOOTING TIME IS $\theta_0 = 0$ ON THE LEFT (PERI-), WHILE IT IS $\theta_0 = \pi$ ON THE RIGHT (APO-). 106

FIGURE 70: PERIODICITY VALIDATION SHOWN FOR BOTH PERI-GROUP (LEFT) AND APO-GROUP (RIGHT), BOTH GENERATED FOR THE M₁N₁ H-LYAPUNOV RESONANCE SOLUTION AT L₁. 107

FIGURE 71: ANALYSIS OF CHARACTERISTIC MULTIPLIERS FOR BOTH THE PERI-GROUP (TOP) AND APO-GROUP (BOTTOM) GENERATED FOR THE M₁N₁ H-LYAPUNOV RESONANCE SOLUTION AT L₁. NOTE CHANGES IN THE ORDER OF INSTABILITY, DUE TO A DIFFERENT BIFURCATION OF BOTH REAL UNITARY EIGENVALUES (SEE TEXT). 107

FIGURE 72: EXAMPLE IS SHOWN OF THE STARTING RESONANCE ORBIT (M₂N₁) AT L₁ FOR THE H-LYAPUNOV FAMILY. ON THE LEFT THE 3D-PLOT IS GIVEN IN BOTH CO-ROTATING AND INERTIAL FRAMES, WHILE ON THE RIGHT THE PERIODICITY IS SHOWN TOGETHER WITH ALL SIX CHARACTERISTIC MULTIPLIERS (IN MODULE). 109

FIGURE 73: THE RESONANCE M₂N₁ H-LYAPUNOV ORBIT AT L₁ IS SHOWN IN BOTH NO-PULSATING (TOP) AND PULSATING (BOTTOM) COORDINATES. NOTE THE EXISTENCE OF TWO FAMILIES WHERE THE FIRST ORTHOGONAL CROSS HAS BEEN CONSIDERED RESPECTIVELY AT THE LEFT AND RIGHT ON THE X-AXIS. 109

FIGURE 74: PERIODICITY VALIDATION FOR BOTH THE LEFT-FAMILY (LEFT) AND RIGHT-FAMILY (RIGHT) GENERATED FOR THE M₂N₁ H-LYAPUNOV RESONANCE SOLUTION AT L₁. 110

FIGURE 75: ANALYSIS OF CHARACTERISTIC MULTIPLIERS FOR THE LEFT-FAMILY (TOP) AND RIGHT-FAMILY (BOTTOM) GENERATED FOR THE M₂N₁ H-LYAPUNOV RESONANCE SOLUTION AT L₁. NOTE CHANGES IN THE ORDER OF INSTABILITY, DUE TO A DIFFERENT BIFURCATION OF BOTH REAL UNITARY EIGENVALUES (SEE TEXT). 110

FIGURE 76: EXAMPLE IS SHOWN OF THE STARTING RESONANCE ORBIT (M₂N₁) FOR THE V-LYAPUNOV FAMILY AT L₁. ON THE LEFT THE 3D-PLOT IS GIVEN IN BOTH CO-ROTATING AND INERTIAL FRAMES, WHILE ON THE RIGHT THE PERIODICITY IS SHOWN TOGETHER WITH CHARACTERISTIC MULTIPLIERS. 112

FIGURE 77: THE LEFT-FAMILY (TOP) AND THE RIGHT-FAMILY (BOTTOM) ARE SHOWN RESPECTIVELY ON THE xy-PLANE (LEFT SIDE) AND ON THE xz-PLANE IN NO-PULSATING COORDINATES. BOTH FAMILIES BIFURCATED FROM THE M₂N₁-RESONANCE ORBIT FOUND WITHIN THE VERTICAL LYAPUNOV FAMILY AT L₁. 112

FIGURE 78: PERIODICITY VALIDATION (TOP) AND EIGENVALUES ANALYSIS (BOTTOM) GENERATED FOR THE M₂N₁ V-LYAPUNOV RESONANCE SOLUTION AT L₁, WHERE THE LEFT-FAMILY AND THE RIGHT-FAMILY HAVE BEEN SHOWN, BOTH ARISING FROM THE e -BIFURCATION AT $e \cong 0$. SEE DISCUSSION IN THE TEXT. 113

FIGURE 79: ANALYSIS OF THE CHARACTERISTIC MULTIPLIERS AS SHOWN IN FIGURE 78 FOR BOTH LEFT AND RIGHT BIFURCATED FAMILIES, BUT NOW FURTHER EXTENDED TO AN HIGH ECCENTRICITY WITH $e_{TEST} = 0.1$ 113

| | |
|---|-----|
| FIGURE 80: THE LEFT-FAMILY (TOP) AND THE RIGHT-FAMILY (BOTTOM), BOTH BIFURCATING FROM THE SELECTED M2N1-RESONANCE WITHIN THE V-LYAPUNOV FAMILY AT L1, HAVE BEEN HERE ILLUSTRATE IN A 3D-PLOT, BASED ON A NO-PULSATING REFERENCE FRAME, WITH THE NOMINAL ECCENTRICITY $e_{EM} = 0.0549$ | 114 |
| FIGURE 81: STARTING RESONANCE ORBIT (M2N1) FOR THE HALO FAMILY AT L1. IT SHOWS THE 3D-PLOT IN BOTH CO-ROTATING AND INERTIAL FRAMES (LEFT) AND THE RELATIVE PERIODICITY/EIGENVALUES (RIGHT)..... | 115 |
| FIGURE 82: STARTING RESONANCE ORBIT (M3N1) FOR THE HALO FAMILY AT L1. IT SHOWS THE 3D-PLOT IN BOTH CO-ROTATING AND INERTIAL FRAMES (LEFT) AND THE RELATIVE PERIODICITY/EIGENVALUES (RIGHT)..... | 115 |
| FIGURE 83: ILLUSTRATION OF THE LEFT/RIGHT-FAMILIES BIFURCATING FROM THE M2N1-RESONANCE ORBIT OF THE HALO FAMILY AT L2. THE 3D-PLOT (TOP), THE PERIODICITY VALIDATION (MIDDLE) AND THE EIGENVALUES ANALYSIS (BOTTOM) HAVE BEEN SHOWN AS WELL EXPLAINED IN THE EARLIER RESULTS..... | 116 |
| FIGURE 84: ILLUSTRATION OF THE PERI/APO-GROUPS BIFURCATING FROM THE M3N1-RESONANCE ORBIT OF THE HALO FAMILY AT L2. THE 3D-PLOT (TOP), THE PERIODICITY VALIDATION (MIDDLE) AND THE EIGENVALUES ANALYSIS (BOTTOM) HAVE BEEN SHOWN AS WELL EXPLAINED IN THE EARLIER RESULTS..... | 117 |
| FIGURE 85: ILLUSTRATION OF THE MOTION IN THE COMPLEX-PLANE OF ALL SIX EIGENVALUES FOR THE PERI-GROUP (TOP) AND THE APO-GROUP (BOTTOM) BIFURCATED FROM THE M3N1-RESONANCE OF THE HALO FAMILY AT L2. IN BLUE/MAGENTA THE INITIAL/FINAL VALUES, WHILE IN RED THE FULL “PATH” IS SHOWN. | 120 |
| FIGURE 86: ILLUSTRATION OF THE M3N1-RESONANCE ORBIT INTEGRATED IN THE FULL DYNAMICS OF THE ELLIPTIC PROBLEM $e_{EM} = 0.0549$, STARTING WITH THE SHOOTING CONDITION PREVIOUSLY FOUND IN THE CIRCULAR MODEL. IN MAGENTA BOTH LIBRATION POINTS HAVE BEEN SHOWN. | 121 |
| FIGURE 87: NUMERICAL INTEGRATION OF THE M3N1 HALO AT L2, USING THE FULL ER3BP-DYNAMICS AND STARTING WITH SHOOTING CONDITIONS FOUND RESPECTIVELY FOR THE PERI-GROUP (LEFT) AND FOR THE APO-GROUP (RIGHT). IN MAGENTA BOTH LIBRATION POINTS HAVE BEEN SHOWN. | 122 |
| FIGURE 88: NUMERICAL INTEGRATION OF THE M3N1 HALO RESONANCE ORBIT AT L2 FOR THE PERI-GROUP (TOP) AND THE APO-GROUP (BOTTOM), WHERE POSITION AND VELOCITY DISPLACEMENTS FROM RESPECTIVE INITIAL CONDITIONS (IN ORANGE). ALL T_E -PERIODICITY ERRORS ARE SHOWN (IN RED-DOTS). | 123 |
| FIGURE 89: ILLUSTRATION OF POSITION AND VELOCITY “PERIODICITY ERRORS” REFERRING TO 18 SYSTEM REVOLUTIONS AND A RANGE OF PHASE-SHIFT FROM THE NOMINAL SHOOTING-TIME AS $\pm\pi/360$. ABSOLUTE ERRORS ARE GIVEN IN A LOGIO SCALE, WHILE TIME-SHIFT IS BASED ON MINUTES FOR THE EM-SYSTEM. | 124 |
| FIGURE 90: IT SHOWS GRAPHICAL RESULTS BASED ON THE COMPARISON AMONG DIFFERENT ORDERS OF INSTABILITY, THUS NUMERICALLY INTEGRATING FOR 60 SYSTEM REVOLUTIONS (CORRESPONDING TO 5 YEARS) THE THREE MEMBERS OF THE HALO FAMILY AT L2 IN THE EARTH-MOON SYSTEM (SYNODIC FRAME). | 137 |
| FIGURE 91: PLOT OF THREE PERIODIC SOLUTIONS (HALO FAMILY AT L2 IN THE EARTH-MOON SYSTEM) WITH THREE DIFFERENT ORDERS-OF-INSTABILITY. DISPLACEMENT IN POSITION (TOP), VELOCITY (MIDDLE) AND ENERGY (BOTTOM) IS SHOWN OVER AROUND 60 SYSTEMS REVOLUTIONS, AS DESCRIBED IN THE TEXT..... | 138 |
| FIGURE 92: ILLUSTRATION OF THE OVERALL PHASE-SPACE OF SHOOTING CONDITIONS FOR ALL THREE FAMILIES ANALYSED IN THIS WORK, REFERRING TO BOTH L1 AND L2 LIBRATIONS POINT OF THE EARTH-MOON CR3BP. MORE DETAILS CAN BE FOUND IN CHAPTER 3, WHILE FOR THE NOTATION WE REFER TO THE LEGEND..... | 141 |
| FIGURE 93: ADDITIONAL PLOTS FOR THE PHASE-SPACE OF SHOOTING CONDITIONS FOR ALL THREE FAMILIES ANALYSED IN THIS WORK, REFERRING TO L1 AND L2 LIBRATIONS POINT OF THE EARTH-MOON CR3BP. MORE DETAILS CAN BE FOUND IN CHAPTER 3, WHILE FOR THE NOTATION WE REFER TO THE LEGEND..... | 142 |
| FIGURE 94: ILLUSTRATION OF HALO FAMILY BIFURCATIONS FROM THE H-LYAPUNOV ONE AT L1 (TOP) WITH MAIN PARAMETERS CONSIDERED IN OUR ANALYSIS. FOR THE INTERPRETATION WE REFER TO SECTION 2.4..... | 143 |
| FIGURE 95: ILLUSTRATION OF HALO FAMILY BIFURCATIONS FROM THE H-LYAPUNOV ONE AT L2 (TOP) WITH MAIN PARAMETERS CONSIDERED IN OUR ANALYSIS. FOR THE INTERPRETATION WE REFER TO SECTION 2.4..... | 144 |
| FIGURE 96: ILLUSTRATION OF THE AXIAL FAMILY (IN DARK YELLOW) OF PERIODIC SOLUTION AT L1/L2 (IN MAGENTA) FOR THE EARTH-MOON CR3BP ($\mu = 0.0121506$). NOTE THEIR INTERSECTION (\diamond) WITH THE HORIZONTAL FAMILY (IN RED) ON THE xz -PLANE, DUE TO THE TANGENT BIFURCATION. SEE SECTION 3.7..... | 145 |

List of Tables

| | |
|--|-----|
| TABLE 1: BULK AND ORBITAL PARAMETERS RELATIVE TO BOTH EARTH AND MOON BODY (NASA, 2016)..... | 16 |
| TABLE 2: THE THIRD ORDER ANALYTIC APPROXIMATION OF PERIODIC SOLUTIONS NEAR L1/L2. HERE $\{x, y, z\}$ ARE DISPLACEMENT-POSITIONS FROM BOTH L-POINTS, WHILE w_{pert} AND ω_{xy} RESPECTIVELY THE PERTURBED AND UNPERTURBED PULSATION OF THE APPROXIMATED SOLUTION. SEE (RICHARDSON, 1980A)..... | 36 |
| TABLE 3: DETAILED DATA RELATED TO BIFURCATIONS POINTS AND ORDER-OF-INSTABILITY WITHIN EACH ONE OF THE THREE FAMILIES INVESTIGATED AT L1/L2 LIBRATION POINTS IN THE DYNAMICS OF THE CR3BP FOR THE EARTH-MOON SYSTEM. FOR THE NOTATION ADOPTED, THE READER IS REFERRED TO THE TEXT ABOVE. | 72 |
| TABLE 4: RANGE FOUND FOR THE ORBITAL PERIOD T_c IN THE THREE FAMILIES OF PERIODIC SOLUTIONS ANALYSED AT L1 AND L2 (EARTH-MOON CR3BP). NOTE THAT MIN & MAX VALUES HAVE BEEN NORMALIZED BY 2π , SO ALLOWING DIRECTLY OBSERVING THE RATIO "N/M" UP TO FOUR DIGITS..... | 96 |
| TABLE 5: SUMMARY OF ALL FOUR POSSIBLE GROUPS RELATED TO PERIODIC SOLUTIONS EXTENDED IN THE ER3BP STARTING FROM A PARTICULAR RESONANCE PERIODIC ORBIT OF THE CIRCULAR PROBLEM (CR3BP). | 100 |
| TABLE 6: MAIN RESONANCE ORBITS AVAILABLE HERE FOR EACH FAMILY (AT BOTH L1/L2 IN THE EARTH-MOON CIRCULAR PROBLEM). THE RANGE HAS BEEN LIMITED TO $N_{max} = 2, M_{max} = 5$, AFTER REMOVING REDUNDANT CASES AS EXPLAINED IN SECTION 4.4.2. FOR EACH CASE, THE ORDER-OF-INSTABILITY AND THE LARGEST CHARACTERISTIC MULTIPLIER ARE SHOWN, BASES ON WHAT HAS BEEN STATED IN THE TEXT ABOVE. | 104 |
| TABLE 7: NUMERICAL VALUES OF THE TWO REAL UNITARY EIGENVALUES λ_i IN THE CR3BP, WITH THE RELATIVE SPIT DUE TO THE EXTENSION TO THE ELLIPTIC PROBLEM WITH ECCENTRICITY AS $e_{EM} = 0.0549$ | 108 |
| TABLE 8: NUMERICAL VALUES OF THE TWO REAL UNITARY EIGENVALUES λ_i IN THE CR3BP, WITH THE RELATIVE SPIT DUE TO THE EXTENSION TO THE ELLIPTIC PROBLEM WITH ECCENTRICITY AS $e_{EM} = 0.0549$ | 111 |
| TABLE 9: NUMERICAL VALUES OF THE FOUR UNITARY EIGENVALUES λ_i IN THE CR3BP FOR THE M2N1 HALO RESONANCE ORBIT, WITH THEIR FINAL VALUES IN THE ELLIPTIC PROBLEM COMPUTED AT $e_{EM} = 0.0549$ | 118 |
| TABLE 10: NUMERICAL DATA OF THE E-BIFURCATION FOUND WITHIN THE LEFT-FAMILY, WHEN STARTING FROM A M2N1- RESONANCE ORBIT OF THE HALO FAMILY AT L1. MAIN SETTINGS ARE GIVEN IN APPENDIX-B. | 118 |
| TABLE 11: NUMERICAL VALUES OF ALL THE SIX EIGENVALUES λ_i FOR THE M3N1 HALO RESONANCE ORBIT, WHERE THEIR FINAL VALUES IN THE ELLIPTIC PROBLEM HAVE BEEN COMPUTED AT $e_{EM} = 0.0549$. IN RED, EIGENVALUES WITH A MODULE LARGER OR SMALLER THAN 1 (SO LYING OUTSIDE THE UNITARY CIRCLE) | 119 |
| TABLE 12: SHOOTING CONDITIONS FOUND IN THE CIRCULAR AND ELLIPTIC MODEL FOR A M3N1-RESONANCE HALO ORBIT AT L2 IN THE EM-SYSTEM. DATA REFERS TO PULSATING COORDINATES (SEE SECTION 4.1.1.2)..... | 122 |
| TABLE 13: LOCATION OF COLLINEAR LAGRANGE POINTS (L-POINTS) AND THEIR SCALAR DISTANCE γL FROM THE NEAREST MASS. ALL THREE FOUND ALONG THE SYZGY IN A CO-ROTATING FRAME FOR $\mu_{EM} = 0.0121506$ | 132 |
| TABLE 14: MAIN PARAMETERS USED FOR THE NUMERICAL COMPUTATION IN BOTH CR3BP AND ER3BP ARE HERE SHOWN, MEANWHILE THEIR "DIMENSIONAL VALUES" CAN BE COMPUTED USING EQ. (A-2). | 133 |
| TABLE 15: THREE PERIODIC SOLUTIONS SELECTED FROM THE HALO FAMILY AT L2 (EARTH-MOON SYSTEM). DIFFERENT ORDERS-OF-INSTABILITY HAVE BEEN CHOSEN AND ALL SHOOTING CONDITIONS x_0, v_{y0}, z_0 HAVE BEEN SHOWN TOGETHER WITH THE LARGEST EIGENVALUE'S MODULE λ_{MAX} AND THE ORBITAL PERIOD T. | 137 |
| TABLE 16: POSSIBLE ORGANIZATION IN DIFFERENT CLASSES OF SOME FAMILIES WITHIN THE DYNAMICAL MODEL OF THE EARTH-MOON SYSTEM; NOTE THE CONNECTION BETWEEN RESONANCE ORBIT ORBITING THE SECONDARY MASS M_2 (HERE THE MOON), AS ALSO FOR THE CONNECTION (DUE TO BIFURCATIONS) OF FAMILIES EXISTING AROUND LAGRANGE POINTS. MORE DETAILS CAN BE FOUND IN (FOLTA ET AL., 2015). | 146 |

Nomenclature

List of Acronyms & Abbreviations

| | |
|---------------------|---|
| 2BP | Two Body Problem |
| 3BP | Three Body Problem |
| CR3BP | Circular Restricted Three Body Problem |
| DST | Dynamical System Theory |
| ER3BP | Elliptic Restricted Three Body Problem |
| ESA | European Space Agency |
| NASA | National Aeronautics and Space Administration |
| PR3BP | Parabolic Restricted Three Body Problem |
| R3BP | Restricted Three Body Problem |
| SPM | State Propagation Matrix |
| STM | State Transition Matrix |
| DC-algorithm | Differential Correction algorithm |
| EM-system | Earth-Moon-Satellite restricted three body system |
| LP-method | Linstedt-Poincaré method |
| SE-system | Sun-Earth-Satellite restricted three body system |
| L-points | Lagrange points (or equilibrium points) of the system |

List of Symbols

| Symbol | Description |
|-----------------------------|--|
| a | Semi-major axis of the main Kepler orbit for $\{M_1, M_2\}$ |
| α | Acceleration rate of the main Kepler orbit for $\{M_1, M_2\}$ |
| A_x, A_z | Amplitude parameters of the analytic approximation at collinear L-points |
| A | State Propagation Matrix |
| B | Constant matrix described by Floquet's Theorem (T-periodic) |
| c_j | Coefficients of the Taylor expansion for the dynamics at the L-point |
| C_j | Jacobi constant "J" (First integral of motion for the Circular problem) |
| $\Delta_j, \Delta\lambda_j$ | Relative and absolute errors on the eigenvalue of the Monodromy matrix |
| Δe | Eccentricity step-size in the continuation from the Circular to the Elliptic problem |
| $\Delta P_T, \Delta V_T$ | Displacement tolerances (position and velocity) after one orbital revolution T |
| $\Delta Y, \Delta V_{xz}$ | Error tolerances (position and xz -velocity) for the DC-algorithm |
| e | Eccentricity of the main Kepler orbit for $\{M_1, M_2\}$ |
| ϵ | Generic small positive parameter |
| f | Generic vector-function of a non-linear differential system |
| γ_L | Scalar distance of each L-point from the nearest principal mass |
| G | Universal gravitational constant, given in $[m^3 kg^{-1} s^{-2}]$ |
| H | Hamiltonian function of the differential system |
| J_E | Elliptic-Jacobi integral for the Elliptic problem (not First integral of Motion) |
| λ_{xy} | Eigenvalues of the linearized dynamics at the L-point for an unbounded motion |
| λ_i | Eigenvalues of the Monodromy matrix (or <i>characteristic multipliers</i>) |

| | |
|----------------------------------|--|
| L_i | Lagrange point (five in total) |
| μ_{EM} | Mass-ratio parameter μ for the Earth-Moon system |
| m_3 | Third negligible mass of P_3 for the ‘restricted problem’ |
| M-matrix | Monodromy matrix associated to periodic solutions |
| M_i | Principal masses of the system (two in total) |
| MxNy | Resonance with Mx and Ny respectively number of orbital and system revolutions |
| μ | Mass-ratio parameter expressed by M_2/M_{TOT} |
| μ_i | Product between G and M_i variables, given in [m^3s^{-2}] |
| N_{iter}^{MAX} | Maximum number of iterations for the Differential Correction algorithm |
| n | Mean motion of the main Kepler orbit for $\{M_1, M_2\}$ |
| ω_{xy}, ω_z | Horizontal and Vertical pulsation of the linearized CR3BP-dynamics at the L-point |
| ω_{XY}, ω_Z | Horizontal and Vertical pulsation of the linearized ER3BP-dynamics at the L-point |
| Ω | Potential function, with Ω_C for the Circular problem |
| ω | Rotation rate of the main Kepler orbit for $\{M_1, M_2\}$ |
| P | Periodic matrix described by Floquet’s Theorem (T-periodicity) |
| P_i | Principal point-masses of the system (three in total) |
| ϕ | Generic solution of the non-linear differential system |
| Φ | State transition Matrix |
| ψ | Auxiliary θ -dependent variable used in the Elliptic problem |
| Q | Generic state-vector of a system, also used as state-vector for the Elliptic problem |
| q_i | Generic time-dependent variable |
| R_{IN} | Position of P_3 in an inertial frame respect to the barycentre of the system |
| R | Position of P_3 in a synodic frame respect to the barycentre of the system |
| R_i | Scalar distance of P_3 from M_i in the pulsating synodic frame |
| r_i | Scalar distance of P_3 from M_i in the non-pulsating synodic frame |
| r | Scalar distance between main masses $\{M_1, M_2\}$ |
| ρ | Absolute module of the λ_i characteristic multipliers |
| σ | Auxiliary variable used in the Elliptic problem |
| t | Non-dimensional time of the differential system |
| T | Orbital period, with T_C and T_E for the circular and the elliptic case |
| θ | Relative phase of the main Kepler orbit for $\{M_1, M_2\}$ |
| u_x, u_y, u_z | Co-rotating velocity components of P_3 respect to the θ time-like parameter |
| v_x, v_y, v_z | Co-rotating velocity components of P_3 respect to the t time parameter |
| v_i | Eigenvectors of the Monodromy matrix |
| V_X, V_Y, V_Z | Pulsating co-rotating velocity components of P_3 respect to the θ time-like parameter |
| x_{in}, y_{in}, z_{in} | Inertial position coordinates for the third body P_3 |
| x, y, z | Co-rotating position coordinates for the third body P_3 |
| X, Y, Z | Pulsating co-rotating position coordinates for m_3 |
| X | State-vector of the differential system for the Circular problem |
| $X_0, X_{T/2}$ | Initial and half-period state-vector for the Circular problem (or <i>shooting condition</i>) |
| ξ_i | General mass-ratio defined by M_i/M_{TOT} |

NOTE: all symbols considered are here dimensionless, while when necessary the dimension will be provided directly within the description. The dot-notation in the text refers to the derivative respect to the physical time t , while the prime-notation has been used for the derivative respect to the θ -phase.

1

Introduction

In the past decades, main interest in celestial mechanics has been given to the so-called 3-Body Problem (3BP), concerning the definition of the trajectory for three masses only under their mutual gravitational force and subjected to Newton's acceleration law. However, an analytic expression of the general solution does not exist yet, as consequence the "restricted problem" is usually being investigated, where the third mass is assumed many orders smaller than the two principal bodies. Nonetheless, a simpler model commonly adopted, is the 2-Body Problem (2BP), with very well-known "*closed form solutions given in terms of elementary functions*" ([Musielak & Quarles, 2014](#)).

Originally, the general 3-Body Problem has been analysed and formulated in the "*Philosophiæ naturalis Principia Mathematica*" (simply known as *Principia*) published in the 1687 by Sir. I. Newton (1642-1726). Later, following his work, the two French mathematicians, J.B.R. D'Alembert (1717-1783) and A.C. Clairaut (1713-1765), tried to tackle the problem, as described in the memories collected with the "*Histoires*" of the Académie Royale des Sciences for 1745. With L. Euler (1707-1783) and then with J.L. Lagrange (1736-1813), two kinds of periodic solutions were respectively found: the first named *straight line* (1767) and the second *equilateral triangle* (1772), both better known as *central configurations solutions*. From that moment until the publication of "*Les Méthodes Nouvelles de la Mécanique Céleste*" (1892) by J.H. Poincaré (1854-1912), many attempts have been made in order to investigate solutions of this problem. Several famous scientists have been involved, as P.S. Laplace (1749-1827), K.G.J. Jacobi (1804-1851), G.W. Hill (1838-1914), W.R. Hamilton (1805-1865), with a great interest on the dynamical proprieties of the simpler Restricted 3-Body Problem (R3BP).

With the advent of Poincaré, the Dynamical System Theory (DST) was founded, as mean to provide a "*geometrical view for the set of all possible states of a system*" ([Vázquez, Pallé, & Rodríguez, 2010](#)). Even if, unfortunately, its work did not provide any real solutions, it was the 'pivot' of an exhaustive study of specific solutions, known as *periodic solutions*. Studied by many authors as I.O. Bendixson (1861-1935), F.R. Moulton (1872-1952), G.D. Birkhoff (1884-1944), their stability was later analysed by mathematicians as T. Levi-Civita (1873-1941) and A.M. Lyapunov (1857-1918). Only in 1912, a solution in a series expansion was presented by K.F. Sundman (1873-1949), which "*converges very slowly and it cannot be used for any practical applications*" ([Musielak & Quarles, 2014](#)).

In the past century, different approaches (both numerical and analytical) have been adopted, leading to many results as it will be shown steps by steps within this work. For more historical notes the reader is referred to ([Barrow-Green, 1997](#)), while strongly suggested is here ([Szebehely, 1967](#)), for a complete survey on the 'restricted problem'.

1.1 Problem formulation

The problem here investigated concerns the inspection of some periodic solutions in the dynamical model provided by the Restricted 3-Body Problem. Based on its foretold assumption, it is possible to well-approximate the motion of a small body (e.g., a spacecraft or an asteroid) under the gravitational influence of the other two principal masses. These last two are supposed to move in simple Kepler orbits, as consequence of their expression in a general 2-Body Problem, while the third body has a negligible mass. With this scheme, and adopting some particular reference frames, the existence of five equilibrium points (called Lagrange or libration points) has been proved, as also the possibility of having a bounded motion in their neighbourhood. ([Szebehely, 1967](#))

As clarified in the next Section 1.2, main interest is related to two libration points, named L1, L2 and by convention located here near the Secondary mass M2. Together with L3, they are defined as collinear points (known to be linearly unstable), where two mono-parameter families of periodic solutions arise, also denoted as Horizontal and Vertical Lyapunov families. Moving away, additional families with a similar continuous character can be found, e.g. the Halo family, mentioned for the first time in ([Farquhar, 1968](#)), almost a decade after preliminary studies on “*low-energy lunar transfer*” based on the 3BP, performed by C.C. Conley (1933-1984) and R.P. McGehee (1943-).

First analytic results at L2 in the Earth-Moon-Spacecraft restricted problem have been shown in ([Farquhar & Kamel, 1973](#)) using the Perturbation Theory, in particular the Linstedt-Poincaré method. In their work they have taken into account also “*non-linearity, lunar orbit eccentricity and the Sun’s gravitational field*”, as later discussed in Section 2.1.3, while few years later a numerical extension was presented in ([Breakwell, 1979](#)), mostly focused on the determination of Halo solutions. Next milestones in the process were the third-order analytic approximation presented in ([Richardson, 1980a](#)) and the extensive numerical investigation performed in ([Howell, 1984](#)), based on a numerical shooting algorithm. Both aforementioned works have been examined in the framework of the Circular Restricted 3-Body Problem (CR3BP), where both masses (here the Earth and the Moon) are assumed to move in circular orbits respects the centre of mass (barycentre) of the system. Extension to a more complete dynamical model is well represented by the Elliptic Restricted 3-Body Problem (ER3BP), where Kepler motion is now described by ellipses around their barycentre and periodic trajectories for the third mass are assumed to exist, mostly due to the ‘periodic character’ of main variations within the gravitational field. ([Szebehely, 1967](#))

Both CR3BP and ER3BP are indeed only models, approximations of the more complete ‘real’ dynamics, nevertheless this full dynamics is anything but simple. It follows that the research progress is usually easier to be achieved steps by steps, so starting with a model, analysing it and later extending it, thus in a continuous process towards a better approximation of the real physical world. Under this perspective, in this work the CR3BP will be analysed, limiting the investigation to three main families of periodic orbits at the two collinear Lagrange point (L1, L2). As discussed in Section 2.1, test-case here considered is the Earth-Moon system, while the analysis could be easily extended to other systems following a similar procedure. Successive step is the extension to the ER3BP, in order to highlight differences for what is supposed to be a more complete model, nevertheless involving a much more complex “mathematical structure”.

1.2 Heritage of past missions

The importance of investigating periodic motion around Lagrange points is due to many possible applications in space-observation missions, as also for communication purposes. First spacecraft orbiting around L₁ (Sun-Earth) has been the Sun/Earth Explorer 3 (ISEE-3), able to prove that such a suspension between gravitational fields is feasible only when considering two bodies at the same time. Moreover, starting from a Halo orbit, it entered in a Lissajous orbit around L₂, after a Moon fly-by, making use of a thruster burn. A bounded motion near these points, even if unstable, is very profitable for space operations, in particular for solar observations, astrophysics researches or more in general for scientific missions. Successful example is the Solar and Heliospheric Observatory (SOHO), launched in December 1995 ([Domingo, Fleck, & Poland, 1995](#)) within a Halo orbit at L₁ (Sun-Earth) in collaboration between the National Aeronautics and Space Administration (NASA) and the European Space Agency (ESA). In fact, it has been able to discover around 2007 comets over the past decades, while also remarkable are the Advanced Composition Explorer (ACE) mission by NASA, for solar research studies, and the Deep Space Climate Observatory (DSCOVR), which is a recent space weather satellite launched in February 2015. ([Shirobokov, 2014](#))

Many other scientific missions can be find in the general literature as ([Dunham & Roberts, 2001](#)), while worthy here to be mentioned is the James Webb Space Telescope (JWST), planned to be launched in 2018 ([Abraham, 2014](#)) in a Halo orbit around the L₂ point (Sun-Earth) as join project of ESA, NASA and the Canadian Space Agency (CSA). Considering the L₂-point for the Earth-Moon system, it is indeed feasible “*to create constellations that are not possible in Earth orbit, while still being able to communicate with Earth constantly*” ([Rohner, 2014](#)). As stated, for L₂ in the Earth-Moon system, a greater interest is usually related to communication purposes, initially suggested in ([Farquhar & Kamel, 1973](#)). More recently, such aspects have been examined for the Orbiting Low-Frequency Antennas for Radio astronomy (OLFAR) mission at L₂, “*where the Moon can additionally shield the satellites from Earth-emitted interfering radio waves*” ([Vermeiden, 2014](#)).

For what concerns the L₃ point, situation becomes more complex due to “*severe communication limitations*” as fully explained in ([Tantardini et al., 2010](#)). Only with the recent ESA Cosmic vision, the Evolved Laser Interferometer Space Antenna (eLISA) mission has been selected as major candidate for a possible L₃ mission (Sun-Earth), in order to detect and study gravitation waves ([Wilson, European Space, European Space, & Technology, 2005](#)). Nonetheless, also the triangular points L₄-L₅ have been not investigated here due to their less suitability and higher costs in practical scientific missions. Consequences related to their linear stability has been investigated in ([Giorgilli & Skokos, 1997](#)), when considering “*the Sun-Jupiter model and the Trojan asteroids in the neighbourhood of the point L₄*”.

For these last two triangular equilibrium points the reader is referred to the extensive analysis performed in ([Gómez, 2001b](#)) and later revised in ([Gómez, 2001d](#)). With a very similar approach, more information on the collinear points here investigated, can be found in ([Gómez, 2001a](#)), again later revised in ([Gómez, 2001c](#)). At this point we can continue defining some fundamental *Research Objectives* relevant to our work.

1.3 Research objectives and tasks

Before presenting main guidelines and tasks for this work, a brief discussion is required in relation to “*An Analytic approach to find periodic and quasi-periodic Lagrange orbits*” (Massarweh, 2015), Literature Study previously performed by the author for the Master thesis work. Indeed, an investigation has been made on the feasibility of using analytic techniques (as the cited Linstedt-Poincaré perturbation method) in order to completely approximate solutions at collinear libration points. As it will be discussed in Chapter 2 and Chapter 4, in a preliminary stage of the work, these methods have been found as not really efficient. Furthermore, the indispensable numerical validation of these results has contributed to the decision of considering both approaches as complementary parts of a sole investigation. In this way, the entire procedure has shown a very high efficiency, balancing accuracy and computation efforts, as later explained.

In this report, we will always refer to this preliminary work always as “Literature Study”, while here we still need to establish a main scientific question and relative sub-questions, along with main research objectives.

Main Scientific Question:

“Which are the most critical aspects that arise in the dynamics of main periodic solutions at L1/L2 Lagrange points, after extending them from the Circular Restricted 3-Body Problem to the Elliptic problem?”

Sub-Questions:

- I. How it is possible to locate and characterized families of periodic solutions in the dynamics of the CR3BP? Are there limitations or particular behaviours associated to this class of solutions?
- II. How is it possible to investigate bifurcations within each previously generated family? Are they fundamental for assessing the linear stability of these particular bounded trajectories?
- III. How can the so-called “elliptical perturbations” change the dynamics? What are the principal consequences of considering the Elliptic problem?
- IV. Do periodic solutions survive when considering the Elliptic problem and what are the main conditions for their extension in such a new advanced model?
- V. Are there practical advantages of considering this more complex model? Which main strategies allow retrieving useful insights into its dynamical structure and what are their prominent limitations?

Research Objectives:

- i. Develop a general procedure in order to completely analyse some main families of periodic solutions near collinear L-points (here L1 and L2), thus exploiting proprieties like linear stability and some possible bifurcations.
- ii. Investigate the principal aspects of the Elliptic Restricted 3-Body Problem, in this way highlighting differences respect to the simpler Circular problem.
- iii. Assess to what extent the new model provides a better approximation of the real physical world, thus examining some major consequences when its different dynamics is omitted.

1.4 Content and structure of this report

The structure for this Master report has been illustrated in Figure 1, based on major subsequent blocks. As mentioned, first we will investigate the Circular problem (CR3BP) in Chapter 2, where an introduction to the problem and its proprieties is given. Within the same chapter, the Dynamical System Theory is presented, later discussing two main approaches (respectively *analytical* and *numerical*) as complementary parts of this analysis. In Chapter 3, results will be shown for both L1 and L2 Lagrange points of the Earth-Moon systems (selected in all simulations), thus taking into account three main families of periodic solutions: both Horizontal/Vertical Lyapunov families and the Halo one. For all these six cases, the possible existence of few main resonance orbits will be discussed. It follows an extension to the Elliptic problem (ER3BP) in Chapter 4, in a very analogous way as shown for the CR3BP, while main results will be presented in Chapter 5 in relation to some resonance solutions previously found. Second part involves a comparison between both models, mostly based on their linear stability, while at the very end conclusions and recommendations for future work are summarized in Chapter 6.

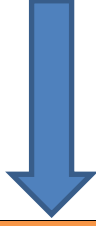
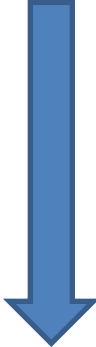
| | | |
|--------------|---|------------------------------------|
| Ch. 2 | CR3BP Dynamics: | |
| | <ul style="list-style-type: none"> - Introduction & Dynamical System Theory - Analytic + Numeric approach | |
| Ch. 3 |  | CR3BP Results: |
| | | Bifurcations within each family |
| | | Linear stability |
| | | Existing resonance orbits |
| Ch. 4 | ER3BP Dynamics: | |
| | <ul style="list-style-type: none"> - Introduction & Dynamical System Theory - Analytic + Numeric approach | |
| Ch. 5 |  | ER3BP Results: |
| | | Analysis resonance solutions |
| | | Differences in bifurcated families |
| | | Linear stability |
| | Comparison models with linear stability: | <i>Circular vs Elliptical</i> |
| Ch. 6 | Conclusions | |

Figure 1: Workflow diagram of the content and structure of this Master thesis report. In orange colour the two chapters related to the description of main analyses and methodologies for both two models (Circular and Elliptical). In green all chapters relative to results and last, in red the final chapter related to the conclusions. See text for more details and information.

NOTE:

Appendices-A/B/C follows the main structure, as supplements for this Master work.

2

CR3BP: Analysis and Methods

In this Chapter 2 we consider the Circular Restricted 3-Body Problem (CR3BP). First, in Section 2.1 we present some main aspects of the dynamical model, with a brief overview of its properties and the choice of a “test-case”, later adopted in all simulations. Thus, in Section 2.2, the Dynamical System Theory (DST) is introduced for this circular case, using concepts from Floquet Theory in order to investigate linear stability and possible bifurcations in certain families of periodic solutions. After this analysis, Sections 2.3-2.4 will illustrate two different methodologies (the first *Analytic* and the second *Numeric*) that could be considered as complementary parts of an exhaustive investigation of the problem introduced here.

2.1 Introduction to the Circular problem

The Circular problem is an approximation of a more general model given by the so-called *3-Body Problem* (3BP), originally formulated by Sir I. Newton (1642-1727) in his “*Principia*”, concerning the motion in space of three bodies P_1, P_2, P_3 exclusively under their mutual gravitational attraction and subjected to Newton’s gravitational law. This general model has been simplified considering the mass of the third body as negligible respect to the other two, and consequently the motion of P_3 does not affect the mutual interaction between P_1 and P_2 bodies (henceforth defined as *Primary* and *Secondary*). ([Musielak & Quarles, 2014](#))

Under this last assumption, we refer to the *Restricted 3-Body Problem* (R3BP), fully justified by the fact that in most of real space missions the mass of the spacecraft is many orders of magnitude smaller than planets or other celestial bodies involved in the system ([Szebehely, 1967](#)). Consequently, the motion of P_1, P_2 is given by the Kepler solution to the general *2-Body Problem* (2BP), where their relative distance r can be defined as

$$r = \frac{a \cdot (1 - e^2)}{1 + e \cdot \cos(\theta)} \quad (2-1)$$

with a semi-major axis of the orbit, e eccentricity and θ phase between both principal masses in some specific reference frames. All basics aspects related to this motion have been fully discussed within the previous Literature Study, and are also well-known in common literature, so we refer the reader to main textbooks as ([Szebehely, 1967](#)), ([Marchal, 1990](#)) and ([Barrow-Green, 1997](#)).

A very interesting outcome of such motion is related to the existence of different models, depending on the eccentricity value e , thus leading to four possible formulations:

- Circular problem for $e = 0$
- Elliptic problem for $e \in (0,1)$
- Parabolic problem for $e = 1$
- Hyperbolic problem for $e > 1$

As discussed in Chapter 1, in this work we consider always a bounded motion between principal masses and so we restrict the analysis to the case $e < 1$, while the model $e \geq 1$ is not treated. Due to the continuous nature of this small positive parameter e , many observations on these last two cases could directly follow from our investigation, but it is important to proceed gradually, starting with the simpler model: the Circular case.

2.1.1 Dynamical model and reference frame

The dynamics of the Circular Restricted 3-Body Problem has been originally studied in (Euler, 1767), making use of a synodic reference frame with the origin fixed in the centre of mass of the system and uniformly co-rotating with both masses. The latter is clearly a non-inertial reference frame, therefore the dynamics of P_3 is subject to both the gravitational acceleration by P_1, P_2 and all additional “inertial accelerations”, such that

$$\frac{d^2\mathbf{R}}{dt^2} = \frac{d^2\mathbf{R}_{in}}{dt^2} - 2\boldsymbol{\omega} \times \frac{d\mathbf{R}}{dt} - \boldsymbol{\omega} \times (\boldsymbol{\omega} \times \mathbf{R}) - \frac{d\boldsymbol{\omega}}{dt} \times \mathbf{R} \quad (2-2)$$

where $\mathbf{R} = [x, y, z]$ is the P_3 position vector (the third mass-less body) in this new frame, $\mathbf{R}_{in} = [x_{in}, y_{in}, z_{in}]$ refers to the inertial frame, t is the system’s time and $\boldsymbol{\omega} = [n, 0, 0]$ is the angular velocity of the system (here the same of the Kepler mean motion n). In the following Figure 2 we can observe the system with the convention of having the larger mass (the *Primary*) always on the negative side of the rotating \hat{x} -axis (known as *Syzygy*).

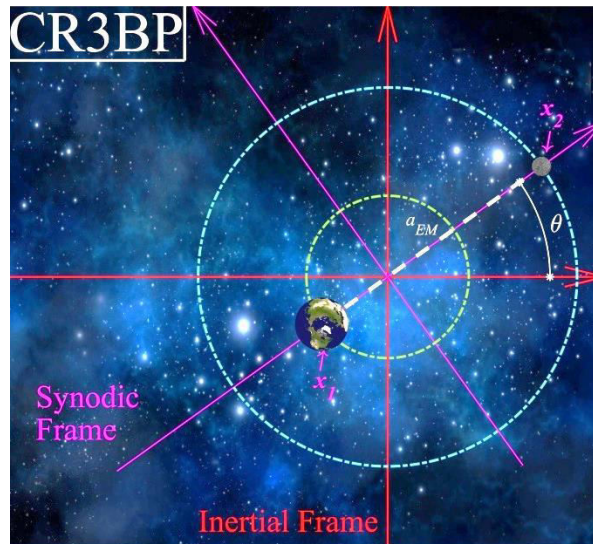


Figure 2: Inertial in red $\{\hat{x}_I, \hat{y}_I, \hat{z}_I\}$ and synodic co-rotating in magenta $\{\hat{x}, \hat{y}, \hat{z}\}$ reference frame for the Earth-Moon-Satellite Circular Restricted 3-Body Problem.

First three terms in Eq. (2-2) are respectively the contribution of Gravitational, Coriolis and Centrifugal accelerations, while the last term is zero for the circular case, due to the fact that the synodic frame is rotating with an uniform velocity (mean motion n), so

$$n = \sqrt{\frac{G(M_1 + M_2)}{a}} \equiv \sqrt{\frac{\mu_1 + \mu_2}{a}} = \sqrt{\frac{\mu_{TOT}}{a}} \quad (2-3)$$

such that G is the univesal gravitational parameter, M_i is the mass of each principal body and μ_i the product of both these previous quantities. The position of the two masses is completely fixed in this new frame and the dynamics of P_3 can be fully defined by three second-order non-linear differential equations (see Literature Study), such that

$$\begin{aligned} \frac{d^2x}{dt^2} &= -\mu_1 \frac{r_{1x}}{r_1^3} - \mu_2 \frac{r_{2x}}{r_2^3} + 2n \frac{dy}{dt} + n^2 x \\ \frac{d^2y}{dt^2} &= -\mu_1 \frac{r_{1y}}{r_1^3} - \mu_2 \frac{r_{2y}}{r_2^3} - 2n \frac{dx}{dt} + n^2 y \\ \frac{d^2z}{dt^2} &= -\mu_1 \frac{r_{1z}}{r_1^3} - \mu_2 \frac{r_{2z}}{r_2^3} \end{aligned} \quad (2-4)$$

with r_1, r_2 as scalar distances from the Primary and Secondary body, and their subscripts referring to each projection on reference axes. As common in literature, the non-dimensional form is given, where time, space and mass have been adimensionalize as

- SPACE [km]: $a = 1$
- MASS [kg]: $M_{TOT} = M_1 + M_2 = 1$
- TIME [1/s]: $\omega = n = 1$

leading to $G/\omega^2 = 1$ and with a main orbital period given as $T = 2\pi$. ([Szebehely, 1967](#)) The final non-dimensional form, once defining $\mu = M_2/M_{TOT}$, is given below

$$\begin{aligned} \ddot{x} - 2\dot{y} &= x - (1 - \mu) \frac{(x + \mu)}{r_1^3} - \mu \frac{(x + \mu - 1)}{r_2^3} \\ \ddot{y} + 2\dot{x} &= y \cdot \left[1 - (1 - \mu) \frac{1}{r_1^3} - \mu \frac{1}{r_2^3} \right] \\ \ddot{z} &= -z \cdot \left[\frac{(1 - \mu)}{r_1^3} - \frac{\mu}{r_2^3} \right] \end{aligned} \quad (2-5)$$

$$\begin{aligned} r_1 &= \sqrt{(x + \mu)^2 + y^2 + z^2} \\ r_2 &= \sqrt{(x + \mu - 1)^2 + y^2 + z^2} \end{aligned} \quad (2-6)$$

while from the previous adimensionalization it follows that P_1, P_2 are located respectively at $x_1 = -\mu, x_2 = 1 - \mu$ on the \hat{x} -axis (see Figure 2). By convention, the Primary has been placed on the negative \hat{x} -axis, allowing to consider a range for the mass-ratio parameter as $\mu \in [0, 0.5]$. Boundary cases for $\mu = 0$ (*Restricted 2-Body Problem*) or for $\mu = 0.5$ (known also as *Copenhagen problem*) are here not considered, since they present only particular situations that are not very relevant for a realistic space mission's orbit design.

2.1.2 Lagrange points and existing symmetries

The dynamics described by Eq.(2-5) fully defines the P_3 motion within the synodic frame, and for a specific initial condition there is a unique trajectory, as it will be explained in Section 2.2.1. Furthermore, there are particular points where all forces balance each other allowing P_3 maintaining unperturbed its position for any time $t > 0$ arbitrarily large. Two classes for these five equilibrium points (sometimes called *libration* points) can be found, all located within the $\hat{x}\hat{y}$ -plane (sometimes referred as *ecliptic* plane) for $z = 0$ and described in (Musielak & Quarles, 2014) as follows:

1. The **Collinear** points L_1, L_2, L_3 discovered by L. Euler (1707-1783) in 1767 with the “*De moto rectilineo trium corporum se mutuo attrahentium*”. They are located along the syzygy direction, and are defined by

$$x - (1 - \mu) \frac{(x + \mu)}{|x + \mu|^3} - \mu \frac{(x + \mu - 1)}{|x + \mu - 1|^3} = 0 \quad \forall y = 0 \quad (2-7)$$

2. The **Equilateral** points L_4, L_5 discovered later by J.L. Lagrange (1736-1813) in 1772 with the “*Essai sur le problème des trois corps*”. They are located at the vertex of an equilateral triangle connected to both main masses, and defined by

$$\begin{cases} x - (1 - \mu) \frac{(x + \mu)}{r_1^3} - \mu \frac{(x + \mu - 1)}{r_2^3} = 0 \\ 1 - \frac{(1 - \mu)}{r_1^3} - \frac{\mu}{r_2^3} = 0 \end{cases} \quad \forall y \neq 0 \quad (2-8)$$

A graphical example of this distribution for all libration points (also known as Lagrange points or L-points) is given in Figure 3, relative to the Earth-Moon Circular problem.

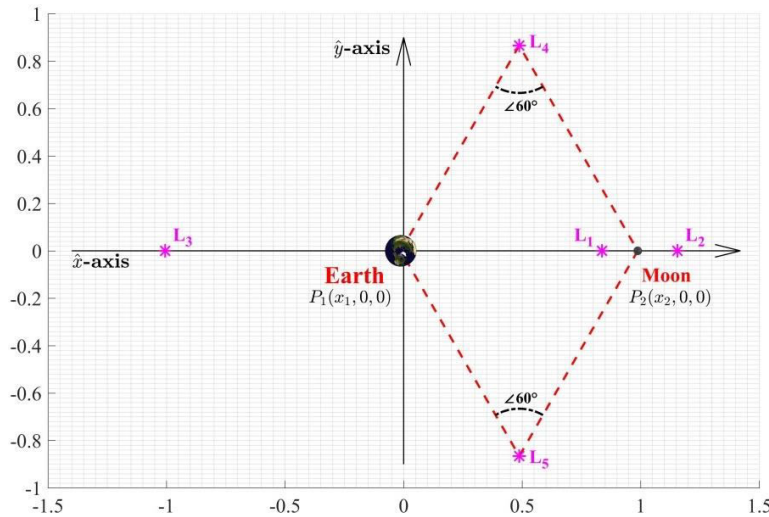


Figure 3: Location in the co-rotating synodic frame $\{\hat{x}, \hat{y}, \hat{z}\}$ of all five libration points within the $\hat{x}\hat{y}$ -plane for the Earth-Moon Circular problem. The size of masses has been enlarged $\times 4$.

Note that L-points still exist in the original inertial frame, moving all together with P_1 and P_2 , while their proper definition holds only within the synodic frame, where the location is totally fixed by the mass-ratio μ -value, along with many other proprieties.

The two equilateral points can be computed by solving analytically Eq. (2-8), and their linear stability has been intensively studied in the CR3BP by many authors, e.g. (Murray, 1999), leading to the definition of the “Routh value” for $\mu_R \approx 0.03852$, “value at which linear instability is reached” (Sicardy, 2010). As discussed before, these two locations are less suitable for practical space observation missions due to the higher energy required in order to reach them, so they will not be considered in following sections.

The location of the three collinear points is fixed on the syzygy axis after numerically solving Eq. (2-7), ‘quintic equation’ given in (Szebehely, 1967) respect to a γ_L -parameter (scalar distance between the libration point and the nearest mass), so leading to

$$\gamma_L^5 \mp (3 - \mu)\gamma_L^4 + (3 - 2\mu)\gamma_L^3 - \mu\gamma_L^2 \pm 2\mu\gamma - \mu = 0 \quad (2-9)$$

where the upper sign refers to L1 and the lower one to L2. For what concerns L3, we are able to define its position simply solving the same ‘lower’ equation once adopting $\mu^* = 1 - \mu$, such that the the system is simply reversed, while keeping the convention of having the Primary always on the negative \hat{x} -axis. Collinear libration points are shown in Figure 4 for the entire μ -range [0,1], highlighting this symmetry for μ larger than 0.5 .

CR3BP: Motion Lagrange points $L_1, L_2, L_3, L_{4/5}$ with $\mu \in [0,1]$

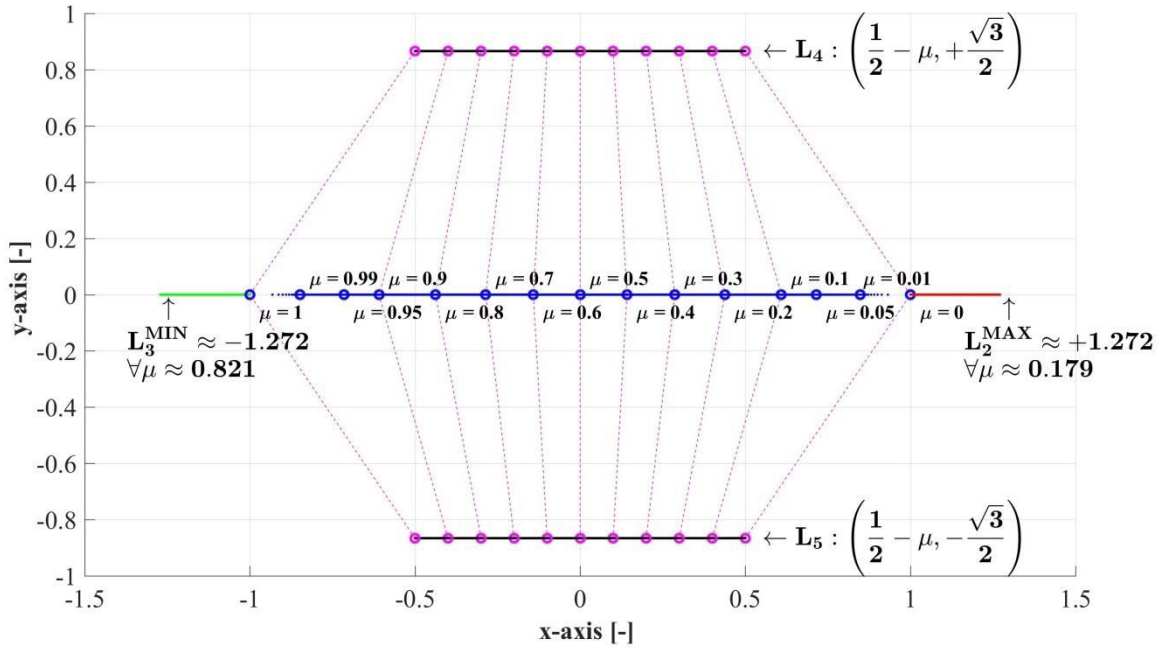


Figure 4: Location of all five libration points on the $\hat{x}\hat{y}$ -plane with a varying μ -parameter between 0 and 1. Note the symmetric behaviour respect to $\mu = 0.5$, as explained in the text.

The two limit cases, previously mentioned, are visible here where L1/L2 shrink near M2 when $\mu \rightarrow 0$ (called *Hill's Problem*), while L3 is exactly in opposition to M2 respect to M1 (so on the negative \hat{x} -axis). Symmetric distribution is given for $\mu \rightarrow 0.5$, since L1 exists at the barycentre of this almost perfect binary configuration, while both L2 and L3 would be symmetrically located along the syzygy direction. (Szebehely, 1967)

2.1.2.1 Integral of motion: the Jacobi constant

Before presenting main symmetries in the equations of motion, a very brief note has to be discussed in relation of the so-called Jacobi constant, the only existing Integral of Motion determined by (Jacobi, 1836) and later used in (G. W. Hill, 1886) to “determine the motion of an asteroid in the three-body problem and to introduce the so-called zero velocity curves (ZVC), which establish regions in space where the bodies are allowed to move” (Musielak & Quarles, 2014).

The previous can be simply illustrated by considering the existence of a potential function $\Omega = \Omega(x, y, z)$, such that Eq. (2-5) is reduced to a more compact form as

$$\begin{cases} \ddot{x} - 2\dot{y} = \Omega_{,x} \\ \ddot{y} + 2\dot{x} = \Omega_{,y} \\ \ddot{z} = \Omega_{,z} \end{cases} \quad (2-10)$$

with the subscript referring to each first partial derivatives (so each component of the gradient ∇ -operator). After few manipulations well-known in common literature, we have

$$C_J = 2\Omega - V^2 = 2 \left[\frac{x^2 + y^2}{2} + \frac{1 - \mu}{r_1} + \frac{\mu}{r_2} \right] - (\dot{x}^2 + \dot{y}^2 + \dot{z}^2) \quad (2-11)$$

where the Jacobi constant C_J (non-dimensional) is totally defined by the initial condition. Most of this theory has been covered by several authors and is well documented in general textbooks, as listed before, while a very remarkable aspect here is the relation of the C_J with the physical energy of the system.

In fact, as detailed in (Szebehely, 1967), the Jacobi constant can be seen as twice the P3 total energy ¹, where for the Restricted problem the most correct assumption is that $m_3 \ll M_1, M_2$. Often misleading in literature is the assumption that $m_3 = 0$, while Eq.(2-2) actually requires to divide both terms by the non-zero P3 mass. Furthermore, the energy conservation that holds for the general 3-Body Problem is consequently here also approximated by this “*uncoupling nature*” of the Restricted problem, thus justifying the possibility of considering P1/P2 in a Kepler motion (also conservative). As described in the cited paper, the Jacobi integral “*is not an expression of the conservation of energy*” and “*it should be simply regarded as an integral of the differential equations of the restricted problem*”.²

On this point we will come back once talking about the Non-Existence of First Integrals for elliptic case (Section 4.1.4), while now we can proceed exploiting symmetries of the Circular problem, above the one already discussed and related to the μ -parameter. In fact, the latter will be fixed for all our simulations (defined by the Earth-Moon system), as later discussed in Section 2.1.3.

¹ The Jacobi constant can be expressed also in an inertial frame, and this was exactly the case originally published in (Jacobi, 1836), even if, according to (Wintner, 1941), he has been the one “*re-discovering the synodic frame*”.

² For sake of completeness we have to point out that commonly in literature the Jacobi integral includes also a constant term as $\mu(1 - \mu)/2$, not used in this work. The latter does not affect the equations of motion but was only used to obtain a different expression for C_J . (Szebehely, 1967).

2.1.2.2 Symmetries in the equations of motion

The differential system in Eq. (2-5) can provide many insights into this dynamical model, especially when considering all the existing symmetries in the equations of motion. In (Miele, 1960), the author presents two theorems, which can be summarized as follow:

Theorem 1.1 (The Irreversibility Theorem)

“If a trajectory is physically possible in the xyz-space, the reverse trajectory is not physically possible”.

Theorem 1.2 (The Theorem of Image Trajectory)

“If a trajectory is physically possible in the xyz-space, three image trajectories are physically possible:

- a) The image with respect to the xy-plane, flown in the same sense of the original trajectory.*
- b) The image with respect to the xz-plane, flown in the opposite sense.*
- c) The image with respect to the x-axis, flown in the opposite sense.”*

The model adopted for both theorems is once again the CR₃BP, in particular the Earth-Moon system, while his results are evidently valid for any other systems, therefore for any constant μ -values. Both theorems refer to synodic coordinates, where it has been shown in the previous Literature Study that the *Lagrangian* can be expressed as

$$\mathcal{L}_{ROT} = \frac{(\dot{x} - y)^2 + (\dot{y} + x)^2}{2} + \left[\frac{1 - \mu}{r_1} + \frac{\mu}{r_2} \right] \quad (2-12)$$

If considering the Irreversibility Theorem we refer to the “reverse trajectory” as the path followed after a time-transformation as $t^* \rightarrow -t$. Consequently it is trivial to observe that the Lagrangian is not invariant under such transformation (Wintner, 1941), and the reverse trajectory cannot exist. In fact, for a general coordinate $q = q(t)$, we have that

$$\frac{dq}{dt} = -\frac{dq}{d(-t)} \equiv -\frac{dq}{dt^*} \quad \xrightarrow{\text{it follows that}} \quad \frac{dq}{dt} \neq \frac{dq}{dt^*} \quad (2-13)$$

and velocity terms are not more equivalent to previous ones, as also for the value of \mathcal{L}_{ROT} .

The Theorem of Image Trajectory is fundamental for the study of periodic motion in the neighbourhood of collinear libration points, as also reviewed in (Miele, 2010) for the 50th anniversary of the original theorem. Starting with Eq. (2-5), two main transformations can be found, here denoted as Mirrored and Backward transformation.

MIRRORED TRANSFORMATION:

$$z^* \rightarrow -z \quad (2-14)$$

BACKWARD TRANSFORMATION:

$$y^* \rightarrow -y, \quad t^* \rightarrow -t \quad (2-15)$$

Both previous transformations are described in point “a” and “b” of **Theorem 1.2** and from the moment that they are *not* mutually exclusive, it is possible to combine both in a third type, defined as Backward Mirrored, indeed symmetric respect to the \hat{x} -axis.

BACKWARD MİRRORED TRANSFORMATION:

$$y^* \rightarrow -y, \quad z^* \rightarrow -z, \quad t^* \rightarrow -t \tag{2-16}$$

In fact, point “c” of the **Theorem 1.2** refers exactly to this last type of symmetry at the same time respect to both the $\hat{x}\hat{z}$ -plane and $\hat{x}\hat{y}$ -plane, consequently respect to the \hat{x} -axis.

Once again, from Eq. (2-12) the expression of the Lagrangian in synodic coordinates confirms all these proprieties, which the reader could prove simply applying the given transformations on the full differential system shown in Eq. (2-5). The application of all symmetries will be discussed later. In Figure 5 an example of the three “image trajectories” has been presented starting from a nominal one, integrated numerically for a certain time in the Earth-Moon CR3BP, where also initial conditions (“ \diamond ”) have been changed according to each proper transformation, so assuring consistency in results.

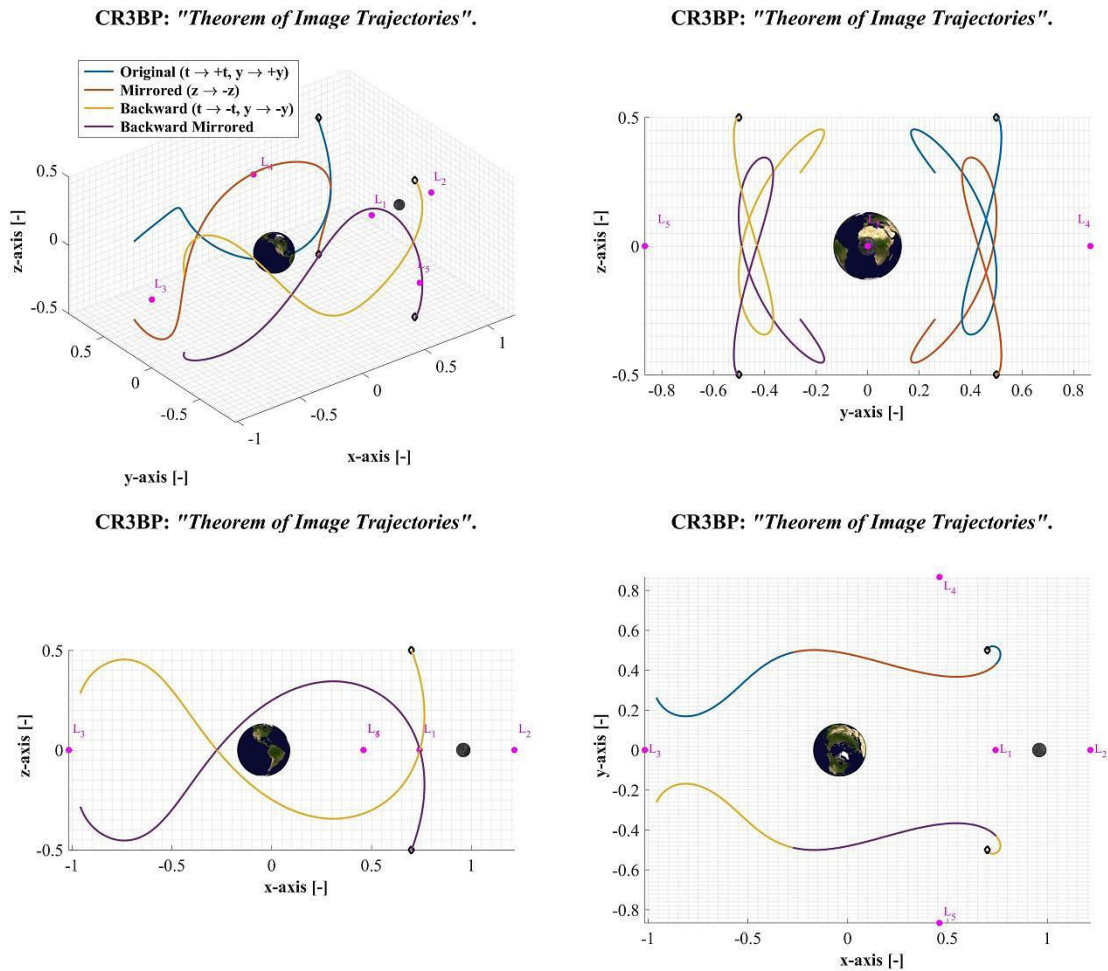


Figure 5: Main three symmetries for the Earth-Moon Circular Restricted 3-Body Problem given in synodic coordinates. The masses’ size has been enlarged [$\times 8$] for graphical reasons.

2.1.3 TEST-CASE: the Earth-Moon system

So far, main basic proprieties have been shown for the general Circular problem (CR3BP) and later they will be employed for the analysis of certain families of periodic solutions near collinear Lagrange points. What has been analysed in this work is a “model”, later extended and compared with a more complete one, once considering the Elliptic problem (ER3BP). Unfortunately, the real physical world involves a dynamics much more complex and for a realistic mission’s design it is absolutely necessary to take into account all different perturbations acting on the system. ([Lynch, 2001](#))

Despite this last consideration, one of the main purposes here is the investigation and comparison of two basic models, commonly adopted for studies in many space-related fields (e.g., interplanetary transfers, space observation missions, etc...). Both these models represent already a revision and upgrade of older theories, for example the very well-known 2-Body Problem with its several proprieties and solutions, successfully employed for decades in hundreds of space missions. ([Szebehely, 1967](#))

For all the mentioned reasons, we feel the necessity to underline again that the investigation presented in this paper has not to be treated as an attempt to design or neither to optimize a real specific space mission, but it can be seen more as a “theoretical pivot”, necessary step for improving the current knowledge on a problem that “*has attracted the attention of many scientists for more than 300 years*” ([Musielak & Quarles, 2014](#)). Furthermore, a very broad analysis for various μ -parameters on the entire range is not really suitable and some boundary cases will be physically worthless. In fact, in the Solar system most of known mass-ratios are confined within certain limits, and in addition to this, none of such binary systems discovered “*has been yet visited by a spacecraft*” ([Bosanac, Howell, & Fischbach, 2015](#)).

Here the decision of fixing the μ -value and to consider a specific three body system, adopted later also for the Elliptic problem. Our analysis will aim to create a “robust procedure” for the investigation of particular solutions in the general CR3BP and later in the ER3BP. The same could also be applied to different μ -values, in this way studying different physical systems as well as binary ones (e.g., binary stars/asteroid or double planets), recently arising much more interest among scientists and researchers.³

Hence, we will consider the Earth-Moon system as the nominal one, modelling its dynamics as a perfect Circular Restricted 3-Body Problem, thus focusing on the investigation of periodic motion near both libration points L1 and L2. As discussed in Section 1.2, for the L3-point there are currently only few “*mission concepts designed to detect and accurately measure gravitational waves*” ([Mueller, 2014](#)), while several dynamical aspects of periodic motion at L3 have been already studied in ([Barrabés & Ollé, 2006](#)). Additional reason for the exclusion of L3 is due to the fact that, at the time of writing, no space mission is active or has been confirmed; beside that, many other complications arise at L3 for its application in real space scientific missions, as adequately documented in ([Tantardini et al., 2010](#)). At this point we can proceed providing some numerical data and further discussing the ‘real’ Earth-Moon system.

³ Worthy to be mentioned are some recent researches performed at Delft University of Technology detailed in ([J. Feng, Noomen, Yuan, & Ambrosius, 2014](#)), ([J. L. Feng, Noomen, Visser, & Yuan, 2015](#)), ([J. Feng, Noomen, & Yuan, 2015](#)) and ([J. Feng, Noomen, Visser, & Yuan, 2016](#)), concerning an extensive research over different types of periodic motion in a contact binary asteroid system.

2.1.3.1 Additional simplifications in the Earth-Moon model

As stated at the beginning of this Chapter, the CR3BP is usually modelled considering M_1 , M_2 as point-masses orbiting in circular Keplerian orbits around their barycentre, while the third mass m_3 is negligible and has not influence on them. Nonetheless, in the real physical world several other dynamical elements are present, for example the already mentioned eccentricity. Without getting lost in the definition of all possible “perturbations”, e.g. general relativity effects, additional bodies perturbation (*N-Body Problem*) and so on, here we are going to briefly present few principal contributors to the real Earth-Moon system’s dynamics, and in general for many other 3-Body systems.

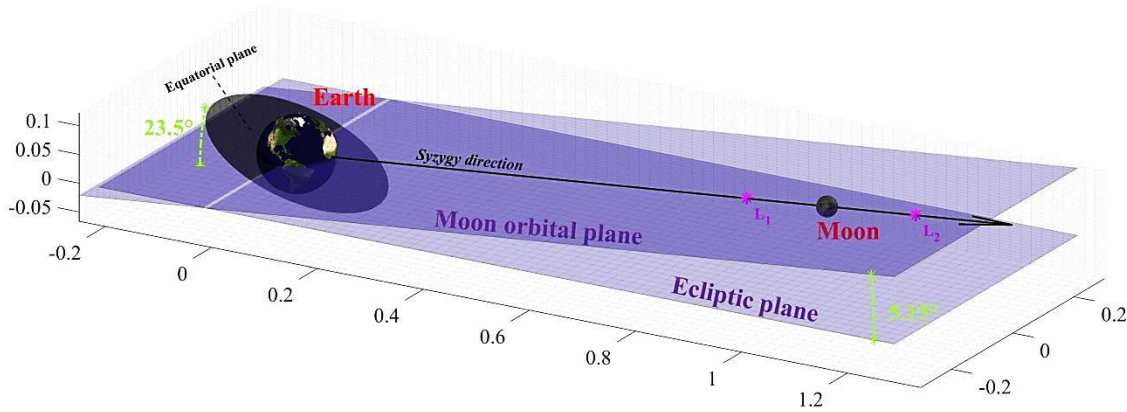


Figure 6: The geometry and the motion of the Earth-Moon system is shown, with a sketch of all main reference planes involved (in purple) and relative angles (in green).

In Figure 6, an example for the Earth-Moon system is given, with relative basic geometry and main angles, while in the following Table 1 some planetary data has been provided.

Table 1: Bulk and Orbital parameters relative to both Earth and Moon body (NASA, 2016)

| | Units | Earth | Moon |
|---------------------------|--------------|---------|---------|
| Bulk Parameters | | | |
| Mass | 10^{24} kg | 5.9724 | 0.07346 |
| Equatorial Radius | km | 6378.1 | 1737.4 |
| Polar Radius | km | 6356.8 | 1736.0 |
| J2-term | 10^{-6} | 1082.63 | 202.7 |
| Orbital Parameters | | | |
| Semi-major axis | 10^6 km | 149.60 | 0.3844 |
| Eccentricity | — | 0.0167 | 0.0549 |

Once taking into consideration a more realist model for the Earth-Moon system, it is possible to summarize most important additional forces in three main contributors:

- The barycentre of the entire EM-system is revolving around the Sun in a not perfect circular orbit ($e \approx 0.0167$), making the system not inertial anymore.
- Both masses are not exactly spheres, but they can be described as oblate spheroids, so the gravitational potential will include additional terms, based on two types known as Zonal and Tesseral harmonics (Cunningham, 1970).
- The Sun generates a solar radiation pressure, which could affect not only the motion of the spacecraft, but also the entire CR3BP dynamics, as for example the location itself of equilibrium points. (Simo & McInnes, 2009)

The effects of the Moon on the Sun-Earth circular problem has been numerically studied in (Farquhar, 1970), showing a shift in the location of L2 of around 300 km, where “*the maximum distance to the perturbed path is about 20 km*”. For what concerns our EM-model, in Section 1.9 from (Szebehely, 1967) many different perturbations has been presented, as also for the Moon effect on the Earth motion compared to the probe one (around 16 orders of magnitude smaller). The latter totally justifies the possibility of adopting the “restricted problem”, while neglecting one of the two main masses can have much larger effects depending on the relative P3-position.

Many models have been proposed in the past decades for what can be seen as a Restricted 4-Body Problem, having the Sun-Earth-Moon-Satellite system. In this system some periodic solutions has been study originally by (Cronin, Richards, & Russell, 1964) where the model has been “*regarded as a perturbation of the R3BP*”. Very extensive investigation was later made by (K. Hill, Lo, & Born, 2006), showing that “*in the four-body problem, there are no longer any periodic solutions because the same positions of the primaries do not repeat within any reasonable length of time. Instead, trajectories must be computed that are fairly close to periodic, at least for the time interval desired*”.

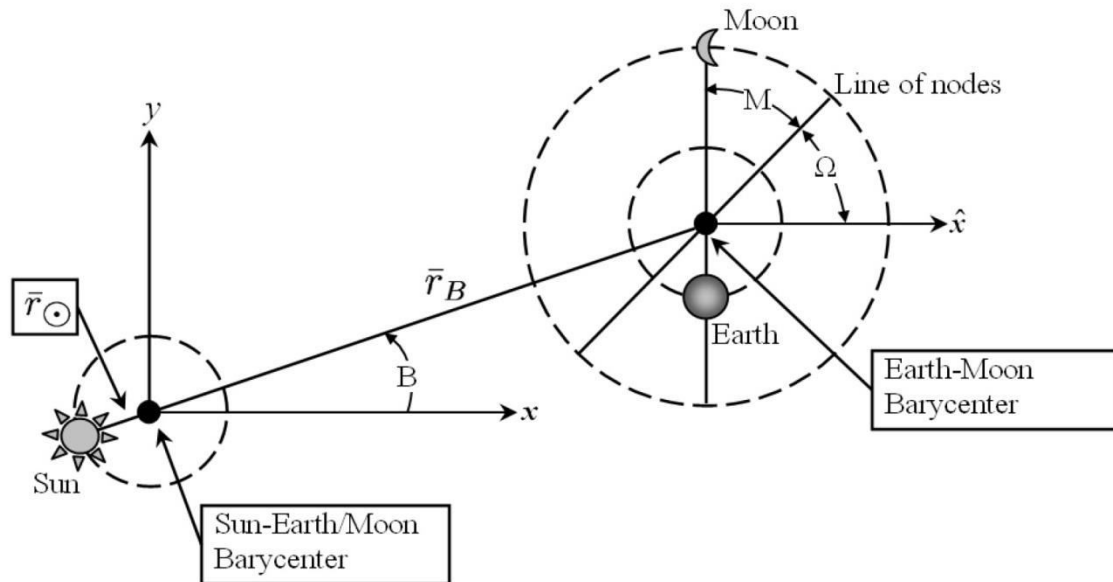


Figure 7: Geometry of the inclined Inertial Bi-circular Model by courtesy of (K. Hill et al., 2006). For the notation adopted and more details on the model used, we refer to their paper.

For sake of completeness, here in Figure 7 we have provided the sketch of the more correct and complete *inclined* Inertial Bi-circular Model adopted in (K. Hill et al., 2006). All details can be found in their paper, where the inclination between planes (in Figure 6), has been taken into account also with Solar Radiation Pressure (SRP) effects.

As results of that analysis, some consequences on the orbit determination error by LiAISON⁴ (Linked Autonomous Interplanetary Satellite Orbit Navigation) have been summarized as roughly 3% for the Sun’s gravity and 1% due to the relative inclination w.r.t. the ecliptic plane, while the SRP “*does not seem to effect the dynamics enough to cause an increase in the orbit determination error*” (K. Hill et al., 2006).

⁴ More Information can be found on the NASA Website, Jason Leonard, *University of Colorado, Boulder*, 2013. https://www.nasa.gov/spacetechnology/strg/2013_nstrf_leonard.html#.V5iBArh96hc

All mentioned aspects are very significant and necessary to further improve the dynamical model, as suggested in Section 6.2 (“*Recommendations for future works*”). Here, once again we only consider both Circular and Elliptic problems, in their ‘standard’ formulation and using the Earth-Moon system only as main reference model. The latter is commonly used in some recent papers for the examination of the ER3BP and periodic motions around libration points, in this way allowing having reliable results to be compared with, as also in order to validate and then verify the final outcome of this work.

Last step of this systematic examination over perturbations involves an example of the extended CR3BP dynamics, with the *Primary* radiating and the *Secondary* as an oblate (e.g., as for the Sun-Earth system). Following the notation adopted in ([Sharma, 1987](#)) for the planar 2D-problem and later in ([Tiwary & Kushvah, 2015](#)) for the spatial 3D-problem, it is possible to express the motion similarly to Eq. (2-10), so leading to

$$\begin{cases} \ddot{x} - 2n_{ro}\dot{y} = \Omega_{,x}^{ro} \\ \ddot{y} + 2n_{ro}\dot{x} = \Omega_{,y}^{ro} \\ \ddot{z} = \Omega_{,z}^{ro} \end{cases} \quad (2-17)$$

with the definition of a new mean motion n_{ro} and a new pseudo-potential function Ω^{ro} , both referring to the new Radiating-Oblate Circular problem. Clearly, n_{ro} is affected by the oblateness of the Secondary mass, as also for its orbital period T_{ro} (here expressed in non-dimensional units), such that we arrive at

$$n_{ro} = \sqrt{1 + \frac{3}{2} \left(\frac{R_e^2 - R_p^2}{5r^2} \right)} \quad \xrightarrow{\text{by definition}} \quad T_{ro} = \frac{2\pi}{n_{ro}} \quad (2-18)$$

with r distance between the two masses (here $r = a$) and R_e, R_p respectively equatorial and polar radii of the oblate M_2 . The new pseudo-potential function Ω^{ro} is written as

$$\Omega^{ro} = n_{ro}^2 \frac{x^2 + y^2}{2} + \frac{1 - \mu}{r_1} [1 - \beta] + \frac{\mu}{r_2} \left[1 + \frac{1}{2r_2^2} \left(\frac{R_e^2 - R_p^2}{5r^2} \right) \right] \quad (2-19)$$

with r_1, r_2 distances previously defined in Eq. (2-6), while $\beta = F_{rad}/F_g$ is ratio between solar radiation and gravitational attraction forces, sometimes expressed by $q = 1 - \beta$, with q as *mass reduction factor*, constant for a given particle. A very complete survey on this radiation parameter β can be found in ([Schuerman, 1980](#)), while typical values for spacecraft without solar sail have been computed as $\beta \approx 1.5 \times 10^{-5}$ for the Sun-Earth system when considering both L1 and L2 points. ([McInnes, 2000](#))

More details of all these dynamical aspects can also be found in the cited papers, and most of these researches are currently being carried out in order to improve the standard dynamical model. For a general overview on some state-of-the-art works we suggest to consider ([Musielak & Quarles, 2014](#)), while now we will continue the analysis relative to the standard Circular problem (CR3BP), so introducing the Dynamical System Theory, one of the most important concepts in this work.

2.2 Dynamical System Theory for the circular case

The *Dynamical System Theory* (DST) is a field of mathematics introduced by J.H. Poincaré (1854-1912) for studying the 3-Body Problem in “*Les Methodes Nouvelles de la Mecanique Celeste*”, published between 1892-99 ([Musielak & Quarles, 2014](#)). As reported in ([Barrow-Green, 1997](#)), “his objective was to provide a geometrical study of the solution curves of a first-order differential equation, and indeed it was his geometrical insight which becomes one of the hallmarks of his work on differential equations”.

All background knowledge has been covered in the Literature Study and main basic definitions or theorems can be found in many common textbooks as ([Barrow-Green, 1997](#)), ([Verhulst, 2000](#)) and ([Perko, 2001](#)), while here we provide some theoretical key elements for a better interpretation of all results given in Chapter 3.

2.2.1 Proprieties of “autonomous differential systems”

We start considering the Circular Restricted 3-Body Problem, defined by a system of three second-order differential equations, as shown in Eq. (2-5). The latter is known to be an *autonomous* differential system from the moment that each equation does not depend explicitly upon the time-like parameter used (so far t , non-dimensional physical time).

One of the most important advantages of the Dynamical System Theory (DST) is the possibility of re-writing a general n -order differential system into a new first-order one. For example, we can start with a time-dependent variable $q = q(t)$, such that

$$\frac{d^n q}{dt^n} = g\left(q, \frac{dq}{dt}, \dots, \frac{d^{n-1}q}{dt^{n-1}}\right) \quad (2-20)$$

with g general function. We can define new variables based on some transformations as

$$q_1 = q, \quad q_2 = \frac{dq}{dt}, \quad \dots, \quad q_n = \frac{d^{n-1}q}{dt^{n-1}} \quad (2-21)$$

and then, re-writing the differential system in Eq. (2-20), we arrive at

$$\begin{cases} \dot{q}_1 = \frac{dq_1}{dt} = q_2 \\ \dot{q}_2 = \frac{dq_2}{dt} = q_3 \\ \dots \\ \dot{q}_n = \frac{dq_n}{dt} = g(q_1, q_2, \dots, q_n) \end{cases} \quad (2-22)$$

The latter can be also expressed in a more compact vector form, so leading to

$$\dot{\mathbf{Q}} = \frac{d\mathbf{Q}}{dt} = \mathbf{f}(\mathbf{Q}) \quad (2-23)$$

where \mathbf{f} is a vector-function, while \mathbf{Q} is the state-vector of the system, $\forall \mathbf{Q} \in \mathbb{R}^n, \forall t \in \mathbb{R}$.

Expressions in Eq. (2-22) and Eq. (2-23), can describe a n -dimensional space, in literature also denoted as “Phase-space” of the dynamical system, in this way allowing having a complete geometrical view of each solution and of the vector-field described by $f(\mathbf{Q})$.

NOTE:

Before going further in the description of the DST, one important remark is given by the so-called “**Existence and Uniqueness Theorem**” (but here not formulated), which assures that the solution exists and for some given initial conditions it is also unique. Basically at each time t , a phase-point describes the particular state of the original differential system, thus basically it is a solution of the system itself. ([Verhulst, 2000](#))

2.2.1.1 Critical points and their neighbourhoods

In this n -dimensional Phase-space each trajectory represents a specific solution that can be periodic or not. Moreover, straightforward is to shown that orbits in the Phase-space can never really intersect in a finite time, direct consequence of the previous theorem. However, as seen in Section 2.1.2, the CR3BP has some particular equilibrium solutions, such that they are usually referred as *critical points* (or *stationary points*) of the system, as points $\bar{\mathbf{Q}} = \mathbf{a}$ of the domain where f has its zeros, so with $f(\mathbf{a}) = \mathbf{0}$. ([Perko, 2001](#))

Looking at the Circular problem, it is trivial to understand that each Lagrange point is exactly a critical point of the dynamical system, but only when considering synodic coordinates. Moreover, all components of the P_3 -velocity can be seen simply as additional variables of our differential system, based on the Eq. (2-21), and consequently they generate a six-dimensional Phase-space, defined by the following expression

$$\begin{cases} \dot{x} = v_x \\ \dot{y} = v_y \\ \dot{z} = v_z \\ \dot{v}_x = 2v_y + x - (1 - \mu) \frac{(x + \mu)}{r_1^3} - \mu \frac{(x + \mu - 1)}{r_2^3} \\ \dot{v}_y = -2v_x + y \cdot \left[1 - \frac{(1 - \mu)}{r_1^3} - \frac{\mu}{r_2^3} \right] \\ \dot{v}_z = -z \cdot \left[\frac{(1 - \mu)}{r_1^3} - \frac{\mu}{r_2^3} \right] \end{cases} \quad (2-24)$$

where the transformation $v_q = dq/dt$ has been used for all three variables as $q = \{x, y, z\}$. In this six-dimensional geometrical view, coordinates of each L-point can be defined as

$$\mathbf{X}_{Li} = [x_{Li}, y_{Li}, z_{Li}, 0, 0, 0] \quad (2-25)$$

with the new state-vector $\mathbf{X} = \mathbf{X}(t) \in \mathbb{R}^6$ ($\forall t \in \mathbb{R}$), involving all positions coordinates described by Eqs. (2-7)(2-8). Usually main interest point in real space missions is the behaviour within a certain neighbourhood of these “mathematical points”. In fact, it is almost impossible to achieve such exact initial conditions, thus this so-called “stability” can have a great influence on the costs (e.g., DV-budget for station-keeping manoeuvres) necessary in order to maintain the spacecraft as close as possible to a nominal trajectory or sufficiently close to these points. ([Koon, Lo, Marsden, & Ross, 2008](#))

Before further proceeding, we introduce the definition for some different types of stability, which can also be found in the suggested textbooks. Now, we take a differential system for the general state-vector $\mathbf{Q} \in \mathbb{R}^n, \forall t \in \mathbb{R}$ with the definition of a generic vector function $\mathbf{f} \in C^0[\mathbf{Q}, t]$, Lipschitz in \mathbf{Q} , and $\bar{\mathbf{Q}} = \mathbf{a}$ as critical point. ([Verhulst, 2000](#))

Definition 1.1a (Lyapunov Stability)

Assuming that $\exists \delta = \delta(t_0, \epsilon) > 0, \forall \epsilon > 0$ such that

$$\text{if } \|\mathbf{Q}(t_0; t_0, \mathbf{Q}_0) - \mathbf{a}\| \leq \delta \quad \text{then} \quad \|\mathbf{Q}(t; t_0, \mathbf{Q}_0) - \mathbf{a}\| \leq \epsilon, \forall t \geq t_0$$

the critical point is **Stable** in the “sense of Lyapunov” and, starting sufficiently close to it, the solution will remain always bounded in its neighbourhood.

Definition 1.1b (Asymptotic Stability)

Assuming that $\exists \delta = \delta(t_0, \epsilon) > 0, \forall \epsilon > 0$ such that

$$\text{if } \|\mathbf{Q}(t_0; t_0, \mathbf{Q}_0) - \mathbf{a}\| \leq \delta \quad \text{then} \quad \lim_{t \rightarrow \infty} \|\mathbf{Q}(t; t_0, \mathbf{Q}_0) - \mathbf{a}\| = 0$$

the critical point is **Asymptotically Stable** and, starting sufficiently close to it, the solution will tend asymptotically toward it.⁵

Based on these previous definitions we will refer to *linear stability* as the stability assessed by looking at the dynamics linearized in a neighbourhood of each critical point. Consequently considering a first-order Taylor expansion around L-points, we obtain

$$\dot{\mathbf{X}} = \mathbf{f}(\mathbf{X}_{Li}) + \frac{\partial \mathbf{f}}{\partial \mathbf{X}} \Big|_{\mathbf{X}_{Li}} \cdot \Delta \mathbf{X}_{Li} + \mathcal{O}(\Delta \mathbf{X}_{Li}^2) \quad \forall \Delta \mathbf{X}_{Li}(t) = \mathbf{X}(t) - \mathbf{X}_{Li} \quad (2-26)$$

with the \mathcal{O} -Landau notation ([Landau, 1974](#)), where by definition $\mathbf{f}(\mathbf{X}_{Li}) = \mathbf{0}$ and after neglecting higher order terms, we can define the displacement motion $\tilde{\mathbf{X}}(t) = \Delta \mathbf{X}_{Li}(t)$ as

$$\frac{d}{dt} \begin{bmatrix} \tilde{x} \\ \tilde{y} \\ \tilde{z} \\ \tilde{v}_x \\ \tilde{v}_y \\ \tilde{v}_z \end{bmatrix} = \begin{bmatrix} 0 & 0 & 0 & 1 & 0 & 0 \\ 0 & 0 & 0 & 0 & 1 & 0 \\ 0 & 0 & 0 & 0 & 0 & 1 \\ \Omega_{,xx} & \Omega_{,xy} & \Omega_{,xz} & 0 & 2 & 0 \\ \Omega_{,yx} & \Omega_{,yy} & \Omega_{,yz} & -2 & 0 & 0 \\ \Omega_{,zx} & \Omega_{,zy} & \Omega_{,zz} & 0 & 0 & 0 \end{bmatrix} \cdot \begin{bmatrix} \tilde{x} \\ \tilde{y} \\ \tilde{z} \\ \tilde{v}_x \\ \tilde{v}_y \\ \tilde{v}_z \end{bmatrix} \triangleq \frac{d\tilde{\mathbf{X}}(t)}{dt} = A|_{\mathbf{X}_{Li}} \cdot \tilde{\mathbf{X}}(t) \quad (2-27)$$

where $\Omega = \Omega(x, y, z)$ is again the pseudo-potential function, where its Hessian matrix⁶ generates the third quadrant of the constant A -matrix, usually referred as **State Propagation Matrix (SPM)**. All these aspects have been previously treated in the Literature Study, and are really well-known in the suggested general literature. However these last definitions serve as main reference points, later adopted for the numerical approach (Section 2.4), as also for extending these main concepts to the elliptic case.

⁵ The mentioned “*Existence and Uniqueness theorem*” assures that the critical point cannot be reached in a finite time, thus this explains the use of a limit and its appellative ‘asymptotic’.

⁶ Squared matrix that involves all the second-order partial derivatives of the scalar potential Ω , while its symmetry is due to the *Schwarz’s theorem*. See ([James, 1966](#)) for more information.

At this point, worthy to be mentioned is the so-called “*Hartman-Grobman Theorem*” (or also known as *Linearization Theorem*), able to show, under certain hypotheses, that “near an hyperbolic equilibrium point \mathbf{a} , the non-linear system has the same qualitative structure as the linear system” ([Perko, 2001](#)). In fact, Eq. (2-27) can be seen as a *Variational Equation* respect to the initial condition, so again being represented by a simply linear system of six first-order differential equations. It follows an associated Eigen-problem, here studied in order to characterize the behaviour of each L-point. In brief, this “Linearization Theorem” assures that in a neighbourhood of hyperbolic points⁷ the linear behaviour found is qualitatively the same also for the original non-linear system. A general classification of such points in 2-dimensional (or also n-dimensional) differential systems can be found in common literature, and for the Circular problem their stability has been extensively assessed in ([Szebehely, 1967](#)), so we can proceed here by introducing some essential concepts related to periodic solutions.

2.2.1.2 Periodic solutions and their stability

Concept of periodic solutions is related to the existence of a solution $\mathbf{X}(t) = \boldsymbol{\phi}(t)$ to the differential system, dependent on the time-like parameter t , such that

$$\boldsymbol{\phi}(t) = \boldsymbol{\phi}(t + T) \quad \forall t \in \mathbb{R} \quad (2-28)$$

where T is a positive scalar that defines the period. As observed in ([Verhulst, 2000](#)), if a solution is T -periodic, it means that it is also $2T$ -periodic, $3T$ -periodic and so on. This concept will be further discussed later, when introducing “Resonance orbits”, types of solutions that can ‘survive’ in the Elliptic problem (see Section 4.2). For now we only provide an important propriety within **Lemma 1**, concerning autonomous systems.

Lemma 1

“A periodic solution of the autonomous equation $\dot{\mathbf{Q}} = \mathbf{f}(\mathbf{Q})$ corresponds with a closed orbit (cycle) in phase-space and a closed orbit corresponds with a periodic solution.”

Significance of **Lemma 1** becomes more clear considering the *Poincaré Map* theory, known also as *First Recurrence Map* $\mathcal{P}^{[1]}$. The latter represents a powerful tool for analysing and assessing the existence of periodic solutions, which by definition need to repeat after a period T (returning at the same initial phase-point, named as *Initial* or *Shooting Condition*). Such theory is so extensive that will require an entire chapter in order to be summarized (but it is not the purpose here), therefore we suggest to look at ([Teschl, 2012](#)) for a deeper comprehension of all following mathematical concepts. Here we only re-define some types of stability, but now mainly related to periodic orbits.

Definition 1.2 (Lyapunov Stability for periodic solutions)

Assuming that $\exists \delta = \delta(t_0, \epsilon) > 0, \forall \epsilon > 0$ such that

$$\text{if } \|\mathbf{Q}(t_0; t_0, \mathbf{Q}_0) - \boldsymbol{\phi}(t_0)\| \leq \delta \quad \text{then} \quad \|\mathbf{Q}(t; t_0, \mathbf{Q}_0) - \boldsymbol{\phi}(t)\| \leq \epsilon, \forall t \geq t_0$$

the periodic solutions is **Stable** in the “sense of Lyapunov”, as seen in **Definition 1.1a**.

⁷ With “hyperbolic points” we refer to points in the Phase-space having real eigenvalues with different signs when studying Eq. (2-27), such that orbits in their neighborhood are defined hyperbolic. The latter is easy to visualize on a 2D-case, while considering a general n-dimensional Phase-space the situation becomes more complex, as it will be shown later.

Definition 1.2 requires that a phase-point in the n -dimensional Phase-space, which is initially close to the one belonging to a periodic solution, needs to remain close enough during its entire motion. However, in trajectories near to the nominal one, but having slightly different T-period, the displacement in time can grow fast due to an initial phase-shift.⁸ It follows now a new definition of stability, necessary for periodic solutions and based on the so-called First Recurrence Map (evaluated on a Poincaré Sections). The example in Figure 8 shows two Poincaré Maps (blue diamonds) on a 2D-plane (the Poincaré Section in violet) for both a periodic and non-periodic orbits (in dashed red).

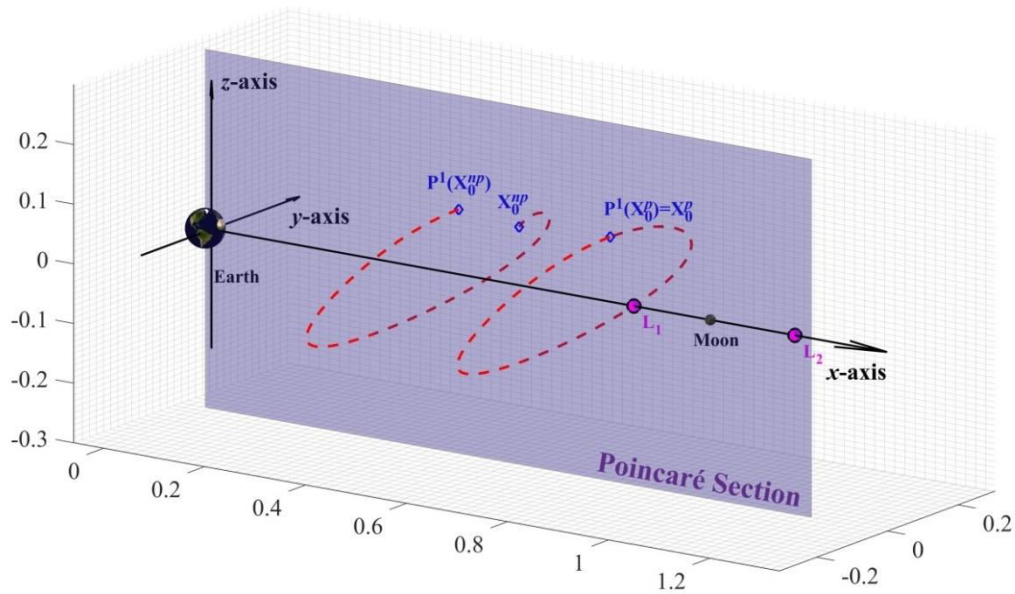


Figure 8: Illustration of two Poincaré Maps (blue diamonds) on a 2-dimensional Poincaré Section (in violet) for periodic/no-periodic solutions (respectively X_0^p and X_0^{np} in dashed red).

In continuous dynamical systems we are able to fix one or more coordinates in order to define a sub-space $\mathbb{V} \subset \mathbb{R}^n$ of the original n -dimensional Phase-space $\mathbb{M} \subseteq \mathbb{R}^n$. In this way we are able to study closed orbits simply as points within \mathbb{V} , referred as *Transversal* (Verhulst, 2000), as it requires to intersect the Phase-flow *transversally*. So considering the closed trajectory as fixed point on a specific \mathbb{V} -Transversal, we define a third type of stability starting from Eq. (2-28), thus looking at the ‘local’ dynamics within such sub-set.

Definition 1.3 (Orbital Stability for periodic solutions)

Assuming that it is possible to define a Poincaré Map \mathcal{P}^n on the \mathbb{V} -Transversal for the periodic solution $\phi(t)$, such that \mathbf{a} is a fixed point on it with the initial condition $\mathbf{Q}_0 \in \mathbb{V}$. Now $\exists \delta = \delta(\epsilon) > 0, \forall \epsilon > 0$ such that

$$\text{if } \|\mathbf{Q}_0 - \mathbf{a}\| \leq \delta \quad \text{then} \quad \|\mathcal{P}^n(\mathbf{Q}_0) - \mathbf{a}\| \leq \epsilon, \forall n \geq 1$$

it follows that the periodic solutions is **Orbitally Stable**.⁹

⁸ In order to better visualize this concept, it is possible to think about a phase-shift as $\approx \pi$ in a sine or cosine component of the solution, so leading to a large displacement during this new motion.

⁹ Note that Definition 1.3 clearly matches with both **Definition 1.1a** and **Definition 1.1b**, and it also admits the “asymptotic formulation” once considering the new condition

$$\lim_{n \rightarrow \infty} \|\mathcal{P}^n(\mathbf{Q}_0) - \mathbf{a}\| = 0, \forall n \geq 1$$

2.2.2 The Monodromy matrix and its eigenvalues

After giving the main basic concepts of this Dynamical System Theory, it is necessary to provide much more insights into the dynamics of the CR3BP, consequently linking it with some practical aspects of real space missions. So far we have seen how it is possible to study the local dynamics near libration points, while great interest is usually also given to the possible existence of periodic solutions around collinear L-points. Once again, only L1/L2 will be considered in this work and the investigation will focus on three different types of periodic solutions, as described later in Section 2.3.

As seen in the Eq. (2-26), we are capable of studying the stability in a neighbourhood of a nominal periodic motion, when linearizing the dynamics around it. Considering here a shooting condition \mathbf{X}_0 for the periodic solution $\phi(t; \mathbf{X}_0)$, this last one can be expressed as shown in Eq. (2-28), but differentiated at $t = t_1$ respect to the initial condition, such that

$$\delta \mathbf{X}(t_1) = \phi(t_1; \mathbf{X}_0 + \delta \mathbf{X}_0) - \phi(t_1; \mathbf{X}_0) \cong \frac{\partial \phi}{\partial \mathbf{X}_0} \cdot \delta \mathbf{X}_0 + \mathcal{O}(|\delta \mathbf{X}_0|^2) \quad (2-29)$$

Neglecting again higher order terms $\mathcal{O}(|\delta \mathbf{X}_0|^2)$ it is possible to related both the *initial* and the *final* displacement using the **State Transition Matrix (STM)** defined as

$$\Phi(t_1, t_0) = \frac{\partial \phi(t_1; \mathbf{X}_0)}{\partial \mathbf{X}_0} \quad (2-30)$$

and it can be shown through few manipulations ([Gómez et al., 2004](#)) that

$$\frac{d}{dt} \Phi(t_1, t_0) = A \cdot \Phi(t_1, t_0) \quad \forall \Phi(t_0, t_0) = \mathbb{I}_n \quad (2-31)$$

where A has been already presented as SPM in Eq. (2-27), while \mathbb{I}_n is the identity matrix. At this point, the STM can be propagated and evaluated¹⁰ at each instant for an entire period till $t_1 = t_0 + T$, and so leading to the definition of M , the **Monodromy Matrix**. Using Eq. (2-29) we are trying to determine effects due to an initial displacement after a complete revolution of the nominal trajectory (closed curve in the phase-space), with

$$\delta \mathbf{X}_T = \Phi(t_0 + T, t_0) \cdot \delta \mathbf{X}_0 = M \cdot \delta \mathbf{X}_0 \quad (2-32)$$

Note that M is here constant and the associated Eigen-problem could be studied to assess this “linear stability”. Indeed, one major constraint is related to the approximation of the dynamics respect to a reference trajectory, thus the validity itself of Eq. (2-29) holds only as long as the term $\mathcal{O}(|\delta \mathbf{X}_0|^2)$ remains small. Many previous notions are part of a more general theory called *Floquet theory*, and better described in Section 4.2.2 for the elliptic case, meanwhile here we are still discussing main aspects related to the Circular problem.

¹⁰ This system requires to be numerically integrated since the State Propagation Matrix has to be evaluated along the nominal solution, which is not known analytically (even if there are some approximations as described in Section 2.3, “Analytic approach”). Applications and all main numerical aspects will be discussed later in Section 2.4 (“Numerical Approach”).

2.2.3 Symplectic form: behaviour of “characteristic multipliers”

The discussion over linear stability involves not only closed trajectories around libration points, but more in general almost any periodic solutions of the CR3BP. Furthermore, eigenvalues λ_i of the Monodromy matrix (sometimes referred as *Variational matrix*) are also called “characteristic multipliers” from the moment that given a general component $X^i(t)$ of the State vector $\mathbf{X}(t)$ it is possible to write, for a general n -dimensional case, that

$$\delta X_T^i = \lambda_i \cdot \delta X_0^i \quad \forall i = 1 \dots n \quad (2-33)$$

with $\lambda_i \in \mathbb{C}$, complex eigenvalue and $\delta X_0^i, \delta X_T^i$ respectively initial and final displacements. At this point, one wise way to proceed is questioning if there are proprieties of the system that can help further simplifying such analysis. In general literature ([Goldstein, Poole, & Safko, 2002](#)) it is well-known that the CR3BP involves an Hamiltonian system, thus it can be fully defined by the so-called “Hamiltonian”, scalar function $H = H(\mathbf{p}, \mathbf{q}, t)$. After describing the system with generalized coordinates as $(\mathbf{p}, \mathbf{q}) \in \mathbb{R}^{2n}$, such that \mathbf{q} and \mathbf{p} are respectively defined as ‘position’ and ‘momentum’, the associated Hamilton equations can be written based on the following system

$$\begin{cases} \frac{d\mathbf{q}}{dt} = -\frac{\partial H}{\partial \mathbf{p}} \\ \frac{d\mathbf{p}}{dt} = +\frac{\partial H}{\partial \mathbf{q}} \end{cases} \quad (2-34)$$

The previous formulation, even though mathematically elegant, is not completely suitable for our problem since these generalized coordinates sometimes does not provide a direct physical interpretation of the problem, as also discussed in the Literature Study. However, first very important feature of Hamiltonian systems is that they have a structure denoted as *Symplectic*, which means that the evolution differential equations can be written ([Ott, 2002](#)) in the subsequent form

$$\frac{d}{dt} \begin{bmatrix} \mathbf{q} \\ \mathbf{p} \end{bmatrix} = S_{2N} \cdot \begin{bmatrix} \partial_{\mathbf{q}} H(\mathbf{q}, \mathbf{p}) \\ \partial_{\mathbf{p}} H(\mathbf{q}, \mathbf{p}) \end{bmatrix} \quad \xrightarrow{\text{more compactly as}} \quad \frac{d\mathbf{x}}{dt} = S_{2N} \cdot \nabla_{\mathbf{r}} H(\mathbf{x}) \quad (2-35)$$

with the new State vector $\mathbf{x} = [\mathbf{q}, \mathbf{p}]^T \in \mathbb{R}^{2n}$, its Jacobian $\nabla_{\mathbf{r}} = [\partial_{\mathbf{q}}, \partial_{\mathbf{p}}]^T$ and $S_{2N} \in \mathbb{R}^{2n \times 2n}$ defined by a block matrix $[2n \times 2n]$, such that

$$S_{2n} = \begin{bmatrix} \mathbb{O}_n & \mathbb{I}_n \\ -\mathbb{I}_n & \mathbb{O}_n \end{bmatrix} \quad (2-36)$$

composed by \mathbb{O}_n as null matrix $[n \times n]$ and \mathbb{I}_n as identity matrix $[n \times n]$. Obviously, this particular structure has substantial implications on the aforementioned characteristic multipliers, as also on the T-mapping discussed in relation to the Monodromy matrix, for indeed defined as a *symplectic map* in ([Howell & Campbell, 1999](#)).

In order to fully comprehend practical consequences of having such symplectic structure, we need to briefly enunciate the well-known *Liouville's Theorem*, with respect to autonomous differential system. ([Goldstein et al., 2002](#))

Theorem 1.3 (Liouville's Theorem)

“The flow generated by a time-independent Hamiltonian system is volume preserving.”

The latter can be easily visualized in the Phase-space as the propriety of an infinitesimal volume element (in our case six-dimensional) to be constant under the flow. The mathematical proof is very straightforward, as given in ([Verhulst, 2000](#)), but it requires additional notions/theorems not relevant in this work. Hence, we will just present the expression for the variation at $t = t_0$ of a general infinitesimal volume v , such that

$$\frac{dv}{dt}|_{t_0} = \int_{D(0)} \nabla \cdot \mathbf{f} d\mathbf{Q} = 0 \quad (2-37)$$

where $D(0) \in \mathbb{R}^n$ is a domain with initial volume $v(0)$, \mathbf{f} and \mathbf{Q} are vector-functions described before in Eq. (2-23) and $\{\nabla \cdot \}$ is the divergence respect to \mathbf{Q} -coordinates. From the Eq. (2-24), it can be observed that the divergence of the vector-field will be always zero, thus *any* infinitesimal volumes of the Phase-space is preserved in time. ([Ott, 2002](#))

With some basic linear algebra proprieties, it has been shown by ([Howard & MacKay, 1987](#)) that the characteristic multipliers come always in complex conjugate pairs, denoted as *quadruplets* $(\lambda, \lambda^{-1}, \lambda^*, \lambda^{*-1})$ with the asterisk symbol meaning conjugate. Their paper treats in a very complete way the “four-dimensional” symplectic maps, commonly related to six-dimensional autonomous differential problems, as explained later. Nonetheless, the product of all eigenvalues is always ± 1 , as also the value of the determinant of M, while applying **Theorem 1.3** on the system given with the Eq. (2-31) we obtain that $\det(M) = \det(\Phi(t_0 + T, t_0)) = +1, \forall t \geq t_0$, due to the initial condition as $\Phi(t_0, t_0) = \mathbb{I}_n$.

2.2.4 Geometrical meaning of “characteristic multipliers”

The principal outcome of studying eigenvalues of the Monodromy matrix can be easily summarized in three main points, thus following ([Howell & Campbell, 1999](#)).

- The CR3BP is Hamiltonian (time-independent) and consequently symplectic as given in Eq. (2-35). It follows that the STM can be considered as a Symplectic Map, so having pairs of reciprocal eigenvalues.
- The Monodromy matrix M (STM over a T-period) is real and for the symplectic propriety it has all its eigenvalues λ in quadruplets $(\lambda, \lambda^{-1}, \lambda^*, \lambda^{*-1})$. It follows from a positive initial condition in Eq. (2-31) that its determinant is always +1.
- When M is associated to a periodic solution $\phi(t)$ there exists at least a real $\lambda = +1$ and there will always exists an additional $\lambda_2 = +1$, for what seen in the first point.

The last point is one of the most important features of the Circular problem, where periodic solutions are always enclosed in *continuous* families, differently from what it will be extensively discussed for the elliptic case (in Chapter 4). Indeed, once looking at these periodic trajectories in a time-invariant six-dimensional Phase-space, it seems obvious how any initial displacements “along” such closed trajectory, remains bounded within this solution, and its orbital period does not change at all. ([Perko, 2001](#))

In a very recent work by (Nagata et al., 2016) the geometrical meaning of characteristic multipliers is fully exploited using the Centre Manifold Theory, originally applied in (Jorba & Masdemont, 1999) using a normal form scheme “to semi-analytically construct the high-order solutions about the dynamics in the centre manifolds of the collinear libration points”. More historical aspects can be found in (Shiobokov, 2014). At this point, it is clear why even if starting with a six-dimensional Phase-space, we have a four-dimensional symplectic map, even if the meaning of λ_2 still needs to be clarified. With a multiplicity larger than one, for its associated eigenvector \mathbf{v}_2 we can write that

$$\mathbf{M} \cdot \mathbf{v}_2 = \lambda_2 \cdot \mathbf{v}_2 + \epsilon \cdot \mathbf{v}_1 \quad (2-38)$$

where \mathbf{v}_2 “corresponds to the direction to another closed orbit near the original closed orbit, and ϵ is not zero due to the variation of the orbital period by the orbit shift” (Nagata et al., 2016). Focusing on the remaining four eigenvalues of the M-matrix, it is possible to summarize them within few possible cases, and starting with a general complex value as $\lambda = a + ib$, $\forall a, b \in \mathbb{R}$, we are able to arrive at

$$\text{if } b = 0 \ (\lambda \in \mathbb{R}) \quad \Rightarrow \quad \begin{cases} \lambda_I = \pm 1, \lambda_{II} = \pm 1 & , \forall |\lambda| = 1 \\ \lambda_I = a, \lambda_{II} = \frac{1}{a} & , \forall |\lambda| \neq 1 \end{cases} \quad (2-39)$$

$$\text{if } b \neq 0 \ (\lambda \in \mathbb{C}) \quad \Rightarrow \quad \begin{cases} \lambda_I = \lambda, \lambda_{II} = \lambda^* & , \forall |\lambda| = 1 \\ \lambda_I = \lambda, \lambda_{II} = \lambda^*, \lambda_{III} = \frac{1}{\lambda}, \lambda_{IV} = \frac{1}{\lambda^*} & , \forall |\lambda| \neq 1 \end{cases} \quad (2-40)$$

as main combinations possible for the last two pairs of eigenvalues. Each of them can actually increase the *order of instability*¹¹, while an initial small displacement remains bounded to the periodic solution, as long as all eigenvalues are on the unit circle. The meaning of first case given in Eq. (2-40) is quite evident, especially if writing eigenvalues in a polar form, where ρ is the module and ψ the complex phase, such that

$$\lambda = \rho \cdot e^{i\psi} \quad \xrightarrow{\text{considering the N-mapping}} \quad \lambda^N = \rho^N \cdot e^{iN\psi} \quad (2-41)$$

where $\forall \rho = 1$ we have the existence of a quasi-periodic orbit, as part of an invariant tori surrounding the nominal closed trajectory (Gómez, Masdemont, & Simó, 1998). More precisely, with $\psi = 2\pi \frac{k}{N}$ ($\forall k \geq 1$) the new quasi-periodic motion will repeat itself after exactly N-revolutions of the nominal one. Interesting is also to observe that when $\lambda = -1$ we have $\psi = \pi$ and since $N = 2k$ the trajectory will repeat only every $2k$ revolutions, and consequently doubling the original orbital T-period. (Howell & Campbell, 1999)

¹¹ Here with p-order of instability we refer to the existence of p-directions that diverge from the nominal periodic solutions. Due to the symplectic form and its proprieties (as also the time-independence) the max order here is 2, while a 3-order cannot be related to periodic solution, since no eigenvalues would be equal to +1. The latter can be an additional constraint for testing and further validate the numerical computation of periodic solutions. Very important indeed to not forget that the existence of a $\lambda = +1$ is only a propriety related to the periodic motion in autonomous systems, while the symplectic structure holds in general for most of the Hamiltonian systems. (Howard & MacKay, 1987)

For both first cases in Eqs. (2-39)(2-40) there are no effects on the order of instability since $|\lambda| = 1$, so an initial small displacement will not expand and neither shrinks in time. However, the second case in Eq. (2-39) is related to the so-called Manifolds Theory, documented in many textbooks and in the most recent literature related to the CR3BP. Eigen-vectors associated with eigenvalues in module larger (or smaller) than one, indeed define particular directions, called *invariant manifolds*¹², able to collect asymptotic solutions leaving (or reaching) a neighbourhood of the nominal periodic solution. In a similar way, we can note that in the second case of Eq. (2-40) the existence of a combination of both oscillating and growing (or shrinking) effects, nonetheless they are indeed related to a 2-order instability, so involving all four remaining eigenvalues.

COMMENT

It is possible to conclude that for periodic solutions (p.s.) of Hamiltonian time-invariant systems (such as the CR3BP) the innate symplectic structure leads to the existence of at least two real eigenvalues +1 (so leading to continuous families). Furthermore, seven possible behaviours can be found in a neighbourhood of each periodic solution, based on all different combinations of the four remaining eigenvalues, as given in Eqs. (2-39)(2-40).

2.2.5 Bifurcation Theory: types and consequences

Successive step to all the previous discussion is related to the Bifurcation Theory, originally introduced in (Poincaré, 1885) for the study of dynamical systems¹³. This theory can be applied to both continuous and discrete dynamical systems, but in our case we will consider the discrete case when looking at the Poincaré Map for small displacements in a neighbourhood of periodic solutions. Example of bifurcations in continuous system has been given before with the Routh parameter μ_R , value after which the equilateral libration points start to be linearly unstable (Section 2.1.2).

A definition of “bifurcation” is given in (Vladimir, 1972) “to describe any situation in which the qualitative, topological picture of the object we are studying alters with a change of the parameters on which the object depends”. Basically each bifurcation depends upon a “bifurcation parameters”, as the mass-ratio μ in the previous example or the eccentricity when considering the extension to the Elliptic problem. In our case, to analyse bifurcations within a continuous family of closed trajectories, we are going to make use of the distance from the relative L-point, starting point for the generation of the entire family. More details on the numerical computation are given later in Section 4.4.

As shown in the previous section, there are multiple possible combinations (seven in total) for the remaining two pairs of characteristic multipliers $\{\lambda_3, \lambda_4$ and $\lambda_5, \lambda_6\}$, thus now we should be fully capable of locating (within each family) all main bifurcations in the qualitatively behaviour of eigenvalues, as also for changes in the order of instability.

¹² In (Gómez et al., 2002) and (Gómez et al., 2004) it has been shown that “these tubes can be used to construct new spacecraft trajectories, such as a ‘Petit Grand Tour’ of the moons of Jupiter”, and without any doubts they represent one of the most promising research field for future interplanetary low cost transfers. However, here they have not been considered for both the time constraint related to the Master thesis and other aspects, as discussed later.

¹³ First studies on bifurcation were made in (Euler, 1744), but “modern development of the subject starts with Poincaré and the qualitative theory of differential equations” (Crawford, 1991).

For four-dimensional symplectic maps, this linear stability (or “*spectral stability*”) can be lost in three different ways, so leading to three different types of bifurcation points. They can be summarized as in (Howard & MacKay, 1987), so assuming all four eigenvalues initially disposed within the unit circle (as represented below in Figure 9):

i. Tangent (or Fold) bifurcation [T-B]

“Two eigenvalues coalesce at $+1$ and split on the real axis, so increasing the order of instability from zero to one.”

ii. Period-Doubling (or Flip) bifurcation [P-D]

“Two eigenvalues coalesce at -1 and split on the real axis, so increasing the order of instability from zero to one.”

iii. Krein collision [K-C]

“Two complex conjugate pairs of eigenvalues collide and split on the complex plane, so increasing the order of instability from zero to two.”

First type of bifurcation leads to the generation of one stable/unstable manifold, while the second type has been already discussed before, with a new periodic solution having twice the original period. Last, the Krein collision in 4D symplectic maps completely fix the behaviour of the remaining eigenvalues, so generating two stable/unstable manifolds.

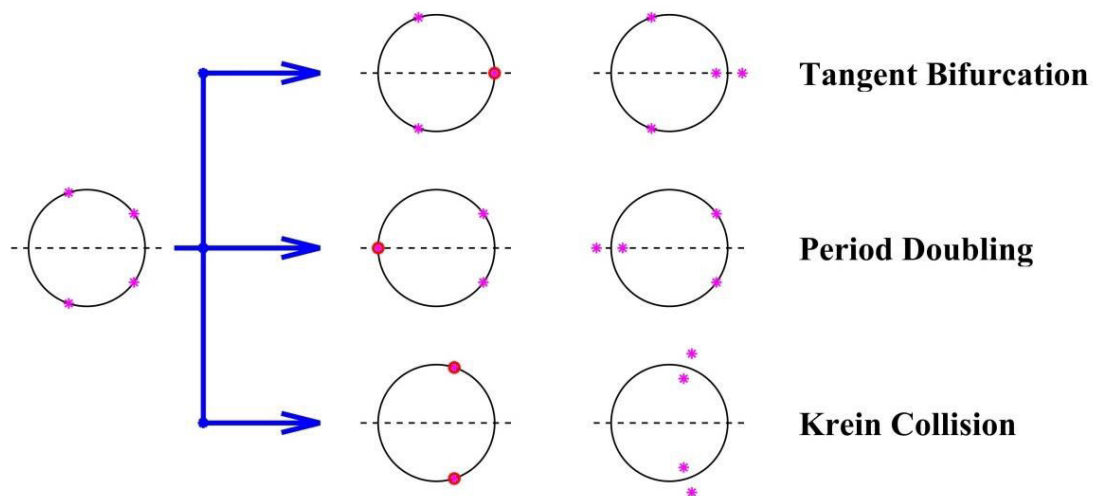


Figure 9: The three possible bifurcations considered here, leading to the destabilization of the 4-dimensional symplectic map and consequently increasing the order of instability.

For the sake of completeness we mention an additional bifurcation that can take place within a family, without influencing the order of instability. (Howell & Campbell, 1999)

iv. Modified secondary Hopf bifurcation

“Two real pairs of eigenvalues collide on the real axis (but not at ± 1) and separate on the complex plane.”

In this last case “iv”, even if the 2-order of instability does not change, the new solution is qualitatively different, due to the existence of an oscillating motion around the solution.

2.3 The Analytic approach

Objective of the previous discussion is only to introduce some principal aspects of the Dynamical System Theory related to the Circular problem. Nonetheless, this theory is much more extensive, and has been successfully applied within several works as ([Gómez, Jorba, Masdemont, & Simó, 1993](#)), ([Howell, Barden, & Lo, 1997](#)), and most recently ([Vaquero & Howell, 2014](#)). These works have been mostly focused on transfer problems using the Invariant Manifolds Theory, as for the Genesis spacecraft mission “to collect solar wind samples from a Halo orbit about the Sun-Earth L1 point” ([Lo et al., 2001](#)). Regardless this fact, here we are principally looking at some families of periodic solutions around the L1/L2 points, without any real remarks about transfer trajectories ([Lo & Ross, 1998](#)), possible connecting orbits ([Gómez et al., 2004](#)) or the so-called ballistic capture problem ([Belbruno & Miller, 1993](#)).

The DST can already be seen as an analytic way to tackle the problem, but now it is necessary to exploit a more specific technique, in particular for accurately studying stability at collinear libration points. Moreover, from the previous linear analysis provided in Eq. (2-27), a solution can be easily found, described also by general literature as ([Hénon, 1974](#)), such that the complete linearized motion of small displacements around each collinear libration points is described by a solution in the following form, as

$$\begin{cases} \tilde{x}(t) = a_x \cdot \cos(\omega_{xy}t) + b_x \cdot \sin(\omega_{xy}t) + c_x \cdot e^{\lambda_{xy}t} + d_x \cdot e^{-\lambda_{xy}t} \\ \tilde{y}(t) = a_y \cdot \cos(\omega_{xy}t) + b_y \cdot \sin(\omega_{xy}t) + c_y \cdot e^{\lambda_{xy}t} + d_y \cdot e^{-\lambda_{xy}t} \\ \tilde{z}(t) = a_z \cdot \cos(\omega_z t) + b_z \cdot \sin(\omega_z t) \end{cases} \quad (2-42)$$

with a, b, c, d integration constants, ω_z and ω_{xy} respectively as vertical and horizontal pulsations, with λ_{xy} as the real eigenvalue directly associated to the unbounded motion. The expression for these last three values can be written respect to the mass-ratio μ as

$$\omega_z = \sqrt{\frac{1 - \mu}{|1 + \gamma_L|^3} + \frac{\mu}{|\gamma_L|^3}} \quad (2-43)$$

$$\xrightarrow{\text{using } \omega_z} \begin{cases} \omega_{xy} = \sqrt{1 - \frac{\omega_z^2}{2} + \frac{\omega_z}{2} \sqrt{9\omega_z^2 - 8}} \\ \lambda_{xy} = \sqrt{\frac{\omega_z^2}{2} - 1 + \frac{\omega_z}{2} \sqrt{9\omega_z^2 - 8}} \end{cases} \quad (2-44)$$

with γ_L positive distance found previously from Eq. (2-9). Particular initial conditions allow removing the unbounded dynamics, thus considering only bounded solutions in what represents only a linear approximation around L-points. Furthermore, for any μ , the in-plane and out-of-plane pulsation are fixed, while in a close neighbourhood to equilibrium point they are different ([Howell, 1984](#)). It follows the possibility of having still bounded trajectories, where $\tilde{x}, \tilde{y}, \tilde{z}$ are non-dimensional distances from L-points, but no more properly periodic, thus leading to three dimensional “quasi-periodic” orbits, better known in literature as *Lissajous orbits*. ([Howell & Pernicka, 1988](#))

Periodicity can be achieved only if the ratio between out-of-plane and in-plane motion is a rational number larger than 1, case not really possible since $\omega_z \neq \omega_{xy}$, $\forall \mu \in (0,0.5)$. A general example is given in Figure 10, showing some possible periodic trajectories (where $t_{END} = 18 \times 2\pi$) compared with Lissajous curves for some irrational ratios. Note that the general pulsation can be referred for example to the orbital 2π -revolution of both M_1, M_2 .

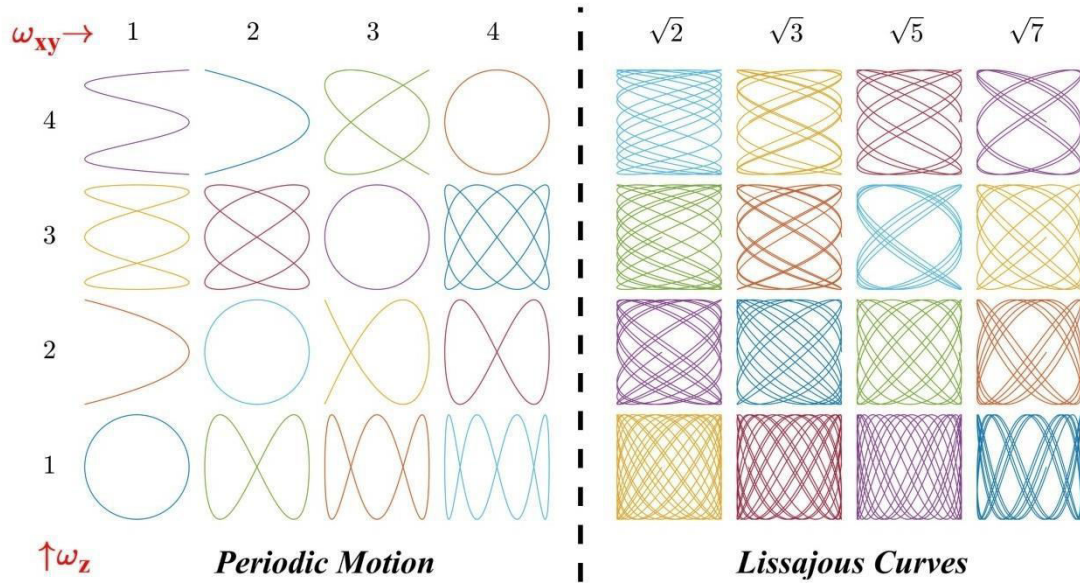


Figure 10: Illustration on the \hat{y}^2 -plane of some possible periodic orbits (LEFT) and Lissajous curves (RIGHT) using a general unitary reference pulsation, with ω_{xy} and ω_z respectively horizontal and vertical pulsations of the dynamics linearized around L-points. See text above.

NOTE ON LISSAJOUS ORBITS

Even if only periodic solutions have been considered here, one main remark has to be made on a possible application of Lissajous orbits around L-points in observation space missions, due to their bounded motion, as explained before. Examples given in (Shirobokov, 2014) are the WMAP mission at the Sun-Earth L2, ACE and DSCOVR at Sun-Earth L1, as also the aforementioned Genesis mission. (Lo et al., 2001)

2.3.1 Existence of two mono-parametric Lyapunov families

Under the assumption of having a linearized motion, so neglecting terms as $\mathcal{O}(\Delta X_{Li}^2)$ in Eq. (2-26), we still are able to define two families of solutions ‘theoretically’ bounded in two distinctive motions (*in-plane* and *out-of-plane*). As we will see, once considering also non-linear terms with perturbation techniques (Section 2.3.2), the situation becomes more complex, but as long as we remain close enough to the libration point, the expression in Eq. (2-42) can well approximate the dynamics. (Gómez & Mondelo, 2001)

Two families of solutions can be considered, also called Lyapunov families and, indeed their continuous character can be clearly observed also from Eq. (2-42), where different initial conditions lead to different possible amplitudes for each possible orbit. An example of few trajectories for the Horizontal (in red) and Vertical (in green) family is shown in Figure 11, where the Earth-Moon Lagrange points have been considered in relation to the Circular Restricted 3-Body Problem.

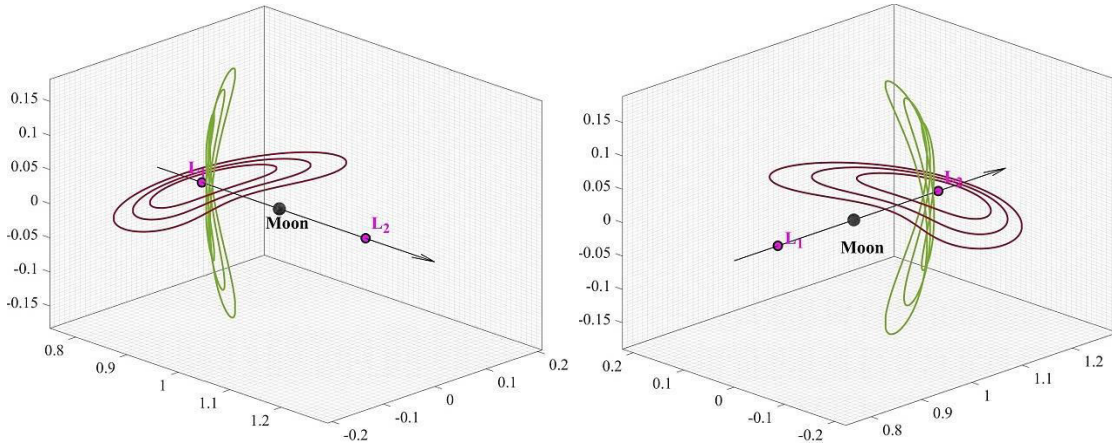


Figure 11: Illustration of Horizontal and Vertical Lyapunov families at L1 (LEFT) and at L2 (RIGHT) in the Earth-Moon CR3BP, where the size of the Moon has been enlarged $\times 2$.

For real space observation missions is necessary to extend the previous analysis, including non-linear terms, thus studying other possible families beside those two found. In a certain way, the latter can be seen as an inspection of the non-linear stability for collinear L-points, where basic techniques previously shown are not really adequate, neither sufficient for such purpose. A semi-analytic method has already been mentioned as the Centre Manifold Reduction given in (Jorba & Masdemont, 1999), also known as “normal form scheme”. Here we are going to consider an alternative, defined as the Lindstedt-Poincaré method (or “method of strained coordinates”), commonly used in order “to find convergent series of periodic solutions” (Verhulst, 2000)

2.3.2 Perturbation technique: the Lindstedt-Poincaré method

The Lindstedt -Poincaré technique (or LP-method) is based on the assumption that in differential systems dependent upon a small parameter ϵ , the solution of the perturbed system is also periodic and its frequency can consequently be expressed simply as a perturbation of the one related to the unperturbed problem (Waters & McInnes, 2007). Second important assumption is associated with the so-called Poincaré Expansion Theorem (or PE-Theorem), here not given but very well described in some specific textbooks, for example in (Kevorkian & Cole, 1996) and (Nayfeh, 2007).

Considering an autonomous case, the PE-Theorem briefly states that if a Taylor expansion exists (in a certain \mathbf{X} -domain) at $\epsilon = 0$ for the vector-function $\mathbf{f} = \mathbf{f}(\mathbf{X}, \epsilon)$, such that it is convergent respect to the small parameter $\epsilon \ll 1$, it follows that

$$\mathbf{f}(\mathbf{X}, \epsilon) \cong \mathbf{f}(\mathbf{X}, 0) + \epsilon \cdot \mathbf{f}_1(\mathbf{X}) + \epsilon^2 \cdot \mathbf{f}_2(\mathbf{X}) + \dots \tag{2-45}$$

and also the solution $\mathbf{X} = \mathbf{X}(t, \epsilon)$ can be expanded in a Taylor series, convergent for any $\epsilon < \epsilon_0$ on a time-scale $\mathcal{O}(1)$, where ϵ_0 is the *radius of convergence* of the series, reliant on the m-order chosen for the truncation. Neglecting terms as $\mathcal{O}(\epsilon^{m+1})$, we arrive at

$$\mathbf{X}^{app}(t) = \mathbf{X}_0(t) + \epsilon \cdot \mathbf{X}_1(t) + \epsilon^2 \cdot \mathbf{X}_2(t) + \dots + \epsilon^m \cdot \mathbf{X}_m(t) \tag{2-46}$$

with an approximation error as $\|\mathbf{X}(t) - \mathbf{X}^{app}(t)\| = \mathcal{O}(\epsilon^{m+1})$, valid on a time-scale $\mathcal{O}(1)$.

More correctly, all previous assumptions refer to general perturbation techniques, while a more general background with many historical details can be found in the mentioned textbooks. Very remarkable here is to note that one of the principal field for the application of Perturbation Theory in the 18th century was exactly the description of the motion of celestial bodies under different perturbations, e.g. the presence of an additional mass ([Verhulst, 2000](#)). Such techniques have been adopted in many other fields, in general to determine solutions of partial and ordinary non-linear differential equations, as also as an approximation for particular integrals ([Nayfeh, 2007](#)) and in algebraic equations, for example to approximate the quintic equation in Eq. (2-9).

Such technique has been successfully applied in ([Masdemont, 2005](#)) “for computing the stable and unstable manifolds of libration point orbits in series expansions” (as also for the mentioned *Hill's Problem*, $\forall \mu \rightarrow 0$), while crucial to remember here that we are looking at bounded periodic solutions, so consequently there could be additional constraints on these approximations. In fact, one limitation of general perturbation techniques is usually related to the presence of *secular terms*, arising at higher orders of the expansion and for which time t appears as an amplitude factor.¹⁴ These terms clearly destroy any periodicity, from the moment that the subsequent approximated solution grows indefinitely with time t . In fact, sometimes they are also called *mixed-secular* as consequence of the fact that they are “product of both linear and trigonometric functions of time” ([Kevorkian & Cole, 1996](#)). In general, substituting the expansion in Eq. (2-46) within the original differential system, all terms at the same ϵ -order are collected and later equations are recursively solved at each level, as discussed in the Literature Study.

2.3.2.1 The introduction of “strained coordinates”

Starting with a general perturbed harmonic oscillator in the non-dimensional variable $x = x(t) \in \mathbb{R}$, $\forall t \in \mathbb{R}$ and a time-independent function $f = f(x, \dot{x}, \epsilon)$, such that

$$\ddot{x} + x = \epsilon \cdot f(x, \dot{x}, \epsilon) \quad (2-47)$$

we are able to substitute a general n-order expansion, as described before, leading to

$$[\ddot{x}_0 + \epsilon \ddot{x}_1 + \dots + \epsilon^n \ddot{x}_n] + [x_0 + \epsilon x_1 + \dots + \epsilon^n x_n] = \epsilon \cdot [f_0 + \epsilon f_1 + \dots + \epsilon^n f_n] \quad (2-48)$$

and, after collecting all terms with a same ϵ -order, we arrive at

$$\begin{cases} \ddot{x}_0 + x_0 = 0 \\ \ddot{x}_1 + x_1 = f_0(x_0, \dot{x}_0) \\ \dots \\ \ddot{x}_n + x_n = f_{n-1}(x_0, \dot{x}_0, x_1, \dot{x}_1, \dots, x_{n-1}, \dot{x}_{n-1}) \end{cases} \quad (2-49)$$

where $f_0(x_0, \dot{x}_0)$ includes solutions as $x_0 = a_0 \cdot \cos(t) + b_0 \cdot \sin(t)$, but also parts of the homogeneous solution $x_1^{\text{om}} = x_1^{\text{om}}(t)$, thus leading to new particular solutions in the form as “ $t \cdot \cos(t)$ ” or “ $t \cdot \sin(t)$ ”. The latter trivially shows the formation of these secular terms, while a similar pattern repeats for all the other orders of the expansion in Eq. (2-49).

¹⁴ More correct way is to consider them as **resonance effects** at a certain order of the expansion, due mostly to solutions found at lower orders of the expansion. ([Verhulst, 2000](#))

At this point the principal idea of the Lindstedt-Poincaré method is to introduce a coordinate transformation on the original time t , in such way that new periodic solutions of the perturbed problem have same T -periodicity, but in a new time-like variable. We have already encountered a similar time transformation, adopting the non-dimensional time-like parameter in Section 2.2.1, such that the motion of the principal masses was 2π -periodic. Now, for our example the situation is slightly different since the transformation is no more a simple rescaling, but dependent upon the small parameter ϵ and this explains the appellative “strained coordinate method”. In fact, we can write

$$\theta = w t \quad \text{with} \quad w = \frac{1}{\sqrt{1 + \epsilon \cdot \eta(\epsilon)}}, \quad \forall \eta(\epsilon) = \sum_{i=1}^n \epsilon^i \cdot \eta_i(\epsilon) \quad (2-50)$$

where w is a new pulsation. With the notation $x' = dx/d\theta$ we use Eq. (2-47) to arrive at ¹⁵

$$x'' + \frac{x}{w^2} = \epsilon \cdot \frac{f(x, x', \epsilon)}{w^2} \quad \Leftrightarrow \quad x'' + x = \epsilon \cdot g(x, x', \epsilon) \quad (2-51)$$

in this way having a system similar to the previous one, but now knowing that periodic solutions are 2π -periodic in θ . Is it exactly this last imposed condition (known as “periodicity condition”) that allows us removing *secular terms* at each order of the expansion of Eq. (2-49). Consequently, it is possible to fix initial conditions at a lower level in such way that we avoid the appearance of resonance terms. Very last step, after iteratively solving the system, is to express the approximated solution $x^{\text{app}} = x^{\text{app}}(\theta)$ considering constraints on initial conditions found, so leading to

$$x(\theta) \approx x^{\text{app}}(\theta) = x_0(\theta) + \epsilon \cdot x_1(\theta) + \dots + \epsilon^n \cdot x_n(\theta) \quad (2-52)$$

and the new T -period of the perturbed solution will be simply given in a ϵ -series as

$$T \approx T_n^{\text{app}}(\epsilon) = T_0 + \sum_{i=1}^n \epsilon^i \cdot T_i(\epsilon) \quad (2-53)$$

where the nominal period is $T_0 = 2\pi$, while $T_n^{\text{app}}(\epsilon)$ is the new approximated perturbed period, converged for any $\epsilon < \epsilon_0$.

2.3.2.2 Third-order analytic approximation by [\(Richardson, 1980a\)](#)

At this point we can briefly introduce the third-order analytic approximation found using the LP-method and given in [\(Richardson, 1980a, 1980b\)](#). Purpose is here not to re-discover what has been already presented in his work, but only to identify critical aspects of that expansion (and the method itself), thus to use such approximated solution as first guess for the numerical method presented in the following Section 2.4. For a very well detailed description of his procedure we strongly suggest [\(Thurman & Worfolk, 1996\)](#).

¹⁵ Note that both forms in Eq. (2-51) are equivalent and related by the following expression

$$g(x, x', \epsilon) = f(x, x', \epsilon) \cdot [1 + \epsilon \cdot \eta(\epsilon)] - x \cdot [\epsilon \cdot \eta(\epsilon)]$$

We start with a system linearized respect to the libration point, as presented in Eq. (2-27), but now considering only collinear libration points (more precisely only L1 and L2, for the reasons earlier discussed). In (Richardson, 1980a) all positions $\{\tilde{x}, \tilde{y}, \tilde{z}\}$ have been adimensionalize by γ_{Li} , distance between M2 and each L_i -point, which represents a simply rescaling that can only influence the numerical value of coefficients in each equations, without really altering the dynamics.¹⁶ It follows a system in $\{x, y, z\}$, such that

$$\begin{cases} \ddot{x} - 2\dot{y} - (1 + 2c_2)x \cong \sum_{j=3}^N c_j \cdot f_{xj}(x, y, z) \\ \ddot{y} + 2\dot{x} + (c_2 - 1)y \cong \sum_{j=3}^N c_j \cdot f_{yj}(x, y, z) \\ \ddot{z} + c_2 z \cong \sum_{j=3}^N c_j \cdot f_{zj}(x, y, z) \end{cases} \quad (2-54)$$

with f_{xj}, f_{yj}, f_{zj} functions of all three position variables, outcomes of the Taylor N-order expansion of the potential Ω and having order [j-1]. The nominal system, after neglecting the right side of Eq. (2-54) is exactly the same one as given in Eq. (2-27), but here evaluated at the Lagrange point, with a vertical pulsation expressed by $c_2 = -\Omega_{,zz} = \omega_z^2$. As discussed before, the mismatch between in-plane and out-of-plane is unavoidable once close enough to the L-point, where the linearization represents a very accurate approximation. However, nothing can be stated for non-linear terms, and as additional assumption we have that $\omega_z^2 = \omega_{xy}^2 - \Delta\omega$, with $\Delta\omega = \mathcal{O}(x^2, y^2, z^2)$ as correction on the Eigen-frequency, neglectable in the first-order approximation, so leading to

$$\begin{cases} x_0 = A_x \cos(\omega_{xy}t + \phi) \\ y_0 = kA_x \sin(\omega_{xy}t + \phi) \\ z_0 = A_z \sin(\omega_{xy}t + \psi) \end{cases} \quad (2-55)$$

that is again directly comparable with Eq. (2-42), but now having a synchronized motion due to the last assumption made. Moreover, unbounded solutions from Eq. (2-42) have been removed (see previous example), while both phases ϕ and ψ are related by the initial conditions of the physical problem. For this first-order approximation, we see a constant term k relating both x_0 and y_0 solutions, where first and second equations in the system of Eq. (2-54) are actually coupled (Szebehely, 1967), such that

$$k = \frac{\omega_{xy}^2 + 1 + 2\omega_z^2}{2\omega_{xy}} \triangleq \frac{2\omega_{xy}}{\omega_{xy}^2 + 1 - \omega_z^2} \quad (2-56)$$

¹⁶ Note that the rescaling introduced in (Richardson, 1980a, 1980b) changes the numerical value of c_j , related to the order [j-1] and consequently having that c_j^R (used by Richardson in his paper) are related to the coefficients used here simply as

$$c_j^R = c_j \cdot \gamma_L^{j-1} \quad \forall c_j = (-1)^j \cdot \left[\frac{\mu}{(\mp \gamma_L)^{j+1}} + \frac{1-\mu}{(1 \mp \gamma_L)^{j+1}} \right]$$

with the negative sign for L1 and the positive one for L2.

The third order solution from (Richardson, 1980a) is given in Table 2 and with the same notation, so we refer to his paper for the calculation of all coefficients $\{a, b, d\}$. Moreover, interesting is the correction on the T-period by the perturbed pulsation w_{pert} , such that

$$T_{pert} = \frac{2\pi}{w_{pert}} = \frac{2\pi}{\omega_{xy} \cdot (1 + s_1 A_x^2 + s_2 A_z^2)} \quad (2-57)$$

where, the previous Taylor expansion is based on small displacement-amplitudes, here named as A_x and A_z . Both two are related simply to the two Lyapunov families shown in Figure 11, while main objective is here to look also at non-linear terms of this expansion. The latter allows identifying possible 3D motions, where both in-plane and out-of-plane equations are synchronized, so leading to two additional constraints on the motion as

Amplitude Constraint: $l_1 A_x^2 + l_2 A_z^2 + \Delta\omega = 0$ (2-58)

Phase Angle Constraint: $\psi = \phi \pm \frac{\pi}{2}$

Both previous arise only at the third-order and are related to terms $\mathcal{O}(A_x^2, A_z^2)$, as also for w_{pert} , correction of the unperturbed pulsation ω_{xy} , since no terms $\mathcal{O}(A_x, A_z)$ have been found. An incredible result is the appearance of what can be considered an “analytic bifurcations” within the Horizontal Lyapunov family, due to the **Amplitude Constraint**, since $l_1 < 0$, $l_2 > 0$ for each μ -value (numerically checked) in a valid range $\forall \mu \in (0, 0.5)$. Consequently it follows the existence of a boundary real value A_x^{MIN} for the 3D motion as

$$A_x \geq A_x^{MIN} = \sqrt{\Delta\omega / -l_1} \quad (2-59)$$

different at each μ -value, while $A_z \geq A_z^{MIN} = 0$ for what has been declared before.

Table 2: The third order analytic approximation of periodic solutions near L1/L2. Here $\{x, y, z\}$ are displacement-positions from both L-points, while w_{pert} and ω_{xy} respectively the perturbed and unperturbed pulsation of the approximated solution. See (Richardson, 1980a).

| | I° order | II° order | III° order |
|--------------------------------|----------------------|--|---|
| x | $-A_x \cos(\tau_1)$ | $A_x^2 [a_{21} + a_{23} \cos(2\tau_1)] \dots$ $+ A_z^2 [a_{22} - a_{24} \cos(2\tau_1)]$ | $A_x [a_{31} A_x^2 - a_{32} A_z^2] \cos(3\tau_1)$ |
| y | $k A_x \sin(\tau_1)$ | $[b_{21} A_x^2 - b_{22} A_z^2] \sin(2\tau_1)$ | $A_x [b_{31} A_x^2 - b_{32} A_z^2] \sin(3\tau_1)$ |
| z | $A_z \cos(\tau_1)$ | $d_{21} A_x A_z [\cos(2\tau_1) - 3]$ | $A_z [d_{32} A_x^2 - d_{31} A_z^2] \cos(3\tau_1)$ |
| $\frac{w_{pert}}{\omega_{xy}}$ | 1 | 0 | $s_1 A_x^2 + s_2 A_z^2$ |

LEGEND: A_x, A_z are amplitude-terms and ϕ phase-term, all constant outcomes of the recursive integrations, where the time-argument is given as $\tau_1 = \tau + \phi = w_{pert} \cdot t + \phi$.¹⁷

¹⁷ Time transformation used in (Richardson, 1980a) is $\tau = w_{pert} \cdot t$, with its relative expansion respect to the small parameter, as shown in the previous example. Look to Eq. (2-50) at page 34.

2.3.2.3 A third family of periodic solutions: the Halo family

The new family of 3D orbits found is well-known in literature and usually called “Halo”, name originally provided in the PhD thesis (Farquhar, 1968) and successfully considered for several missions described in Section 1.2. As it will be discussed later, for their numerical computation “*halo orbits are difficult to obtain because the problem is highly non-linear and small changes in the initial conditions break the periodicity of the orbits*”. (Bernelli, Toppo, & Massari, 2004)

Differently from Horizontal and Vertical Lyapunov orbits (once setting respectively $A_z = 0$ and $A_x = 0$), the Halo family is totally dependent upon only one single amplitude parameter from the moment that the “**Amplitude Constraint**” relates both in-plane and out-of-plane amplitudes, so $A_z^{HALO} = A_z^{HALO}(\mu, A_x^{HALO})$. Overview of all three families of periodic trajectories investigated in this report at L1/L2 is given in next Figure 12.

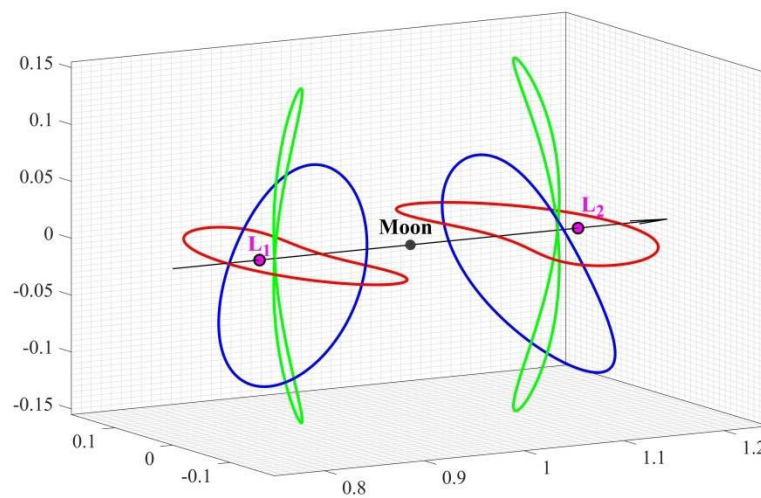


Figure 12: Illustration of investigated families at L1/L2 in the Earth-Moon system: Horizontal Lyapunov (red), Vertical Lyapunov (green) and Halo (blue) are shown at same energy-level.

The analytic approach, as described in the Literature Study, was originally supposed to be the main tool for our analysis, nonetheless due to its complexity and low efficiency, the investigation turn out to be mostly numerical (the “Numerical Approach” in Section 2.4), but still strongly supported by all the aforementioned mathematical theories. The limited accuracy of such types of approximations for a full analysis of all three families does not allow having robust results and indeed the LP-method ‘fails’ far away from libration points (Howell, 1984), while higher orders in the expansion involves very ‘tedious’ expressions (Jorba & Masdemont, 1999). Moreover, “*since the (out of plane) halo orbits have a minimum amplitude, it is not clear whether the approximation is valid*” (Thurman & Worfolk, 1996), thus results from (Richardson, 1980a) have been used here only as first guess for an initial numerical generation of all periodic solutions.

Furthermore, the LP-method is strictly driven to find specific periodic solutions, while the CR3BP the system is known to be Hamiltonian and the existence of a continuous family leads to additional complications. In fact, as discussed, isolated periodic solutions do not actually exist and consequently the “*Unicity conditions*” of the method is not satisfy, while integration terms can be fixed only taking higher orders of expansion (without additional benefits on the accuracy). More information can be found within Section 10.4 from (Verhulst, 2000), while here we continue with the numerical approach.

2.4 The Numeric approach

The numerical approach, here presented, is based on an algorithm written in a MATLAB software environment. Further description and main settings adopted can be found in Appendix-B, very important for having a reliable analysis and in particular to assure reproducibility of all results obtained. Here we focus on methodologies, underlining main limitations and advantages, in a similar way to what has been done before for the analytic approach. Nonetheless, similar application of such technique can be found in other recent Master theses at Delft University of Technology, as ([Van der Ham, 2012](#)), ([Vermeiden, 2014](#)) and ([Rohner, 2014](#)). For a more complete and accurate discussion on numerical techniques we remind to ([Szebehely, 1967](#)), but more suitable for our problem is ([Howell, 1984](#)), where the ‘standard method’ has been taken from. Modifications added to this ‘standard method’ will be justified step by step, based on what we have seen so far, while for Lissajous solutions (not treated here) the discussion over numerical multi-shooting methods in ([Howell & Pernicka, 1988](#)) could be a good starting point.

2.4.1 Differential Correction algorithm

The main technique described here has been originally adopted¹⁸ in ([Howell, 1984](#)) for “a largely numerical study of families of three dimensional, periodic, ‘halo’ orbits near collinear libration points”. The method is basically a single shooting method, applied in many other boundary-value problems and based on the Dynamical System Theory.

As seen in Section 2.2.2, the State Transition Matrix $\Phi(t_1, t_0)$ is able to relate the initial and final displacement (at t_0 and t_1) relatively to a reference solution. In this way it is possible to correct the *initial conditions* (or *shooting conditions*), so looking at the trajectory that better satisfies some boundary conditions at $t = t_f$, as given in Figure 13. We remind once again that STM comes from a linearized dynamics in Eq. (2-30) and its suitability is related to the error-term $\mathcal{O}(|\delta X_0|^2)$, which needs to be small enough in order to have convergence of the DC-algorithm, consequently the necessity of having a first “sufficiently close” guess.

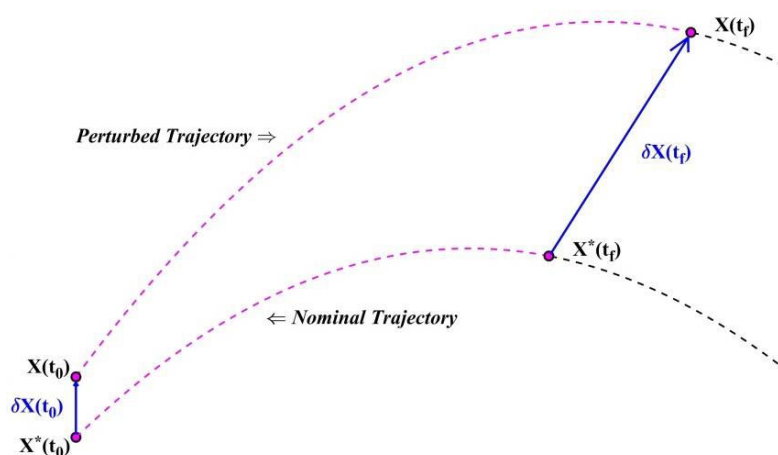


Figure 13: Example of perturbed trajectory $X(t)$ deviating respect to the nominal one defined by $X^*(t)$, where $\delta X(t_0)$ and $\delta X(t_f)$ are respectively the initial and the final displacement.

¹⁸ More correctly first application of numerical methods for periodic solution at L1/L2 is given in ([Breakwell, 1979](#)), but considering only the Earth-Moon mass ratio. As reported in ([Howell, 1984](#)), in their work very significant is the range of stable (linear stability or what we call zero-instability) “roughly halfway between the libration point and the Moon”.

In order to define constraints on the periodicity it is necessary to re-consider for a moment both symmetries previously found, thus applying them to periodic solutions. First type, described in Eq. (2-14), does not involve any time-transformation and it is correlated only to the existence of two Halo families: a *Southern* and a *Northern* family, symmetric in the z -coordinate. Meanwhile, for both Lyapunov families there is not such distinction, in fact Horizontal Lyapunov orbits are totally bounded within the $\hat{x}\hat{y}$ -plane (without any z -components). Regarding Vertical Lyapunov orbits, actually they follow the third symmetry in Eq. (2-16), crossing the x -axis twice at the same point during a complete orbital revolution (so also named *doubly-symmetric*). (X. Y. Hou & Liu, 2009)

In general, for all 3-dimensional periodic solutions in the CR3BP (so in particular for the Halo family), it holds a second symmetry as given in Eq. (2-15), inborn propriety of the equations of motion. Nonetheless, for closed trajectories crossing the $\hat{x}\hat{z}$ -plane (here plane of symmetry) it is also possible to define additional constraints starting within such plane ($\forall y_0 = 0$). In fact, Eq. (2-15) assures that a symmetric reverse orbit exists, and from the transformation $\{y, t\} \rightarrow \{-y, -t\}$ it follows that new initial conditions are also given as $\{x_0, 0, z_0, \dot{x}_0, \dot{y}_0, \dot{z}_0\} \rightarrow \{x_0, 0, z_0, -\dot{x}_0, \dot{y}_0, -\dot{z}_0\}$. Once setting¹⁹ $t_0 = 0$, the state-vector $X(t)$ at $t = T$ and $t = -T$ needs to be the same as $X(0)$, due to the definition of T -periodicity. As consequence of this previous symmetry (Miele, 2010), we obtain two conditions as

$$\dot{x}_0 = \dot{x}(t_0) = 0, \quad \dot{z}_0 = \dot{z}(t_0) = 0 \quad (2-60)$$

and it is also possible to shown that starting at any $t_0 \neq 0$ within the plane of symmetry, both conditions in Eq. (2-60) do not change for this non-autonomous system. At this point, the DC-algorithm can be formulated in mathematical terms, where now we also consider an uncertainty on the T -period, differently from Eq. (2-29). More conveniently, we can numerically integrate till half of the orbital T -period, as shown in Figure 14, thus evaluating conditions at different crosses within the $\hat{x}\hat{z}$ -plane.

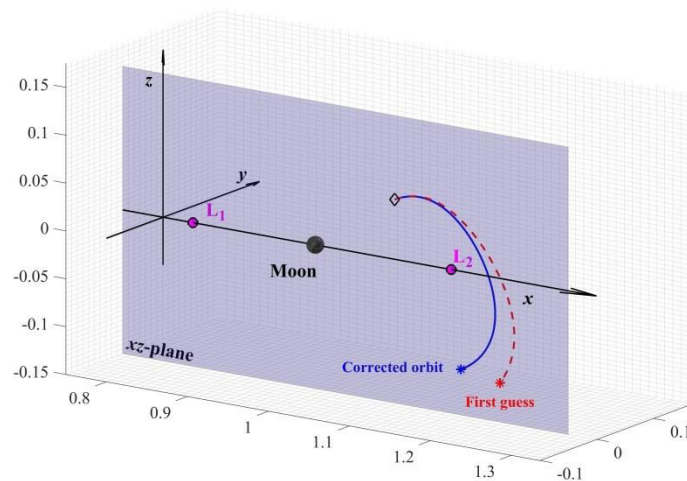


Figure 14: Example of initial guess (red) and final path (blue) corrected by the DC-algorithm, having the “orthogonality conditions” at the shooting (◊) and at the first cross (blue star).

¹⁹ Note that for autonomous systems, the time t does not appear directly in the equations of motion, but only through the “derivative operator”. As consequence it is always possible to define a general time-transformation as $\tau = t + c$, with c constant and having that $\tau_0 = 0$. The latter represents simply a time-shift that does not alter at all the dynamical motion. (Verhulst, 2000)

It follows an expression (neglecting higher order terms) for the final displacement as

$$\delta\mathbf{X}(t_1) \cong \Phi(t_1, t_0) \cdot \delta\mathbf{X}(t_0) + \frac{\partial\mathbf{X}}{\partial t}|_{t_1} \cdot \delta t_1 \quad (2-61)$$

where $\delta\mathbf{X}(t_0)$ and δt_1 needs to be uniquely determined. Nevertheless, constraints within the $\hat{x}\hat{z}$ -plane holds for each cross and consequently at $t_1 = t_0 + T/2$ we have that

$$\begin{pmatrix} \delta x \\ \delta y \\ \delta z \\ \delta v_x \\ \delta v_y \\ \delta v_z \end{pmatrix}_{t_1} = \begin{bmatrix} \Phi_{11} & \Phi_{12} & \Phi_{13} & \Phi_{14} & \Phi_{15} & \Phi_{16} \\ \Phi_{21} & \Phi_{22} & \Phi_{23} & \Phi_{24} & \Phi_{25} & \Phi_{26} \\ \Phi_{31} & \Phi_{32} & \Phi_{33} & \Phi_{34} & \Phi_{35} & \Phi_{36} \\ \Phi_{41} & \Phi_{42} & \Phi_{43} & \Phi_{44} & \Phi_{45} & \Phi_{46} \\ \Phi_{51} & \Phi_{52} & \Phi_{53} & \Phi_{54} & \Phi_{55} & \Phi_{56} \\ \Phi_{61} & \Phi_{62} & \Phi_{63} & \Phi_{64} & \Phi_{65} & \Phi_{66} \end{bmatrix} \cdot \begin{pmatrix} \delta x \\ \delta y \\ \delta z \\ \delta v_x \\ \delta v_y \\ \delta v_z \end{pmatrix}_{t_0} + \delta t_1 \cdot \begin{pmatrix} \dot{x} \\ \dot{y} \\ \dot{z} \\ \dot{v}_x \\ \dot{v}_y \\ \dot{v}_z \end{pmatrix}_{t_1} \quad (2-62)$$

with values of $\partial\mathbf{X}/\partial t$ evaluated at t_1 based on Eq. (2-24), while $\delta\mathbf{X}(t_0)$ has been evaluated on the $\hat{x}\hat{z}$ -plane following symmetry conditions. This linear system can be solved as shown in the Literature Study, also well described in (Howell, 1984), while after removing unused terms (in grey colour) we arrive at a more compact form, such that

$$\begin{pmatrix} \delta y_1 \\ \delta v_{x1} \\ \delta v_{z1} \end{pmatrix}_{T_0/2} = \begin{bmatrix} \Phi_{21} & \Phi_{23} & \Phi_{25} & \dot{y} \\ \Phi_{41} & \Phi_{43} & \Phi_{45} & \dot{v}_x \\ \Phi_{61} & \Phi_{63} & \Phi_{65} & \dot{v}_z \end{bmatrix}_{T_0/2} \cdot \begin{pmatrix} \delta x_0 \\ \delta z_0 \\ \delta v_{y0} \\ \delta[T_0/2] \end{pmatrix} \quad (2-63)$$

for $\delta[T_0/2]$ correction on the expected orbital period T_0 and $\{\delta x_0, \delta z_0, \delta v_{y0}\}$ corrections on all three shooting conditions, while $\{\delta x_1, \delta z_1, \delta v_{y1}\}$ are values found numerically after integrating the system from t_0 till $t_1 = t_0 + T_0/2$, thus leading to

$$\mathbf{X}_1^{vf} + \delta\mathbf{X}_1^{corr} = \begin{pmatrix} y_1 \\ v_{x1} \\ v_{z1} \end{pmatrix}_{\text{values found}} + \begin{pmatrix} \delta y_1 \\ \delta v_{x1} \\ \delta v_{z1} \end{pmatrix}_{\text{correction}} = \begin{pmatrix} 0 \\ 0 \\ 0 \end{pmatrix} \quad (2-64)$$

This previous relation is called ‘‘correction step’’ of the DC-algorithm, aiming to minimize the final displacement at t_1 . Again, settings and threshold values for the numerical computation can be found in both Appendices-A/B, while here we principally focus on methodologies. Note that the linear system in Eq. (2-63) is defined by a $[3 \times 4]$ matrix, so underdetermined since having four variables but with only three conditions.²⁰ One way to overcome this problem is to find a solution in a ‘‘Least Square sense’’²¹, minimizing a cost function, which in our case it is supposed to be the final displacement norm $\|\mathbf{X}_1^{vf}\|$.

²⁰ Also when considering the Horizontal Lyapunov family (totally bounded in the $\hat{x}\hat{y}$ -plane), we have that $\delta z_0, \delta v_{z1} = 0$ and the new system is given by $[2 \times 3]$ matrix, so still undetermined.

²¹ The Least Squared method has been applied by C.F. Gauss (1777-1855) in 1809 for calculating the motion of celestial bodies (Gauss, Davis, & Gauss, 1963), but this fact caused a severe dispute with A.M. Legendre (1752-1833), who published the method in (Legendre, 1806) few years before.

Unfortunately, using a Least Square method, the solution found is unique and most likely it is the one that better minimize the cost function. As seen before, periodic solutions in the CR3BP arise in a continuous family, thus with the Least Square method we cannot really ‘control’ the generation of each member of the family, as explained later for the Numerical Continuation technique (Section 2.4.3). Furthermore, other possible closed trajectories can exist in a neighbourhood within the Phase-space, as also periodic solutions orbiting around both M_1 or M_2 , as mentioned in Appendix-C.

Strategy here adopted is to fix one of the four unknowns, usually x_0 or z_0 for what concerns the generation of each family, while we can fix the orbital period T_0 only when looking to particular resonance solutions, necessary step for the extension to the ER3BP, (see Section 4.4.1). Before presenting the Numerical Continuation technique, we need to briefly discuss how assessing periodicity, so numerically validating each periodic orbit.

2.4.2 Periodicity constraints and numerical validation

We have seen that the algorithm works iteratively, starting with an initial guess (e.g., using the analytical approximation), fixing one of the two position coordinates $\{x_0, z_0\}$ and then correcting all remaining shooting conditions, based on outputs of the numerical integration from t_0 till t_1 . The latter uses both the state-vector $X(t)$ and the State Transition Matrix $\Phi(t, t_0)$, which requires to be evaluated at each time-step. It follows a new ‘total’ state-vector of $36+6=42$ components and a new differential system, combination of Eq. (2-24) and Eq. (2-31), that is once again non-linear since we are numerically integrating the full dynamical motion.

These corrected shooting conditions are re-processed in a similar way till reaching the convergence of the iterative algorithm. Clearly, this convergence is achieved only when both following criteria have been simultaneously satisfied at $t_1 = T/2$ ($\forall t_0 = 0$):

- i. The scalar value of the velocity within the $\hat{x}\hat{z}$ -plane “ v_{xz} ” is smaller than a certain tolerance ΔV_{xz} , such that

$$v_{xz}(T/2) = \sqrt{v_x^2(T/2) + v_z^2(T/2)} \leq \Delta V_{xz} \quad (2-65)$$

- ii. The absolute value of the position “ y ” is smaller than a certain tolerance ΔY , as

$$\|y(T/2)\| \leq \Delta Y \quad (2-66)$$

where it is possible to consider the first condition also as an estimation of DV-budget necessary for manoeuvres or for trajectory adjustments. Nonetheless, as we will see later, both thresholds have been chosen to be very small, thus allowing us to have a very robust analysis on eigenvalues for the linear stability assessment (consequently also for bifurcations). Obviously, a perfect zero displacement is unlikely, where there are numerical limitations due to a limited precision of the floating-point format (*double-precision*), as also related to the accuracy of the integration scheme here adopted. All these aspects have been carefully detailed in Appendix-B, where main settings are justifying by a rigorous trade among the minimum accuracy, the computation time (e.g., maximum number of iterations for convergence) and most important on a necessary reliability for all the simulations performed.

Results and family plots will be given later, while now an example is given in Figure 15, where a “periodicity-validation” is shown for the Halo family generated at L2 in the Earth-Moon system. On the right, we can see all three displacements at $T/2$ with a threshold of 10^{-12} (used in the iterative algorithm), as described before. On the left, we see also an additional condition, later described, for the periodicity when $t = T$, while also the number of necessary iteration for each member of the family is shown. Note that the maximum number has been fixed here to 25, for practical computational reasons.

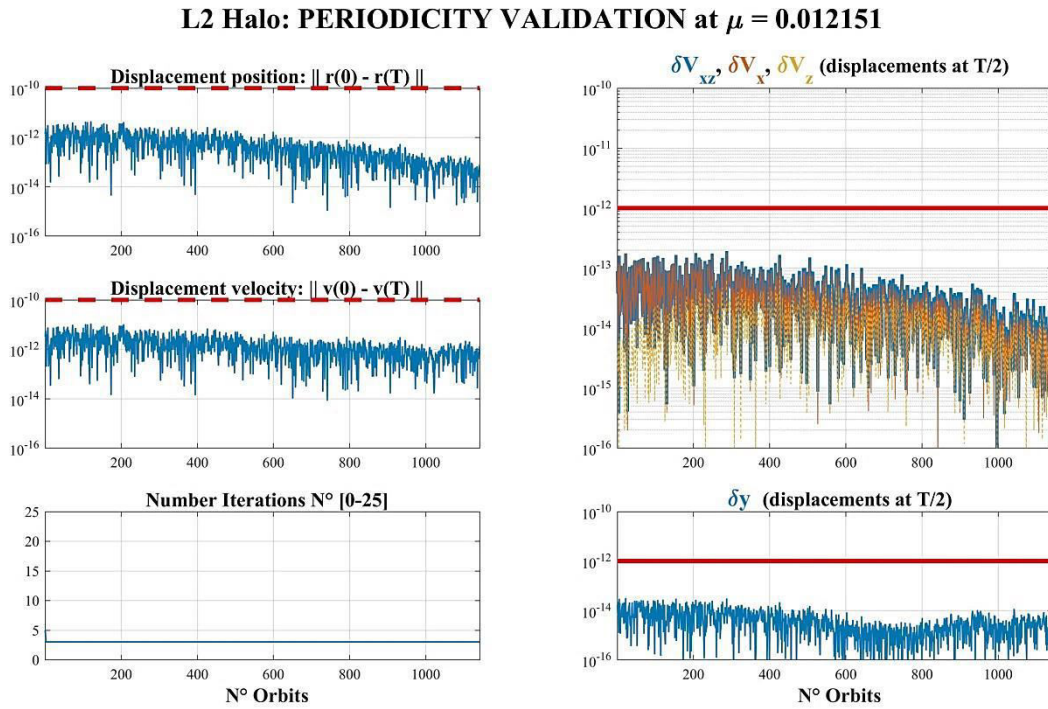


Figure 15: Example of “periodicity-validation” for the Halo family at L2 in the Earth-Moon system ($\mu = 0.012151$). The complete description will be given in Chapter 3, with also results.

Even if not really used as “exit-points” in the algorithm (Figure 15, left), two additional conditions are now introduced in order to further verify the periodicity, also defined as

I – CLOSING CONDITION:

First condition is related simply to the definition of periodicity, thus evaluating the error after one complete revolution at $t = T$ (again assuming $t_0 = 0$). The latter can be given separately for both position $\mathbf{P} = \mathbf{P}(t)$ and velocity $\mathbf{V} = \mathbf{V}(t)$ displacement-vectors as

$$\|\mathbf{P}(T) - \mathbf{P}_0\| \leq \Delta P_T \quad \& \quad \|\mathbf{V}(T) - \mathbf{V}_0\| \leq \Delta V_T \quad (2-67)$$

where $\Delta P_T, \Delta V_T$ are scalar threshold values (see again Appendix-A).

II – EIGENVALUES CONDITIONS:

Second condition is related with all the previous discussion on Hamiltonian systems and the symplectic form, such that the Monodromy matrix for periodic solutions always involves at least two real eigenvalues as $\lambda_1 = \lambda_2 = +1$. See Section 2.2.4 for more details.

Without any doubts, periodicity conditions could also be verified on a longer time-span, for example looking at $t_1 = 2T, 3T, \text{etc} \dots$, as it will be shown later for resonance orbits. One important remark is related to a really unstable dynamics, here under investigation, due to the presence of unstable manifolds that complicate much more the entire analysis. This is not only a consequence of the numerical integration, which we will prove to be extremely accurate, but mostly to the very unstable behaviour in a neighbourhood of periodic solutions, where trajectories are actually “trapped” within these manifolds. More details can be found in the Appendix-B, while here we continue presenting the “Numerical Continuation” technique adopted for the generation of each family.

2.4.3 Numerical continuation

As stated before, the algorithm starts with a first analytical guess very close the libration points (where the approximation is supposed to be more accurate), thus the DC-method leads to a precise numerical periodic solution, fixing for example x_0 and so correcting all remaining shooting variables. These guesses come from the III-order analytic expression in (Richardson, 1980a), e.g. setting arbitrary²² small amplitudes A_{x_0} and A_{z_0} to $\sim 10^{-3}$.

At this point the successive orbit can be generated starting from $\mathbf{X}^{\{I\}}$, the corrected initial condition, and after slightly changing the previously fixed parameter we arrive at

$$\mathbf{X}_0^{\{I\}} \xrightarrow{\text{Numerical Continuation}} \mathbf{X}_0^{\{II\}} \quad \text{with} \quad x_0^{\{II\}} = x_0^{\{I\}} + \Delta x_0 \quad (2-68)$$

with Δx_0 as step-size within the family. The choice of z_0 as main variable to generate the family along a vertical direction (so correcting the horizontal shooting position x_0) is also possible, except for the Horizontal Lyapunov family for obvious reasons. Nonetheless, the correction works on the linearized dynamics, therefore a too large step-size will cause the algorithm to diverge, especially if the next member within the same family has substantial different shooting conditions. For CR3BP with small μ -values we have also L1/L2 very close to the mass M_2 and this is why it is here recommended to express Δx_0 as fraction of $\gamma_{L_i} = \gamma_{L_i}(\mu)$, again the distance between M_2 and each collinear L-point.

During this generation process the algorithm stops if it reaches the maximum number of iterations without satisfying all mentioned criteria or when the “Eigenvalues condition” has been violated. The latter is indeed a fundamental propriety of periodic solutions in the CR3BP, while the “Closing condition” has not been used as exit-point for the algorithm but only as a benchmark, but still visible in the analysis output (see Figure 15).

2.4.3.1 Numerical continuation by “Pseudo-Arclength”

This previous Numerical continuation by “*natural parameter*” unfortunately reveals some issues near bifurcation-points, especially due to the existence of other families, for example requiring a too high number of iterations in order to converge (Bosanac, 2012). In fact, a unique solution is assured for each six-dimensional initial condition in the Phase-space due to the “**Existence and Uniqueness Theorem**”, while the algorithm could literally “jumps” to a different family located near these bifurcation points.

²² It is important to take in consideration the **Amplitude Constraint** for the Halo family as given in Eq. (2-58) and Eq. (2-59). Note that, as explained in Sub-Section 2.3.2.2, both amplitudes A_x, A_z are scaled by Richardson respect γ_L , so their values in the example are actually equal to $\{10^{-3} \cdot \gamma_L\}$.

A more advanced type of Numerical continuation (usually defined “Pseudo-Arclength”) is based on the knowledge of two solutions X_0^{I}, X_0^{II} , where a third one can be expressed as

$$X_0^{III} = X_0^{II} + \Delta X_0^{III} \quad \text{with} \quad \Delta X_0^{III} = (X_0^{II} - X_0^{I}) \quad (2-69)$$

Consequently, we are in a certain way guessing the successive initial state-vector using a “linear extrapolation”, supported by the fact that each family of N-orbits is continuous and I.Cs. within the Phase-space are represented by a continuous set $X_0^{i}, \forall i = 1..N$. Making use of such “linear trend” in Eq. (2-69), we are basically approximating the real set X_0^{i} for each member of the family. Given both shooting positions on the $\hat{x}\hat{z}$ -plane in Figure 16, we are able to qualitatively observe the different outcome of both techniques, thus using Δx_0 as family step-size, meanwhile x_0^I, x_0^{II} are actually components of the shooting solutions for the family generated (in dark yellow).

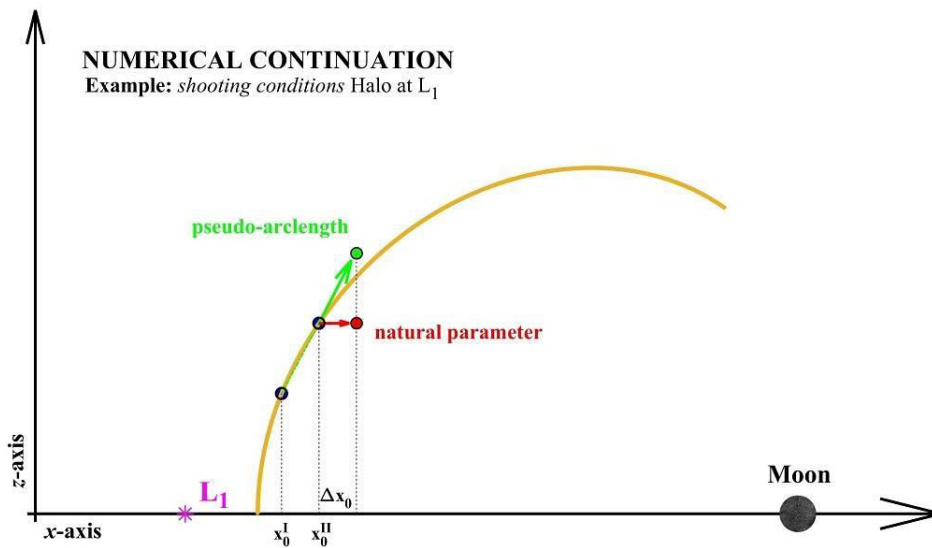


Figure 16: Example is given of Numerical continuation by “natural parameter” (RED) and “pseudo-arclength” (GREEN), where we consider the $\hat{x}\hat{z}$ -plane of the Earth-Moon system. In blue both initial solutions, while in dark yellow the set of corrected shooting positions $\{x_0, z_0\}_i$.

It is clear that, in general, ΔX_0^{i} comes from the knowledge of two previous shooting conditions X_0^{i-1}, X_0^{i-2} . Adopting this new continuation method, we are capable of better predicting the successive guess for the DC-method, while first two steps will be given again from the third-order analytic approximation. In Figure 15, it can be seen that the algorithm needs usually 4-5 iterations to converge, leading to a very fast computation.²³ The Pseudo-Arclength continuation can be also based on more than two known solutions, for example adopting a spline extrapolation able to provide a much more accurate guess (Doedel et al., 2007). Of course, for a general polynomial extrapolation “Polyn”, m -solutions need to be known, thus having $X_0^{m+1} = \text{Polyn}(X_0^{1}, X_0^{2}, \dots, X_0^{m})$.

²³ From this discussion, it seems plausible to conclude that smaller step-sizes lead to a more accurate guess, where the linear extrapolation is more efficient and the DC-algorithm requires less iteration. On the other hand, trade has to be made, due to the fact that with smaller step-size the generation of the entire family will requires more orbits and a larger overall computational time.

2.4.4 Summary of the numerical algorithm

The main steps of the numerical algorithm are here summarized, while in the next Chapter 3 results will be presented and discussed, while for the accuracy and thresholds adopted in the computation we refer again to Appendix-B.

ALGORITHM: Periodic L-Orbit Generator

1. Select a μ -value and a family of orbits (H-Lyapunov, V-Lyapunov or Halo).
2. Compute the location and energy level of the selected libration point (L1 or L2).
3. Calculate coefficients for the third-order analytic approximation as presented in ([Richardson, 1980a](#)). See Section 2.3.2.2.
4. Select two small amplitudes A_I, A_{II} to obtain two different initial conditions, as also two guesses for the integration period, such that

$$\mathbf{X}_0^{\{1,2\}} = \left[x_0^{\{1,2\}}, 0, z_0^{\{1,2\}}, 0, v_{y0}^{\{1,2\}}, 0 \right]^T \quad \& \quad T_0^{\{1,2\}} \quad (2-70)$$

5. Correct previous guesses with the DC-method (Section 2.4.1), thus use $\mathbf{X}_0^{\{1c\}}$ and $\mathbf{X}_0^{\{2c\}}$ in order to find a third one $\mathbf{X}_0^{\{3\}}$, as described in Eq. (2-69). Perform the same for finding the new guessed period $T_0^{\{3\}}$, based again on $T_0^{\{1c\}}$ and $T_0^{\{2c\}}$.

Start Iterative cycle:

6. Correct with DC-method the shooting guess $\mathbf{X}_0^{\{i\}}$ integrated till $T_0^{\{i\}}$, so leading to new corrected values as $\mathbf{X}_0^{\{ic\}}$ and $T_0^{\{ic\}}$.
7. Check the exit-criteria given by Eq. (2-65) and Eq. (2-66):
 - a. If not satisfied (so the maximum number of iterations has been reached), the iterative cycle stops.
 - b. If both satisfied, proceed with the next point.
8. Integrate the STM and the state-vector for one complete revolution till $T_0^{\{ic\}}$, starting with the corrected shooting condition $\mathbf{X}_0^{\{ic\}}$.
9. Study eigenvalues λ_j of the Monodromy matrix (STM over a T-period) in order to assess the linear stability. Also check the “*Eigenvalue condition*” (Section 2.4.2):
 - a. If there are no real eigenvalue $\lambda = +1$ (so orbit found is not periodic), the iterative cycle stops.
 - b. If there are at least two real $\lambda = +1$, proceed with the next point.
10. Save parameters and analysis relative to this i-member of the family.
11. Set new shooting conditions $\mathbf{X}_0^{\{i+1\}}$ and $T_0^{\{i+1\}}$, as described in Eq. (2-69).
12. Iterate again from point 6.

End Iterative Cycle.

➔ **Plot Family results.**

➔ **Save Family parameters.**

END ALGORITHM

3

CR3BP: Results

In this Chapter 3 we present main results for the investigation of the Circular Restricted 3-Body Problem (CR3BP), previously analysed in Chapter 2. Most of the theory has been already described as also principal methodologies discussed, while here we proceed with more practical aspects. Once again, we refer to the Earth-Moon Circular problem as “Test-Case” (see Section 2.1.3), considering both L1 and L2 libration points and three families of periodic solutions: both Horizontal/Vertical Lyapunov families and the Halo one. For the latter, we present only the “Southern family”, since for symmetry results holds also in the “Northern family”, as explained in Section 2.4.

In Sections 3.1, 3.2 and 3.3 we focus on the L1-point, while in Sections 3.4, 3.5 and 3.6 we treat orbits at the L2-point, so again investigating all three aforementioned families, generated using the algorithm of Section 2.4.4. For each one of these six analyses we present a graphical plot of the family (every 50 orbits), thus its main properties, order of instability and consequently bifurcations. It follows a Verification and Validation part as outlined in Section 2.4.2, thus the existence of some “resonance orbits” is given, fundamental step for the extension to the Elliptic problem. Last, in Section 3.7, conclusions on all these six sections allow having a complete summary of all three families at L1/L2 (Earth-Moon CR3BP). Note that for each one, the Phase-space of initial conditions has been reduced to three dimensions defined by three shooting variables as $\{x_0, z_0, v_{y0}\}$, while in Appendix-C we provide a more general overview, as also for an additional family here not considered. Now, before proceed with the graphic results, we briefly mention few additional settings involved in the research process.

ADDITIONAL SETTINGS

The computation starts at each L-point with the two solutions given by an analytic approximation (Section 2.3.2.2), thus applying differential correction and continuation on each member of the family. In addition to the “exit-conditions”, the algorithm stops also if the shooting x_0 -position (current orbit) cross the M_2 (so x_2), since we consider only a range in the \hat{x} -direction spanning from the L-point to the Secondary mass. For the V-Lyapunov family, mostly extended along the z -direction, the algorithm stops once the “Initial Conditions” (I.C.) trend starts to reverse its direction, so going from M_2 to the relative L-point. Last setting to be mentioned is related to the numerical continuation by pseudo-arclength, used for guessing a close I.C. for the next member of each family, so following the Eq. (2-69). The latter has been normalized in order to have a distance on the $\hat{x}\hat{z}$ -plane between members of around $\gamma_L/1000$, thus minimizing “lacks or holes” during the propagation process. All constants, settings and threshold values adopted can be found in Appendices-A/B, while here we proceed presenting the results.

3.1 The Horizontal Lyapunov family at L1

L1 H-Lyap: PLOT at $\mu = 0.0121506$

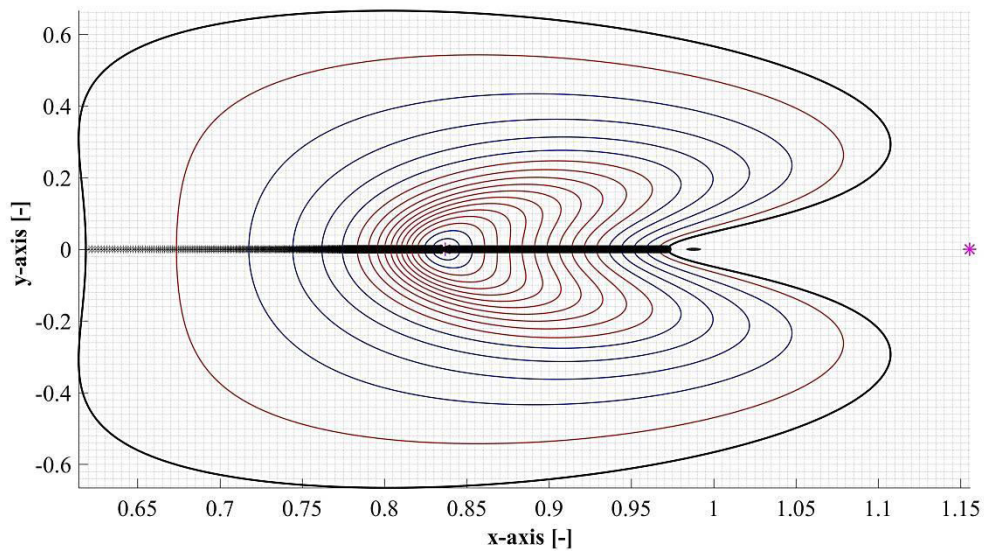


Figure 17: Graphical plot of the H-Lyapunov family of periodic orbits, every 50 members with their relative order of stability (0-green, 1-blue, 2-red). It also shows the Moon (Grey), with the L-points (magenta star), shooting conditions (black dots) and last orbit (black line).

3.1.1 Proprieties and main bifurcations

The orbital period (T) and orbital energy (J) are here shown in magenta for each member of the family. In addition, using the Jacobi constant, the energy-error in the integration along each orbit is given as *mean value* (blue) and *standard deviation* (red).

L1 H-Lyap: ORBITAL ENERGY/PERIOD at $\mu = 0.0121506$

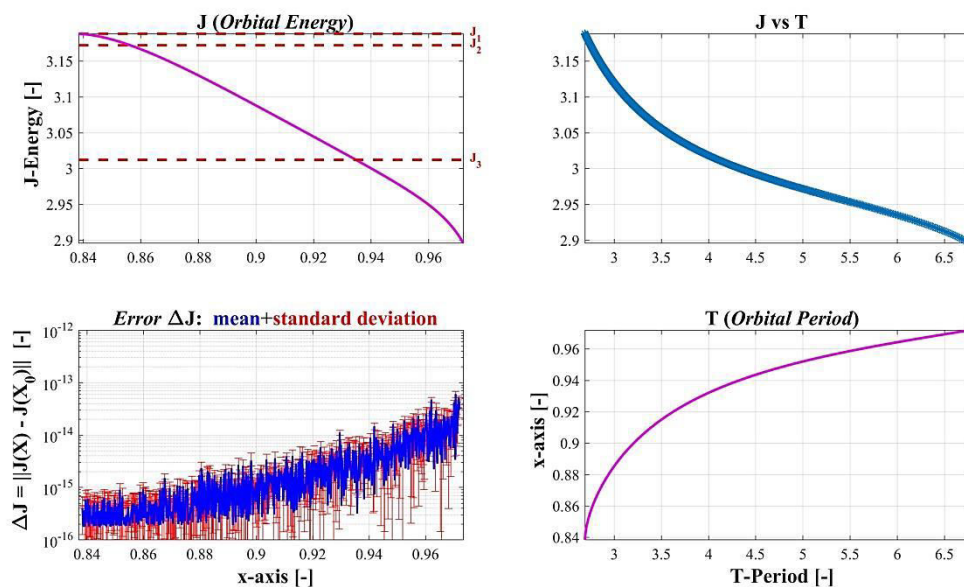


Figure 18: Graphical representation of orbital energy “ J ” (Top-Left), with its error along each trajectory (Bottom-Left) based on mean and standard deviation. Last, the Orbital Period “ T ” (Bottom-Right) is shown also compared with the same orbital energy (Top-Right).

The analysis of the Monodromy matrix and its eigenvalues λ_i (characteristic multipliers) is here shown focusing on different orders of instability, eigenvalues module with a zoom at its boundary value (10^{-3}) adopted to define λ_i still “lying on” the unit circle. Note that the error on the "Det(M)" has been found after using directly the MATLAB *det*-function (in blue) or also using the product of eigenvalues (in orange).

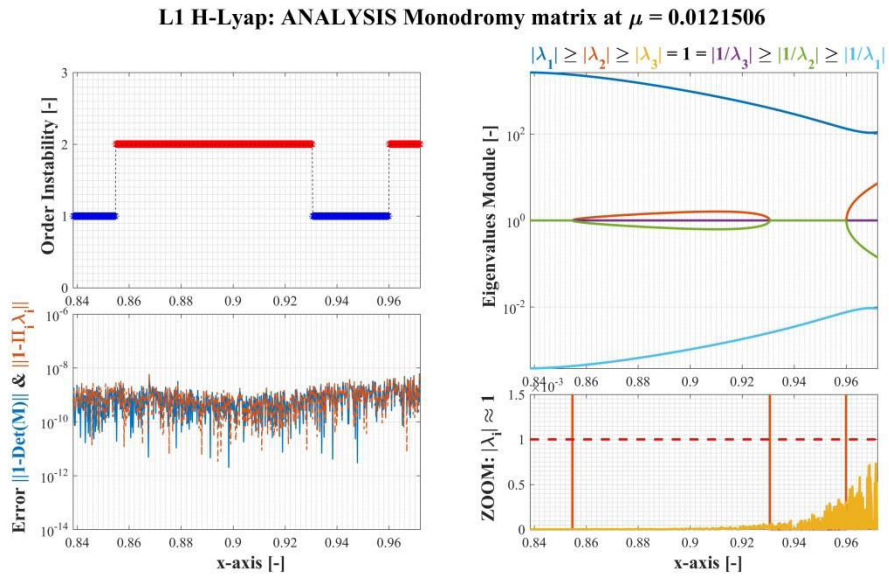


Figure 19: Analysis on the Monodromy matrix, showing on the Left the orders of instability (0-green, 1-blue, 2-red) and the error on the determinant, as described in Section 2.2.4. On the Right, the module of all six “characteristic multipliers” is shown, with a zoom on the threshold value used for calculating the order-of-instability (Right-Bottom).

The following plot shows more in details the eigenvalues’ behaviour in the generation of the family, separating each “pair” due to the Symplectic propriety (Section 2.2.3). Main parameters and considerations will be given later in the *Final comment* section.

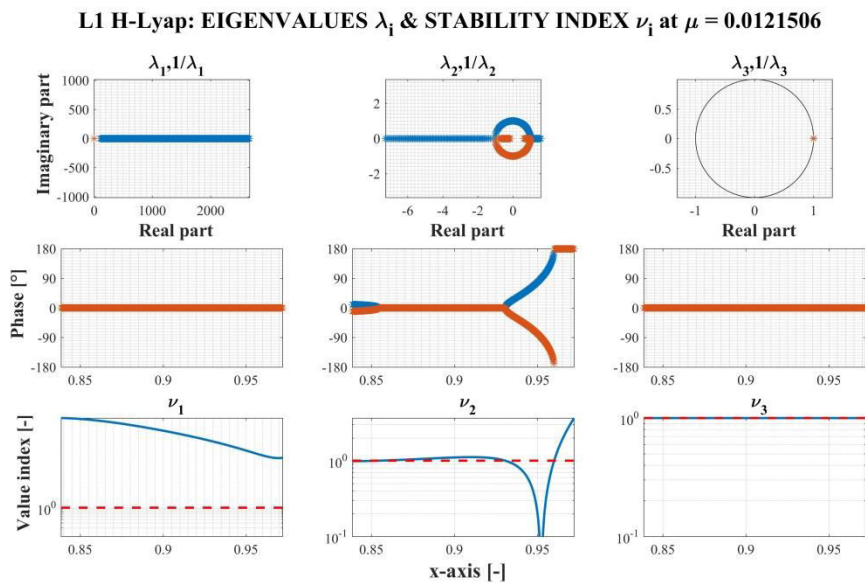


Figure 20: Illustration of six eigenvalues λ_i and three stability indices $\nu_i = |\lambda_i + \lambda_i^{-1}|/2$, given for each pair of reciprocal value. Motion on complex plane (Top), relative phase (Middle) and Stability Index (Bottom) are shown, as they will be explained in the *Final comment* section.

3.1.1.1 Verification and Validation

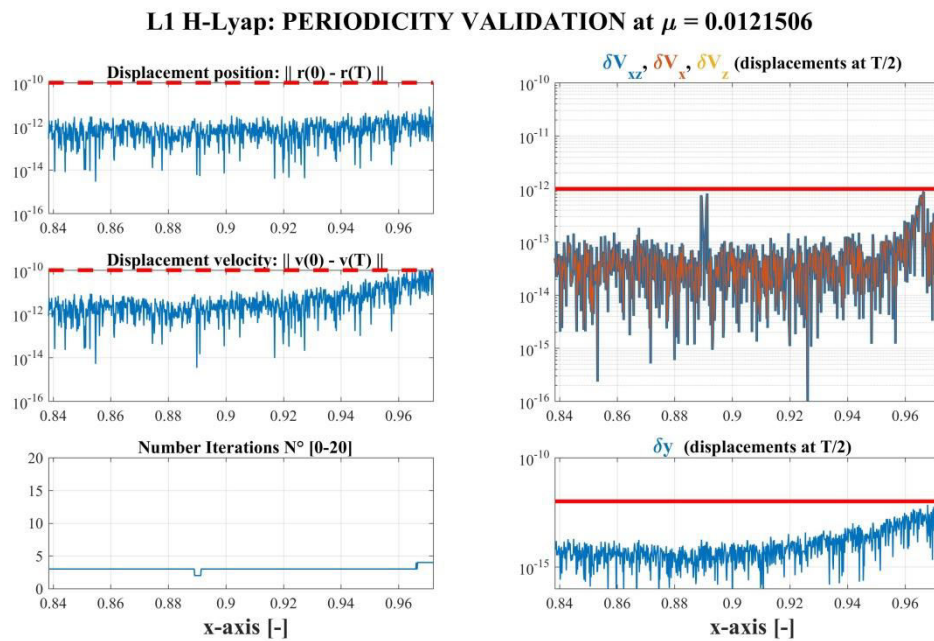


Figure 21: Illustration of the Validation and Verification performed during the Numerical continuation process. All relative information and notation can be found in the Section 2.4.2 .

3.1.1.2 Existing “resonance orbits”

The location of few main resonance orbits within the family is here shown, based on the ratio N/M with M number of orbit-revolutions and N number of system-revolutions, limited to $N \leq 4$ and $M \leq 12$. It follows a period $T_C = 2\pi \cdot N/M$ as explain in Section 4.4.1.

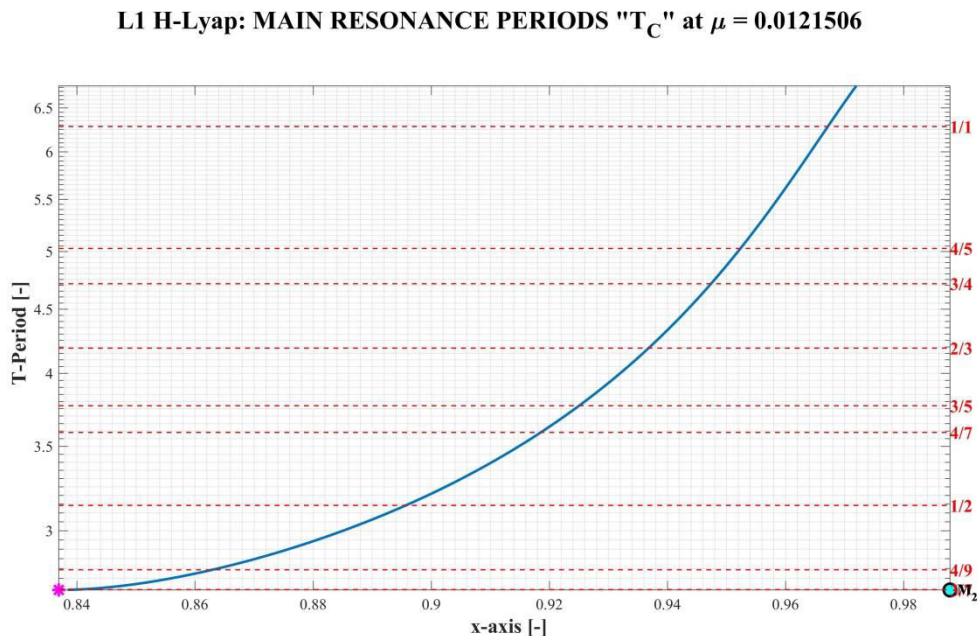


Figure 22: Main resonance orbits existing within the family are given using combinations of M -value (orbit revolutions) and N -value (system revolutions), with $M_{max} = 12$ and $N_{max} = 4$. The system 2π -period is given by $N = 1$, while more details can be found later in Section 4.4.1.

3.1.2 Final comment on the family results

The **Horizontal Lyapunov family** has been generated starting from L1, thus extending it to M2 with a total of 887 members. The propagation has stopped since last orbit was no more periodic²⁴, while in the figure below we provide an image of the Phase-space of shooting conditions where both crosses have been considered (for $t_0 = 0$ and $t_0 = T_C/2$). The color-notation for each order-of-instability is described in the LEGEND.

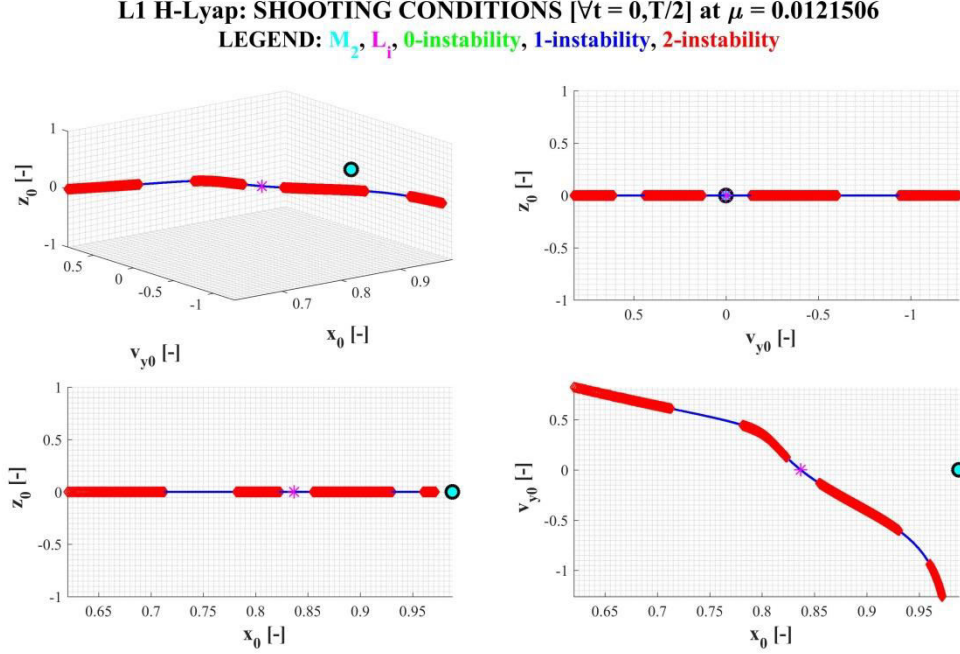


Figure 23: Set of shooting conditions at both $\hat{x}\hat{z}$ -plane crossings [$t_0 = 0, T_C/2$] with the relative order of instability. Look at the LEGEND for information on the colour-notation adopted.

FINAL COMMENT

The orbital period T_C increases monotonically far from the L-point, thus spanning a range approximatively between 2.6917 and 6.7695 (in non-dimensional units), and consequently between around 11.70 and 29.44 days. Interesting to note that this is the only family (in the limits of our generation) that shows orbits with period equal or larger than one for the system revolution (2π), allowing extension of the resonance orbit M1N1. Near the libration point we have I-order instability till the first bifurcation, which actually generates the Halo family. In Figure 19 and Figure 20, the H-Lyapunov family is II-order unstable till a second Tangent-Bifurcation, which reduces again the instability. The latter is well-known to be related to the **Axial family**, here not treated but briefly discussed in Appendix-C. Differently, the last bifurcation occurs at the point -1 in the complex plane, so it is a Period-Doubling Bifurcation (not related to any new family) and leading again to a II-order of instability. It is possible to also observe a ν_i index, as stability parameter defined for each pairs of characteristic multipliers, such that

$$\nu_i = 0.5 \cdot \left\| \lambda_i + \lambda_i^{-1} \right\|, \forall i = 1, 2, 3 \quad (3-1)$$

while additional main aspects will be examined and summarized in Section 3.7.

²⁴ The last computed orbit has a 3-order instability where the unitary eigenvalues was found as $|\lambda| = 1 + 1.122 \cdot 10^{-3}$, outside our “boundary margin” of 10^{-3} from the unit circle (for $|\lambda| = 1$).

3.2 The Vertical Lyapunov family at L1

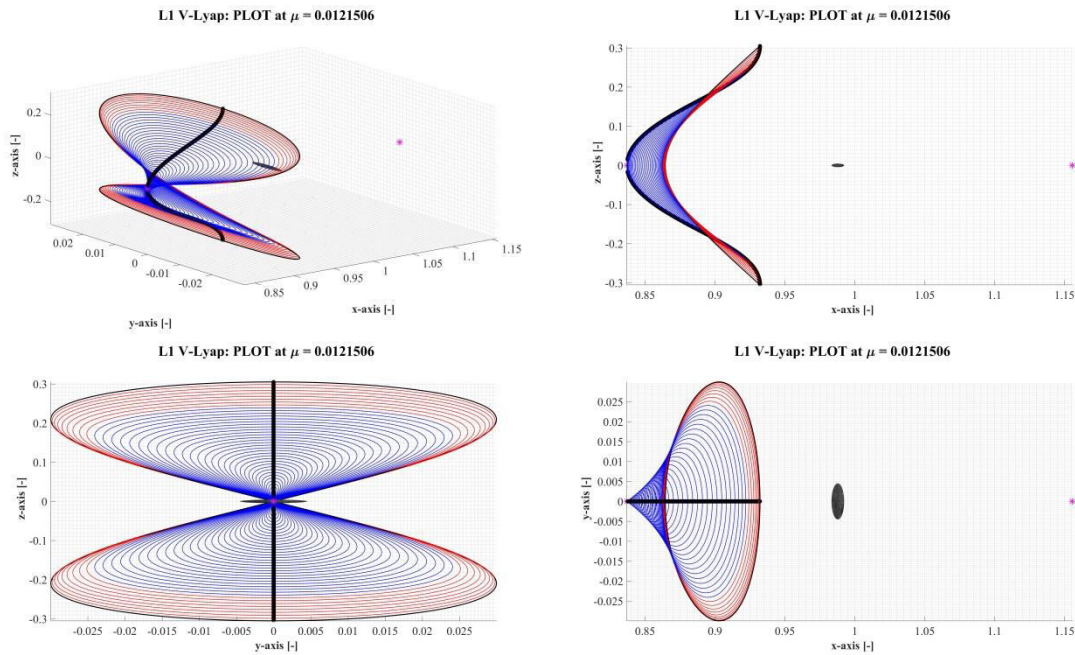


Figure 24: Graphical plot of the V-Lyapunov family of periodic orbits, every 50 members with their relative order of stability (0-green, 1-blue, 2-red). It also shows the Moon (Grey), with the L-points (magenta star), shooting conditions (black dots) and last orbit (black line).

3.2.1 Proprieties and main bifurcations

The Orbital Period (T) and Orbital Energy (J) are here shown in magenta for each member of the family. In addition, using the Jacobi constant, the Energy-error in the integration along each orbit is given as *mean value* (blue) and *standard deviation* (red).

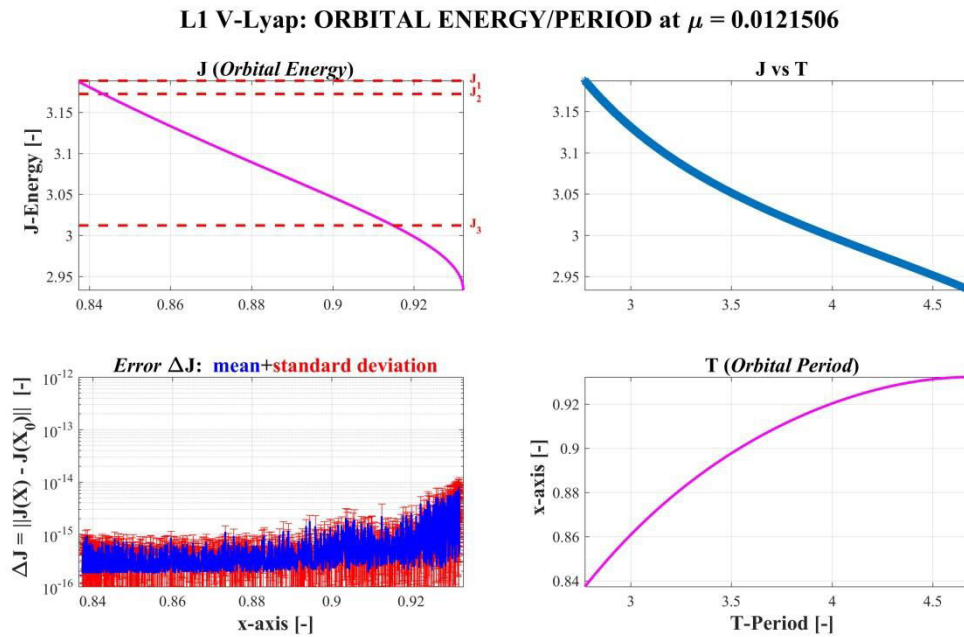


Figure 25: Graphical representation of orbital energy “J” (Top-Left), with its error along each trajectory (Bottom-Left) based on mean and standard deviation. Last, the Orbital Period “T” (Bottom-Right) is shown also compared with the same orbital energy (Top-Right).

The analysis of the Monodromy matrix and its eigenvalues λ_i (characteristic multipliers) is here shown focusing on different orders of instability, eigenvalues module with a zoom at its boundary value (10^{-3}) adopted to define λ_i still “lying on” the unit circle. Note that the error on the "Det(M)" has been found after using directly the MATLAB *det*-function (in blue) or also using the product of eigenvalues (in orange).

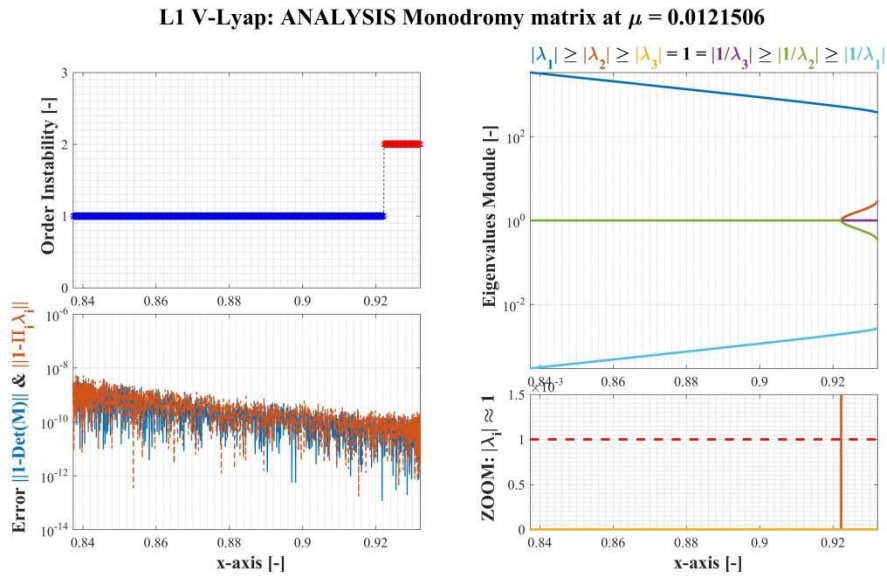


Figure 26: Analysis on the Monodromy matrix, showing on the Left the orders of instability (0-green, 1-blue, 2-red) and the error on the determinant, as described in Section 2.2.4. On the Right, the module of all six “characteristic multipliers” is shown, with a zoom on the threshold value used for calculating the order-of-instability (Right-Bottom).

The following plot shows more in details the eigenvalues’ behaviour in the generation of the family, separating each “pair” due to the Symplectic propriety (Section 2.2.3). Main parameters and considerations will be given later in the *Final comment* section.

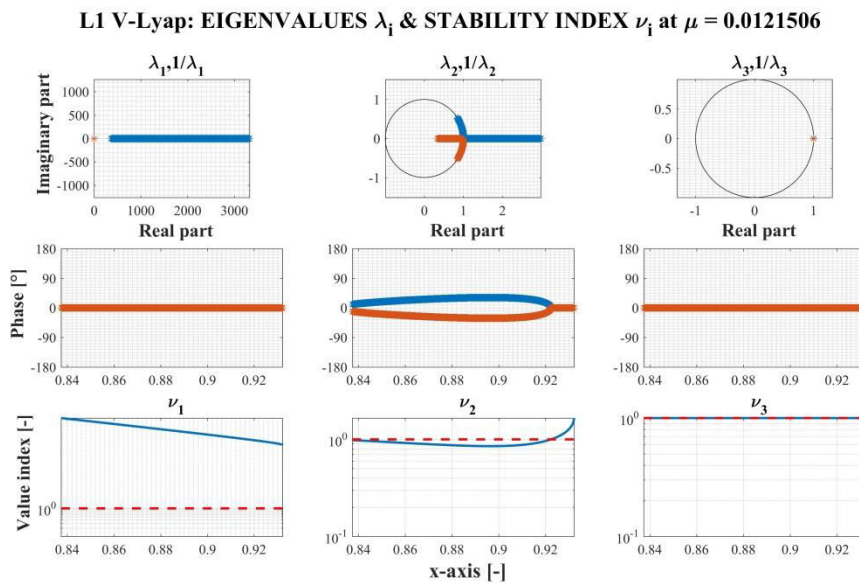


Figure 27: Illustration of eigenvalues λ_i and stability indices $\nu_i = |\lambda_i + \lambda_i^{-1}|/2$, given for each pair of reciprocal value. Motion on complex plane (Top), relative phase (Middle) and Stability Index (Bottom) are shown and they will be explained in the *Final comment* section.

3.2.1.1 Verification and Validation

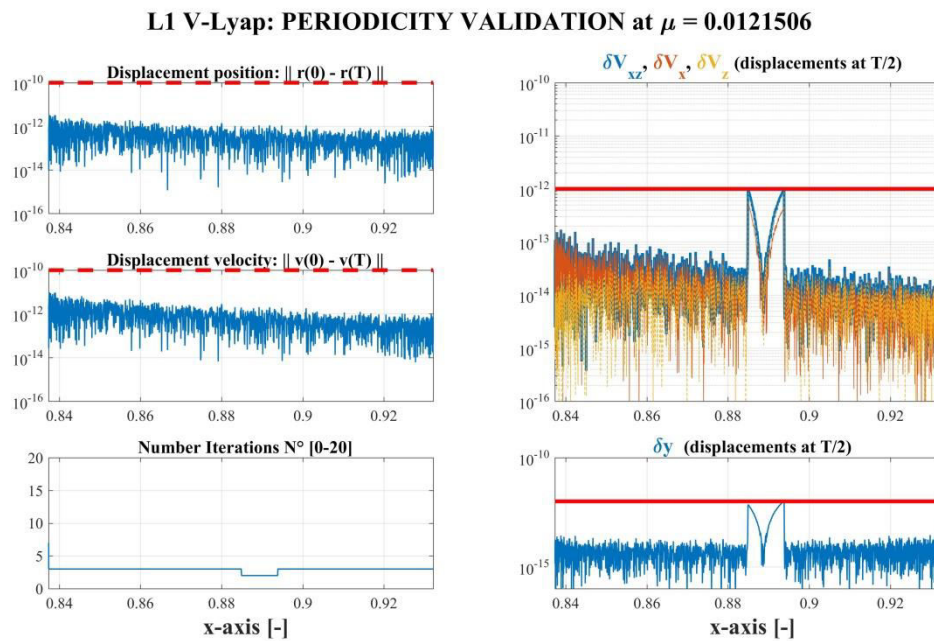


Figure 28: Illustration of the Validation and Verification performed during the Numerical continuation process. All relative information and notation can be found in the Section 2.4.2 .

3.2.1.2 Existing “resonance orbits”

The location of few main resonance orbits within the family is here shown, based on the ratio N/M with M number of orbit-revolutions and N number of system-revolutions, limited to $N \leq 4$ and $M \leq 12$. It follows a period $T_C = 2\pi \cdot N/M$ as explain in Section 4.4.1.

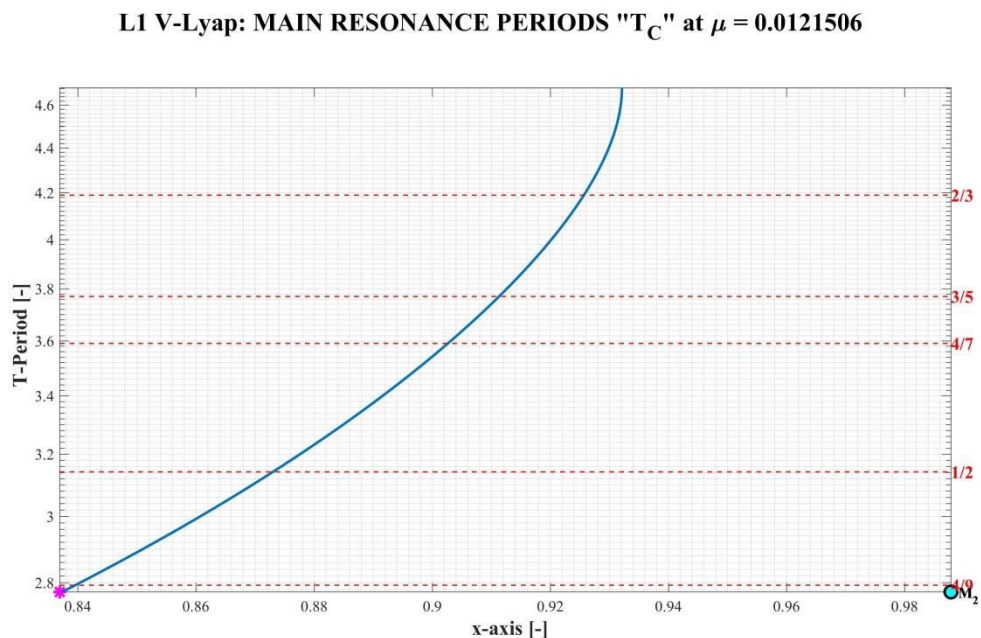


Figure 29: Main resonance orbits existing within the family are given using combinations of M -value (orbit revolutions) and N -value (system revolutions), with $M_{max} = 12$ and $N_{max} = 4$. The system 2π -period is given by $N = 1$, while more details can be found later in Section 4.4.1.

3.2.2 Final comment on the family results

The **Vertical Lyapunov family** has been generated starting from L1, thus extending it to M2 with a total of 2044 members. The propagation has stopped since last orbit reached a turning point, while in the figure below we provide an image of the Phase-space of shooting conditions where both crosses have been considered (for $t_0 = 0$ and $t_0 = T_C/2$). The color-notation for each order-of-instability is described in the LEGEND.

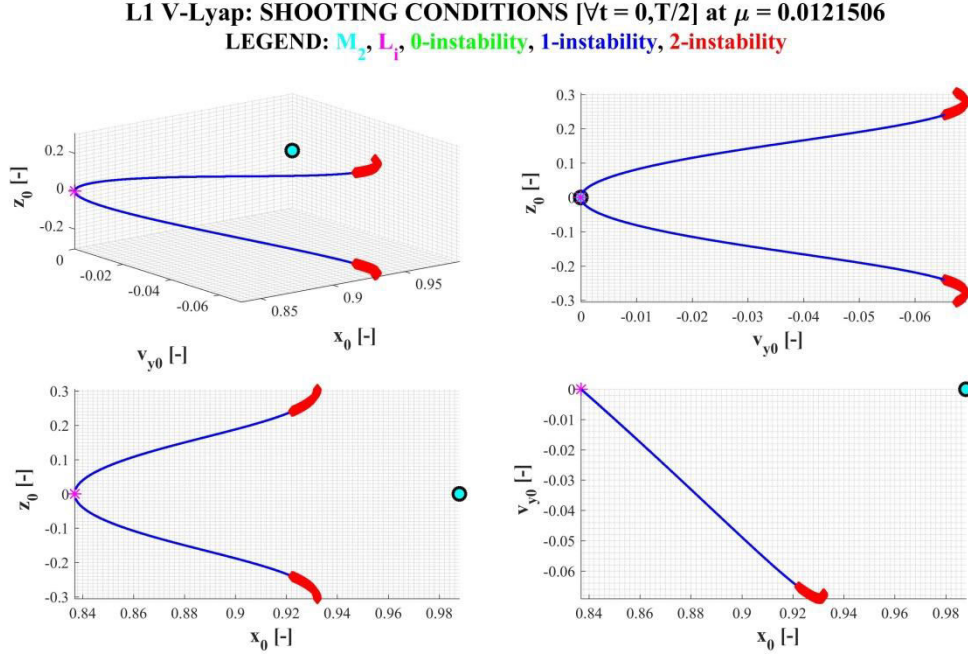


Figure 30: Set of shooting conditions at both $\hat{x}z$ -plane crossings [$t_0 = 0, T_C/2$] with the relative order of instability. Look at the LEGEND for information on the colour-notation adopted.

FINAL COMMENT

The orbital period T_C increases monotonically far from the L-point, thus spanning a range approximatively between 2.7734 and 4.6835 (in non-dimensional units), and consequently between around 12.06 and 20.37 days. Looking at the trend in Figure 29, we expect an increasing period beyond the turning point (where the algorithm has stopped), while at the same location we observe also a reverse trend of the shooting velocity in the Phase-space (Figure 30, Right-Bottom). In the three-dimensional Phase-space the double-symmetry of Vertical Lyapunov solutions (mentioned in Section 2.4.1) is clear, while the vertical extension is not really visible due to a different scale used for both the x and z axes (Figure 30, Left-Bottom).

Talking about instability, the I-order is almost constant and it only increases at the bifurcation point, which is a Tangent-Bifurcation (at +1 in the complex plane) and consequently related to a new family of periodic solutions. As seen for the H-Lyapunov one, this new family is again the **Axial family** (described in Appendix-C) intersecting the x -axis at two different points, originally referred also with the name **Y-family** in (Doedel et al., 2007) and later in (Shirobokov, 2014). The former, in his work, has fully investigated this new family, well-known in literature to be a connection between both the Horizontal and the Vertical Lyapunov family. Additional details on bifurcations will be discussed in Section 3.7, while an example is shown in Figure 96.

3.3 The Halo family at L1

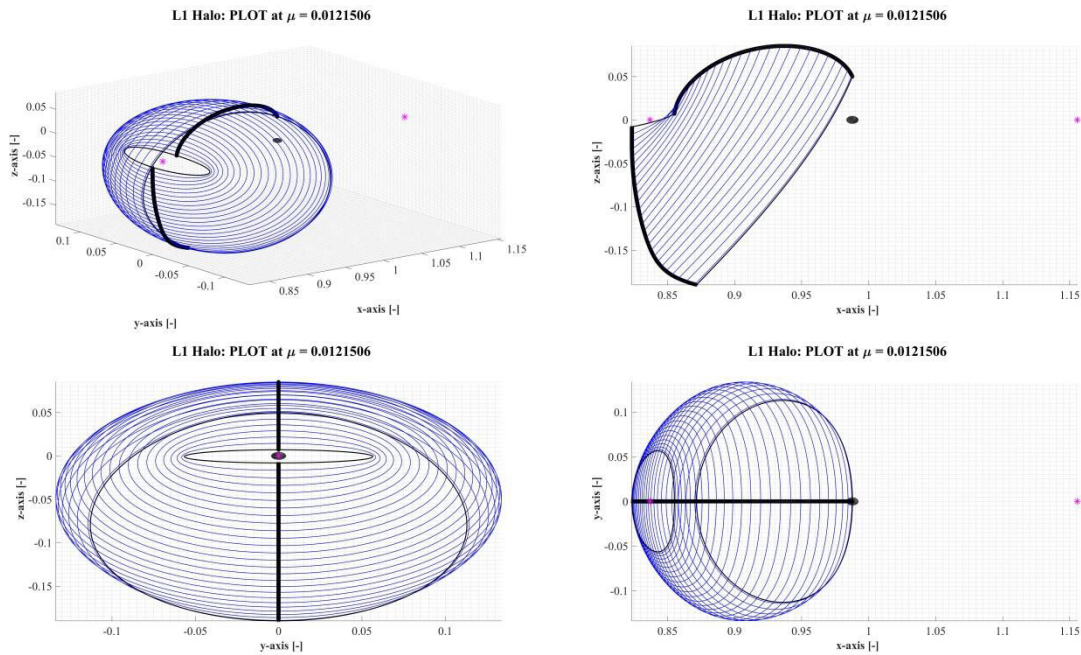


Figure 31: Graphical plot of the Halo family of periodic orbits, every 50 members with their relative order of stability (0-green, 1-blue, 2-red). It also shows the Moon (Grey), the L-points (magenta star), shooting conditions (black dots) and last orbit (black line).

3.3.1 Proprieties and main bifurcations

The Orbital Period (T) and Orbital Energy (J) are here shown in magenta for each member of the family. In addition, using the Jacobi constant, the Energy-error in the integration along each orbit is given as *mean value* (blue) and *standard deviation* (red).

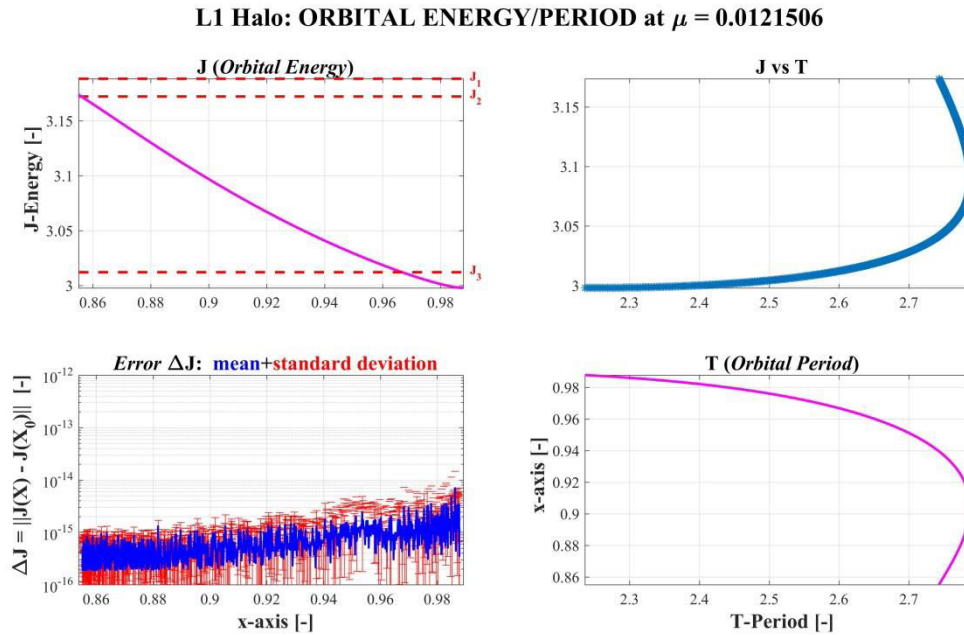


Figure 32: Graphical representation of orbital energy “J” (Top-Left), with its error along each trajectory (Bottom-Left) based on mean and standard deviation. Last, the Orbital Period “T” (Bottom-Right) is shown also compared with the same orbital energy (Top-Right).

The analysis of the Monodromy matrix and its eigenvalues λ_i (characteristic multipliers) is here shown focusing on different orders of instability, eigenvalues module with a zoom at its boundary value (10^{-3}) adopted to define λ_i still “lying on” the unit circle. Note that the error on the "Det(M)" has been found after using directly the MATLAB *det*-function (in blue) or also using the product of eigenvalues (in orange).

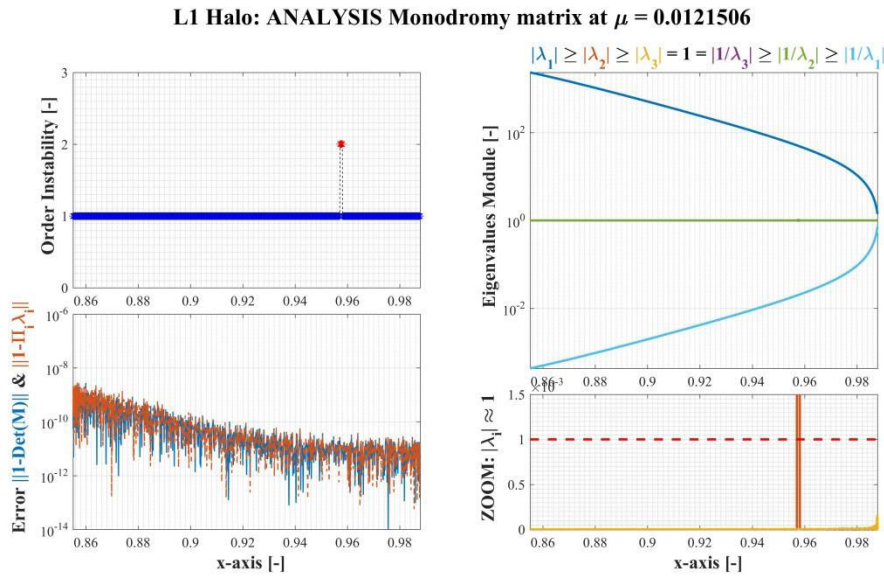


Figure 33: Analysis on the Monodromy matrix, showing on the Left the orders of instability (0-green, 1-blue, 2-red) and the error on the determinant, as described in Section 2.2.4. On the Right, the module of all six “characteristic multipliers” is shown, with a zoom on the threshold value used for calculating the order-of-instability (Right-Bottom).

The following plot shows more in details the eigenvalues’ behaviour in the generation of the family, separating each “pair” due to the Symplectic propriety (Section 2.2.3). Main parameters and considerations will be given later in the *Final comment* section.

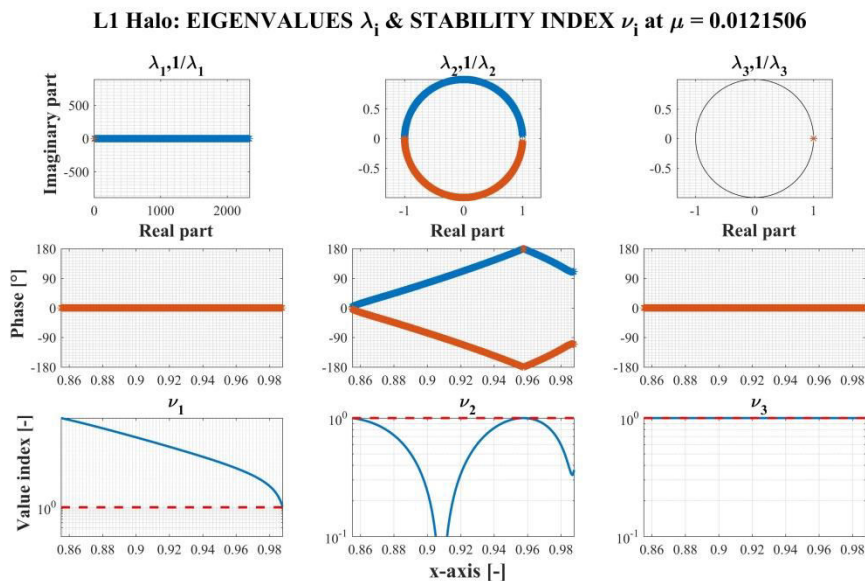


Figure 34: Illustration of eigenvalues λ_i and stability indices $\nu_i = |\lambda_i + \lambda_i^{-1}|/2$, given for each pair of reciprocal value. Motion on complex plane (Top), relative phase (Middle) and Stability Index (Bottom) are shown and they will be explained in the *Final comment* section.

3.3.1.1 Verification and Validation

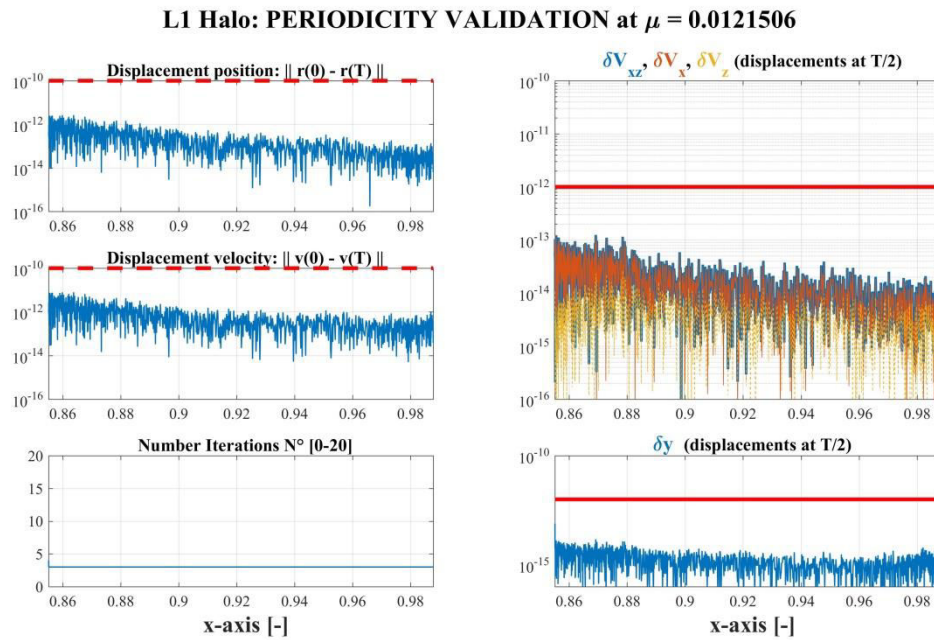


Figure 35: Illustration of the Validation and Verification performed during the Numerical continuation process. All relative information and notation can be found in the Section 2.4.2 .

3.3.1.2 Existing “resonance orbits”

The location of few main resonance orbits within the family is here shown, based on the ratio N/M with M number of orbit-revolutions and N number of system-revolutions, limited to $N \leq 4$ and $M \leq 12$. It follows a period $T_C = 2\pi \cdot N/M$ as explain in Section 4.4.1.

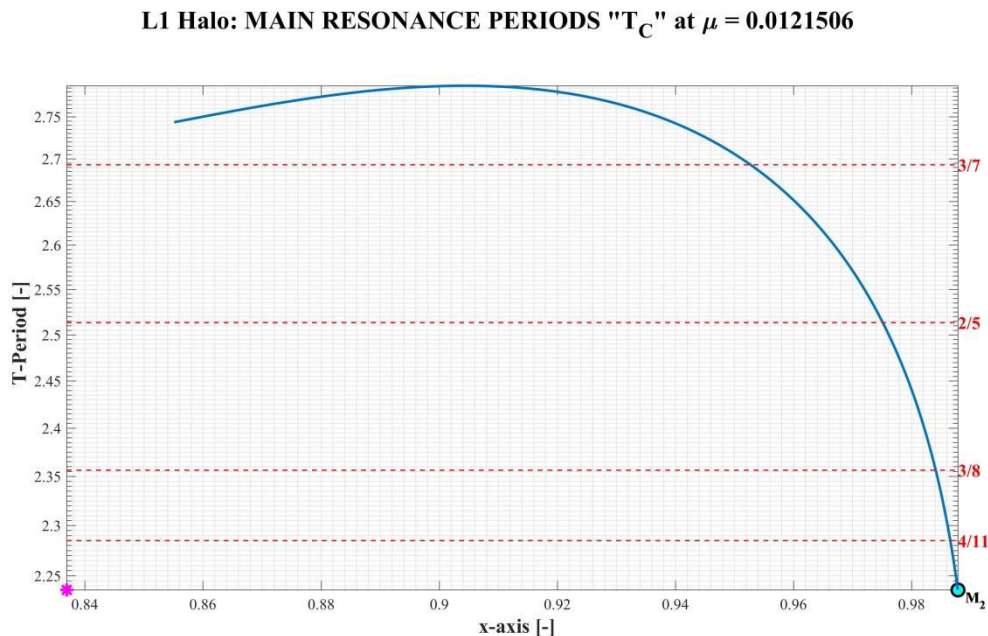


Figure 36: Main resonance orbits existing within the family are given using combinations of M-value (orbit revolutions) and N-value (system revolutions), with $M_{max} = 12$ and $N_{max} = 4$. The system 2π -period is given by $N = 1$, while more details can be found later in Section 4.4.1.

3.3.2 Final comment on the family results

The **Halo family** has been generated starting from L1, thus extending it to M2 with a total of 1259 members. The propagation has stopped since last orbit has reached the x_2 position of M_2 , while in the figure below we provide an image of the Phase-space of shooting conditions where both crosses have been considered (for $t_0 = 0$ and $t_0 = T_C/2$). The color-notation for each order-of-instability is described in the LEGEND.

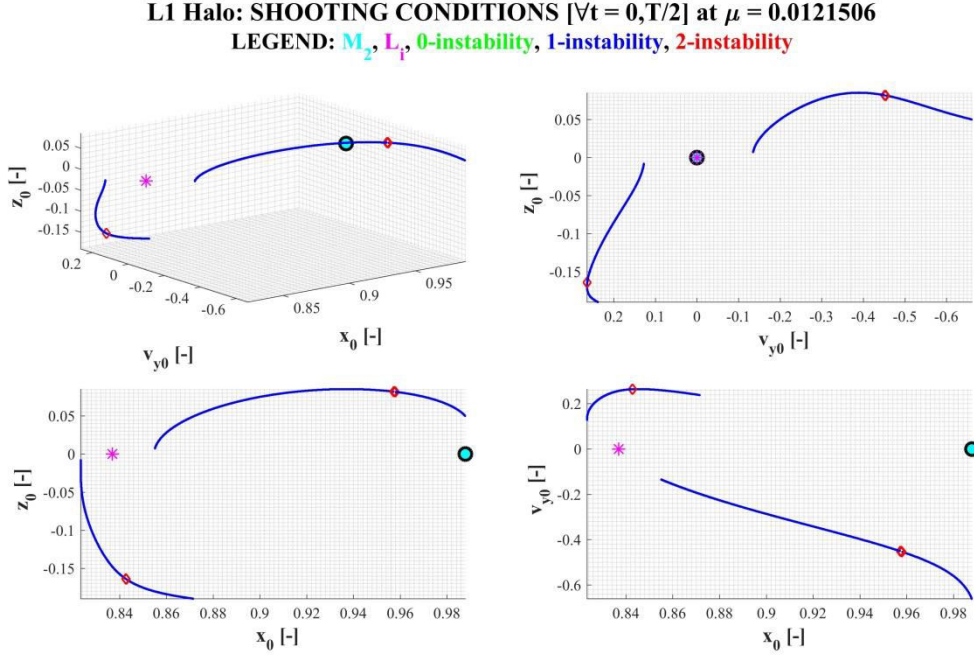


Figure 37: Set of shooting conditions at both $\hat{x}z$ -plane crossings [$t_0 = 0, T_C/2$] with the relative order of instability. Look at the LEGEND for information on the color-notation adopted.

FINAL COMMENT

The orbital period T_C starts increasing and then decreases going toward the M2 mass, with an initial value as 2.7434 (~ 12 days) and a maximum one at around $x_0^{T_{max}} \cong 0.9045$, and consequently around 32000 km from the Moon (along the syzygy) and 26000 km from L1. However, the T-range spans approximatively between 2.2362 and 2.7872 (in non-dimensional units), so consequently between around 9.72 and 12.12 days. As shown in Figure 37 (Left-Bottom), the family is getting closer to the Moon, where for the last member generated (with $x_0^{END} \cong x_2$) we have that $z_0^{END} \cong 0.05$ (equivalent to 19200 km out-of-plane). Very interesting to note in Figure 33 that the entire family has I-order of instability except for a narrow area between 11779 and 11452 km from M2 (with a very small horizontal range of 327 km). Here there is a peak as $|\lambda| \approx 1 + 1.696 \cdot 10^{-2}$, not related to the very small determinant error ($\sim 10^{-11}$). More information will be presented in Section 3.7, in particular based on additional literature for a very similar analysis. As last, another very important aspect visible is the ‘probable’ stability reached at the end of the family when looking at the trend in Figure 33, in a strong agreement with results of (Breakwell, 1979). Moreover, in their paper, they have further extended the generation at L1 for the Earth-Moon CR3BP, so leading to a “second narrow band of stable orbits with perilune, however below the lunar surface”. In (Doedel et al., 2007) this bifurcation also exists ($\forall \lambda_1 \rightarrow +1$) and it is actually related to the new-born **W4/5-family**, as connection with **V-Lyapunov** orbits existing at the $L_{4/5}$ -points.

3.4 The Horizontal Lyapunov family at L2

L2 H-Lyap: PLOT at $\mu = 0.0121506$

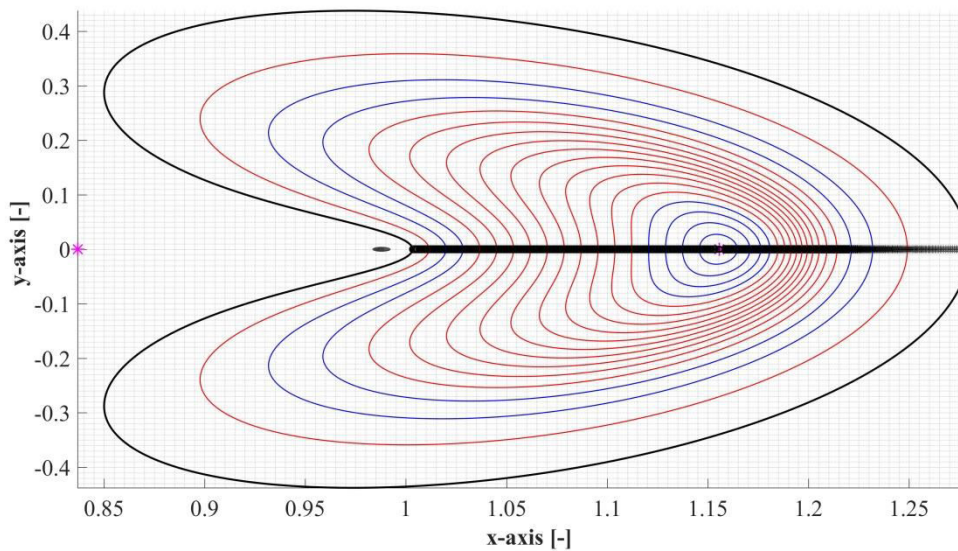


Figure 38: Graphical plot of the H-Lyapunov family of periodic orbits, every 50 members with their relative order of stability (0-green, 1-blue, 2-red). It also shows the Moon (Grey), with the L-points (magenta star), shooting conditions (black dots) and last orbit (black line).

3.4.1 Proprieties and main bifurcations

The Orbital Period (T) and Orbital Energy (J) are here shown in magenta for each member of the family. In addition, using the Jacobi constant, the Energy-error in the integration along each orbit is given as *mean value* (blue) and *standard deviation* (red).

L2 H-Lyap: ORBITAL ENERGY/PERIOD at $\mu = 0.0121506$

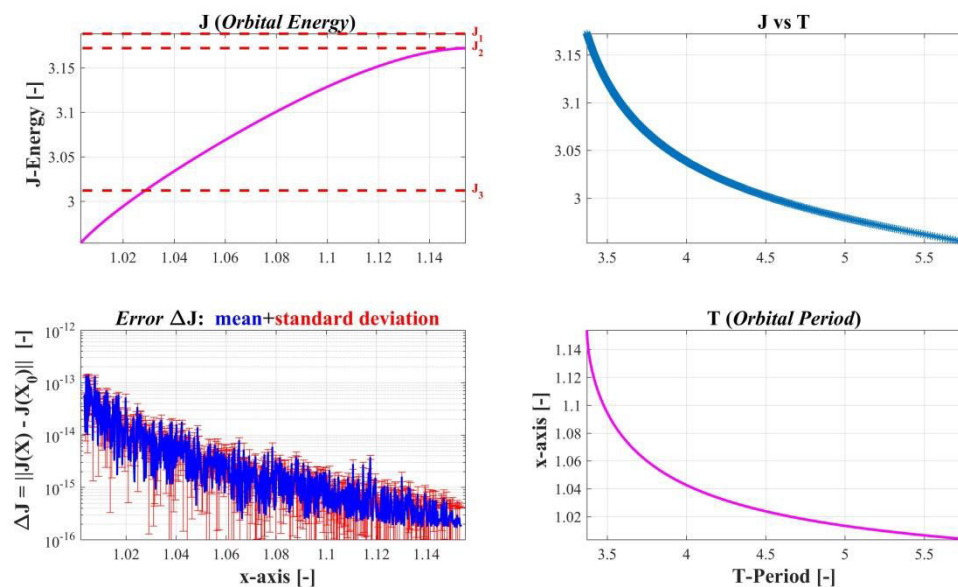


Figure 39: Graphical representation of orbital energy “J” (Top-Left), with its error along each trajectory (Bottom-Left) based on mean and standard deviation. Last, the Orbital Period “T” (Bottom-Right) is shown also compared with the same orbital energy (Top-Right).

The analysis of the Monodromy matrix and its eigenvalues λ_i (characteristic multipliers) is here shown focusing on different orders of instability, eigenvalues module with a zoom at its boundary value (10^{-3}) adopted to define λ_i still “lying on” the unit circle. Note that the error on the "Det(M)" has been found after using directly the MATLAB *det*-function (in blue) or also using the product of eigenvalues (in orange).

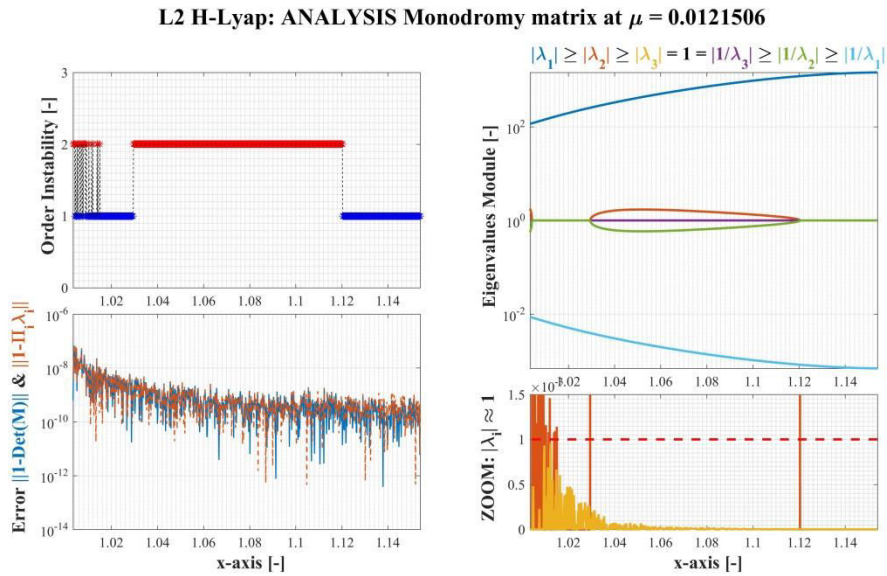


Figure 40: Analysis on the Monodromy matrix, showing on the Left the orders of instability (0-green, 1-blue, 2-red) and the error on the determinant, as described in Section 2.2.4. On the Right, the module of all six “characteristic multipliers” is shown, with a zoom on the threshold value used for calculating the order-of-instability (Right-Bottom).

The following plot shows more in details the eigenvalues’ behaviour in the generation of the family, separating each “pair” due to the Symplectic propriety (Section 2.2.3). Main parameters and considerations will be given later in the *Final comment* section.

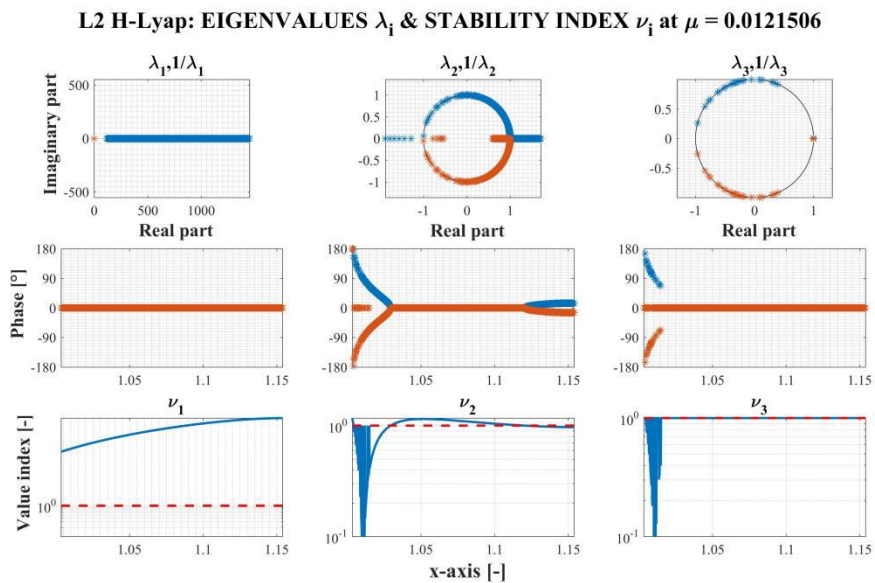


Figure 41: Illustration of eigenvalues λ_i and stability indices $\nu_i = |\lambda_i + \lambda_i^{-1}|/2$, given for each pair of reciprocal value. Motion on complex plane (Top), relative phase (Middle) and Stability Index (Bottom) are shown and they will be explained in the *Final comment* section.

3.4.1.1 Verification and Validation

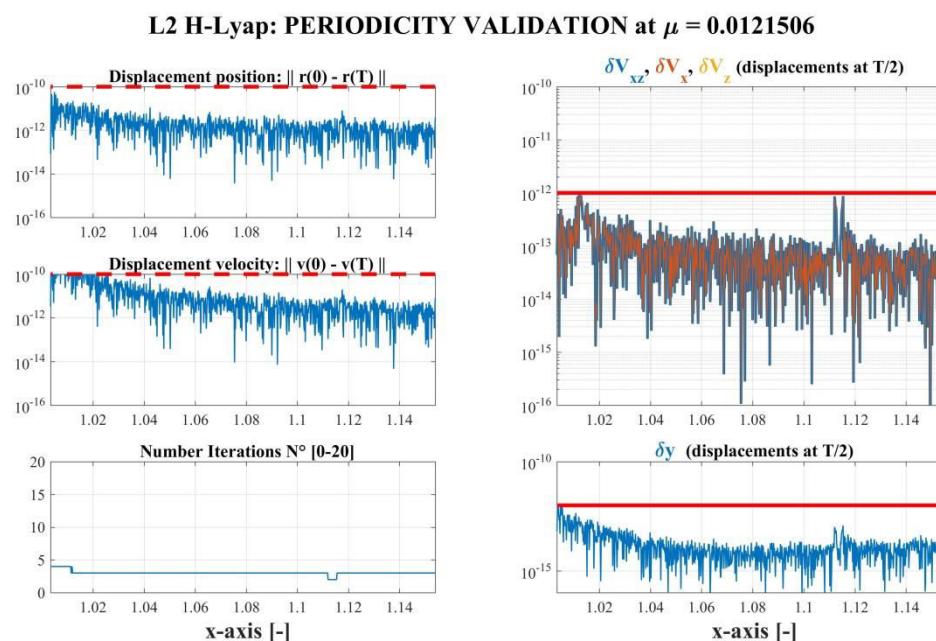


Figure 42: Illustration of the Validation and Verification performed during the Numerical continuation process. All relative information and notation can be found in the Section 2.4.2 .

3.4.1.2 Existing “resonance orbits”

The location of few main resonance orbits within the family is here shown, based on the ratio N/M with M number of orbit-revolutions and N number of system-revolutions, limited to $N \leq 4$ and $M \leq 12$. It follows a period $T_C = 2\pi \cdot N/M$ as explain in Section 4.4.1.

L2 H-Lyap: MAIN RESONANCE PERIODS " T_C " at $\mu = 0.0121506$

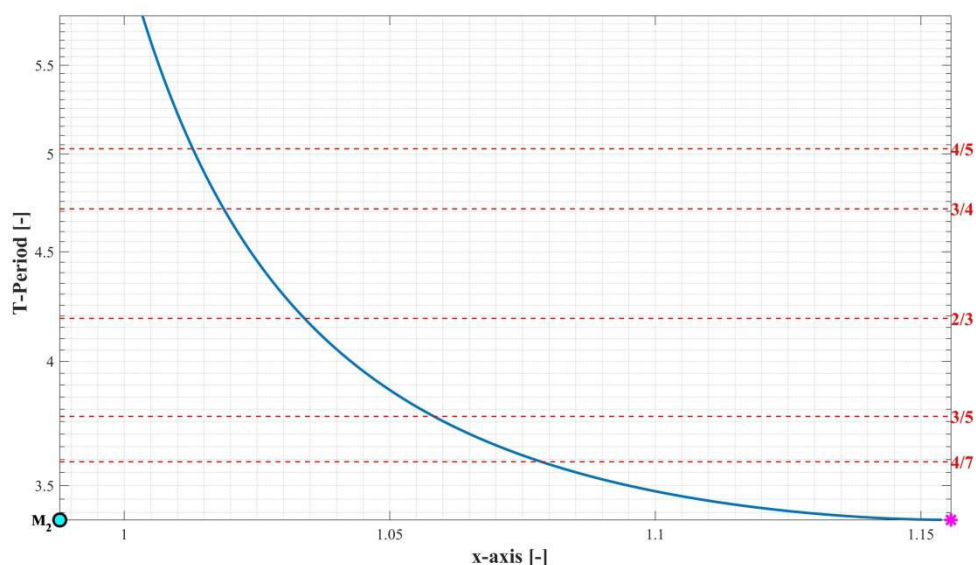


Figure 43: Main resonance orbits existing within the family are given using combinations of M -value (orbit revolutions) and N -value (system revolutions), with $M_{max} = 12$ and $N_{max} = 4$. The system 2π -period is given by $N = 1$, while more details can be found later in Section 4.4.1.

3.4.2 Final comment on the family results

The **Horizontal Lyapunov family** has been generated starting from L2, thus extending it to M2 with a total of 899 members. The propagation has stopped since last orbit was no more periodic²⁵, while in the figure below we provide an image of the Phase-space of shooting conditions where both crosses have been considered (for $t_0 = 0$ and $t_0 = T_C/2$). The color-notation for each order-of-instability is described in the LEGEND.

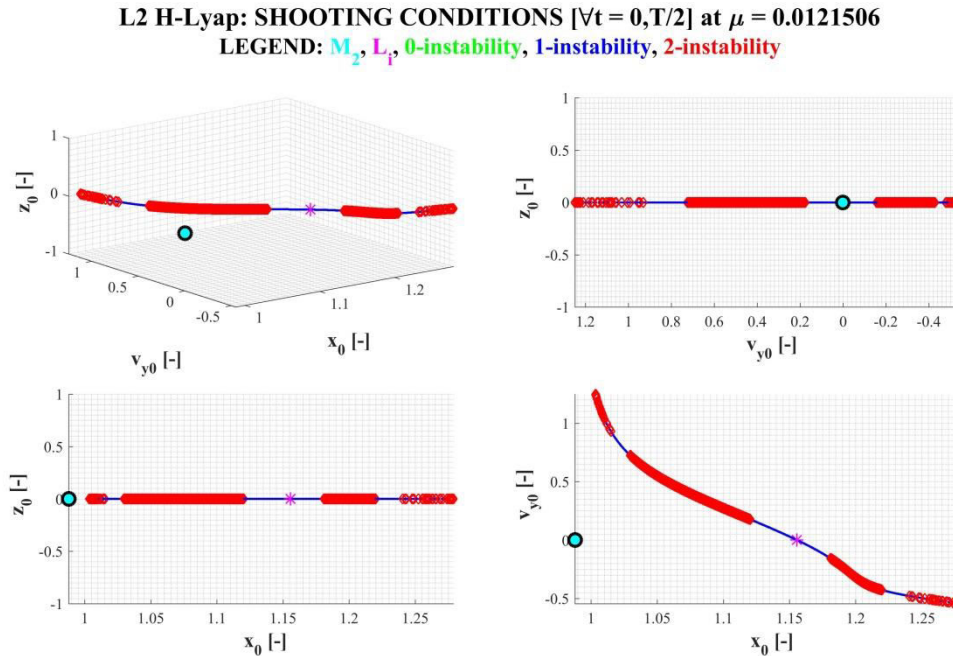


Figure 44: Set of shooting conditions at both $\hat{x}\hat{z}$ -plane crossings [$t_0 = 0, T_C/2$] with the relative order of instability. Look at the LEGEND for information on the colour-notation adopted.

FINAL COMMENT

The orbital period T_C increases monotonically far from the L-point, thus spanning a range approximatively between 3.3734 and 5.7127 (in non-dimensional units), and consequently between around 14.67 and 24.84 days. The analysis resembles the one presented for H-Lyapunov orbits at L1, nonetheless effects due to the Centrifugal force should have a major effects as we are farther from the barycentre/origin of the system. Clearly in Figure 17, compared to Figure 38, effects of the gravitational attraction of M1 are more evident in the ‘deformed’ shape of larger orbits. Interesting in this comparison is also the existence of both bifurcations, respectively related to the creation of Halo and Axial families, as further confirmation of what has been discussed in the mentioned literature. Unfortunately close to M2 the integration of the Total system (state-vector + STM) has some issues, as visible in an increasing error on the Monodromy determinant in Figure 40. In the same figure (Right-Bottom) a more clear behaviour is shown, where the eigenvalue λ_3 is subject to larger noise, still within a boundary $\pm 10^{-3}$ from the unit circle. This noise in the dynamics near M2 starting from L2, clearly affects the order of instability (now oscillating between I° and II°); in particular it can be noted in Figure 41 where both ν_2 and ν_3 lose their “continuous trend”, based on Eq. (3-1), mostly due to the characteristic multipliers motion in the complex plane for different orbits of the family.

²⁵ The last computed orbit has a 3-order instability where the unitary eigenvalues was found as $|\lambda| = 1 + 2.397 \cdot 10^{-3}$, outside our “boundary margin” of 10^{-3} from the unit circle ($\forall |\lambda| = 1$).

3.5 The Vertical Lyapunov family at L2

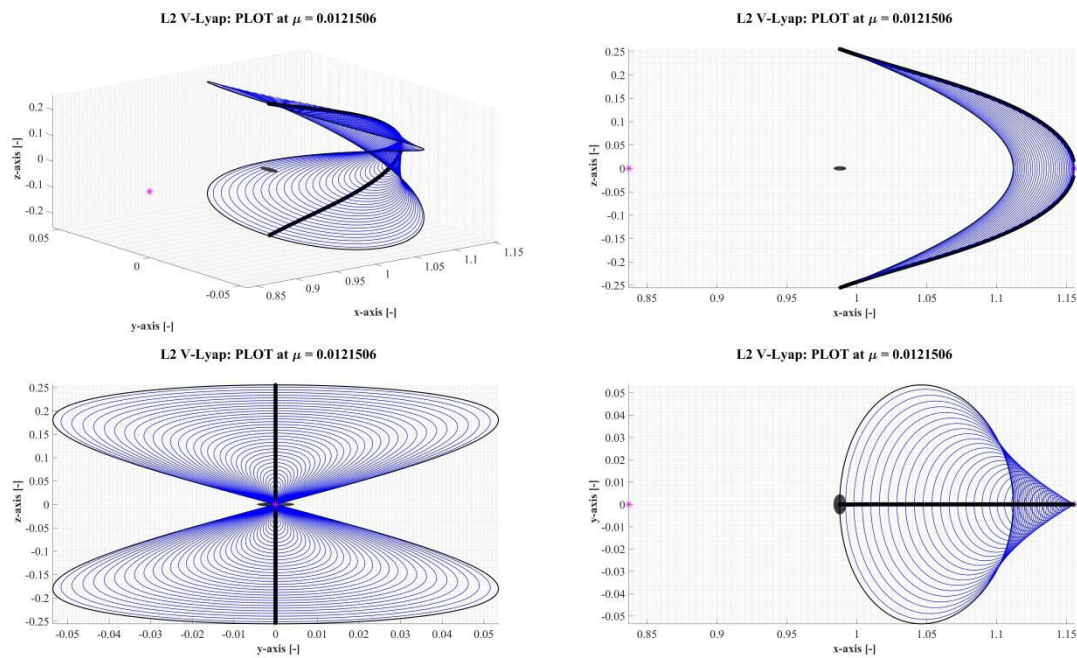


Figure 45: Graphical plot of the V-Lyapunov family of periodic orbits, every 50 members with their relative order of stability (0-green, 1-blue, 2-red). It also shows the Moon (Grey), with the L-points (magenta star), shooting conditions (black dots) and last orbit (black line).

3.5.1 Proprieties and main bifurcations

The Orbital Period (T) and Orbital Energy (J) are here shown in magenta for each member of the family. In addition, using the Jacobi constant, the Energy-error in the integration along each orbit is given as *mean value* (blue) and *standard deviation* (red).

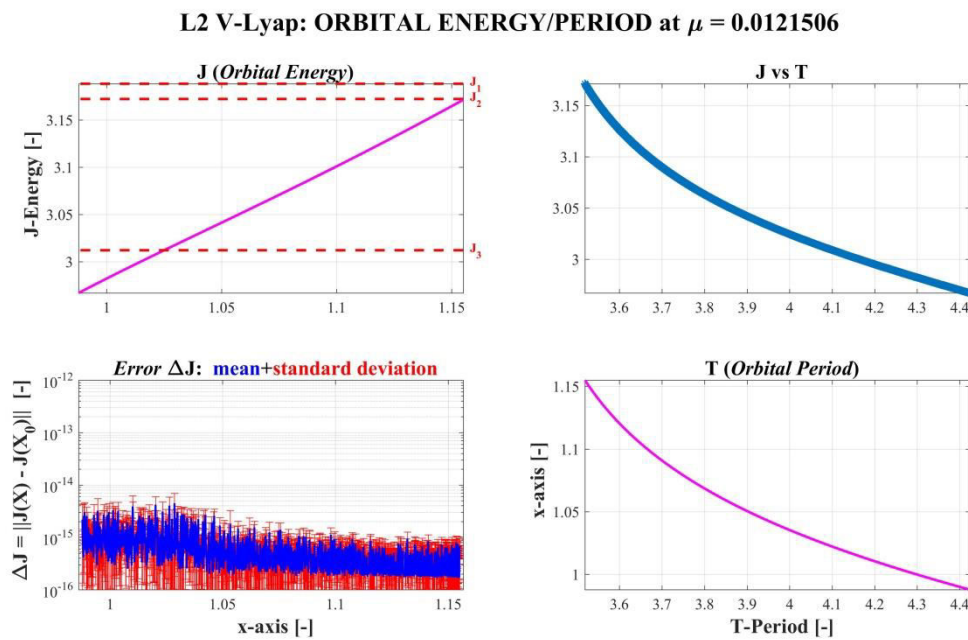


Figure 46: Graphical representation of orbital energy “J” (Top-Left), with its error along each trajectory (Bottom-Left) based on mean and standard deviation. Last, the Orbital Period “T” (Bottom-Right) is shown also compared with the same orbital energy (Top-Right).

The analysis of the Monodromy matrix and its eigenvalues λ_i (characteristic multipliers) is here shown focusing on different orders of instability, eigenvalues module with a zoom at its boundary value (10^{-3}) adopted to define λ_i still “lying on” the unit circle. Note that the error on the "Det(M)" has been found after using directly the MATLAB *det*-function (in blue) or also using the product of eigenvalues (in orange).

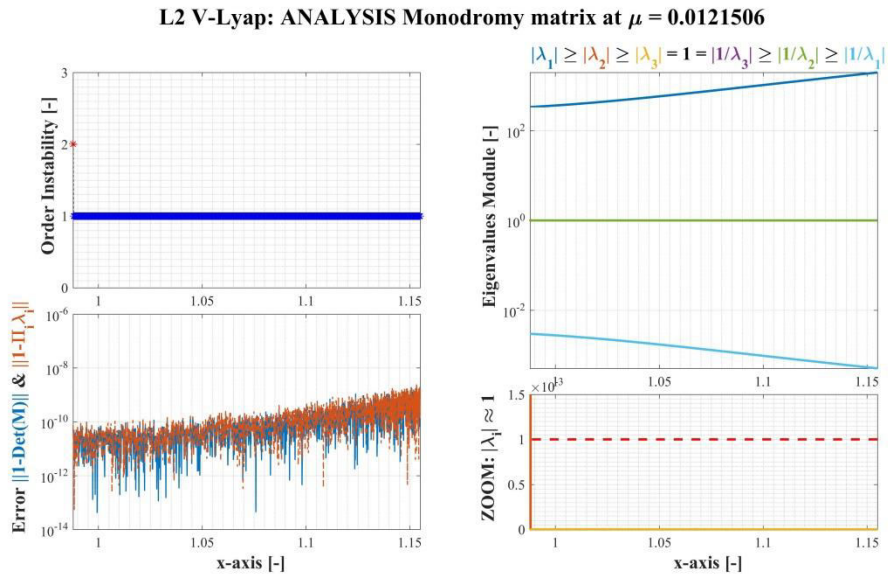


Figure 47: Analysis on the Monodromy matrix, showing on the Left the orders of instability (0-green, 1-blue, 2-red) and the error on the determinant, as described in Section 2.2.4. On the Right, the module of all six “characteristic multipliers” is shown, with a zoom on the threshold value used for calculating the order-of-instability (Right-Bottom).

The following plot shows more in details the eigenvalues’ behaviour in the generation of the family, separating each “pair” due to the Symplectic propriety (Section 2.2.3). Main parameters and considerations will be given later in the *Final comment* section.

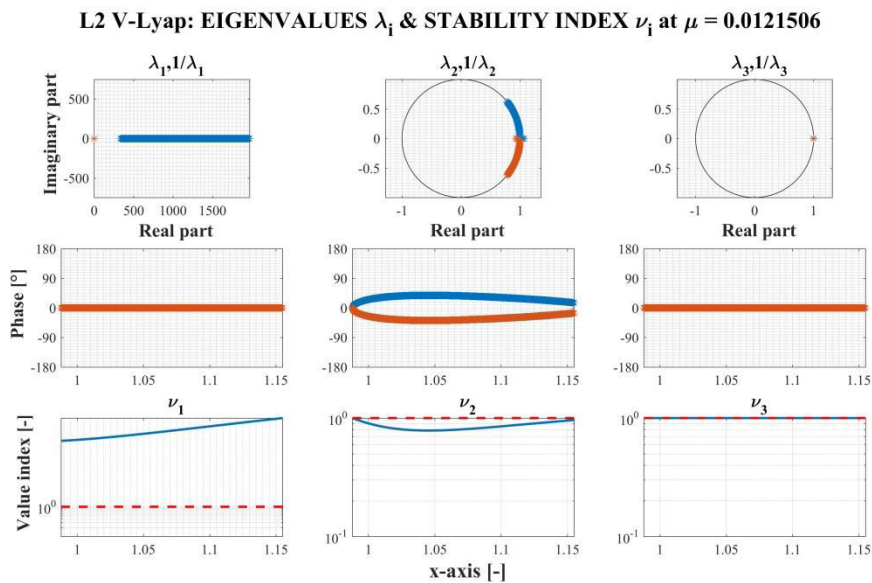


Figure 48: Illustration of eigenvalues λ_i and stability indices $\nu_i = |\lambda_i + \lambda_i^{-1}|/2$, given for each pair of reciprocal value. Motion on complex plane (Top), relative phase (Middle) and Stability Index (Bottom) are shown and they will be explained in the *Final comment* section.

3.5.1.1 Verification and Validation

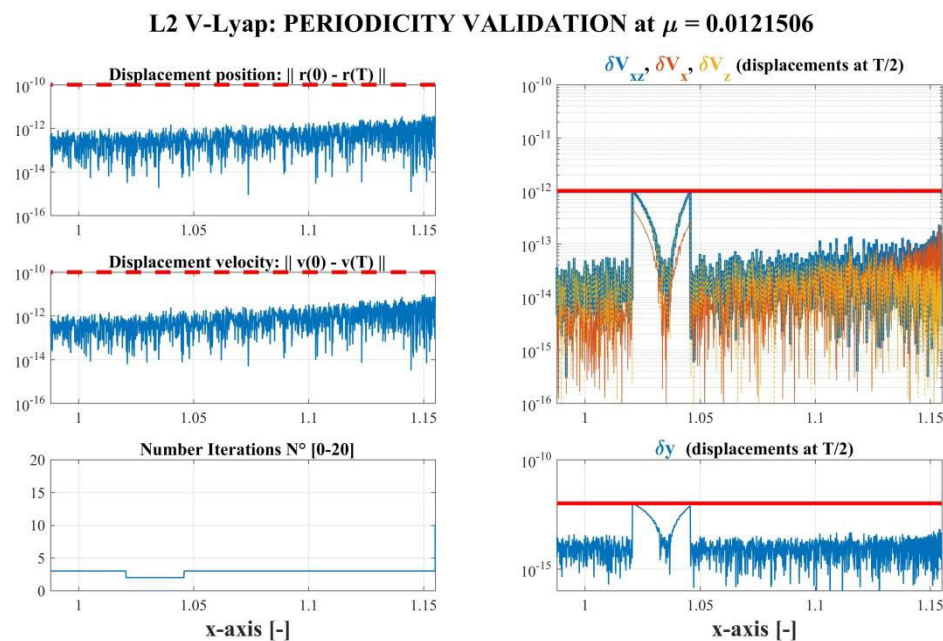


Figure 49: Illustration of the Validation and Verification performed during the Numerical continuation process. All relative information and notation can be found in the Section 2.4.2 .

3.5.1.2 Existing “resonance orbits”

The location of few main resonance orbits within the family is here shown, based on the ratio N/M with M number of orbit-revolutions and N number of system-revolutions, limited to $N \leq 4$ and $M \leq 12$. It follows a period $T_C = 2\pi \cdot N/M$ as explain in Section 4.4.1.

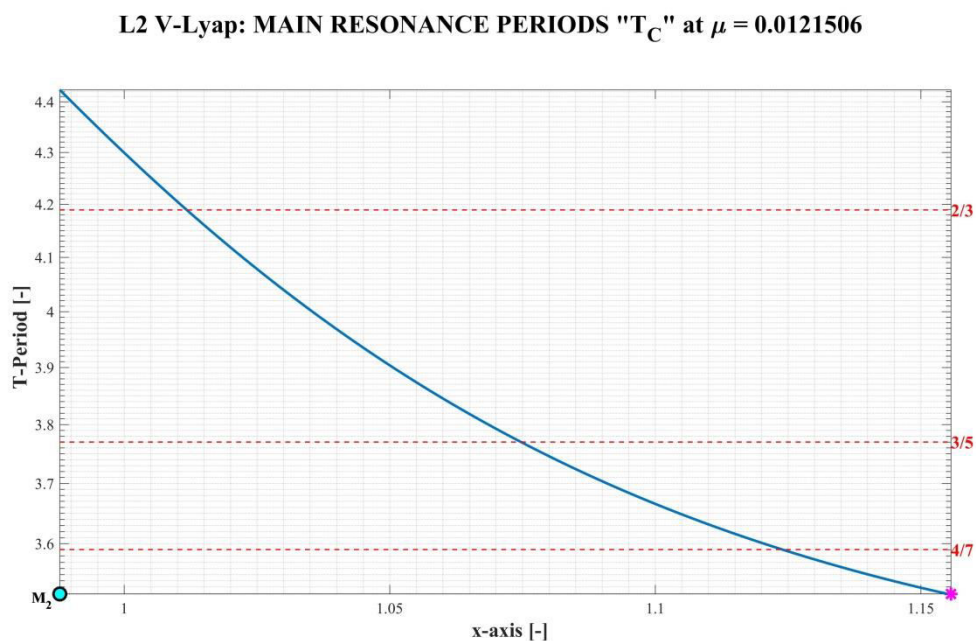


Figure 50: Main resonance orbits existing within the family are given using combinations of M -value (orbit revolutions) and N -value (system revolutions), with $M_{max} = 12$ and $N_{max} = 4$. The system 2π -period is given by $N = 1$, while more details can be found later in Section 4.4.1.

3.5.2 Final comment on the family results

The **Vertical Lyapunov family** has been generated starting from L2, thus extending it to M2 with a total of 1787 members. The propagation has stopped since last orbit has reached the x_2 -value (of M_2), while in the figure below we provide an image of the Phase-space of shooting conditions where both crosses have been considered (for $t_0 = 0$ and $t_0 = T_C/2$). The color-notation for each order-of-instability is described in the LEGEND.

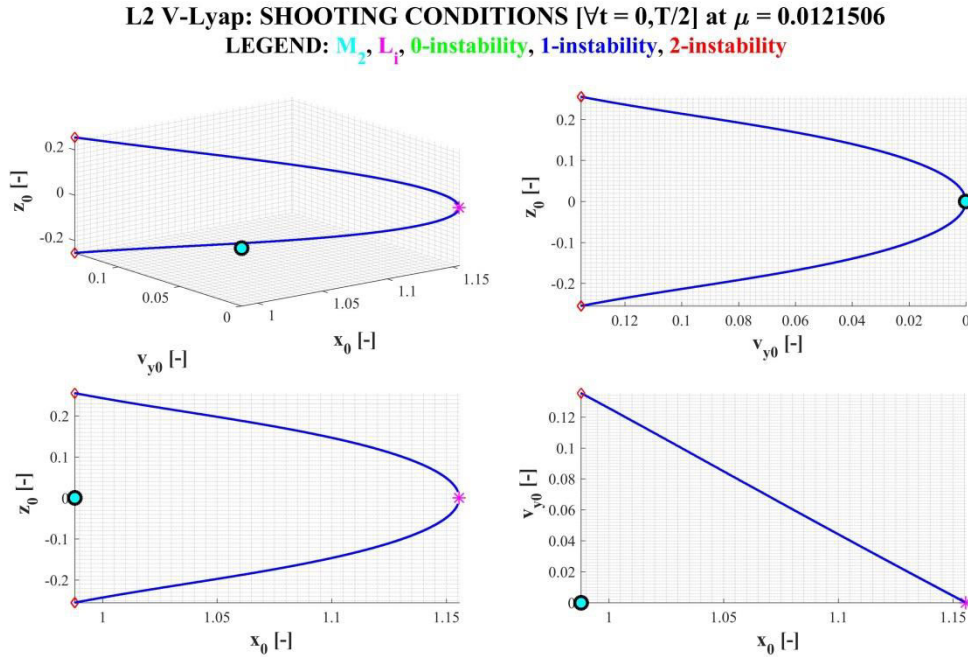


Figure 51: Set of shooting conditions at both $\hat{x}\hat{z}$ -plane crossings [$t_0 = 0, T_C/2$] with the relative order of instability. Look at the LEGEND for information on the color-notation adopted.

FINAL COMMENT

The orbital period T_C increases monotonically far from the L-point, thus spanning a range approximatively between 3.5192 and 4.4234 (in non-dimensional units), and consequently between around 15.30 and 19.24 days. Order of instability is always constant and equal to the I-order, while at the very end of this family we have a bifurcation very close to the x -location of M_2 (where the algorithm stops). This last is again a Tangent-Bifurcation, as demonstrated in Figure 48, and again related to the **Axial family**, which actually exists at all collinear libration points. (Doedel et al., 2007)

Even if not really evident in the 3D plot, V-Lyapunov orbits are expected to be very elongated along the \hat{z} -direction, where indeed the last orbit (Figure 45, in black) is located ‘above’ the Moon at $z_0^{END} \cong 0.2554$, meaning more than 98000 km out-of-plane. This orbits have been studied in (Vermeiden, 2014) in relation to the OLFAR mission, so we refer to that Master thesis for some more details, while many additional graphics plots of the extended family can be found in (Doedel et al., 2007), where all five Lagrange points have been considered, thus highlighting the principal bifurcation points.

3.6 The Halo family at L2

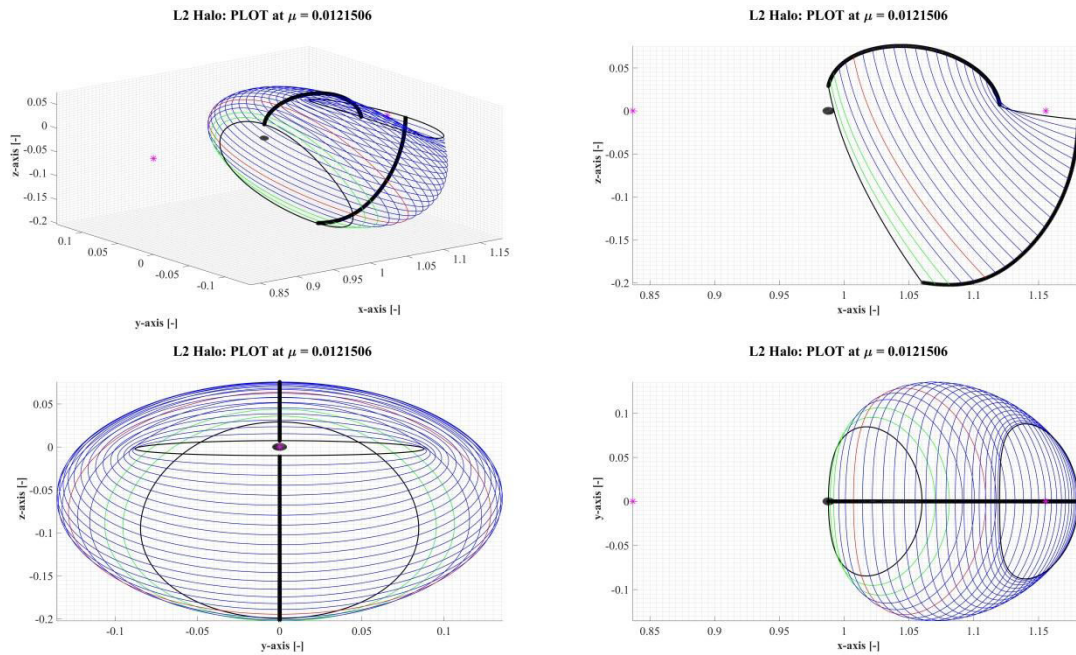


Figure 52: Graphical plot of the Halo family of periodic orbits, every 50 members with their relative order of stability (0-green, 1-blue, 2-red). It also shows the Moon (Grey), the L-points (magenta star), shooting conditions (black dots) and last orbit (black line).

3.6.1 Proprieties and main bifurcations

The Orbital Period (T) and Orbital Energy (J) are here shown in magenta for each member of the family. In addition, using the Jacobi constant, the Energy-error in the integration along each orbit is given as *mean value* (blue) and *standard deviation* (red).

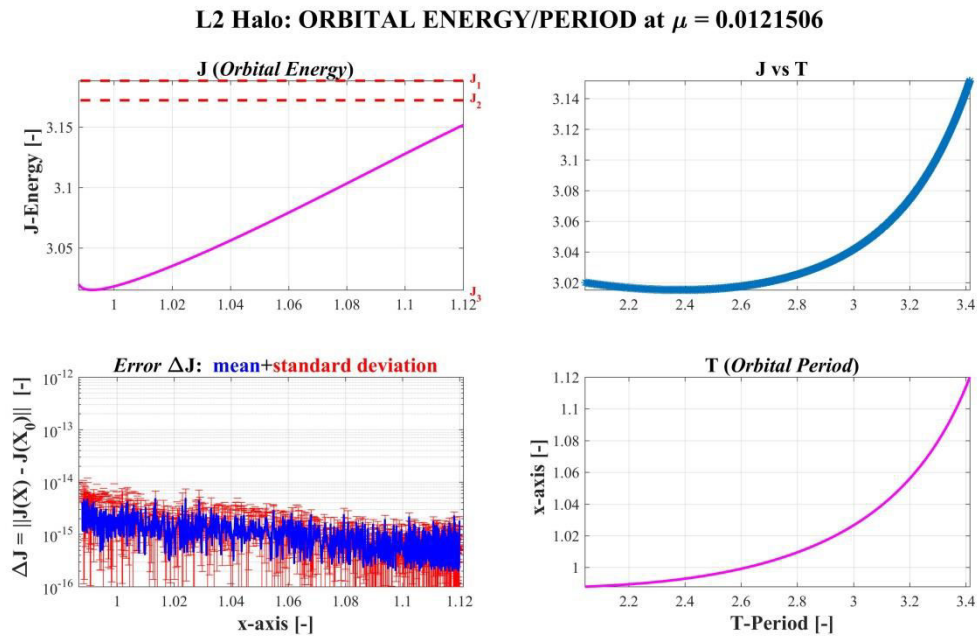


Figure 53: Graphical representation of orbital energy “J” (Top-Left), with its error along each trajectory (Bottom-Left) based on mean and standard deviation. Last, the Orbital Period “T” (Bottom-Right) is shown also compared with the same orbital energy (Top-Right).

The analysis of the Monodromy matrix and its eigenvalues λ_i (characteristic multipliers) is here shown focusing on different orders of instability, eigenvalues module with a zoom at its boundary value (10^{-3}) adopted to define λ_i still “lying on” the unit circle. Note that the error on the "Det(M)" has been found after using directly the MATLAB *det*-function (in blue) or also using the product of eigenvalues (in orange).

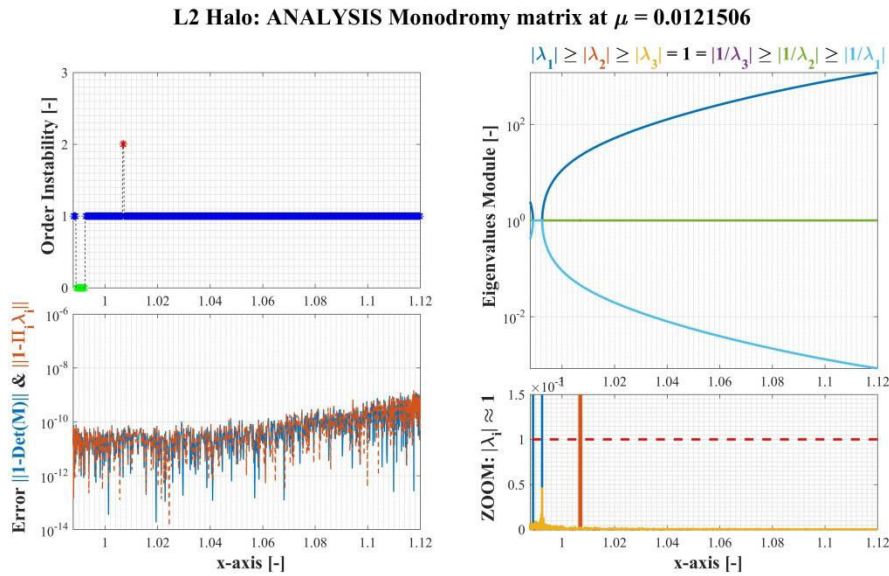


Figure 54: Analysis on the Monodromy matrix, showing on the Left the orders of instability (0-green, 1-blue, 2-red) and the error on the determinant, as described in Section 2.2.4. On the Right, the module of all six “characteristic multipliers” is shown, with a zoom on the threshold value used for calculating the order-of-instability (Right-Bottom).

The following plot shows more in details the eigenvalues’ behaviour in the generation of the family, separating each “pair” due to the Symplectic propriety (Section 2.2.3). Main parameters and considerations will be given later in the *Final comment* section.

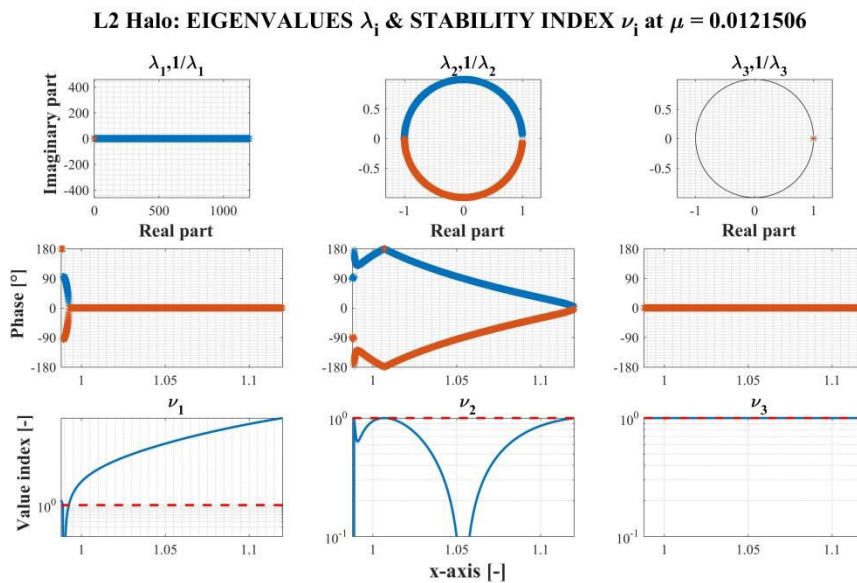


Figure 55: Illustration of eigenvalues λ_i and stability indices $\nu_i = |\lambda_i + \lambda_i^{-1}|/2$, given for each pair of reciprocal value. Motion on complex plane (Top), relative phase (Middle) and Stability Index (Bottom) are shown and they will be explained in the *Final comment* section.

3.6.1.1 Verification and Validation

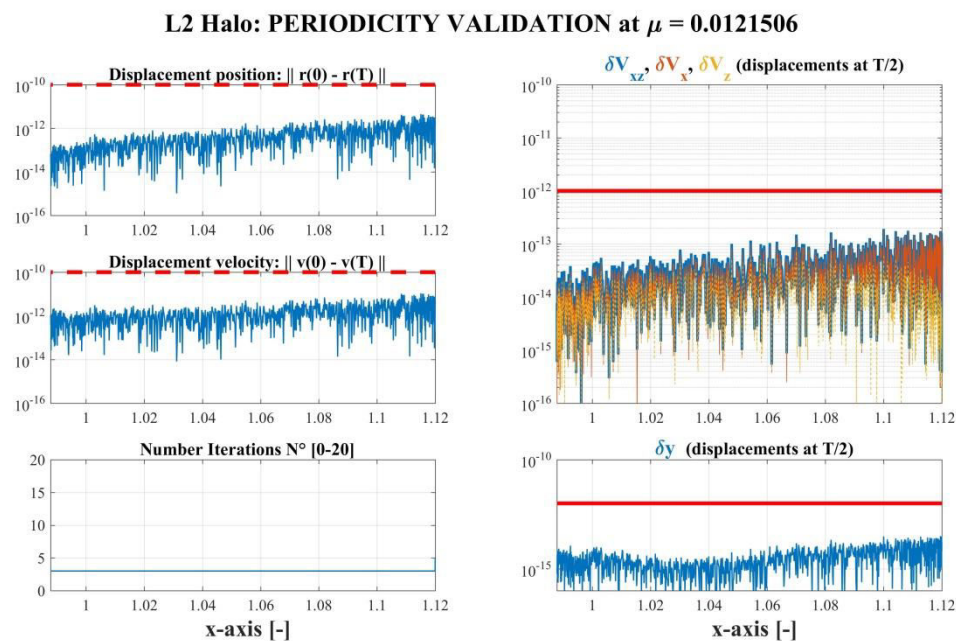


Figure 56: Illustration of the Validation and Verification performed during the numerical continuation process. All relative information and notation can be found in the Section 2.4.2 .

3.6.1.2 Existing “resonance orbits”

The location of few main resonance orbits within the family is here shown, based on the ratio N/M with M number of orbit-revolutions and N number of system-revolutions, limited to $N \leq 4$ and $M \leq 12$. It follows a period $T_C = 2\pi \cdot N/M$ as explain in Section 4.4.1.

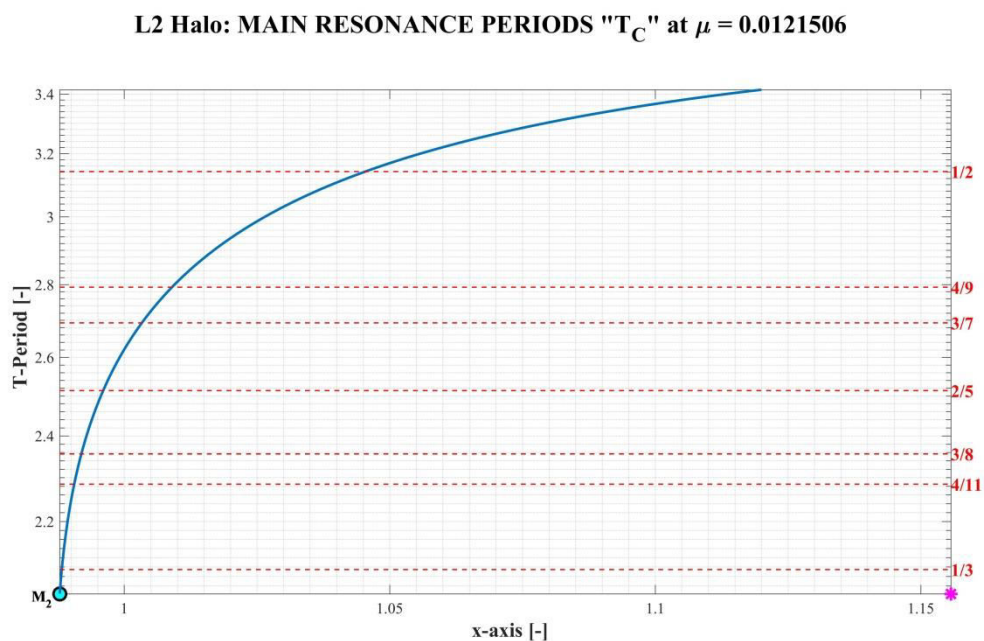


Figure 57: Main resonance orbits existing within the family are given using combinations of M -value (orbit revolutions) and N -value (system revolutions), with $M_{max} = 12$ and $N_{max} = 4$. The system 2π -period is given by $N = 1$, while more details can be found later in Section 4.4.1.

3.6.2 Final comment on the family results

The **Halo family** has been generated starting from L2, thus extending it to M2 with a total of 1142 members. The propagation has stopped since last orbit has reached the x_2 position of M_2 , while in the figure below we provide an image of the Phase-space of shooting conditions where both crosses have been considered (for $t_0 = 0$ and $t_0 = T_C/2$). The color-notation for each order-of-instability is described in the LEGEND.

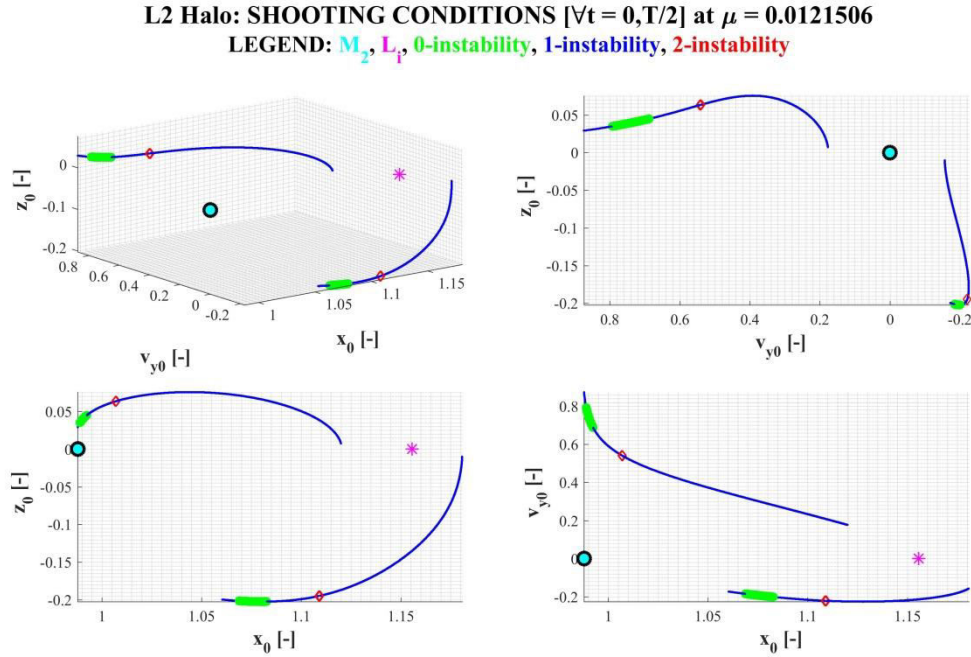


Figure 58: Set of shooting conditions at both $\hat{x}z$ -plane crossings [$t_0 = 0, T_C/2$] with the relative order of instability. Look at the LEGEND for information on the color-notation adopted.

FINAL COMMENT

The orbital period T_C decreases monotonically far from the L-point, thus spanning a range approximatively between 2.0433 and 3.4149 (in non-dimensional units), so as consequence between around 8.88 and 14.8493 days. As for the Halo at L1, we have a zone with a II^o-order instability involving only 4-5 members at around $x_0^B \cong 1.007$, so covering a small range of around 150 km. The latter however is related to a Period-Doubling Bifurcation as eigenvalues “escape” from the unit circle at -1 (see Section 2.2.5), and it is surprising to see a very similar result also for the CR3BP studied in (Howell & Campbell, 1999). In particular, they show for the Halo at L2 a subsequent Fold-Bifurcation and again a Period-Doubling one, in the very similar way as given by the computed phase of λ_2 in Figure 55. This is not the only confirmation of our results, based on similar methodologies, as also in (Breakwell, 1979) they noted that “the L2 family shrinks in size as it approaches the Moon, becoming stable again shortly before penetrating the lunar surface”. Obviously, as stated before, the analysis here performed is not extended till the lunar surface or beyond its x -location (x_2), but it offers a very valid sketch of each family behaviour (at least within small μ -variations), useful for a later extension to the elliptic case, not performed in those papers. We refer to (Howell & Campbell, 1999) for a very nice comparison of the investigation over Halo orbits, even if based on a different system, while very remarkable is the catalogue of several families in the extensive study (on a very large μ -range), presented in (Doedel et al., 2007).

3.7 Conclusive discussion on results

Three main families around L1 and L2 in the Earth-Moon system have been investigated so far in this Chapter 3, while here we simply further discuss some aspects, in particular related to bifurcations existing in each one of these six cases. In fact, in a x -range between the L-point and M2 (here the Moon) we have observed many changes in the order-of-instability, while using the analysis on eigenvalues it has been possible to define the type of each bifurcation, based on what has been explained in Section 2.2.5.

In Table 3, the list of these bifurcations is shown considering a family (**Fam**), the number of orbits within the family (**N°**), the order of instability (**OI**) with the member (**Me**) where it changes. Then, for all these last orbits, types of bifurcation (**Type**) as Tangential-Bifurcation [**T-B**], Period-Doubling [**P-D**] and Krein-Collision [**K-C**] have been given with the respective non-dimensional shooting coordinates $\{x_0^{BIF}, z_0^{BIF}, v_{y0}^{BIF}\}$. Note that these values are provided up to the 15th decimal in order to allow future studies comparing these results, but the reader should carefully consider all settings and methodologies as explained in Section 2.4, as also in both Appendices-A/B.

Table 3: Detailed data related to bifurcations points and order-of-instability within each one of the three families investigated at L1/L2 libration points in the dynamics of the CR3BP for the Earth-Moon system. For the notation adopted, the reader is referred to the text above.

| Fam | N° | OI | Me | Type | x_0^{BIF} | z_0^{BIF} | v_{y0}^{BIF} |
|--------------------|-------------|-----|------|------|-------------------|-------------------|--------------------|
| H-L L1 | 887 | I | 109 | T-B | 0.854746068332264 | 0 | -0.133372161705627 |
| | | II | 611 | T-B | 0.930515109540220 | 0 | -0.603318504951302 |
| | | I | 806 | P-D | 0.959947306822195 | 0 | -0.935511886340790 |
| | | II | | | | | |
| H-L L2 | 899 | I | 201 | T-B | 1.120421768004934 | 0 | 0.175872005992750 |
| | | II | 742 | T-B | 1.029624211956750 | 0 | 0.724089536008752 |
| | | I | 828 | P-D | 1.015190589368683 | 0 | 0.926762357699208 |
| | | '?’ | | | | | |
| V-L L1 | 2044 | I | 1605 | T-B | 0.922240504670069 | 0.239946985133986 | -0.065278557049110 |
| V-L L2 | 1787 | I | 1784 | T-B | 0.988085224026283 | 0.255170595137716 | 0.135229358005970 |
| | | II | | | | | |
| Halo L1 | 1259 | I | 953 | P-D | 0.957063987485636 | 0.081910490155745 | -0.450741645058225 |
| | | II | 960 | P-D | 0.958058233074258 | 0.081549999736737 | -0.454183971737394 |
| | | I | | | | | |
| Halo L2 | 1142 | I | 899 | P-D | 1.007309771070823 | 0.063626789517973 | 0.539125695884842 |
| | | II | 903 | P-D | 1.006781668335796 | 0.063209547140279 | 0.542335262224073 |
| | | I | 1042 | T-B | 0.992517674589760 | 0.045042269428916 | 0.686370335822180 |
| | | 0 | | | | | |
| | | I | 1106 | P-D | 0.988990905929304 | 0.034926868166713 | 0.792858036634374 |

* note the '?’-symbol, due to the uncertainty as described in Section 3.4.2

Main results have been discussed in each relative section, while in Table 3 bifurcations have been summarized more in details. At this point, before proceeding with the introduction of the Elliptic problem (extension from the circular case), few additional aspects require some considerations.

First of all, in agreement with most of the mentioned literature, no Krein-Collision exists within those families, at least in the limit of our propagation from each L-point till the Secondary mass M2. Only uncertainty is given for the last bifurcation of Horizontal Lyapunov orbits at L2, but from the trend shown in Figure 41 (eigenvalue's phase), it seems plausible to have a Period-Doubling bifurcation as it is approaching the real value -1 , right before leaving the unit circle. It follows that no new family of periodic solutions can be found in that neighbourhood.

Also important to be mentioned is the presence of one bifurcation for Vertical Lyapunov and two bifurcations for the Horizontal Lyapunov, in agreement with recent literature. These two are related respectively to the Halo orbit as discussed in Section 2.3.2.3, and to the Axial one that connects both Vertical and Horizontal families. In addition, also at L1 the Halo family stops right before the bifurcation related to the W4/5-family in connection with V-Lyapunov orbits at $L_{4/5}$ -points, as described in (Doedel et al., 2007).

Last, the bifurcation in the Halo at L2 before the “Spectral Stable” green area (with all eigenvalues lying on the unit circle), is actually a Tangent-Bifurcation that has been studied for the Sun-Earth/Moon system in (Howell & Campbell, 1999). As stated, “*every local extremum of the Jacobi Integral, where the order of instability changes, indicates a cyclic-fold bifurcation.*” At the 1042th member of this family, we have indeed a minimum of the energy shown in Figure 53 with a value as $J_C^{MIN} = 3.01517762183665$, and consequently it is related to a so-called **Cyclic-Fold Bifurcation**, where all four eigenvalues $\lambda_1, \lambda_1^{-1}, \lambda_3, \lambda_3^{-1}$ are real and equal to $+1$, as illustrated in Figure 55. Again as discussed in (Howell & Campbell, 1999), for periodic solutions in the CR3BP, “*the cyclic-fold bifurcation represents only a change of instability of the family and no new periodic solutions exist; the only qualitative change is in the order of instability*”. This also explains why this bifurcation has not been mentioned in (Doedel et al., 2007), where the investigation has been focused only on new families of general periodic orbits, thus without taking into account possible Period-Doubling bifurcations.

Let's now proceed with the theory concerning the Elliptic problem, where main interest is now focused on resonance orbits and changes in their linear stability (order-of-stability). All the discussion refers to the eccentricity parameter, while bifurcations within the family itself are not studied from the moment that periodic solutions do not arise anymore in continuous family, as previously seen for the circular case (see Section 4.2.3).

4

ER3BP: Analysis and Methods

In this Chapter 4 we consider the Elliptic Restricted 3-Body Problem (ER3BP). First, in Section 4.1 we present main aspects of the dynamical model in comparison to what has been shown for the Circular problem (Section 2.1). Hence, in Section 4.2, the Dynamical System Theory (DST) is given for what concerns the elliptic case, so further exploiting Floquet Theory in order to study the linear stability. Last, both Sections 4.3-4.4 focus respectively on Analytic and Numeric methodologies, as evolution of main techniques adopted for the circular case. Both approaches will involve mainly “resonance orbits”, as one of the most critical aspects of the ER3BP dynamics.

4.1 Introduction to the Elliptic problem

The Elliptic problem is a much more complete dynamical model able to well describe the motion of a small mass m_3 in the gravitational field produced by two principal masses (again the Primary M_1 and Secondary M_2). In Section 2.1, we have defined four different formulations for the restricted problem ($m_3 \ll M_1, M_2$), all dependent upon the positive e -parameter (also defined as eccentricity). Consequently for the elliptical case we are able to re-consider all assumptions made so far for the ‘standard’ CR3BP, but this time we will describe the Kepler motion of P_1 - P_2 considering a non-zero eccentricity in Eq. (2-1), such that $e \in (0,1)$. ([Szebehely, 1967](#))

Under this perspective, it is straightforward to understand how the previous Circular problem can be simply be considered as a particular case, setting $e = 0$ in the dynamical model of the ER3BP. The latter is fully justified by the continuous character of equations respect to the e -parameter ([Bennett, 1965](#)), while it will be shown later how this dynamic changes radically when $e \geq 1$. For this last case, both principal masses are constrained in an unbounded motion and trajectories for P_3 are mostly unlikely periodic solutions. In a very recent study ([Barrabés, Cors, & Ollé, 2015](#)) over the so-called Parabolic problem (PR3BP) for $e = 1$, it has been asserted that periodic orbits cannot exists at all, differently from what it will be shown later in Section 4.1.4.

Once again, test-case selected is the Earth-Moon system having $e = 0.0549$, while the entire discussion given in Section 2.1.3 on additional perturbations is still valid. In fact, they could be used in future works also for this elliptic case, thus improving the ‘standard’ dynamical model (ER3BP) here analysed. At this point, we continue providing the definition of this new dynamical model within some suitable reference frames.

4.1.1 Dynamical model and reference frame

The dynamics of the Elliptical Restricted 3-Body Problem (ER3BP) has been studied by many authors in the past few years, using different reference frames in order to describe the problem mathematically in the most efficient way possible. Well-known reference frame usually adopted has been provided in (Szebehely, 1967), using Pulsating synodic coordinates, as it will be shown later. However, here we decide to proceed gradually, so starting by a very similar reference system as the one adopted for the CR3BP: the synodic frame (Figure 2), co-rotating with both the Primary M_1 and the Secondary M_2 . Its origin is fixed at the barycentre, while the mass m_3 (e.g., the satellite) is once again neglectable and has no consequences on the Kepler motion (elliptical) of the two principal masses. An illustrative example is shown in the following Figure 59.

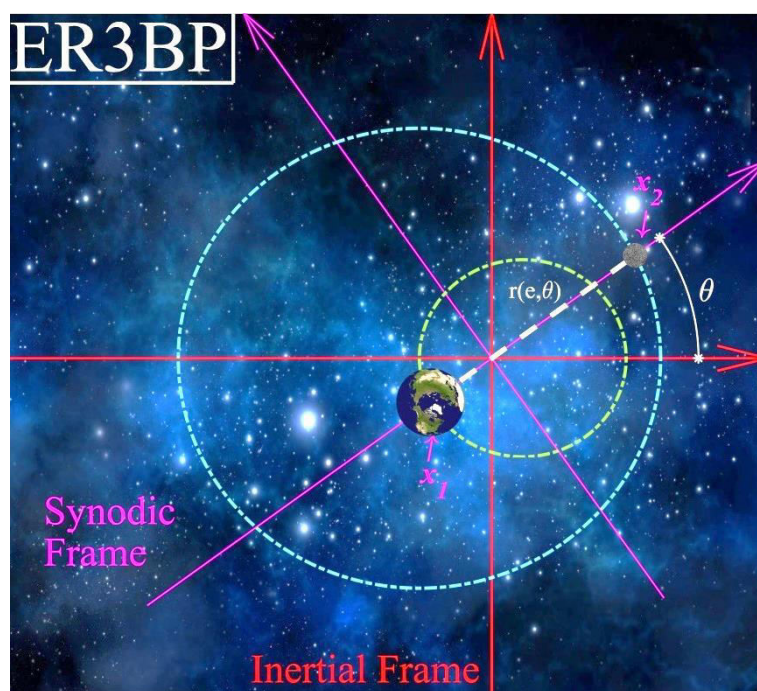


Figure 59: Illustration of both inertial (red) and synodic frames (magenta) for the Elliptical Restricted 3-Body Problem, with distances x_1, x_2 referring to the position of M_1, M_2 along the syzygy. In white, the θ -phase is shown starting from the peri-apsis, while also $r = r(e, \theta)$ is shown as time-dependent relative distance between both masses, as described in Eq. (2-1).

At this point we can use Eq. (2-2) to define²⁶ the dynamics of P_3 in what it is known to be a time-varying gravitational field. Main characteristics and proprieties of the 2-Body Problem (associated to M_1-M_2) have been omitted here since very well-documented in common literature or textbooks as (Goldstein et al., 2002). However, very first difference within the Elliptic problem is this new “oscillation” in the synodic co-rotating frame of both the two masses, such that their position along the syzygy direction can be found from the definition of centre of mass. Their expression follows as

$$x_1 = -r \cdot \xi_2 \quad \& \quad x_2 = +r \cdot \xi_1 \quad (4-1)$$

with r relative distance ($M_2 \xrightarrow{w.r.t.} M_1$) of Eq. (2-1) and $\xi_i = M_i/M_{TOT}$ ratio between masses.

²⁶ Note that here we are still considering a ‘dimensional’ system, and only later it will be adimensionalize, as performed for the Circular problem at page 5.

Three second-order non-linear differential equations follow from Eq. (2-2), such that

$$\frac{d^2}{dt^2} \begin{pmatrix} x \\ y \\ z \end{pmatrix} = -\mu_1 \cdot \frac{\mathbf{r}_{13}}{r_{13}^3} - \mu_2 \cdot \frac{\mathbf{r}_{23}}{r_{23}^3} - \begin{pmatrix} -2\omega\dot{y} \\ +2\omega\dot{x} \\ 0 \end{pmatrix} - \begin{pmatrix} -\omega^2 x \\ -\omega^2 y \\ 0 \end{pmatrix} - \begin{pmatrix} -\alpha y \\ +\alpha x \\ 0 \end{pmatrix} \quad (4-2)$$

with the notation for the P_3 -position as $x = x_3, y = y_3, z = z_3$, while $\mu_i = GM_i$ and r_{i3} are respectively the *planetary mass* of each i -mass and the relative distance of P_3 from them. From now on, the dot-notation will be used only for referring to the derivative respect the physical time t , while the frame rotates non-uniformly as $\omega = d\theta/dt$. The parenthesis terms on the right side of Eq. (4-2) are respectively the Coriolis, the Centrifugal and last, the so-called *Euler force*, in this case non-zero since ω is no more constant. Value for both the r_{i3} -distances is given based on Eq. (4-1), thus leading to

$$r_{i3} \stackrel{\text{def}}{=} r_i = \begin{bmatrix} x - x_i \\ y \\ z \end{bmatrix} = \begin{bmatrix} x \pm r \cdot \xi_i \\ y \\ z \end{bmatrix}, \forall i = 1,2 \quad (4-3)$$

As described in Eq. (2-1), we can well define time-dependent parameters in the Eq. (4-2), such that $\alpha = \alpha(\theta)$ is the angular acceleration and θ is the relative phase (see Figure 59) between masses starting at the peri-apsis of the Kepler motion ($\forall \theta_0 = 0$). As described in the Literature Study²⁷, also given in (Goldstein et al., 2002), we can write $\omega(e, \theta)$ as

$$\omega = \frac{d\theta}{dt} = n \cdot \frac{(1 + e \cdot \cos \theta)^2}{(1 - e^2)^{\frac{3}{2}}} \quad (4-4)$$

with n mean motion given in Eq. (2-3), thus the angular acceleration $\alpha(e, \theta)$ is defined as

$$\alpha = \frac{d\omega}{dt} = \frac{d^2\theta}{dt^2} = \psi \cdot \omega^2, \quad \forall \psi = \frac{-2e \cdot \sin \theta}{1 + e \cdot \cos \theta} \quad (4-5)$$

using $\psi = \psi(e, \theta)$ as auxiliary variable. As seen in Section 2.1.1, all equations of motion can be written in a non-dimensional form, where time-space-mass have been set as

- SPACE [km]: $a = 1$
- MASS [kg]: $M_{TOT} = M_1 + M_2 = 1$
- TIME [1/s]: $n = 1$

leading to $G/n^2 = 1$ and with a main orbital period again as $T = 2\pi$. Differently from the Circular problem, here masses are oscillating in time along the x-axis with impressive effects on the dynamics, as later extensively explain in Section 4.2. In order to present the non-dimensional differential system, we will make use again of $\mu = M_2/M_{TOT}$ where we have that $\xi_1 = 1 - \mu, \xi_2 = \mu$. A brief discussion on some time-related aspects is necessary, for example relative to a possible *time-rescaling* of the previous equations. (Perko, 2001)

²⁷ This is a result of the conservation of the angular momentum for the 2-Body Problem, as also defined by the so-called *Third Kepler's Law*. See (Murray, 1999) for more details.

From Eq. (4-4) it is possible to define the mathematical relation between the physical time t and the θ -phase, such that starting with both $t_0, \theta_0 = 0$ we obtain²⁸

$$t = \frac{1}{n} \cdot \left\{ 2 \cdot \operatorname{atan} \left(\sqrt{\frac{1-e}{1+e}} \cdot \tan \left(\frac{\theta}{2} \right) \right) + \frac{\psi}{2} \cdot \sqrt{1-e^2} \right\} \quad (4-6)$$

Clearly, for $e = 0$ we have that $\theta = nt$, in agreement with what seen for the circular case, while now the differential system can be expressed in the non-dimensional form as

$$\begin{aligned} \ddot{x} &= -(1-\mu) \cdot \frac{x+r \cdot \mu}{r_1^3} - \mu \cdot \frac{x-r \cdot (1-\mu)}{r_2^3} + 2\omega \dot{y} + \omega^2 x + \psi \omega^2 y \\ \ddot{y} &= -(1-\mu) \cdot \frac{y}{r_1^3} - \mu \cdot \frac{y}{r_2^3} - 2\omega \dot{x} + \omega^2 y - \psi \omega^2 x \\ \ddot{z} &= -(1-\mu) \cdot \frac{z}{r_1^3} - \mu \cdot \frac{z}{r_2^3} \end{aligned} \quad (4-7)$$

$$\begin{aligned} r_1 &= \sqrt{(x+r \cdot \mu)^2 + y^2 + z^2} \\ r_2 &= \sqrt{(x-r \cdot (1-\mu))^2 + y^2 + z^2} \end{aligned} \quad (4-8)$$

with all variables previously defined, as also for the dot-notation (meaning d/dt).

4.1.1.1 Time re-scaling respect to a new time-like “ θ -parameter”

We are dealing with a motion based on three second-order differential equations in the physical time t . However, once converting Eq. (4-7) into a first-order system, we can also obtain 1+6=7 differential equations combining Eq. (4-4) and Eq. (4-7). Here, $\theta = \theta(t)$ is the additional t -dependent variable for a new state-vector $\mathbf{X}^* = \mathbf{X}^*(t)$, while based on the *chain's rule*, we are able to transform the time-derivative of a general variable \mathbf{Q} as

$$\frac{d\mathbf{Q}}{dt} \triangleq \frac{d\mathbf{Q}}{d\theta} \cdot \frac{d\theta}{dt} = \frac{d\mathbf{Q}}{d\theta} \cdot \omega(\theta) \quad (4-9)$$

that for the circular case is reduced to a simply time-rescaling, since $\omega = n$ is constant. With Eq. (4-9) the differential system involves again a six-dimensional state-vector $\mathbf{X} = \mathbf{X}(\theta)$, where the aforementioned θ -phase becomes the new time-like parameter ([Perko, 2001](#)). A similar transformation holds for all orders of derivatives in Eq. (4-7), and new velocities can be defined at this point as $u_q, \forall q = \{x, y, z\}$, such that

$$v_q = \frac{dq}{dt} \triangleq \frac{dq}{d\theta} \cdot \omega(\theta) = u_q \cdot \omega(\theta) \quad \text{with} \quad u_q = \frac{dq}{d\theta} \quad (4-10)$$

²⁸ The result can be simply shown using the Leibniz's notation (or *chain's rule*), in such way that it becomes necessary to analytically solve an *elliptical integral* ([Jordan & Smith, 2002](#)), so having

$$\frac{d\theta}{dt} = \omega(\theta) \quad \xrightarrow{\text{it follows that}} \quad t - t_0 = \int_{t_0}^t dt = \int_{t_0}^t \frac{d\theta}{\omega(\theta)}$$

The new differential system is now completely dependent on the θ -parameter, while the physical time t is “*intrinsically*” bounded within the problem through Eq. (4-6). Referring to this reference system as “No-Pulsating”, we are able to re-write Eq. (4-7) as²⁹

$$\begin{aligned} x'' + \psi x' &= -(1 - \mu) \cdot \frac{x + r \cdot \mu}{\omega^2 \cdot r_1^3} - \mu \cdot \frac{x - r \cdot (1 - \mu)}{\omega^2 \cdot r_2^3} + 2y' + x + \psi y \\ y'' + \psi y' &= -(1 - \mu) \cdot \frac{y}{\omega^2 \cdot r_1^3} - \mu \cdot \frac{y}{\omega^2 \cdot r_2^3} - 2x' + y - \psi x \\ z'' &= -\frac{z}{\omega^2} \cdot \left[\frac{(1 - \mu)}{r_1^3} + \frac{\mu}{r_2^3} \right] \end{aligned} \quad (4-11)$$

where both members have been divided by ω^2 , having $\omega \neq 0, \forall \theta$ if $e < 1$. For both r_1, r_2 it holds the very same expression given in Eq. (4-8), while the apostrophe symbol will always be adopted as notation for the derivative respect to θ .

Theoretically, at this point we have obtained the full dynamical model of the ER3BP, again defined by a non-linear differential system in the new time-like θ -variable, but dependent also upon two parameters: the eccentricity e and the mass-ratio μ . After setting $e = 0$, it follows that $r = 1, \omega = 1, \psi = 0$ and the system becomes exactly the same one given in Eq. (2-5), so in perfect agreement with the Circular problem. However, determination of Lagrange points seems to be more complex now, and based on their definition (see Section 2.1.2), we are supposed to solve the following system

$$\begin{cases} x - \frac{1}{\omega^2} \cdot \left[(1 - \mu) \cdot \frac{x + r \cdot \mu}{r_1^3} - \mu \cdot \frac{x - r \cdot (1 - \mu)}{r_2^3} \right] + \psi y = 0 \\ y \cdot \left[1 - \frac{1}{\omega^2} \cdot \left(\frac{(1 - \mu)}{r_1^3} - \frac{\mu}{r_2^3} \right) \right] - \psi x = 0 \end{cases} \quad (4-12)$$

that is dependent upon the θ -variable, while $x', y', z' = 0$ and having again that $z = 0$. A precise solution seems difficult to be found, and most likely its expression is time varying from the moment that masses (and their gravitational potential) are now oscillating. On the other hand, it is important to consider also that in the CR3BP Lagrange points do not really exist in an inertial frame, based on the proper definition of “critical point” in the Phase-space, as given in Section 2.2.1.1. Hence, similarly to (Szebehely, 1967), we are going to define a new reference frame, also denoted as “Pulsating”.

4.1.1.2 Pulsating reference frame for the ER3BP

The complete transformation from an initial “No-Pulsating” system in Eq. (4-11) to the “Pulsating” one in Eq. (4-15) is here not given, but can be retrieved with a straightforward application of following relations in Eqs. (4-13)(4-14). With few additional manipulations, the final expression has been obtained (using “Maple 2016” software) and later it has been verified with some general literature, again as (Szebehely, 1967).

²⁹ In red all additional terms coming from the re-scaling of the second derivative, such that

$$\begin{aligned} \frac{dq^2}{dt^2} &= \frac{d}{dt} \left(\frac{dq}{d\theta} \cdot \frac{d\theta}{dt} \right) = \frac{d}{dt} \left(\frac{dq}{d\theta} \cdot \omega \right) = \frac{d}{d\theta} \left(\frac{dq}{d\theta} \cdot \omega \right) \cdot \omega \\ &= \frac{dq^2}{d\theta^2} \cdot \omega^2 + \frac{dq}{d\theta} \cdot \omega' \cdot \omega = \left[\frac{dq^2}{d\theta^2} + \frac{dq}{d\theta} \cdot \psi \right] \cdot \omega^2 \end{aligned}$$

From this previous adimensionalization, all distances have been scaled by a constant parameter a , semi-major axis of the relative orbital motion of M_2 respect M_1 . Major idea is to re-scale equations using $r(\theta)$, the θ -dependent distance between M_1 - M_2 , such that

$$X = \frac{x}{r(\theta)}, \quad Y = \frac{y}{r(\theta)}, \quad Z = \frac{z}{r(\theta)} \quad \xrightarrow{\text{so having}} \quad \begin{cases} R_1 = r_1/r(\theta) \\ R_2 = r_2/r(\theta) \end{cases} \quad (4-13)$$

As consequence, the entire system is now *pulsating* in time, defined by the θ -variable. However, the definition for the P_3 -velocity is also changed, and starting with a general pulsating coordinate $\bar{Q} = \bar{Q}(\theta)$ we have that its θ -derivative expressed in the new frame is

$$V_{\bar{Q}} = \bar{Q}' = \frac{v_q}{r(\theta)} + \bar{Q} \cdot \frac{\psi}{2}, \quad \forall v_q = \frac{dq}{d\theta} \quad (4-14)$$

The final expression for the ‘‘Pulsating’’ system of the ER3BP is summarized as follows

$$\begin{aligned} X'' - 2Y' &= \frac{1}{1 + e \cdot \cos(\theta)} \cdot \left[X - (1 - \mu) \cdot \frac{X + \mu}{R_1^3} - \mu \cdot \frac{X - (1 - \mu)}{R_2^3} \right] \\ Y'' + 2X' &= \frac{Y}{1 + e \cdot \cos(\theta)} \cdot \left[1 - \frac{1 - \mu}{R_1^3} - \frac{\mu}{R_2^3} \right] \\ Z'' &= -\frac{Z}{1 + e \cdot \cos(\theta)} \cdot \left[\frac{1 - \mu}{R_1^3} + \frac{\mu}{R_2^3} + e \cdot \cos(\theta) \right] \end{aligned} \quad (4-15)$$

or in a more compact form following ([H. Peng & Xu, 2015a](#), [2015b](#), [2015c](#)), such that³⁰

$$\begin{cases} X'' - 2Y' = \frac{\partial U_E}{\partial X} \\ Y'' + 2X' = \frac{\partial U_E}{\partial Y} \\ Z'' = \frac{\partial U_E}{\partial Z} \end{cases} \quad (4-16)$$

where we have used the gradient components of a pseudo-potential function U_E , which is dependent upon this pulsating position coordinates, along with the θ -time. The U_E can be related to Ω_C , potential function adopted in Eq. (2-10) for the circular case, so leading to

$$U_E = \frac{1}{1 + e \cdot \cos(\theta)} \cdot \left[\Omega_C - \frac{Z^2 e \cdot \cos(\theta)}{2} \right], \quad \forall \Omega_C = \frac{X^2 + Y^2}{2} + \frac{1 - \mu}{R_1} + \frac{\mu}{R_2} \quad (4-17)$$

³⁰ A different formulation has been originally given in ([Bennett, 1965](#)), with the definition of a pseudo-potential function $\mathcal{V}_E = \mathcal{V}_E(X, Y, Z, \theta)$ with the last equation as $Z'' + Z = \mathcal{V}_{,Z}$, so having

$$\mathcal{V}_E = \frac{1}{1 + e \cdot \cos(\theta)} \cdot \left[\Omega_C + \frac{Z^2}{2} \right]$$

while we will adopt the notation provided in Eq. (4-16), since easily comparable with Eq. (2-10).

4.1.2 Existence of Lagrange points and the new “symmetry constraint”

Differently from (Szebehely, 1967), with his analysis on the planar Elliptic problem, here we consider the full spatial problem. The latter is not based on the notation originally adopted in (Bennett, 1965), but more conveniently the one previously described and also used in (H. Peng & Xu, 2015a, 2015b, 2015c). So far, we have seen that libration points are most likely difficult to find within the No-Pulsating frame, while for such new formulation in Eq. (4-16) there are many similar features with the Circular problem.

The existence of a function U_E , defined “pseudo-potential” since it depends also upon the time-like parameter θ , is without doubt a significant advantage for all our investigation. First of all, in Eq. (4-15) we note that all five libration points can exist and in addition to that, they actually have the exact same numerical value as the one found solving both the Eq. (2-7) for the collinear and the Eq. (2-8) for the equilateral ones (H. Peng & Xu, 2015a, 2015b, 2015c). As consequence of this pulsating reference frame, it means that within the no-pulsating one (still co-rotating with both masses), their position is oscillating in time around some nominal values. For example considering collinear L-points we have

$$x_{L_i} = X_{L_i} \cdot r(e, \theta) \quad \xrightarrow{\forall e \ll 1} \quad x_{L_i} \approx X_{L_i} \cdot [1 - e \cdot \cos(\theta) + \mathcal{O}(e^2)] \quad (4-18)$$

with X_{L_i} numerically computed solving Eq. (2-9). When looking at the Taylor first-order expansion of $r(\theta, e)$ respect to a small eccentricity $e \ll 1$, we can clearly see the periodic oscillation having similar period as the system’s revolution one. It is possible to assume that the Pulsating system, even if physically less intuitive, is most suitable for our analyses, so providing us a clear definition of libration points. Furthermore, the existence of the pseudo-potential function in Eq. (4-16) is remarkably similar to what has been previously observed for the circular case.

4.1.3 Variation in the symmetry: the shooting-time constraint

In comparison with the CR3BP, it is possible now to investigate the possible existence of particular proprieties or symmetries that could help simplifying the inspection over the elliptical case. Looking at Eq. (4-15), it seems clear that all three symmetries still exist in the new system, due to its similar expression with the Circular problem in Eq. (2-5). Another remarkable aspect is related to the “reverse trajectory”, defined in **Theorem 1.2** (with all three possible transformations), but referring now to the θ -variable adopted as new time-like parameter of the differential system.

In the new “Pulsation notation”, evident is the appearance³¹ of time-dependent terms within the vector-function $\mathbf{f} = \mathbf{f}(\mathbf{X}, \theta)$. The latter is one of the most important aspects characterizing the Elliptic problem, while other perturbations in Eqs. (2-17)(2-18)(2-19) as given in Section 2.1.3.1, did not change radically the nature of the differential system (Musielak & Quarles, 2014). In fact, in their expression, there are no explicit time-related terms, while extremely relevant are effects of having a differential system changing in time. This aspect will be extensively discussed with the Dynamical System Theory, while now we provide a new time-constraint related to symmetry for the Elliptic problem.

³¹ In fact, it is possible to observe a term $\cos(\theta)$ in the pseudo-potential function U_E , thus in all three components of its gradient $\nabla = \left[\frac{\partial}{\partial x}, \frac{\partial}{\partial y}, \frac{\partial}{\partial z} \right]$, which is involved in the system. See Eq. (4-16).

As consequence of what previously stated, all transformations involving the time should leave unchanged the equations of motion of the current “Pulsating” notation, as well as in a “No-Pulsating” frame. Using both Eqs. (4-11)(4-15), the reader could trivially proof that a new necessary condition on periodicity requires that

$$\theta_0 = k \cdot \pi \quad , \forall k \in \mathbb{Z} \text{ (integer)} \tag{4-19}$$

where k is either zero or an integer number (positive or negative). Principal reason is related to the existence of a cosine function (*even* function), having a relevant impact on the possible initial condition for periodic orbits (Section 4.4.2). As already seen in Section 2.1.2.2, here we present a numerical simulation of such symmetry, considering a general eccentricity $e = 0.1$ and starting with $\theta_0 = 0$ and $\theta_0 = \pi/3$. Purpose is here only to “qualitatively” illustrate the different behaviour of same shooting conditions adopted in Figure 5, but now integrated for the ER3BP dynamics.

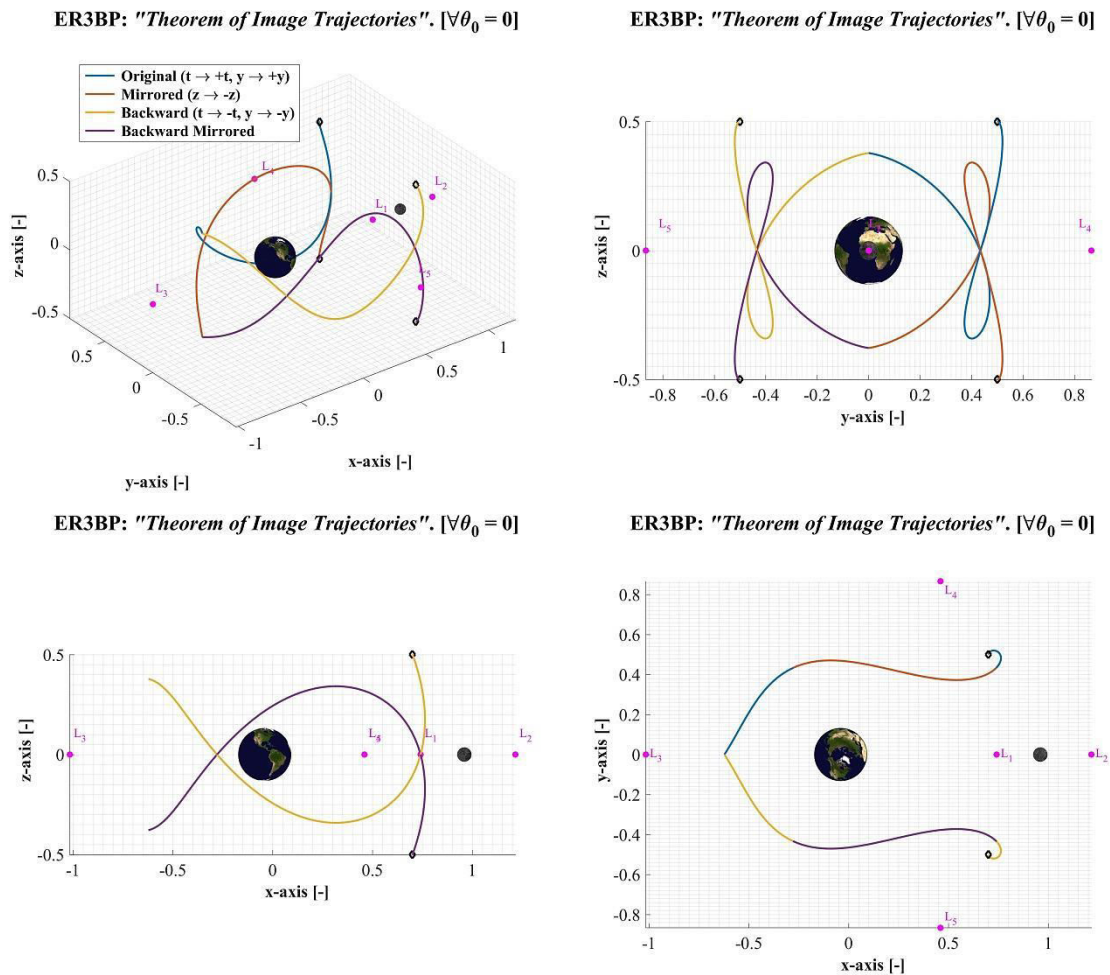


Figure 60: Main three symmetries for the Earth-Moon Elliptical Restricted 3-Body Problem in pulsating synodic coordinates, with $e = 0.1$ and starting at $\theta_0 = 0$. Compare to Figure 5.

As shown in Figure 60, all major three symmetries still hold in the ER3BP, but the trajectory is clearly different from Figure 5, since considering a different dynamical model. In next Figure 61, the same initial conditions have been numerically integrated for the same period, but starting with a different shooting-time given as $\theta_0 = \pi/3$.

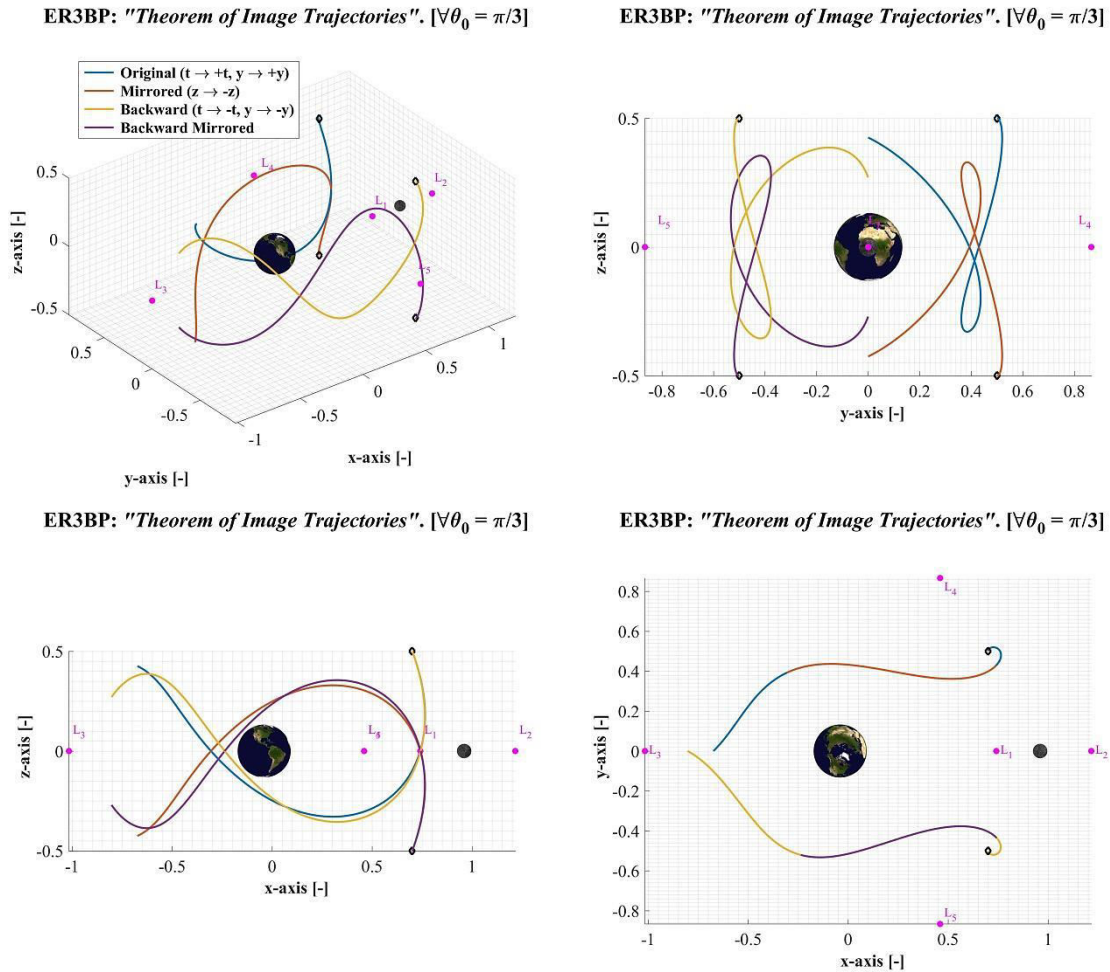


Figure 61: Main three symmetries for the Earth-Moon Elliptical Restricted 3-Body Problem in pulsating synodic coordinates, with $e = 0.1$ and starting at $\theta_0 = \pi/3$. Note the loss of both Backward and Backward-Mirrored symmetries due to the condition given in Eq. (4-19).

Comparing Figure 60 and Figure 61, it is possible to note the breaking of all time-related symmetries (for a Backward and a Backward-Mirrored transformation), while the first type of symmetry (Section 2.1.2.2), involving only the z -variable, still perfectly holds. Further aspects will be treated later in Section 4.4 (“Numerical Approach”), while we proceed now with few considerations on possible First Integrals of motion in the ER3BP.

4.1.4 The non-existence of First Integrals

In Section 2.1.2.1 we have introduced the Jacobi constant, only First Integral for the Circular problem, thus logical is to questioning wherever there are similar quantities also for the elliptic case. In (Contopoulos, 1966), considering a “potential periodic in time”, a so-called ‘third’ integral of motion can be found, so named in order “to distinguish it from the classical energy and angular momentum integrals”. Later, its results were extended by (Sarris, 1982) for a three dimensional ER3BP, but considering both a small eccentricity and small distance from principal masses (studying planetary orbits). Moreover, it has been previously shown that the Jacobi constant can somehow be related to the P_3 -Energy, mostly due to the fact that in Hamiltonian time-independent systems the Hamiltonian-Energy is being conserved. (Goldstein et al., 2002)

Briefly starting with Eq. (4-16) and after few manipulations and we are able to define³², in agreement with (S. Campagnola, Lot, & Newton, 2008), a particular relation as follows

$$\frac{V_{(\theta)}^2 - V_0^2}{2} = U_E(\theta) - U_{E0} - \int_{\theta_0}^{\theta} \frac{\partial U_E}{\partial \theta} d\theta \quad (4-20)$$

where U_{E0}, U_E are respectively the pseudo-function evaluated at θ_0, θ , as also for V_0, V scalar velocity ($V^2 = V_X^2 + V_Y^2 + V_Z^2$). It follows an expression for $J_E = J_E(\theta)$, here named as “Elliptic-Jacobi integral”, which is dependent upon the θ -variable and consequently not really considered as First Integral of Motion³³, such that

$$J_E(\theta) = V_{(\theta)}^2 - 2U_E(\theta) = V_0^2 - 2U_{E0} + \int_{\theta_0}^{\theta} \left[\left(U_E(\theta) + \frac{Z^2}{2} \right) \cdot \psi_{(\theta)} \right] d\theta \quad (4-21)$$

with $\psi_{(\theta)} = \frac{-2e \cdot \sin(\theta)}{1+e \cdot \cos(\theta)}$ as auxiliary variable previously given in Eq. (4-5). From Eq. (4-21), it seems clear that this E-Jacobi integral is not constant and looking carefully at the integral expression we can observe that an explicit expression of the solution is also necessary, since involving P_3 -components $\{X, Y, Z\}$. As correctly noted in (S. Campagnola et al., 2008), “choosing different initial conditions within the same trajectory results in different J_E 's” and as consequence it is not more possible to “uniquely associate a trajectory to a single value of J_E ”. A very complete survey has been provided in their paper, especially for the so-called “sub-regions of motion”, in a very analogous way as seen for the Hill's surfaces (or zero-velocity surfaces).

4.2 Dynamical System Theory for the elliptic case

The Dynamical System Theory for the Elliptic problem is briefly discussed here, mostly focusing on the Pulsating notation and so considering Eq. (4-15) and Eq. (4-16). All basic knowledge has been given in Section 2.2, while here we provide some main differences and additional aspects related to the new dynamics investigated. Indeed, the new differential system is *non-autonomous*, so dependent on the time-like θ -variable and it can be expressed in a vector notation, differently from Eq. (2-23), such that

$$\dot{\mathbf{Q}} = \frac{d\mathbf{Q}}{d\theta} = \mathbf{f}(\mathbf{Q}, \theta) \quad (4-22)$$

where \mathbf{f} is a vector-function, \mathbf{Q} is a general state-vector $\mathbf{Q} \in \mathbb{R}^n, \forall \theta \in \mathbb{R}$.

³² In Eq. (4-20) it is important to remember that $U_E = U_E(X, Y, Z, \theta)$, dependent on the time-like parameter and consequently its differential will include partial derivatives respect to θ , such that

$$dU_E = \sum_{i=1}^3 \frac{\partial U_E}{\partial q_i} \cdot dq_i + \frac{\partial U_E}{\partial \theta} \cdot d\theta \quad , \forall q_i = \{X, Y, Z\}$$

³³ At the moment of this writing, no Integrals of Motion are known for the ER3BP (S. Campagnola et al., 2008), nonetheless more information on periodic orbits can be found when properly adopting averaging techniques. For this last case the reader is referred to (Palacián, 2006).

4.2.1 Proprieties of “non-autonomous differential system”

We assume that the general differential system in Eq. (4-22) consists of a N-set of first order non-linear differential equations in the time-like θ -variable. Nevertheless, the “**Existence and Uniqueness Theorem**” is still valid, as also the definition of the Phase-space, but now no more time-independent. This θ -dependence can be easily shown (Verhulst, 2000), applying the chain-rule to different pairs of equations, such that

$$\frac{dq_j}{dq_i} = \frac{f_j(\mathbf{Q}, \theta)}{f_i(\mathbf{Q}, \theta)}, \forall i, j = 1..N \mid j \neq i \quad (4-23)$$

for each possible combinations of variables and a suitable θ -domain (also requiring that at each phase-point $\mathbf{Q} = \mathbf{Q}^*$ we have a non-zero denominator). It follows that trajectories in the phase-space change with the θ -time and their geometrical characterization loses most of its useful proprieties.³⁴

To be mentioned, before analysing the DST in the Elliptic problem, is the possibility of considering an additional time-rescaling in a new time-like variable “s”, thus combining both Eq. (4-4) and Eq. (4-15). In this way, it is feasible to arrive at an autonomous system having dimension $1+6=7$, thus with an odd number of equations the system is no more a Symplectic one. Nevertheless, in general, the use of alternative reference frames could help the investigation of the problem, as also its expression in a mathematical ‘elegant’ form, even if the physics behind the model chosen is not really changing.

4.2.1.1 Phase-flow in a neighbourhood of critical points

The definition of critical points $\mathbf{Q} = \mathbf{a}$ given in Section 2.2.1.1 remains unchanged, but it is clear that their location needs to be fixed $\forall \theta \in \mathbb{R}$, due to the fact that the Phase-space is actually changing in time. Within a pulsating notation for the ER3BP, equilibrium points still exists and numerically are the same as found the CR3BP, while the reference system itself pulsates in θ -time (Section 4.1.2). However, much more difficult is now the characterization of their linear stability, since the phase-flow in their neighbourhood is varying. After linearizing the non-linear system in Eq. (4-16), as did in Eq. (2-26), and once neglecting higher order terms $\mathcal{O}(\|\tilde{\mathbf{Q}}\|^2)$, we are able to obtain a linear differential system, also written in a matrix form as

$$\frac{d}{d\theta} \begin{bmatrix} \tilde{X} \\ \tilde{Y} \\ \tilde{Z} \\ \tilde{V}_X \\ \tilde{V}_Y \\ \tilde{V}_Z \end{bmatrix} = \begin{bmatrix} 0 & 0 & 0 & 1 & 0 & 0 \\ 0 & 0 & 0 & 0 & 1 & 0 \\ 0 & 0 & 0 & 0 & 0 & 1 \\ U_{E,XX} & U_{E,XY} & U_{E,XZ} & 0 & 2 & 0 \\ U_{E,YX} & U_{E,YY} & U_{E,YZ} & -2 & 0 & 0 \\ U_{E,ZX} & U_{E,ZY} & U_{E,ZZ} & 0 & 0 & 0 \end{bmatrix} \cdot \begin{bmatrix} \tilde{X} \\ \tilde{Y} \\ \tilde{Z} \\ \tilde{V}_X \\ \tilde{V}_Y \\ \tilde{V}_Z \end{bmatrix} \stackrel{\text{def}}{=} \frac{d\tilde{\mathbf{Q}}(\theta)}{d\theta} = A_{|\mathbf{Q}_{L_i}}^E \cdot \tilde{\mathbf{Q}}(\theta) \quad (4-24)$$

with $\mathbf{Q} = \mathbf{Q}(\theta)$ as new state-vector of the Elliptic problem (to distinguish it from the pulsating X-coordinate), and $\tilde{\mathbf{Q}} = \Delta\mathbf{Q}(\theta) = \mathbf{Q}(\theta) - \mathbf{Q}_{L_i}$ as displacement from the L-point.

³⁴ For example, the “time-translation propriety” mentioned for autonomous systems (page 35) is here no more valid and considerations on the initial θ -phase will be undoubtedly relevant.

In Eq. (4-24), similarly to the Eq. (2-27), we arrive at a matrix $A_{|Q_{L_i}}^E = A_{|Q_{L_i}}^E(\theta)$ as **State Propagation Matrix (SPM)**, but this time no more constant, where its third quadrant is constituted by the Hessian of the (time-dependent) pseudo-potential U_E . It follows that solutions to the linear displacement-dynamics are no more trivial, as in Eq. (2-42) for the circular case. Furthermore, eigenvalues of Eq. (4-24) are now meaningless, differently from Eqs. (2-43)(2-44), due to the fact that we are dealing here with a system that is still linear but no more autonomous. (Verhulst, 2000)

At this point we can evaluate the new SPM at each collinear equilibrium Phase-point Q_{L_i} , and consequently from Eq. (4-24) we arrive at the following system

$$\frac{d}{d\theta} \begin{bmatrix} \tilde{X} \\ \tilde{Y} \\ \tilde{Z} \\ \tilde{V}_X \\ \tilde{V}_Y \\ \tilde{V}_Z \end{bmatrix} = \begin{bmatrix} 0 & 0 & 0 & 1 & 0 & 0 \\ 0 & 0 & 0 & 0 & 1 & 0 \\ 0 & 0 & 0 & 0 & 0 & 1 \\ 1 + 2\omega_Z^2 - 3\zeta & 0 & 0 & 0 & 2 & 0 \\ 0 & 1 - \omega_Z^2 & 0 & -2 & 0 & 0 \\ 0 & 0 & \omega_Z^2 & 0 & 0 & 0 \end{bmatrix} \cdot \begin{bmatrix} \tilde{X} \\ \tilde{Y} \\ \tilde{Z} \\ \tilde{V}_X \\ \tilde{V}_Y \\ \tilde{V}_Z \end{bmatrix} \quad (4-25)$$

with $\omega_z = \omega_z(\mu, e, \theta)$ as pseudo-vertical pulsation, in analogy with ω_z previously seen for the Circular problem (from now on called ω_{z0}), while ζ is an auxiliary function such that $\zeta = \frac{e \cdot \cos(\theta)}{1 + e \cdot \cos(\theta)}$. The squared expression of this pseudo-vertical pulsation is given below, but actually cannot be considered as a real pulsation, due to the fact that it is no more possible to make use of the so-called “characteristic equation” for non-autonomous differential systems (Perko, 2001). At the end, value of ω_z in Eq. (4-25) can be found as

$$\omega_z^2 = \frac{1}{1 + e \cdot \cos(\theta)} \cdot \left[\frac{1 - \mu}{|X_{L_i} + \mu|^3} + \frac{\mu}{|X_{L_i} + \mu - 1|^3} + e \cdot \cos(\theta) \right] \quad (4-26)$$

or using the aforementioned circular expression of Eq. (2-43), we arrive at

$$\omega_z^2 = \frac{\omega_{z0}^2 + e \cdot \cos(\theta)}{1 + e \cdot \cos(\theta)} \quad (4-27)$$

Approximations of the non-autonomous linear dynamics around collinear libration points will be discussed later in Section 4.3.1, where the LP-method has turned out to be not totally suitable, thus showing its limitations (e.g., very complex expressions), even if still capable of providing many insights in this new dynamical model.

4.2.2 Floquet Theory for linear stability assessment

In Section 2.2.2, the discussion over the STM, Monodromy matrix and its eigenvalues (or characteristic multipliers) has taken place, where it has been mentioned that those results were part of a more general vast theory, known as Floquet Theory, named after A.M.G. Floquet (1847-1920), and described in many textbooks previously suggested.

We start with a non-autonomous linear differential system, having a very similar notation as for Eq. (4-24), such that

$$\frac{d\mathbf{Q}}{d\theta} = A(\theta) \cdot \mathbf{Q} \quad (4-28)$$

with $\mathbf{Q} \in \mathbb{R}^n$ as state-vector, $\theta \in \mathbb{R}$ time-like variable of the system and $A(\theta) \in \mathbb{R}^{n \times n}$ differential matrix, continuous in θ , with a T-periodicity so that $A(\theta) = A(\theta + T)$. Hence, it is possible to formulate the “*Floquet’s Theorem*” (1883) as follows ([Verhulst, 2000](#))

Theorem 1.4 (Floquet’s Theorem)

“Given system in Eq. (4-28), each fundamental (or STM) matrix $\Phi(\theta, \theta_0)$ can be written as the product of two $[n \times n]$ -matrices

$$\Phi(\theta, \theta_0) = P(\theta) \cdot e^{B(\theta - \theta_0)}$$

with $P(\theta)$ T-periodic and B a constant $[n \times n]$ -matrix.”

Trivially to observe at this point that, for what it has been shown in Section 2.2.2, the Monodromy matrix $M = \Phi(\theta_0 + T, \theta_0)$ is simply related, for the Circular problem, to the exponential matrix $e^{B(\theta - \theta_0)}$ and so its characteristic multipliers are equivalent³⁵ to

$$\lambda_i = e^{v_i(\theta - \theta_0)} \quad (4-29)$$

with v_i eigenvalues of the constant B -matrix, also called “*characteristic exponents*”. Once again, we do not have an analytic expression of the Monodromy matrix, even if a semi-analytic method for calculating such matrix in the ER3BP (using Chebyshev polynomials) has been developed in ([Gurfil & Meltzer, 2007](#)). Here, we have numerically computed it using $A = A|_{\mathbf{Q}_{L_i}}^E(\theta)$, similarly to Eq. (2-31), and so propagating the STM over a T-period.

Basically, the **Theorem 1.4** allows us to reconsider the entire discussion about the use of characteristic multipliers (Section 2.2.3), thus studying the dynamics linearized around periodic solutions and with it also possible bifurcations in the Elliptic problem. Main justification comes from the T-periodicity of the P-matrix, as also from the fact that $A(\theta)$ is now T-periodic. Hence, from the T-periodicity it is correct to write that

$$P(\theta_0 + T) = P(\theta_0) = \mathbb{I}_{n \times n} \quad (4-30)$$

with the initial condition (I.C.) on the STM given as $\Phi_0 = \mathbb{I}_{n \times n}$, such that

$$\Phi_0 = P_0 \cdot e^{B \cdot (\theta_0 - \theta_0)} = P_0 \quad \xrightarrow{\text{using the I.C.}} \quad P_0 = \mathbb{I}_{n \times n} \quad (4-31)$$

For any time θ , as integer multiple of the T-period, the linearized dynamics can so be mapped in a very analogous way of what seen in Section 2.2.1.2 for the Circular problem.

³⁵ Small remark is here related to the use of a different notation respect to ([Verhulst, 2000](#)), where characteristic multipliers (“c.m.”) and characteristic exponents (“c.e.”) are defined in the exact opposite way, so having λ_i as “c.e.” and v_i as “c.m.”.

4.2.3 The loss of continuous families in the ER3BP

The differential system for the Elliptic problem is well-known to be still an Hamiltonian one (Bennett, 1965), so in the form shown by Eq. (2-34). However, the expression of the Hamiltonian $H = H(\mathbf{p}, \mathbf{q}, \theta)$, with \mathbf{p}, \mathbf{q} as vectors of generalized coordinates, is now time-dependent and cannot be related to the energy of the system. (Goldstein et al., 2002)

The Symplectic structure in periodic solution still holds³⁶, consequently the characteristic multipliers can be found again in reciprocal *quadruplets*, and first two points described in Section 2.2.4 can be consider valid also for this elliptic case. For what concerns the third point (existence of at least one real eigenvalue $\lambda = +1$ for periodic orbits), it cannot be taken into account anymore (Broucke, 1969). The geometrical meaning of this last point is not really trivial, but it could be visualized thinking to an initial displacement along the periodic solution itself, so $\delta Q = \delta Q^o(\theta_0)$ at $\theta = \theta_0$. A time-shift is actually able to change the structure of the phase-space in non-autonomous systems, and it can be related to a new solution $Q^{new}(\theta)$, so starting with a new shooting condition as

$$Q_0^{new} \triangleq Q^{new}(\theta_0) = Q^o(\theta_0) + \delta Q^o(\theta_0) \tag{4-32}$$

As stated before, the time-shift propriety is no more applicable here and “in general” we have that $Q^o(\theta_0 + \Delta\theta) \neq Q^{new}(\theta_0)$, since it has been already proved that additional time-constraints on shooting conditions arise in the ER3BP (Broucke, 1969). A graphical example is given in Figure 62, taken from (S. Campagnola et al., 2008), where two different splits of $\lambda_{1/2} = +1$ are shown after passing from the Circular to the Elliptic problem.

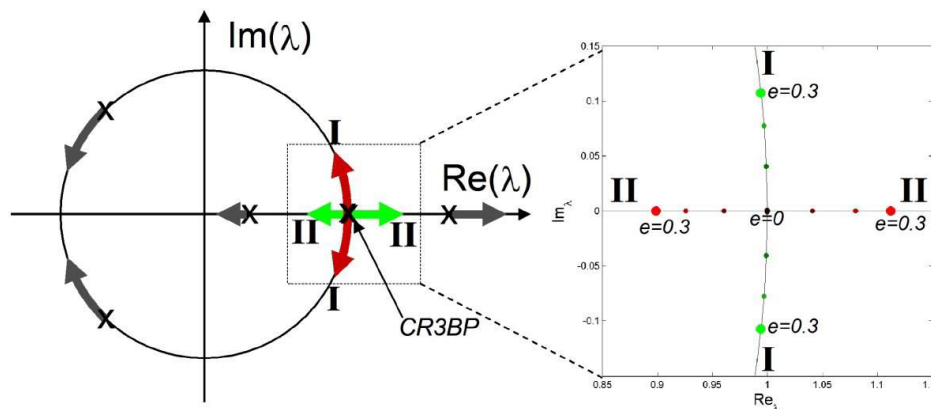


Figure 62: Illustration showing two possible “separations” of the two real unitary eigenvalues of a Halo solution. Branch I (green) leads to additional stable/unstable manifolds, while Branch II (red) leads to complex conjugate values that do not change the order of instability. Courtesy of (S. Campagnola et al., 2008).

In the previous illustration a very interesting aspect is shown for the Halo case, where two different families can be found $\forall e > 0$, allowing to define $e = 0$ as bifurcation point. The latter will be further explained later in Section 4.4.3, also defined as eccentric-bifurcation, while here we continue with a qualitative discussion on possible behaviours for characteristic multipliers associated with generic periodic solutions.

³⁶ To be more precise, the Symplectic structure holds only “at the end of each revolution in the periodic case”, as well-described and proved in (Broucke, Lass, & Boggs, 1976).

In Section 2.2.5, the Bifurcation Theory for the circular case has been introduced, showing three main bifurcations within each family of periodic solutions, as well as for a fourth one that does not really change the order of instability. In the Circular case, the bifurcation parameter is the relative x-position from each libration point, as starting point for the generation of the entire family (Section 2.4.3). However, the loss of both real unitary eigenvalues leads to the vanishing of continuous families, previously described in Eq. (2-38), while periodic orbits exist now only within discrete families based on the so-called “*resonance condition*”, later discussed in Section 4.3.

From what we have seen so far, it is expected to be able to extend single periodic orbits found in the Circular problem to the elliptic case, most likely surrounded by their respective quasi-periodic family (for complex conjugate characteristic multipliers). An example still in the CR3BP is given for the L2-point in Figure 63 taken from (Nagata, Sakamoto, & Habaguchi, 2016), where quasi-periodic families (in red) are shown around their respective periodic solution (in blue), considering both Halo and Lyapunov families. As discussed before, the Lissajous family exists in the neighbourhood of each libration point, around both mono-parameter Lyapunov families, due to the mismatch between ω_{xy} and ω_z , respectively horizontal and vertical linearized pulsations in Eqs. (2-43)(2-44).

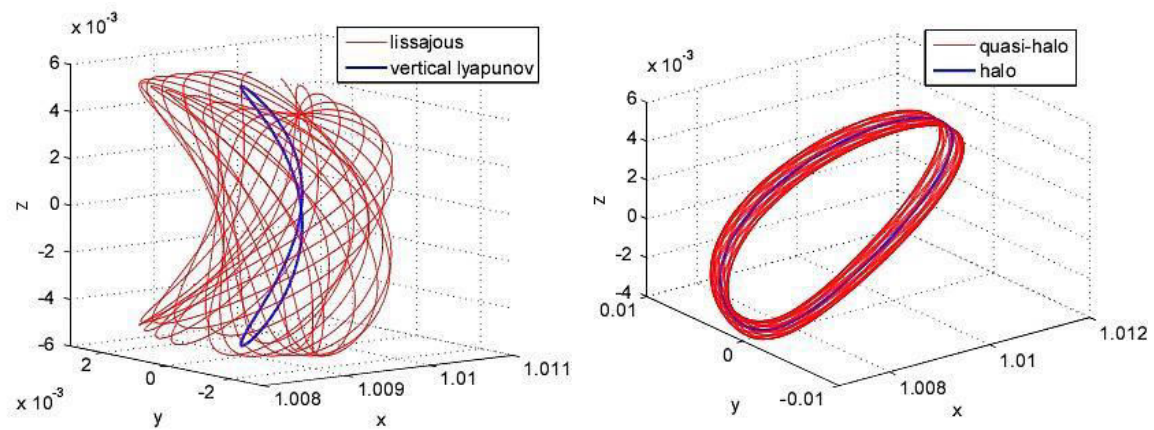


Figure 63: Illustration showing two quasi-periodic families at L2 in the CR3BP. On the left, the Lissajous one exists at each L-point around the Vertical Lyapunov family, while on the right the Quasi-Halo one. Both are consequences of existing complex conjugate eigenvalues in the relative Monodromy matrix. Courtesy of (Nagata et al., 2016).

Considering that both $\lambda_{1/2}$ can have general values, as listed in Eqs. (2-39)(2-40), it follows an higher number of possibilities, no more restricted to seven, as also observed and well summarized in (H. Peng & Xu, 2015b). A remarkable difference is also the existence of periodic solutions (p.s.) with a 3-order instability, consequently having only stable/unstable manifolds (H. Peng & Xu, 2015c), without any quasi-periodic behaviour around the periodic orbit. These additional manifolds have been studied in (H. Peng & Xu, 2015a), revealing that “*the redundant stable manifold affects the probability of feasible transfers in the whole parameter space*”. Even so, in this work we are not considering manifolds or the optimization of general transfer-problems, and so the existence of such *internal/external* manifolds will not be treated here. Nonetheless, the reader is referred to these cited papers, as also to (Parker, 2007) for more details. We can continue with the description of main approaches adopted to tackle the Elliptic problem.

4.3 The Analytic approach

As prelude, we prefer to briefly acknowledge the reader about some decisions taken during the working process of this Master thesis. De facto, during the Literature Study greater effort has been made in the assessment of possible analytic methods (e.g., the mentioned Linstedt-Poincaré technique) in order to tackle the Elliptic problem, so finding approximations of some periodic solutions near collinear libration points. The last task turned out to be possible, as given in (Farquhar & Kamel, 1973) for a more general Earth-Moon system, but not really efficient as well discussed in (Gómez & Mondelo, 2001), where two main analytic methods have been applied. The first is again the LP-method, able to target particular periodic trajectories but with some limitations in the stability assessment (see Section 2.3.2.3). In fact, the method actually removes all unstable ‘modes’ within the approximated solution and consequently it provides a “*poor description of the global picture*” in a neighbourhood of L-points. Second one is the mentioned reduction of the Hamiltonian to Centre Manifold, which “*gives a very good description of the dynamics inside the centre manifold, but it does not produce closed formulas for the solutions, and it is quite expensive from the computational point of view*”. (Gómez & Mondelo, 2001)

As for the circular case, this part is complementary to the principal one, based again on a Differential Correction numerical scheme (necessary also for validation and verification purposes). On the other hand, some insights into the dynamics of the Elliptic problem will be shown here and in addition to that, a brief discussion over a possible extension and application of the LP-technique will take place in Section 4.3.2.

4.3.1 Stability under “elliptic perturbations” using LP-method

The initial differential system is given in Eq. (4-24), where we consider the displacement dynamics on a first-order approximation respect to small amplitudes, and consequently looking to the linear stability of each L-point within the Pulsating frame. Note that the system is still linear but now also θ -dependent, thus not solvable as did in Section 2.3. For this reason, we will apply the LP-method respect³⁷ to a small eccentricity, thus studying what have been named³⁸ “*elliptical perturbations*” in the Literature Study. We can start re-writing Eq. (4-24) using the definition of U_E as given in Eq. (4-17), such that

$$\begin{cases} \tilde{X}'' - 2\tilde{Y}' = \tilde{X} \cdot (1 + 2c_2) \cdot \sigma(e, \theta) \\ \tilde{Y}'' + 2\tilde{X}' = \tilde{Y} \cdot (1 - c_2) \cdot \sigma(e, \theta) \\ \tilde{Z}'' + \tilde{Z} \cdot [c_2 + e \cdot \cos(\theta)] \cdot \sigma(e, \theta) = 0 \end{cases} \quad (4-33)$$

with $c_2 = c_2(\mu)$ previously defined in Eq. (2-54) and the auxiliary function $\sigma = \sigma(e, \theta)$, so leading to a Taylor series at $e = 0$ that can be expressed as follows

$$\sigma(e, \theta) = \frac{1}{1 + e \cdot \cos(\theta)} \cong 1 + \sum_{k=1}^{\infty} e^k [-\cos(\theta)]^k \quad (4-34)$$

³⁷ The discussion is valid here only for small displacements around libration points. In fact we are still considering just a linearized dynamics, where it is possible to examine full effects due to ellipticity of the e -parameter, as well as for its first-order effects on the stability.

³⁸ These “elliptic perturbations” are first-order effects due to the introduction of eccentricity in the problem, but assuming a very small value for it and so neglecting higher order terms as $\mathcal{O}(e^2)$.

From the moment that in Eq. (4-33) we are only considering linear amplitude-terms of the displacement, it follows that both dynamical motions in-plane and out-of-plane are again uncouple, thus they can be studied separately. To be noted that so far no approximation has been made respect to the e -parameter and the previous expression is trivially computed based on Eq. (4-17), where U_E and Ω_C have been related. At this point, considering the Hessian³⁹ of such pseudo-potential (so second derivatives of U_E respect to the pulsating coordinates), it is possible to neglect higher order terms $\mathcal{O}(e^2)$, and so investigating principal effects related to “*elliptical perturbations*”.

4.3.1.1 Out-of-plane motion under “elliptical perturbations”

For the out-of-plane displacement it is required to solve the following

$$\tilde{Z}'' + \tilde{Z} \cdot c_2 = \tilde{Z} \cdot (c_2 - 1) \cdot e \cdot \cos(\theta) \quad (4-35)$$

Considering a first-order expansion of the solution as $\tilde{Z}(\theta) = \tilde{Z}_0(\theta) + e \cdot \tilde{Z}_1(\theta)$ and then collecting all terms at each different order of magnitude in e , we obtain

$$\begin{aligned} \tilde{Z}_0'' + \tilde{Z}_0 \cdot c_2 &= 0 \\ \tilde{Z}_1'' + \tilde{Z}_1 \cdot c_2 &= \tilde{Z}_0 \cdot (c_2 - 1) \cdot \cos(\theta) \end{aligned} \quad (4-36)$$

where solution of the first equation is given using $c_2 = \omega_{Z_0}^2$ (Section 2.3.2.2), such that

$$\tilde{Z}_0 = a_{Z_0} \cdot \cos(\omega_{Z_0}\theta) + b_{Z_0} \cdot \sin(\omega_{Z_0}\theta) \quad (4-37)$$

and substituting it in Eq. (4-36), with some trigonometric manipulations, we arrive at

$$\begin{aligned} \tilde{Z}_1'' + \tilde{Z}_1 \omega_{Z_0}^2 &= \frac{(\omega_{Z_0}^2 - 1)}{2} \cdot a_{Z_0} \{ \cos([1 + \omega_{Z_0}]\theta) + \cos([1 - \omega_{Z_0}]\theta) \} \\ &+ \frac{(\omega_{Z_0}^2 - 1)}{2} \cdot b_{Z_0} \{ \sin([1 + \omega_{Z_0}]\theta) - \sin([1 - \omega_{Z_0}]\theta) \} \end{aligned} \quad (4-38)$$

The solution consists in the sum of a homogeneous and particular one, so leading to

$$\tilde{Z}_1 = \tilde{Z}_1^{om} + \tilde{Z}_1^p \quad (4-39)$$

where the homogeneous one is expressed by integration constants a_{Z_1}, b_{Z_1} simply as

$$\tilde{Z}_1^{om} = a_{Z_1} \cdot \cos(\omega_{Z_0}\theta) + b_{Z_1} \cdot \sin(\omega_{Z_0}\theta) \quad (4-40)$$

³⁹ It is clear that for the term $U_{E,ZZ}$ it is possible to write it using Eq. (4-17), such that

$$\frac{\partial^2 U_E}{\partial Z^2} = \frac{\partial^2}{\partial Z^2} \left(\sigma(e, \theta) \cdot \left[\Omega_C - \frac{Z^2 e \cdot \cos(\theta)}{2} \right] \right) = \sigma(e, \theta) \cdot \left[\Omega_{C,ZZ} - e \cdot \cos(\theta) \right]$$

where $\Omega_{C,ZZ} = -c_2$ for what we have seen in Section 2.3.2.2.

At this point, even if considering only a linear approximation (in both amplitude and eccentricity) we can have a very first insight into the ER3BP dynamics. Note that solution to Eq. (4-35), in a neighbourhood of the L-point and for a sufficiently small eccentricity, represents actually a good approximation of the full non-linear system behaviour. This first-order approximation of the vertical motion for the CR3BP is simply an harmonic oscillator in ω_{z0} , so defined by bounded orbits. However, the new condition on some possible resonances, having time-forces in $[1 - \omega_z]$ and $[1 + \omega_z]$, is now

$$\omega_z = \pm[1 \mp \omega_z] \xrightarrow{\text{satisfied if}} \omega_z = \pm \frac{1}{2} \quad (4-41)$$

so related to an orbit revolving half time during a complete system revolution, which we found to be 2π -periodic in non-dimensional coordinates. The particular solution to the Eq. (4-38) can be found based on a resonance or a no-resonance condition, such that

NO-RESONANCE CASE ($\omega_z \neq \pm 1/2$)

$$\begin{aligned} \tilde{z}_1^p(\theta) = & \frac{(1 - \omega_{z0}^2)}{4} \cdot \frac{[a_{z0} \cdot \cos([1 - \omega_{z0}]\theta) - b_{z0} \cdot \sin([1 - \omega_{z0}]\theta)]}{\omega_{z0} - 1/2} \dots \\ & - \frac{(1 - \omega_{z0}^2)}{4} \cdot \frac{[a_{z0} \cdot \cos([1 + \omega_{z0}]\theta) + b_{z0} \cdot \sin([1 + \omega_{z0}]\theta)]}{\omega_{z0} + 1/2} \end{aligned} \quad (4-42)$$

RESONANCE CASE ($\omega_z = \pm 1/2$)

$$\tilde{z}_1^p(\theta) = \frac{3}{8} \cdot \left[a_{z0} \cdot \cos\left(\frac{3\theta}{2}\right) + b_{z0} \cdot \sin\left(\frac{3\theta}{2}\right) \right] - \frac{3\theta}{4} \cdot \left[b_{z0} \cdot \cos\left(\frac{\theta}{2}\right) + a_{z0} \cdot \sin\left(\frac{\theta}{2}\right) \right] \quad (4-43)$$

Clearly, the perturbed period in Eq. (4-35) is now known and has to be 2π , differently from the example in Section 2.3.2.1 when assuming an autonomous system and introducing *strained coordinates*. At the same time we know that the value of $\omega_z = \sqrt{c_2}$ is almost fixed near the libration points by the mass-ratio parameter μ , while non-linear effects could arise when considering higher orders of the expansion. In the third-order approximation of (Richardson, 1980a), we have seen such non-linear effects, leading to the existence of Halo orbits when considering a synchronize out-of-plane and in-plane motion. At the very end, the first-order approximation can be written as

$$\tilde{Z}(\theta) \approx \tilde{Z}^{app}(\theta) = \tilde{Z}_0(\theta) + e \cdot [\tilde{Z}_1^{om} + \tilde{Z}_1^p] \quad (4-44)$$

This brief example shows how the linearized vertical motion can be also driven to instability under “elliptic perturbation”, mostly due to resonance effects. With a further expansion in Eq. (4-34), terms as $\cos^2(\theta)$, $\cos^3(\theta)$, ..., $\cos^n(\theta)$ will appear at each level of the expansion, and in different combinations with solutions from lower-levels. For these terms as $\sin(\omega_z\theta)$ and $\cos(\omega_z\theta)$, additional resonances can arise and consequently also many other *secular terms*, quickly growing fast, as seen in Eq. (4-43).

NOTE: the entire analysis so far has been based only on a linearized motion (for very small amplitude displacements), while in Section 4.3.2 an extension to non-linear dynamics will be briefly mentioned. Let’s now briefly consider the horizontal motion, more complicated since described by two ‘coupled’ differential linear equations.

4.3.1.2 In-plane motion under “elliptical perturbations”

For the in-plane displacement, once neglecting terms as $\mathcal{O}(e^2)$, it is required to solve

$$\begin{cases} \tilde{X}'' - 2\tilde{Y}' - \tilde{X} \cdot (1 + 2c_2) = -\tilde{X} \cdot (1 + 2c_2) \cdot e \cdot \cos(\theta) \\ \tilde{Y}'' + 2\tilde{X}' - \tilde{Y} \cdot (1 - c_2) = \tilde{Y} \cdot (c_2 - 1) \cdot e \cdot \cos(\theta) \end{cases} \quad (4-45)$$

Considering a first-order expansion of both solutions as $\tilde{X}(\theta) = \tilde{X}_0(\theta) + e \cdot \tilde{X}_1(\theta)$ and $\tilde{Y}(\theta) = \tilde{Y}_0(\theta) + e \cdot \tilde{Y}_1(\theta)$, then collecting e -terms at each order of magnitude, we obtain

$$\begin{cases} \tilde{X}_0'' - 2\tilde{Y}_0' - \tilde{X}_0 \cdot (1 + 2c_2) = 0 \\ \tilde{Y}_0'' + 2\tilde{X}_0' - \tilde{Y}_0 \cdot (1 - c_2) = 0 \\ \tilde{X}_1'' - 2\tilde{Y}_1' - \tilde{X}_1 \cdot (1 + 2c_2) = -\tilde{X}_0 \cdot (1 + 2c_2) \cdot \cos(\theta) \\ \tilde{Y}_1'' + 2\tilde{X}_1' - \tilde{Y}_1 \cdot (1 - c_2) = \tilde{Y}_0 \cdot (c_2 - 1) \cdot \cos(\theta) \end{cases} \quad (4-46)$$

where the solution to the unperturbed system has been already given for the Circular problem, after removing “modes” related to unbounded solutions (real eigenvalues λ_{XY}). The remaining part is so given only by a periodic bounded motion defined as

$$\begin{cases} \tilde{X}_0 = a_{X0} \cdot \cos(\omega_{XY}\theta) + b_{X0} \cdot \sin(\omega_{XY}\theta) \\ \tilde{Y}_0 = a_{Y0} \cdot \cos(\omega_{XY}\theta) + b_{Y0} \cdot \sin(\omega_{XY}\theta) \end{cases} \quad (4-47)$$

and after substituting it in the (perturbed) second system of Eq. (4-46), we arrive at

$$\begin{cases} \tilde{X}_1'' - 2\tilde{Y}_1' - \tilde{X}_1 \cdot (1 + 2c_2) = \\ -\left(\omega_{Z0}^2 + \frac{1}{2}\right) \cdot a_{X0} \{\cos([1 + \omega_{XY}]\theta) + \cos([1 - \omega_{XY}]\theta)\} \dots \\ -\left(\omega_{Z0}^2 + \frac{1}{2}\right) \cdot b_{X0} \{\sin([1 + \omega_{XY}]\theta) - \sin([1 - \omega_{XY}]\theta)\} \\ \tilde{Y}_1'' + 2\tilde{X}_1' - \tilde{Y}_1 \cdot (1 - c_2) = \\ \frac{(\omega_{Z0}^2 - 1)}{2} \cdot a_{Y0} \{\cos([1 + \omega_{XY}]\theta) + \cos([1 - \omega_{XY}]\theta)\} \dots \\ + \frac{(\omega_{Z0}^2 - 1)}{2} \cdot b_{Y0} \{\sin([1 + \omega_{XY}]\theta) - \sin([1 - \omega_{XY}]\theta)\} \end{cases} \quad (4-48)$$

with an homogenous solution (again removing unbounded modes) expressed as

$$\begin{cases} \tilde{X}_1^{om} = a_{X1} \cdot \cos(\omega_{XY}\theta) + b_{X1} \cdot \sin(\omega_{XY}\theta) \\ \tilde{Y}_1^{om} = a_{Y1} \cdot \cos(\omega_{XY}\theta) + b_{Y1} \cdot \sin(\omega_{XY}\theta) \end{cases} \quad (4-49)$$

At this point, it is possible to solve the system in Eq. (4-48) using common algebraic manipulation software (e.g., Maple 2016). Solutions \tilde{X}_1^p and \tilde{Y}_1^p have been not given here since not very relevant, while very interesting here are the resonance conditions given as

$$\omega_{XY} = \pm[1 \mp \omega_{Z0}] \quad \text{with} \quad \omega_{XY} = \sqrt{1 - \frac{\omega_{Z0}^2}{2} + \frac{\omega_{Z0}}{2} \sqrt{9\omega_{Z0}^2 - 8}} \quad (4-50)$$

As mentioned at the beginning of this section, only purpose here is to exploit some main features relative to the elliptic case, without really obtaining an analytic approximation. First of all, as expected, we have seen that the system is driven by a 2π -periodic force, caused by periodic variations of the gravitational field due to the motion of both M_1, M_2 . Furthermore, periodic solutions still exist, but no more embedded in a continuous family (as explained in Section 4.2.3), while they can be actually compute starting with precise initial conditions (now involving also the time-like θ -parameter).

When discussing the linear stability of collinear L-points under “elliptic perturbations”, a qualitative result is that the eccentricity (even if small) can creates resonance effects at some given mass-ratio μ . This parameter indeed defines both linearized pulsations, near each L-points, such that ω_Z and ω_{XY} could match with resonance conditions previously given (in a first-order approximation) with Eq. (4-41) and Eq. (4-50). Nevertheless, a general linear instability of collinear points is still visible due to the existence of unbounded modes, already removed in Eq. (4-47) and Eq. (4-49). An higher order of expansion in e can lead to additional resonance conditions, discussed before, while now we briefly consider also non-linear amplitude displacements, where both in-plane and out-of-plane motions are no more uncoupled, as shown in (Richardson, 1980a).

4.3.2 Extension to a non-linear dynamics and main limitations

The previous example has been based on a first order approximation for small displacement amplitudes, initially given in Eq. (4-33) and then approximated also for small eccentricity effects (called “elliptical perturbations”). At this very basic level of investigation, some insights into the dynamics have been given, while when involving terms $\mathcal{O}(e^k), \forall k \geq 2$ expressions become very long and tedious. For the sake of completeness we provide here a more complete system, based on a full non-linear stability under eccentricity effect. Using Eq. (4-16) and defining U_E as in Eq. (4-17), we are able to make use of the auxiliary function $\sigma(e, \theta)$ from Eq. (4-34) in order to obtain a compact expression, in pulsating coordinates, for the entire dynamics of the ER3BP.

$$\begin{cases} X'' - 2Y' = \sigma(e, \theta) \cdot \frac{\partial \Omega_C}{\partial X} \\ Y'' + 2X' = \sigma(e, \theta) \cdot \frac{\partial \Omega_C}{\partial Y} \\ Z'' = \sigma(e, \theta) \cdot \left[\frac{\partial \Omega_C}{\partial Z} - Z \cdot e \cdot \cos(\theta) \right] \end{cases} \quad (4-51)$$

A Taylor expansion can be performed on the previous expression respect to the amplitude-displacements $\tilde{X}, \tilde{Y}, \tilde{Z}$, as well as respect to the eccentricity e . It follows a non-linear and non-autonomous differential system, which can iteratively be solved applying general perturbations methods, for example with the LP-technique here presented.

In (Lei, Xu, Hou, & Sun, 2013), a similar procedure has been applied (considering also unbounded modes) for computing invariant manifolds associated with both Lissajous and Halo orbits. The Euclidean norm-error of the position has been numerically assessed after half revolution with a Runge-Kutta-Fehlberg 7(8) integrator and with a relative tolerance of 10^{-14} . The reader is referred to their paper for more information, especially on the practical convergence of these higher order solutions, also directly comparable with the approximation also found in (Jorba & Masdemont, 1999) for the CR3BP.

4.4 The Numeric approach

At this point, last part to be presented for the ER3BP is related to some variations on the Numerical approach, in support to what has been introduced for the circular case in Section 2.4. Most of the basic notion has been already presented, but some additional aspects require a further discussion, while the reader is referred to ([H. Peng & Xu, 2015a, 2015b, 2015c](#)) for more information or for different applications of similar concepts and techniques. Let's now discuss the condition on "resonance orbits" and its consequences, from a computational point-of-view, relative to the Differential Correction algorithm (as well as for the numerical continuation), previously adopted in the CR3BP.

4.4.1 Conditions on "MxNy resonance orbits"

As reported in ([S. Campagnola et al., 2008](#)), almost 100 years ago a sufficient criterion for the existence of periodic solutions in the planar Elliptic problem has been formulated in ([Moulton et al., 1920](#)), here re-presented as follows.

Strong Periodicity Criterion

"For an orbit to be periodic [in the planar ER3BP] it is sufficient that it has two perpendicular crossing with the syzygy-axis, and that the crossings happen at moments when the two primaries are at an apse, (i.e., at maximum or minimum elongation, or apo-apsis and peri-apsis)."

The latter, in analogy with the time-symmetry discussed in Section 4.1.2, is a sufficient condition for the existence of periodic solutions in the p-ER3BP, as for the case of the Horizontal Lyapunov family. The new time-constraint is related to the Eq. (4-19), so having the time-like variable $\theta = 0, \pi, 2\pi, 3\pi, \dots$, at the moment of each cross. It follows that the orbit considered has to be in "resonance" with the revolution of principal masses, for example having exactly M-revolutions every N-revolutions of the reference system. As main consequence, a condition can be found on the T-period, such that

$$\begin{cases} T_E = 2\pi \cdot N \\ T_E = M \cdot T_C \end{cases} \xrightarrow{\text{leading to}} T_C = 2\pi \cdot \frac{N}{M}, \forall \{N, M\} \in \mathbb{Z}^+ \quad (4-52)$$

with T_C and T_E orbital periods respectively for the circular and the elliptic case. Basically the period T_E , necessary for a periodic trajectory, is now fixed, thus confirming once again the non-continuous nature of families in the ER3BP, in opposition to what we have discussed with Eq. (2-38). On the other hand, it is also true that every combinations of M and N satisfy Eq. (4-52), and consequently "there are infinite set of $\{M_i, N_i\}_i$ close to any desired period since the rational number is dense" ([H. Peng & Xu, 2015b](#)).

In ([Broucke, 1969](#)), this aspect and the **Strong Periodicity Criterion** have been used to investigate almost 1100 two-dimensional periodic orbits with all ranges of eccentricity $e \in (0,1)$ and mass-ratios $\mu \in (0,0.5)$ showing that "the elliptic problem behaves in a way which is completely different from the circular problem. The main difference is in the stability proprieties of periodic orbits". One very first attempt to numerically investigate periodic solution in the complete ER3BP has been made later in ([Sarris, 1989](#)), focusing on large mass-ratio values as $\mu = 0.4$ (so considering mostly binary systems), and using periodicity conditions in Eqs. (2-65)(2-66) given as $\Delta V_{XZ} \cong 10^{-6}$ and $\Delta Y \cong 10^{-7}$.

In (S. Campagnola et al., 2008), the aforementioned criterion has been extended to a spatial problem, so considering the full ER3BP and leading to the following condition

Elliptic Periodicity Condition

“For an orbit to be periodic in the ER3BP, it is sufficient that it has two perpendicular crossing with either the normal plane (from S1) or the syzygy axis (from S2), or both of them, when the primaries are at an apse.”

Clearly, the new sufficient condition is simply an extension of all the discussion given in Section 2.1.2.2 for the Circular problem, where now the initial shooting time (starting on the XZ-plane) is also an essential aspect (see Section 4.1.3). However, looking at results in Chapter 3, we can clearly note that the period T_c found for every member within each family is actually bounded in a definite range, as summarized in Table 4.

Table 4: Range found for the orbital period T_c in the three families of periodic solutions analysed at L1 and L2 (Earth-Moon CR3BP). Note that Min & Max values have been normalized by 2π , so allowing directly observing the ratio "N/M" up to four digits.

| T_c range [$\times 2\pi$] | L1 | | L2 | |
|-------------------------------|--------|--------|--------|--------|
| | Min | Max | Min | Max |
| H -Lyapunov | 0.4284 | 1.0774 | 0.5369 | 0.9092 |
| V -Lyapunov | 0.4414 | 0.7454 | 0.5601 | 0.7040 |
| Halo | 0.3559 | 0.4436 | 0.3252 | 0.5435 |

In Chapter 3, some possible resonance orbits have been shown within each family, but only considering a range as $N \in [1,4]$ and $M \in [1,12]$ leading to 48 possible cases for each of the six analyses performed (three families at two different L-points). In Table 4, the entire range is given normalized by 2π , so directly showing the ratio "N/M", which will be the principal feature of each trajectory later investigated. From now on, we will refer to resonance orbits using “MxNy”, where x and y are actually integer positive numbers.

4.4.2 Modifications in the Differential Correction scheme

In Section 2.4.4 the numerical algorithm has been summarized, where last step was the saving of all main parameters, e.g. shooting conditions for each member. It is clear that at this point we cannot rely anymore on the continuous character of each family and consequently it is necessary to exactly locate the resonance orbit that we are going to analyse, thus extending it to the elliptic case. Using Eq. (2-63), we see that now the Differential Correction does not involve anymore the uncertainty on the period, and consequently the correction can be expressed, within pulsating coordinates, as follows

$$\begin{pmatrix} \delta Y_1 \\ \delta V_{X1} \\ \delta V_{Z1} \end{pmatrix}_{T_E/2} = \begin{bmatrix} \Phi_{21} & \Phi_{23} & \Phi_{25} \\ \Phi_{41} & \Phi_{43} & \Phi_{45} \\ \Phi_{61} & \Phi_{63} & \Phi_{65} \end{bmatrix}_{T_E/2} \cdot \begin{pmatrix} \delta X_0 \\ \delta Z_0 \\ \delta V_{Y0} \end{pmatrix} \quad (4-53)$$

This is a determined linear system, so solvable in order to apply the correction as given in Eq. (2-64). Even for the 2D case (for H-Lyapunov orbits), the system is still determined and leads to a “unique” solution without the necessity of fixing any parameters.

A small remark on the Differential Correction algorithm is now necessary, from the moment that the correction is still based on a linearization (see Section 2.4.1) and works assuming an initial guess ‘sufficiently close’ to the target solution. In addition, other periodic solutions could exist in the Elliptic problem, having the same period but within other families, where the algorithm still converge but not on the desired trajectory. For all the aforementioned reasons, an additional step has been added to the algorithm before the numerical continuation. Assuming to have selected a “MxNy”-orbit, we look at the two closest members X_0^-, X_0^+ in the family (respectively with a smaller and larger period as T_0^- and T_0^+), thus we perform a *spline interpolation* on shooting conditions, as

$$X_0^{M \times N y} = \text{Interp}\{X_0^-, X_0^+\} \quad \text{with} \quad T_0^- \leq T_0^{M \times N y} \leq T_0^+ \quad (4-54)$$

with X_0 as initial state-vector, referred to the circular case, while such initial guess still requires to be numerically corrected using the DC-method. As shown in Eq. (4-53), in the Elliptic problem the symmetry involves half of the new orbital period T_E , thus evaluating crossing conditions on the XZ-plane at a time θ_1 given as

$$\theta_1 = \theta_0 + \frac{T_E}{2} \triangleq \theta_0 + \frac{M \cdot T_C}{2}, \quad \forall \theta_0 = 0, \pi \quad (4-55)$$

Therefore, the necessary integration period is now M times longer, with an obvious influence on the overall numerical accuracy. To be more precise, two aspects need to be taken into account for this Elliptic problem:

- I. Taking a large N, the integration period used in Eq. (4-53) is given as " $\pi \cdot N$ " and the algorithm could not be able to satisfy both criteria in Eqs. (2-65)(2-66), due to losses in the final accuracy of the numerical integration itself.
- II. Taking a large M, the unstable dynamic related to largest characteristic multipliers $\|\lambda_{MAX}\| \geq 1$ becomes much more evident, where the generic initial displacement is growing at each revolution, so leading to

$$\|\delta X_1\| \geq \|\lambda_{MAX}\|^M \cdot \|\delta X_1\|_0 \quad (4-56)$$

and, for a too large value, such error-estimation becomes clearly meaningless, while what has been defined as “linear stability” is also no more valid, as strongly remarked in Section 2.2.2.

NOTE:

An example of M5N2-Halo orbit at L2, is given in Figure 64 within the Circular problem ($e = 0$), so referring to both the co-rotating (synodic) and the inertial frame, while in Figure 65, some data has been provided for what concerns this numerical integration over T_E . In the CR3BP the period is still $T_C = T_E/M$, thus it follows a repetitive pattern, where the absolute displacement in position and velocity is given starting from the shooting condition. It is expected to have a perfect repetition over a period T_C but due to such unstable dynamics, errors on periodicity (orange circles) increase, as well as for the Energy variations $\Delta J_{(\theta)}$ (Right-Top). The latter are based on the definition of the Jacobi integral (valid only for the CR3BP), as also explained in Appendix-B.

Module of each one of the six eigenvalues is shown in Figure 65 with the overall order of instability (Right-Bottom), while using Eq. (4-56) the final error at $T_E = 2 \cdot 2\pi$ is expected to be in first-order approximation around $\sim 5.8^5 = 6500$ times larger than the initial one. This trend can be directly observed in Figure 65 (Left-Centre), with a slightly increasing value of the periodicity-errors $\Delta r, \Delta V$ after each revolution.

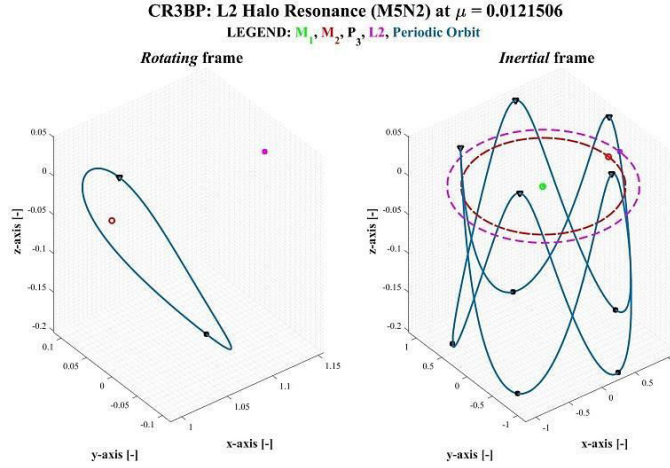


Figure 64: Example showing a Southern Halo “resonance” orbit (M5N2) at L1, libration point for the Earth-Moon CR3BP system in both a Rotating (LEFT) and Inertial frame (RIGHT).

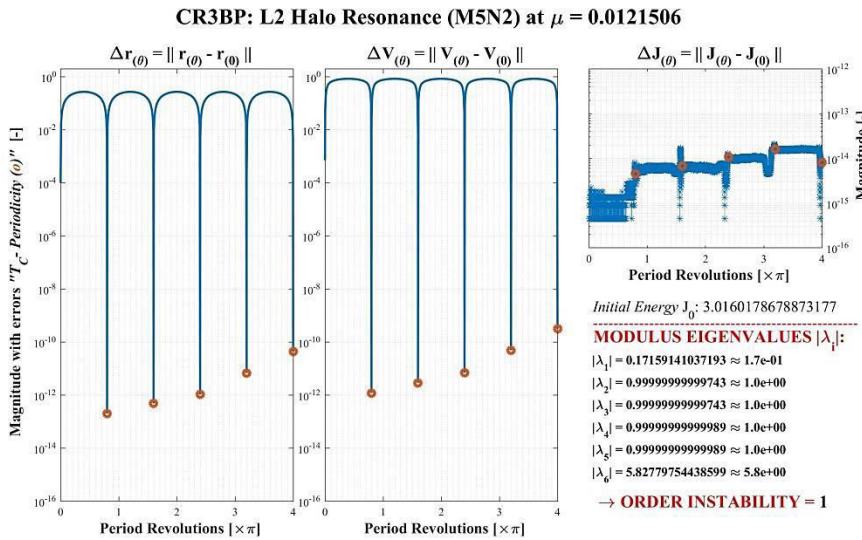


Figure 65: Example of periodicity assessment considering M-revolutions for the “resonance” solution illustrated in Figure 64. The modulus of position and velocity-variations (w.r.t. the Initial Condition) are shown (Left-Centre) with periodicity error (orange circle). Energy error (Right-Top) and absolute value of characteristic exponents (Right-Bottom) are also given.

The previous example shows possible numerical limitations related to our investigation, while for the sake of completeness we have to mention an alternative strategy, adopted in (H. Peng & Xu, 2015a, 2015b, 2015c). The latter is based on a multi-shooting algorithm, in close analogy with some basic methodologies originally described in (Howell & Pernicka, 1988) for studying quasi-periodic solutions. In fact, their “Multi-Segment Optimization Method” fixes multiple conditions between each segment along the entire trajectory, thus it tries to minimize a cost function, as $\Gamma = \sqrt{y_n^2 + v_{xn}^2 + v_{zn}^2}$, sort of scalar distance in the Phase-space from the optimal periodicity condition as $\{y_n, v_{xn}, v_{zn} = 0\}$.

A further characteristic of these multi-shooting technique, as given in ([H. Peng & Xu, 2015a, 2015b, 2015c](#)), is that “*the convergence increases as n increases, but the time-cost increases as well*”, where with “ n ” they refer to the number of internal points along the trajectory. For different reasons (e.g., mostly computational time and an increasing complexity of the algorithm) we have decided to adopt a single-shooting algorithm, previously defined in Section 2.4, thus taking it to the possible limits and with successfully results, as discussed later in Chapter 5. Moreover, for what has been stated before, we have decided to narrow our analysis to a resonance-range given as

$$N_{\max} = 2 \quad \& \quad M_{\max} = 5 \quad (4-57)$$

so leading to eight different cases for each simulation, with cases M2N2 and M4N2 not considered since simply redundant situations as M1N1 and M2N1. In Table 6, these eight cases has been related to the T-range previously given in Table 4 and so allowing investigating 11 cases out of the theoretical 48 possible (having 8 resonances, 3 families and 2 L-points). Important to be mentioned is that other cases can be found further extending each family, as explained in Chapter 3 in the **ADDITIONAL SETTINGS**. The discussion on main periodicity conditions and numerical validation follows again what has been discussed in Section 2.4.2, while now we continue with the Numerical Continuation technique, adopted for extending resonance orbits to the ER3BP.

4.4.3 Numerical Continuation in the eccentricity parameter

Last step of this numeric approach is based again on Numerical Continuation, previously discussed in Section 2.4.3, but here related to a different “continuation parameter”. In fact, for the Circular problem, the continuation has been made on shooting conditions by pseudo-arclength, while using their progressive location on the $\hat{x}\hat{z}$ -plane. Now, we are in a very similar situation but by means of the eccentricity e -parameter, so starting from $e = 0$ till a target value (e.g., the nominal eccentricity of the Earth-Moon system).

The eccentricity becomes now a “bifurcation parameter”, and from Figure 62 it seems clear that all resonance trajectories can be continued in the Elliptic problem based on two different shooting-times, as mentioned in Eq. (4-55). Following the same notation adopted in ([S. Campagnola et al., 2008](#)), it is possible to investigate two main situations:

- i. If M is **odd**, we can study two groups in the ER3BP, after considering the initial conditions at $\theta_0 = 0$ (*peri-family*) or at $\theta_0 = \pi$ (*apo-family*).
- ii. If M is **even**, two families arise as *left-family* or *right-family*, depending on the side (left or right \hat{x} -intercept) of the first crossing.

While the case “i” is very trivial to understand, where both shooting-times are possible for the existence of periodicity, but with clearly different effects, since masses are simultaneously close or far away from the barycentre in a No-Pulsating frame. As seen in Chapter 3, each family has two orthogonal crosses with the “symmetry $\hat{x}\hat{z}$ -plane”, thus the extension to the Elliptic problem can start with the X_0 used to generate each solution or with $X_{T/2}$ state-vector after half revolution. For what concerns the second case “ii”, after exactly $M/2$ revolutions, the orbit is back at the very same initial phase-point, which clearly can be located on the \hat{x} -left or on the \hat{x} -right. ([H. Peng & Xu, 2015a, 2015b, 2015c](#))

Due to time-constraints, only some examples will be provided in Chapter 5, thus using them as comparison in order to investigate some possible different behaviour between such bifurcated families. Clearly, this can have a large impact on real mission designs, especially when focusing on changes in the order-of-stability for different shooting-times. For the sake of completeness, all four possible cases are here summarized in Table 5, also described in (H. Peng & Xu, 2015a, 2015b, 2015c), and then illustrated in Figure 66, based on the 3D-plot for a No-Pulsating reference frame.

Table 5: Summary of all four possible groups related to periodic solutions extended in the ER3BP starting from a particular resonance periodic orbit of the Circular problem (CR3BP).

| | M | θ_0-value | M1-M2 | X-starting ($L_1 - L_2$) |
|--------------------|----------|------------------------------------|--------------|--|
| <i>Left-group</i> | even | 0 | Peri-apsis | $X_0 - X_{T/2}$ |
| <i>Right-group</i> | even | 0 | Peri-apsis | $X_{T/2} - X_0$ |
| <i>Apo-group</i> | odd | π | Apo-apsis | $X_0 - X_0$ |
| <i>Peri-group</i> | odd | 0 | Peri-apsis | $X_0 - X_0$ |

Here M_2 and L_1 are shown respectively in red and magenta for each 3D-plot, while the nominal CR3BP orbit has been given by a continuous blue line. Last, the periodic trajectory in the ER3BP is given for $e = 0.0549$ with an orange dashed line, projected in grey-colour over all three main planes, while initial condition are denoted by " \diamond ".

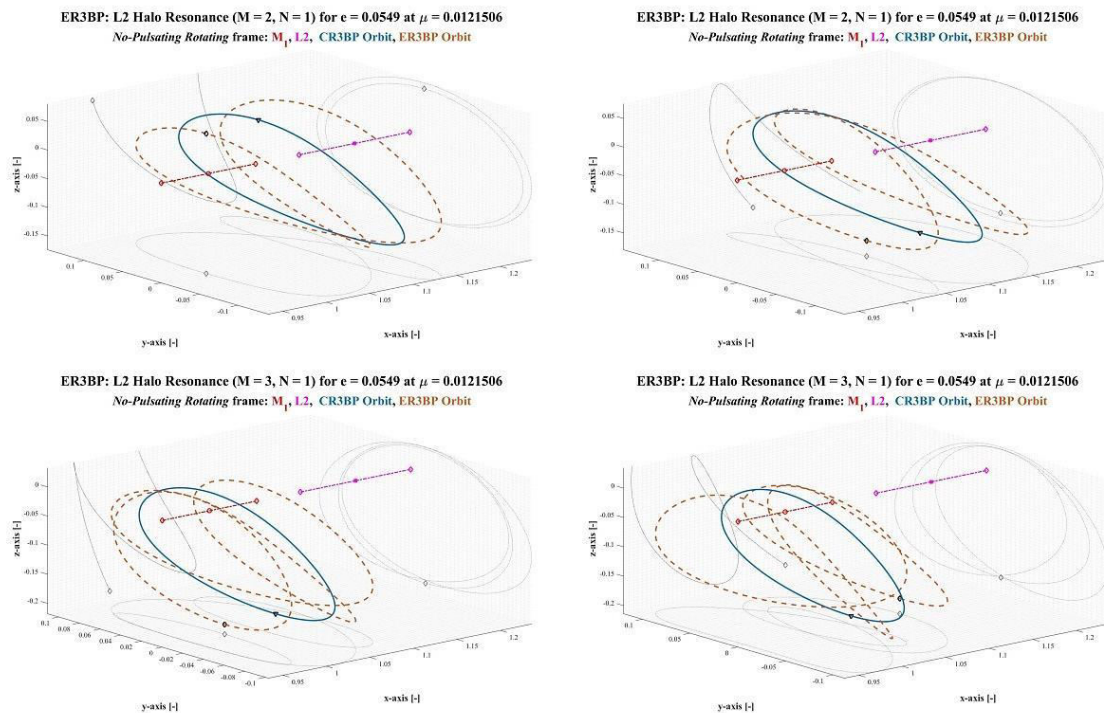


Figure 66: Example showing four examples of resonance orbits extended to the ER3BP with $e = 0.1$ within a No-Pulsating reference frame: Left-Halo "M2N1" (Top-Left), Right-Halo "M2N1" (Top-Right), Apo-Halo "M3N1" (Bottom-Left) and Peri-Halo "M3N1" (Bottom-Right).

Before presenting all results, in the next section we provide a brief summary of this “modified” numerical algorithm, adopted for the investigation on the ER3BP, and closely related to the one previously presented in Section 2.4.4.

4.4.4 Summary of the extended numerical algorithm

Main steps of this extended numerical algorithm are here summarized, using as starting point all main parameters previously saved for each family at both L1-L2. These have been found by the **Periodic L-Orbit Generator** algorithm described in Section 2.4.4, followed by a numerical continuation on the eccentricity parameter (with step-size Δe).

ALGORITHM: Resonance L-Orbit Propagator

1. Select a μ -value, the L-point (L1 or L2) and one family (H-Lyapunov, V-Lyapunov or Halo).
2. Retrieve main parameters relative to each member of the family (e.g., initial conditions X_0 , half-period conditions $X_{T/2}$ and the orbital period T_0).
3. Select a combination $\{M, N\}$ to compute T_C as in Eq. (4-52) and check its availability within the family chosen.
4. Interpolate as in Eq. (4-54) and then correct the initial condition, using Eq. (4-53) with a fixed integration period as $T_E/2$, in order to obtain $X_C^{\{1c\}}$ (Section 4.4.2).
5. Compute a first solution in the Elliptic problem using numerical continuation with $e = \Delta e/2$, small for convergence, and then apply the DC-algorithm. In this way we have obtained two different solutions as $X_C^{\{1c\}}$ and $Q_E^{\{2c\}}$.
6. With continuation by pseudo-arclength find an initial guess at $e = \Delta e$, using both previous solutions, thus leading to $Q_E^{\{3\}}$ as starting guess of the iterative cycle.

Iterative cycle:

The iterative cycle follows the exact same steps of the one given for the **Periodic L-Orbit Generator**, but this time the reference time is always $T_E/2$, with T_E as period of the new propagated orbit. For a coherent notation of the state-vector of Section 4.2, we obtain $Q_E^{\{i\}}$, $Q_E^{\{ic\}}$ referring respectively to the guessed and the corrected value for the state-vector within the Elliptic problem at $e_i \in (0, e_{EM})$.

Exit conditions:

Differently from the circular case, now we do not consider anymore “point-9”, relative to the existence of unitary real positive eigenvalues, due to what has been discussed in Section 2.2.4. Note also that the algorithm clearly stops after reaching the nominal value for the eccentricity $e = e_{EM}$, where the step-size Δe needs to be sufficiently small for assuring convergence.

END ALGORITHM

At this point of the report we are able to provide all main results for the Elliptic problem, mostly obtained through the aforementioned procedure. More information, when strictly necessary, will be given directly within each section of the following Chapter 5.

5

ER3BP: Results

In this Chapter 5 we present the main results relative to the Elliptic Restricted 3-Body Problem (ER3BP), while most of the methodologies have been already discussed within the previous Chapter 4. In analogy with results of the CR3BP, here we extend the problem to a more complex dynamics, based on a “Pulsating” reference frame, but also referring to a “No-Pulsating” frame, both co-rotating with the two principal masses. The first allows effectively calculating and extending orbits in the Elliptic problem, while the second one provides a more intuitive physical interpretation of results, as we will see. In Table 1, the nominal eccentricity for the Earth-Moon system has been approximated to $e_{EM} \cong 0.0549$, while all the entire discussion can clearly be generalized to higher values of eccentricity, still in the limits of a bounded Kepler motion for M_1 - M_2 .

In Section 5.1 we present an overview of main resonance orbits found in Chapter 3, thus in Sections 5.2/5.3 two complete examples are shown for the H-Lyapunov family at L1 (M1N1 and M2N1). It follows a third example in Section 5.4 for the Vertical family at L1. A detailed description is presented in Section 5.5, about the bifurcation of two branches during the propagation of single resonance orbits in the ER3BP, taking the Halo family found at L2 as reference point. Last, in Section 5.6, a numerical comparison on stability allows verifying these previous results, thus ‘better’ comparing the Circular model with the Elliptical model and so exploiting major advantages of this last one.

5.1 Feasible main resonance solutions

In Section 4.4.1, few additional conditions for the existence of periodic solutions have been given, as summarized in the **Elliptic Periodicity Condition**. Moreover, we have also discussed the restriction on the possible T_E -period, defined now by Eq. (4-52), while period-ranges for each family (at both L1 and L2) can be found in Table 4. Considering the Eq. (4-57), we have limited our analysis on “few” main resonance orbits, as explained in Section 4.4.2, but also later summarized in Table 6.

5.1.1 Characteristic multipliers from the CR3BP to the ER3BP

In total, 11 cases are displayed, but only the H-Lyapunov M1N1-resonance at L1 has actually a 2π -period, equal to the system revolution (non-dimensional units). For what concerns the other 10 cases, four are in a 3:2 resonance, three in a 2:1, two in a 5:2 and only one is in a 3:1 resonance. Obviously, this is due to the limitations imposed on the N_{\max} and M_{\max} , as well as for the x -range selected (from the L-point to M2) during the generation of each family. Fundamental remark is related to the discussion of Section 4.4.3, about the existence of a bifurcation in the eccentricity (here called e -bifurcation), thus having two possible cases for M being an even or an odd integer (see Table 5).

Last aspect, to be taken into account, is the linear stability assessment, in particular for the largest eigenvalue's module $|\lambda_{max}|$ of the Monodromy matrix. In a trivial way, we can observe that starting with resonance solutions having $M > 1$, the $|\lambda_{max}|$ is defined as given in Eq. (4-56), such that for the elliptic case its initial value at $e \simeq 0$ is

$$|\lambda_{max}|_{ER3BP} = |\lambda_{max}|_{CR3BP}^M \quad (5-1)$$

In the following Table 6, for each possible resonance orbit the initial order-of-instability ($\forall e \simeq 0$) has been given with the $|\lambda_{max}|$ of both CR3BP and ER3BP. Colour-notation adopted is given in the LEGEND below, while more information on these last aspects have been extensively treated in Section 4.2.

Table 6: Main resonance orbits available here for each family (at both L1/L2 in the Earth-Moon Circular problem). The range has been limited to $\{N_{max} = 2, M_{max} = 5\}$, after removing redundant cases as explained in Section 4.4.2. For each case, the order-of-instability and the largest characteristic multiplier are shown, bases on what has been stated in the text above.

| Family: | H-Lyapunov | | V-Lyapunov | | Halo | |
|---------|--|--|---|---|---|---|
| | L_1 | L_2 | L_1 | L_2 | L_1 | L_2 |
| M1N1 | II – order C: [110] E: [110] | | | | | |
| M2N1 | II – order C: [1080] E: $[1.2 \cdot 10^6]$ | | I – order C: [1547] E: $[2.4 \cdot 10^6]$ | | | I – order C: [155] E: $[24 \cdot 10^3]$ |
| M3N1 | | | | | | I – order C: [2.1] E: [9.3] |
| M4N1 | | | | | | |
| M5N1 | | | | | | |
| M1N2 | | | | | | |
| M3N2 | I – order C: [324] E: $[34.0 \cdot 10^6]$ | II – order C: [287] E: $[23.6 \cdot 10^6]$ | II – order C: [465] E: $[100.5 \cdot 10^6]$ | I – order C: [397] E: $[62.6 \cdot 10^6]$ | | |
| M5N2 | | | | | I – order C: [17] E: $[1.4 \cdot 10^6]$ | I – order C: [5.8] E: [6564] |

***LEGEND:**

In Grey, resonance orbits (r.o.) not available in our generated families.

In Green, r.o. reaching a nominal eccentricity e_{EM} with step-size $\Delta e = 10^{-4}$.

In Orange, r.o. reaching nominal eccentricity e_{EM} with step-size $\Delta e = 0.2 \cdot 10^{-4}$.

In Blue-Marine, r.o. not reaching the nominal eccentricity since diverging, after a value at around $e^* \simeq 0.0327$, to other different families (see Appendix-C).

With darker colour, resonance orbits having a period equal or larger than 2π .

Very interesting here is the very unstable behaviour of periodic resonance orbits, where necessary to underline that now we are indeed considering also a longer period (so multiple orbital revolutions). This variation is mathematically very interested for the investigation of periodic solutions, but not to forget that in practical space missions the stability needs usually to be related to a real physical time (e.g. the expected mission duration) and not exclusively to a nominal orbital revolution. (Parker, 2007)

5.1.2 Additional note on the Differential Correction algorithm

The **Resonance L-Orbit Propagator** has been schematizing in Section 4.4.4, where the iterative cycle works till reaching a convergence, only when both conditions given in Eqs. (2-65)(2-66) are satisfied. Clearly the numerical continuation (respect to e) stops if the DC-algorithm fails within a maximum number of iterations, as found in Appendix-A. As consequence of such new more unstable dynamics, the algorithm is actually stopped only when the error exceed 100 times the original threshold, so in our case at 10^{-10} . The latter allows propagating orbits till the nominal eccentricity, where the new threshold is equivalent to around ~ 4 cm in position for the Earth-Moon system.

In Figure 67, an example of accuracy validation is provided (comparable to Figure 15 of Section 2.4.2), where in black-circles we have highlighted solutions exceeding the original threshold during the propagation, thus reaching the maximum number of possible iterations. Nevertheless, only displacements at $T_E/2$ (RIGHT) have been considered as *exit-condition*, while the Position and the Velocity error at $\theta = \theta_0 + T_E$ (LEFT) have been employed only to further verify such “assumed” periodicity.

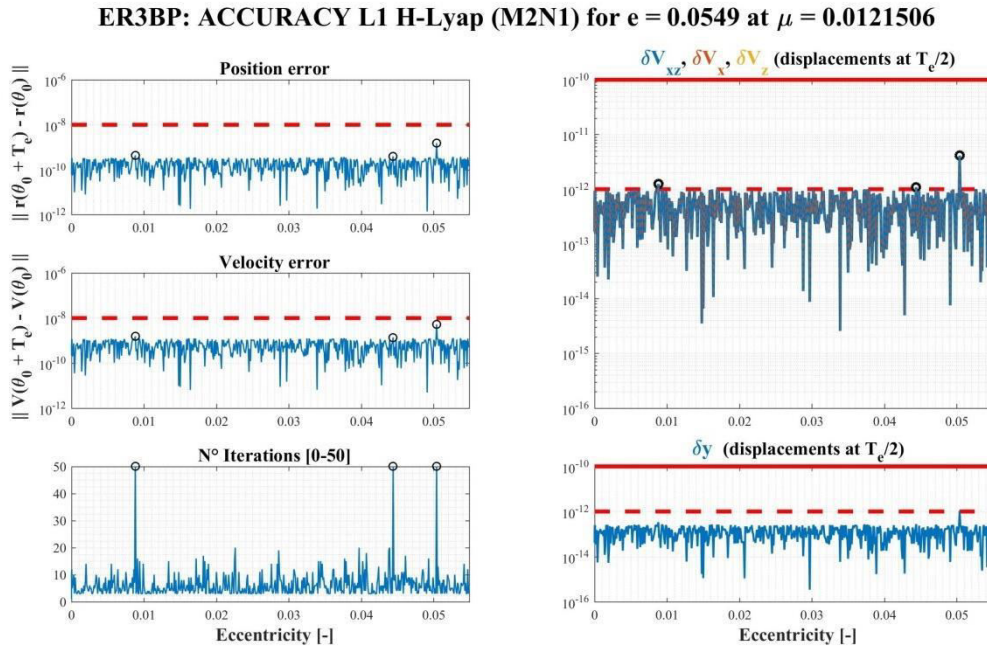


Figure 67: Example of the accuracy verification during the propagation of a M2N1 resonance orbit for the H-Lyap family (L1, Earth-Moon system). See Section 2.4.2 for more details.

At this point we can proceed presenting some main examples, where not all cases have been fully analysed due to time-limitations, thus to provide a more concise presentation of the overall investigation. Under this perspective, only most important features and differences within the Elliptic problem have been the focal point of this entire analysis.

5.2 First example: the H-Lyapunov M1N1 at L1

As mentioned in Section 4.4.3, the extension respect to the eccentricity parameter clearly involves a bifurcation, where Apo/Peri groups (if M odd) or Left/Right families (if M even) arise at $e \simeq 0$. Here we present an example considering the Horizontal Lyapunov family at L1 in resonance 1:1 with the system (so M1N1). Starting orbit has been shown in the Figure 68 below, based on the discussion of Section 4.4.2.

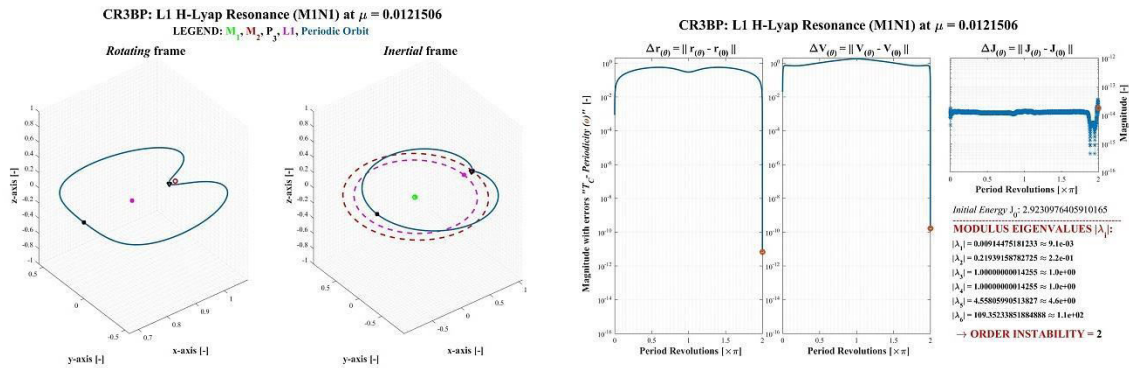


Figure 68: Example is shown of the starting resonance orbit (M1N1) at L1 for the H-Lyapunov family. On the left the 3D-plot is given in both co-rotating and inertial frames, while on the right the periodicity is shown together with all six characteristic multipliers (in module).

To observe also the energy-error $\Delta J_{(\theta)}$ computed along the trajectory, making use of the Jacobi integral since still dealing with the Circular problem (see the Energy condition in Appendix-B). In the following plots, in No-Pulsating coordinates (TOP) the original orbit (blue line) has been shown with both Peri-M1N1 and Apo-M1N1 (dashed orange line), where the position of the L-point and M2 is here obviously “oscillating” around their nominal values. In comparison, also the Pulsating frame has been shown (BOTTOM).

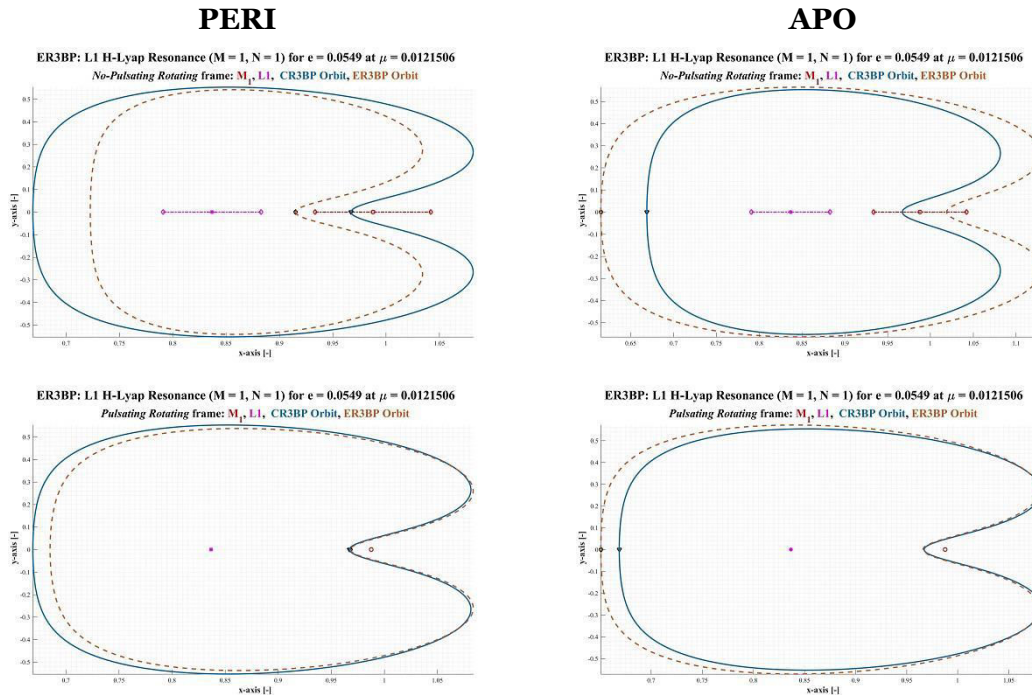


Figure 69: The resonance M1N1 H-Lyapunov orbit at L1 is shown in both No-Pulsating (TOP) and Pulsating (BOTTOM) coordinates. Note the existence of two different groups where the shooting time is $\theta_0 = 0$ on the left (PERI-), while it is $\theta_0 = \pi$ on the right (APO-).

5.2.1 Periodicity validation and eigenvalues analysis

As previously explained, here we present the periodicity validation, where in Figure 70 we have on the left the Peri-group ($\forall \theta_0 = 0$) and on the right the Apo-group ($\forall \theta_0 = \pi$).

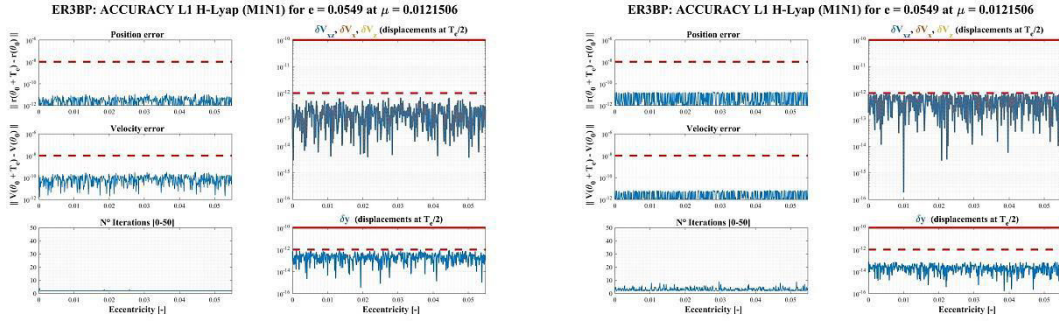


Figure 70: Periodicity validation shown for both Peri-group (LEFT) and Apo-group (RIGHT), both generated for the M1N1 H-Lyapunov resonance solution at L1.

At this point we continue presenting the eigenvalue analysis on the Monodromy matrix, based on Section 2.2.2 and later in-depth with Section 4.2.2. Once again we remind the reader that for this elliptic case no constraint exists on real unitary eigenvalues, therefore it is possible to have up to three stable/unstable manifolds (3-order instability).

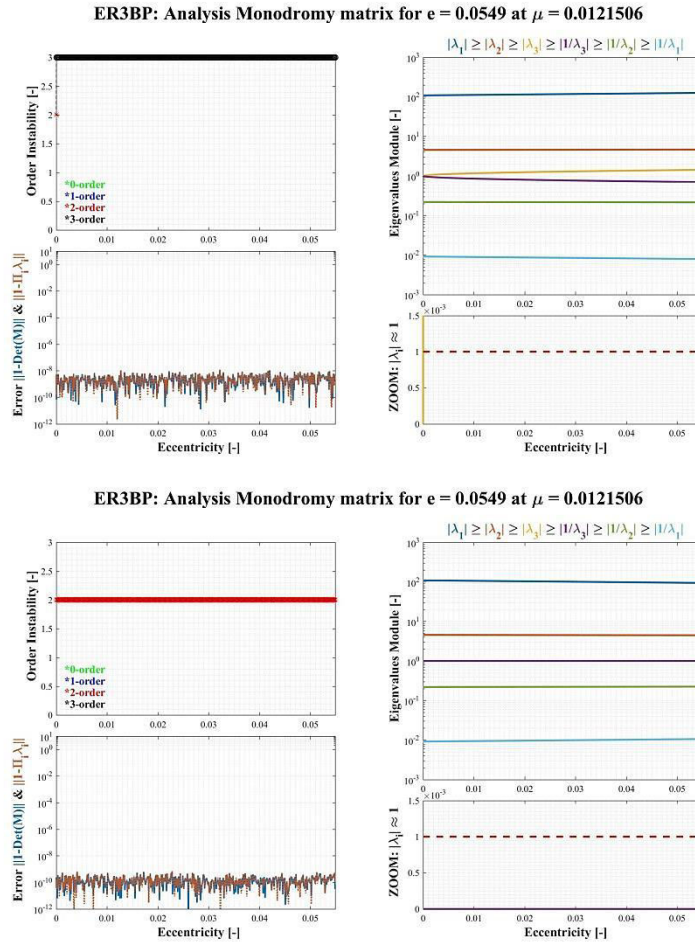


Figure 71: Analysis of characteristic multipliers for both the Peri-group (TOP) and Apo-group (BOTTOM) generated for the M1N1 H-Lyapunov resonance solution at L1. Note changes in the order of instability, due to a different bifurcation of both real unitary eigenvalues (see text).

From Figure 71, straightforward to note that even if the largest characteristic multiplier (in module) is almost constant during the e -continuation to e_{EM} , we have an additional unstable manifold direction for the Peri-group, leading to a 3-order instability. In fact, both two real unitary eigenvalues splits from the unit circle and reach respectively values as ~ 0.70 and ~ 1.43 on the real axis. For the second case (Apo-group) the two eigenvalues move on the unit circle and consequently the order of instability does not really change, ([Stefano Campagnola, 2010](#)), as also well synthetize in the next Table 7.

Table 7: Numerical values of the two real unitary eigenvalues λ_i in the CR3BP, with the relative split due to the extension to the Elliptic problem with eccentricity as $e_{EM} = 0.0549$.

| | Real Part | Imaginary Part | Module |
|-------------------|-------------------|-----------------------|-------------------|
| CR3BP | 0.999993049810342 | 0 | 0.999993049810342 |
| | 1.000006950235670 | 0 | 1.000006950235670 |
| Peri-group | 0.699273238931320 | 0 | 0.699273238931320 |
| | 1.430056155908427 | 0 | 1.430056155908427 |
| Apo-group | 0.931805002659510 | +0.362959277346590 | 0.999999999996624 |
| | 0.931805002659510 | -0.362959277346590 | 0.999999999996624 |

Incredibly, this last result is in total agreement with what we have seen in Figure 62, where two branches have been classified and analysed in ([S. Campagnola et al., 2008](#)), so illustrating the clearly bifurcation dependent upon the initial phase θ_0 selected for the successive extension to the Elliptic problem.

As consequence, the two groups found respectively as Peri- or Apo- (for M odd), have a very different linear stability, while not to forget that main driven element of instability is most-likely associated to the largest eigenvalue, where here we have that

- Max $|\lambda|$ for the **Peri-group** is equal to around 126.47
- Max $|\lambda|$ for the **Apo-group** is equal to around 94.29

again both referred at $e = e_{EM}$. More details on variations in linear stability will be given later, as also numerical simulations, while now we proceed with a comparison for M even, so again considering the Horizontal Lyapunov family at L1.

5.3 Second example: the H-Lyapunov M2N1 at L1

In the previous section, an example of e -bifurcation between Apo and Peri groups has been shown, when considering resonance orbits with M odd. At this point we can present a very similar comparison, but based on a different situation, with M even, thus distinguishing between a **Left** and a **Right** family (see Section 4.4.3). Starting point is here the M2N1-resonance for the H-Lyapunov family at L1, as illustrated in Figure 72. In Table 6, all largest characteristic multipliers have been summarized for the Elliptic problem, taking into account that $M > 1$, so considering multiple revolutions. This last aspect can be better identified in Figure 72 (RIGHT), where periodicity errors (orange circles) at the second revolution $\forall \theta = \theta_0 + 2\pi$ are much larger than the ones found in the first one $\forall \theta = \theta_0 + \pi$. Note that π is indeed the orbital period T_C for the circular case, while, for what concerns the Elliptic problem, the new period is expressed as $T_E = 2\pi$.

Here the starting orbits plotted, as previously did for the M1N1 solution.

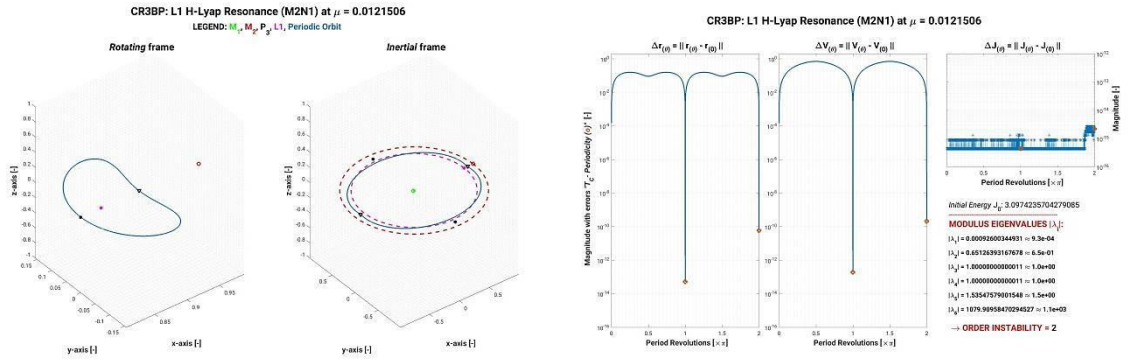


Figure 72: Example is shown of the starting resonance orbit (M2N1) at L1 for the H-Lyapunov family. On the left the 3D-plot is given in both co-rotating and inertial frames, while on the right the periodicity is shown together with all six characteristic multipliers (in module).

Let's now continue illustrating these new families generated, as for the previous M1N1 resonance case. Both Left and Right families are shown in next Figure 73, using No-Pulsating (TOP) and Pulsating (BOTTOM) coordinates, as discussed in Section 4.1.1.

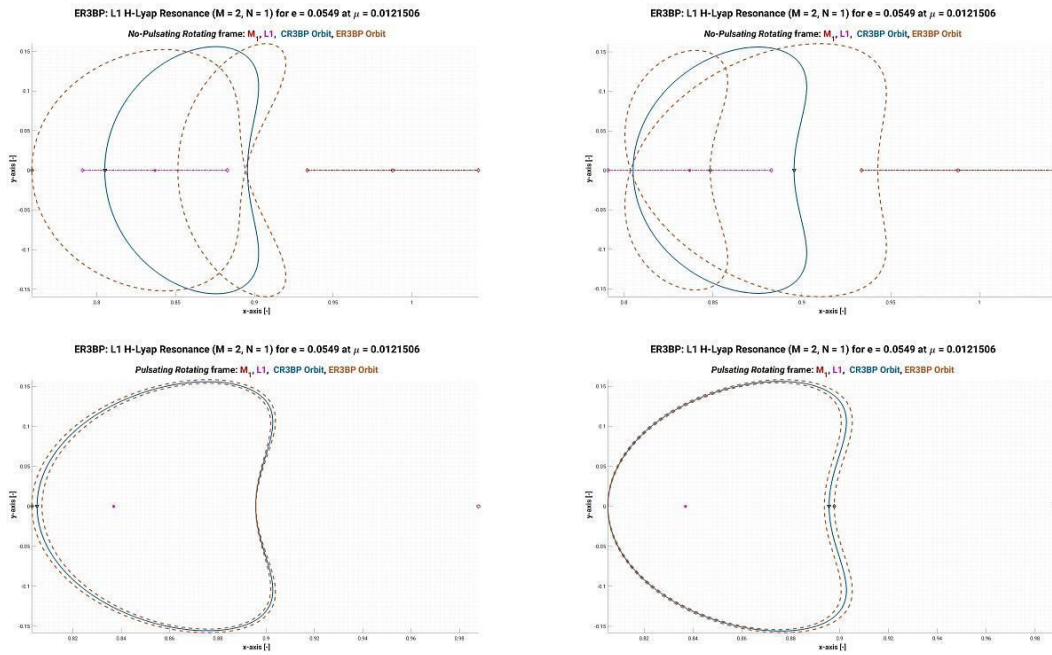


Figure 73: The resonance M2N1 H-Lyapunov orbit at L1 is shown in both No-Pulsating (TOP) and Pulsating (BOTTOM) coordinates. Note the existence of two families where the first orthogonal cross has been considered respectively at the left and right on the \tilde{X} -axis.

5.3.1 Periodicity validation and eigenvalues analysis

In Figure 74, the Periodicity validation shows always a convergence for the Differential Correction algorithm, except in a very single case where the algorithm has reached the maximum number of iterations (here 50). In that case the velocity displacement continues to oscillate between 2 and $4 \cdot 10^{-12}$, thus just above the original threshold. In that circumstance, for what has been explained at the beginning of this chapter, the propagation continues without any problems. In fact, the error is still smaller than 10^{-10} , and so capable of reaching the target value for the Earth-Moon system ($e_{EM} = 0.0549$).

Here the periodicity validation results, as previously shown also for the M1N1 solution.

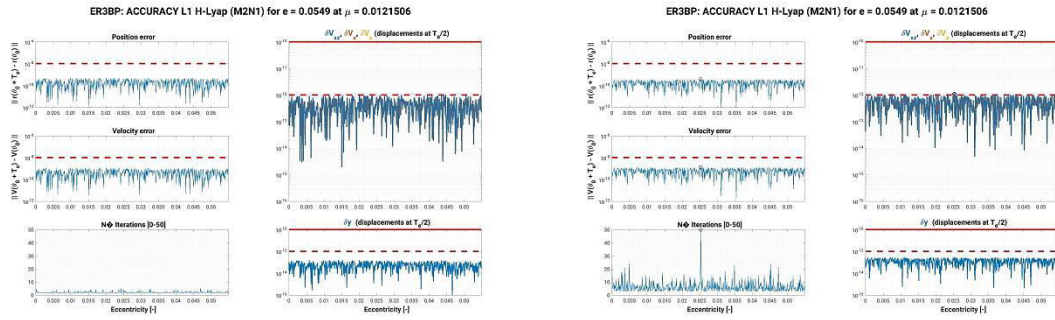


Figure 74: Periodicity validation for both the Left-family (LEFT) and Right-family (RIGHT) generated for the M2N1 H-Lyapunov resonance solution at L1.

A brief remark on a possible non-convergence is related to the high unstable dynamics of some resonance solutions, where even with strict tolerances on the integration it is not always feasible to push displacements below the nominal threshold, thus requiring more iterations. The latter can be seen more as a computational disadvantage (e.g., high CPU-time required), while periodicity has been once again verified here. More details are given in Appendix-B, while now we continue with the analysis on eigenvalues (Figure 75).

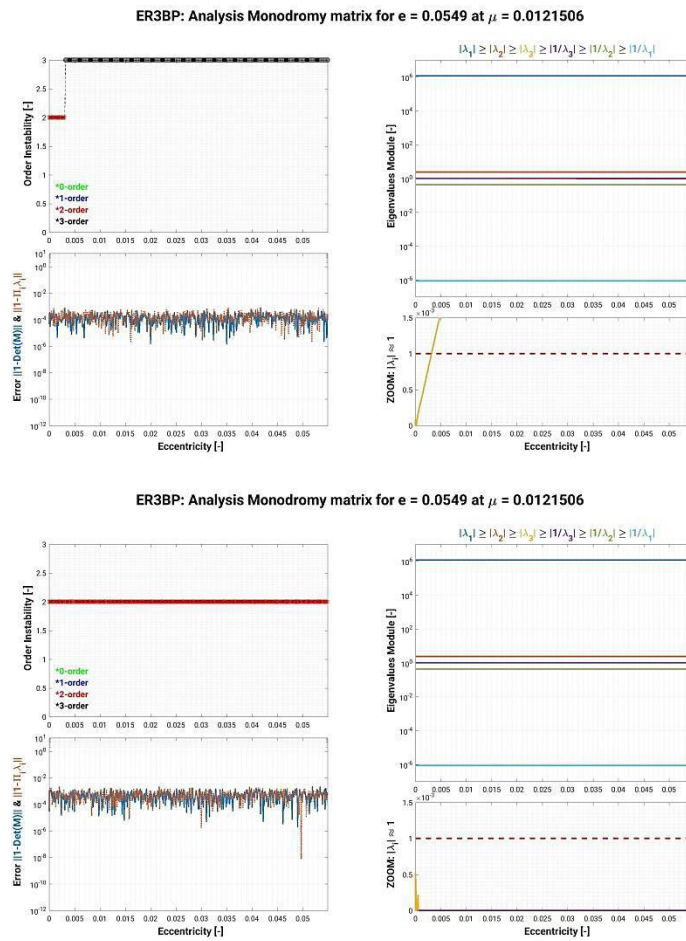


Figure 75: Analysis of characteristic multipliers for the Left-family (TOP) and Right-family (BOTTOM) generated for the M2N1 H-Lyapunov resonance solution at L1. Note changes in the order of instability, due to a different bifurcation of both real unitary eigenvalues (see text).

A different behaviour can be observed for the two different branches of the same starting resonance orbit, once again in agreement with (S. Campagnola et al., 2008). Before further discussing this aspect, a short note is required on the relative higher error found for the determinant of the Monodromy matrix. In Section 2.2.4, we have seen the necessary condition of having the determinant equal to +1, as consequence of the Symplectic form of Hamiltonian problems (so for both the circular and the elliptic case). The absolute error Δ_{tot} follows directly when considering that

$$\det(M) = 1 + \Delta_{\text{tot}} = \prod_{j=1}^6 \lambda_j(1 + \Delta_j) \triangleq \prod_{j=1}^6 (1 + \Delta_j) \quad (5-2)$$

where product of eigenvalues is nominally +1, while Δ_{tot} is the error shown in the previous plots and $\Delta_j = \Delta\lambda_j/\lambda_j$ is the relative error on each eigenvalue λ_j , $\forall j = 1, 2, \dots, 6$. Hence, assuming small errors and so neglecting their mutual product (related to higher order terms), we are able to approximate the total error as

$$\Delta_{\text{tot}} \approx \sum_{j=1}^6 \Delta_j \equiv \sum_{j=1}^6 \left(\frac{\Delta\lambda_j}{\lambda_j} \right) \quad (5-3)$$

From Eq. (5-3), it seems clear that a large error is most-likely related to the smallest λ_j when assuming similar values of $\Delta\lambda_j$. Based on this observation, the smallest eigenvalue found in our simulations and given in Table 6 is around order $\sim 10^{-6}$. It follows that even with small values of $\Delta\lambda_j$ as $10^{-9}/10^{-10}$, we will have still a large contribution to the error as 10^{-4} . Nonetheless, the effectiveness of this entire analysis can be better interfered by the continuous behaviour of all eigenvalues, as shown in Figure 75 (or also in Figure 71).

Last step is to provide some additional data on this e -bifurcation, where with Table 8 this split of the two real unitary eigenvalues becomes evident. The Left-family shows a new stable/unstable manifold direction (with a 3-order instability), while no changes actually exists in the instability order for the Right-family. For this last case, both eigenvalues indeed move exclusively along the unit circle (within the complex plane).

Table 8: Numerical values of the two real unitary eigenvalues λ_i in the CR3BP, with the relative split due to the extension to the Elliptic problem with eccentricity as $e_{EM} = 0.0549$.

| | Real Part | Imaginary Part | Module |
|--------------------|--|--|--|
| CR3BP | 0.999999999866769 1.000000000133231 | 0 0 | 0.999999999866769 1.000000000133231 |
| Left-group | 0.982722689496750 1.017581063567953 | 0 0 | 0.982722689496750 1.017581063567953 |
| Right-group | 0.999848195281841 0.999848195281841 | +0.017423770779575 -0.017423770779575 | 1.000000000698267 1.000000000698267 |

Basically, if M is even, we have two families for the Elliptic problem, where the largest eigenvalue found at e_{EM} is similar for both cases, equal to $\sim 1.165 \cdot 10^6$. At this point, a third example can be shown for M even, but within the Vertical family, which is known to be *doubly-symmetric* (X. Y. Hou & Liu, 2009) in the CR3BP. Look at Section 2.4.1.

5.4 Third example: the V-Lyapunov M2N1 at L1

Starting resonance orbit is shown in the Figure 76 below, where the double symmetry is clear with the behaviour of velocity variations respect to the shooting condition (LEFT), while crossing the \hat{x} -axis twice at the same point as $x^I = x^{II}$ with $v_y^I = v_y^{II}$, $v_z^I = -v_z^{II}$.

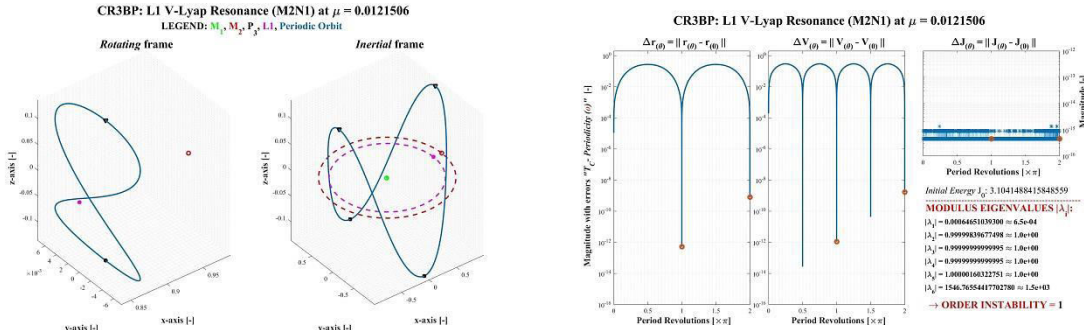


Figure 76: Example is shown of the starting resonance orbit (M2N1) for the V-Lyapunov family at L1. On the left the 3D-plot is given in both co-rotating and inertial frames, while on the right the periodicity is shown together with characteristic multipliers.

This double-symmetry based on the Mirrored-Backward transformation, presented in Eq. (2-16), has an additional evident effect. In fact, for the M2N1-resonance solution within the Vertical family at L1, we are able to compute both Left (TOP) and Right (BOTTOM) families, as shown in the next Figure 77. To note that when M is even, the shooting phase-point repeats itself at $0.5 \cdot T_E$ (or $T_C \cdot M/2$) for $e = 0$. However, it seems also evident the fact that the e -bifurcation leads now to a symmetry with respect to the $\hat{x}\hat{y}$ -plane and consequently creating a new pair of distinct Northern/Southern families.

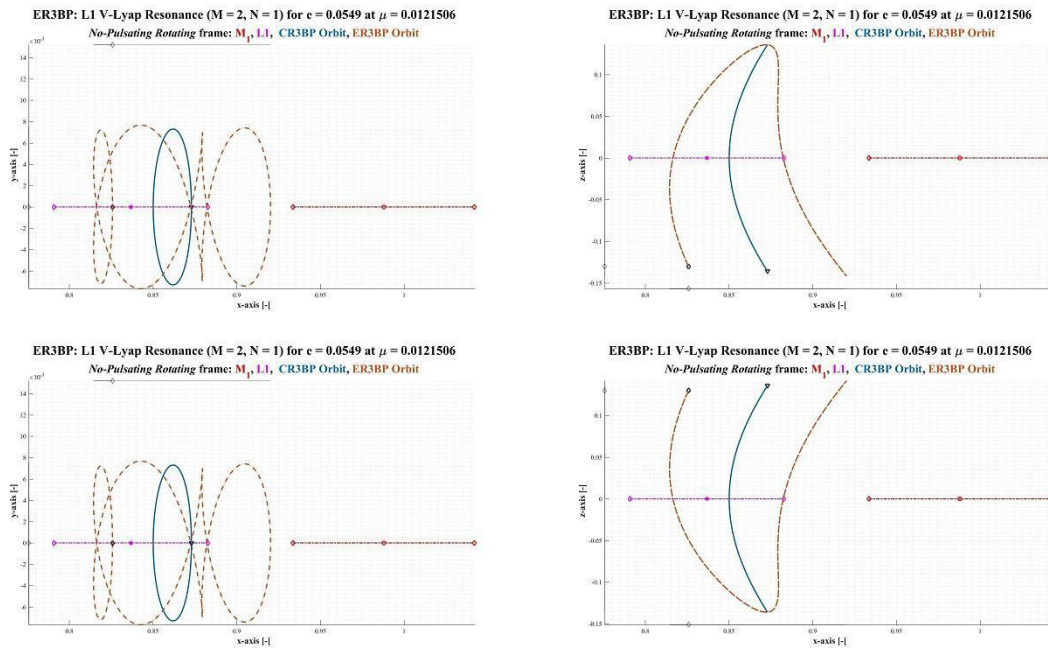


Figure 77: The Left-family (TOP) and the Right-family (BOTTOM) are shown respectively on the $\hat{x}\hat{y}$ -plane (LEFT SIDE) and on the $\hat{x}\hat{z}$ -plane in No-Pulsating coordinates. Both families bifurcated from the M2N1-resonance orbit found within the Vertical Lyapunov family at L1.

In the Circular problem both Northern and Southern Vertical families overlap by cause of the aforementioned double-symmetry, while this is not more the case in the ER3BP.

Instead, two different families arise here, but their stability behaviour is not affected at all, in analogy to Halo orbits in the CR3BP. The latter is due to the fact that the “first symmetry” in the z-direction is still valid within the Elliptic problem, along with all its subsequent proprieties. In the following Figure 78, the periodicity validation (TOP) is shown with the eigenvalue analysis (BOTTOM) for both these two families (the Left and the Right one), starting again with the M2N1-resonance orbit for the Vertical family at L1.

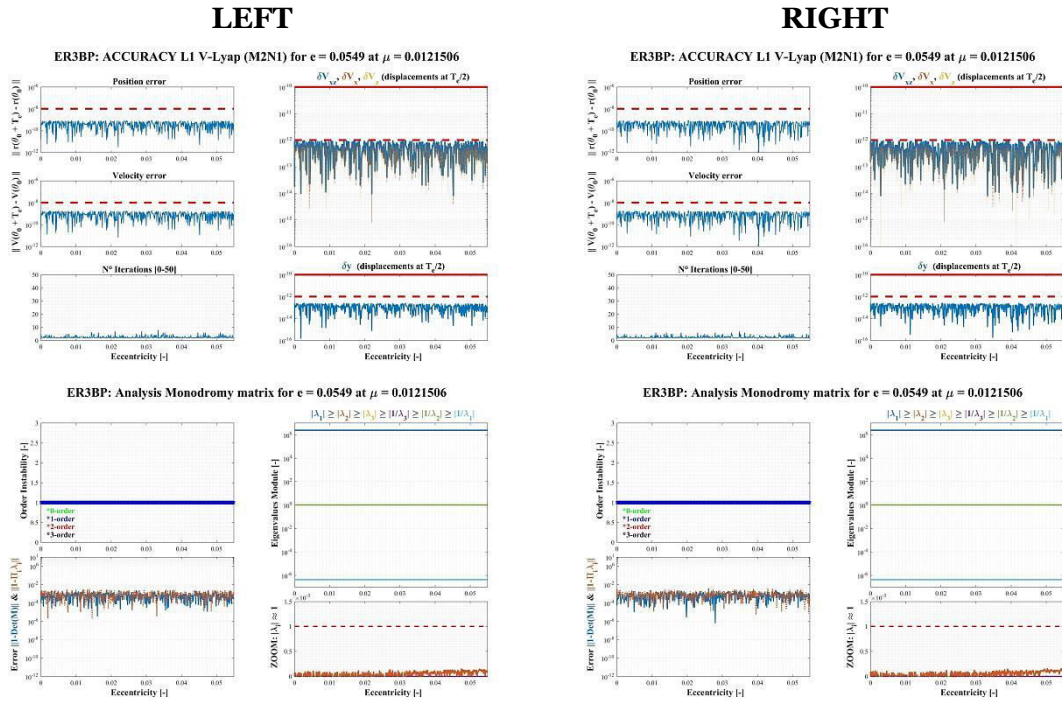


Figure 78: Periodicity validation (TOP) and Eigenvalues analysis (BOTTOM) generated for the M2N1 V-Lyapunov resonance solution at L1, where the Left-family and the Right-family have been shown, both arising from the e -bifurcation at $e \cong 0$. See discussion in the text.

For this last result, in agreement to what has been discussed before, the module of all six eigenvalues seems to not change significantly, while nothing can be added for higher values of eccentricity. In order to deeply validate the previous outcome, we provide here an extension of the analysis to a new nominal value with $e_{TEST} = 0.1$. To observe in next Figure 79, that the increasing eigenvalue (in orange) could probably lead to an additional unstable manifold for much higher eccentricity values ($0.1 \ll e_{TEST} < 1$).

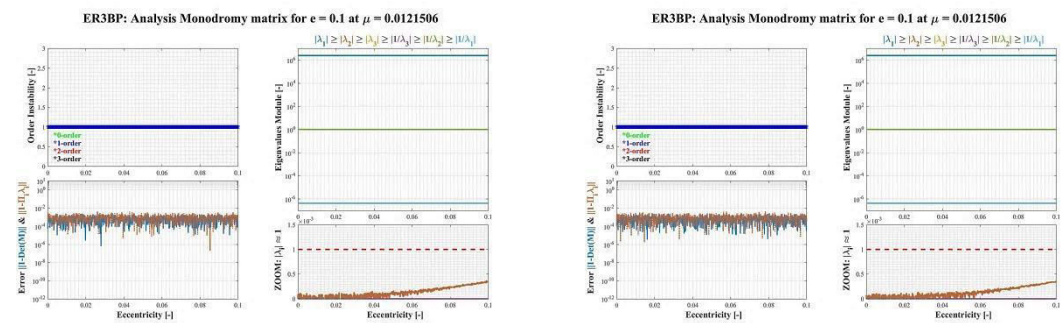
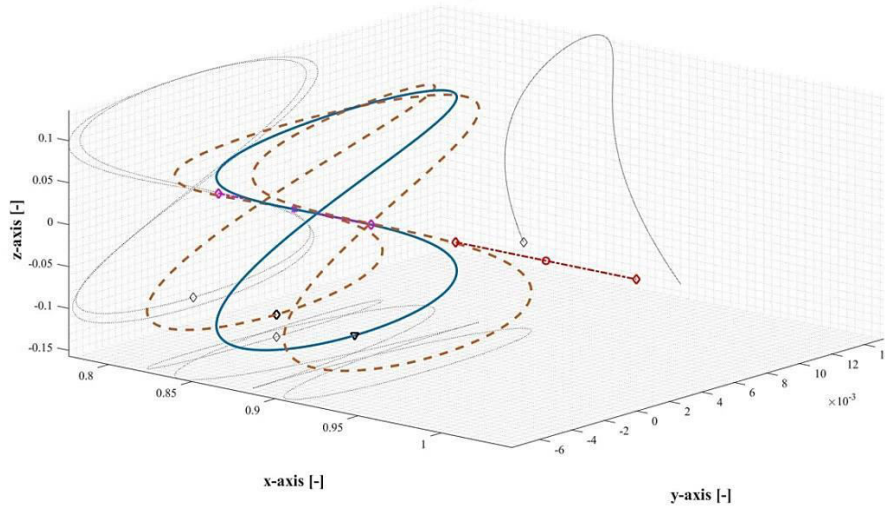


Figure 79: Analysis of the characteristic multipliers as shown in Figure 78 for both Left and Right bifurcated families, but now further extended to an high eccentricity with $e_{TEST} = 0.1$.

The analysis defined by Figure 79 has simply shown that an equivalent system (having the same mass-ratio μ) can actually involve very different behaviours when considering higher values of eccentricity. It seems plausible to infer that instability, in general, is most-likely increasing, probably due to stronger effects associated to these new “*elliptic effects*” on the nominal system. The latter has been further investigated in subsequent sections, while here, for the sake of completeness, we represent a 3D-plot in No-Pulsating coordinates for both V-Lyapunov solutions (M2N1-resonance) found at e_{EM} .

ER3BP: L1 V-Lyap Resonance (M = 2, N = 1) for $e = 0.0549$ at $\mu = 0.0121506$
No-Pulsating Rotating frame: M_1 , L1, CR3BP Orbit, ER3BP Orbit



ER3BP: L1 V-Lyap Resonance (M = 2, N = 1) for $e = 0.0549$ at $\mu = 0.0121506$
No-Pulsating Rotating frame: M_1 , L1, CR3BP Orbit, ER3BP Orbit

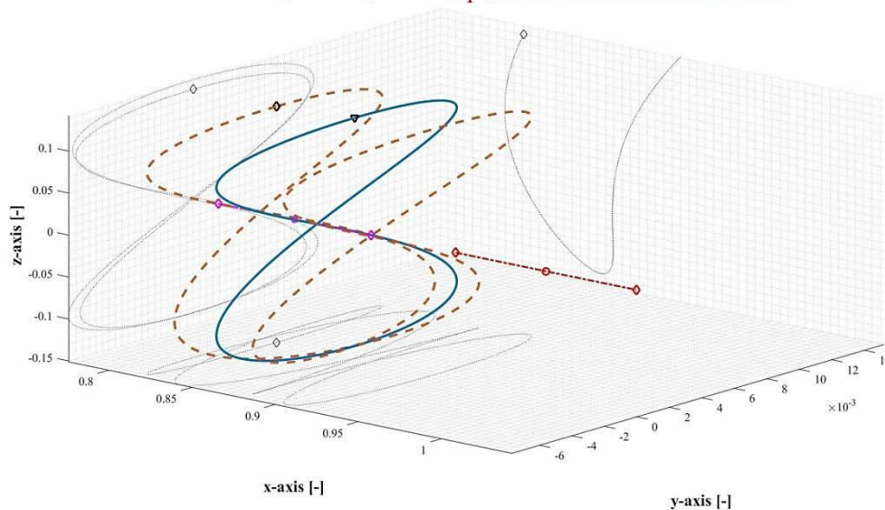


Figure 80: The Left-family (TOP) and the Right-family (BOTTOM), both bifurcating from the selected M2N1-resonance within the V-Lyapunov family at L1, have been here illustrate in a 3D-plot, based on a No-Pulsating reference frame, with the nominal eccentricity $e_{EM} = 0.0549$.

Next step is to summarize adequately some fundamental characteristics of e -bifurcations within the Halo family, also adopted later for stability comparison between the Circular and the Elliptical problem. Above all, we will highlight advantages of making use of such elliptic model in a more realistic space mission’s design. For more practical information and applications of these Elliptic-Halo orbits we refer to ([H. Peng & Xu, 2015a, 2015c](#)).

5.5 Essential aspects of the “eccentricity-bifurcation”

So far we have seen, in full agreement with (S. Campagnola et al., 2008), that a new bifurcation exists at $e \cong 0$, called e -bifurcation since involving the eccentricity positive parameter. Depending on the number of orbital revolutions M (even or odd) we have a division of the original resonance solution in two branches (the Left/Right-family or the Peri/Apo-group), as extensively discussed in Section 4.4.3. At this point the Halo family at L2 has been investigated, in order to better characterize and differentiate these two branches arising in the Elliptic problem.

The importance of considering such comparison is mostly related to time constraints in real space missions, since now the shooting-time window for having periodic orbits has been narrowed around two values, respectively when both masses are at their peri-apsis or apo-apsis. Straightforward is to understand that any deviations from such nominal conditions will in a certain way increase the mission’s costs, e.g., the DV-budget. In particular due to the necessity of perform correcting manoeuvres and so fulfilling the **Elliptic Periodicity Condition**, in addition to all main station-keeping costs related to the stability itself, as discussed in (X. Hou, Liu, & Tang, 2011). We start presenting now respectively the M2N1 and M3N1 Halo Southern resonance orbits, in order to compare first Left/Right families (Section 5.5.1) and later Peri/Apo groups (Section 5.5.2).

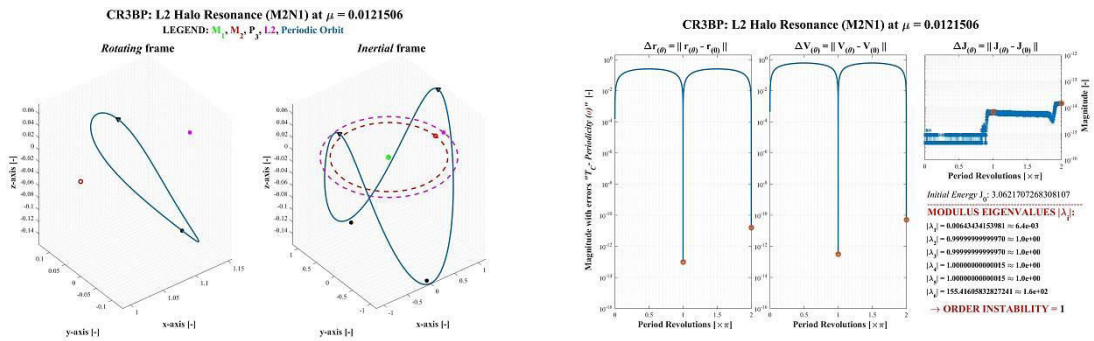


Figure 81: Starting resonance orbit (M2N1) for the Halo family at L1. It shows the 3D-plot in both co-rotating and inertial frames (LEFT) and the relative periodicity/eigenvalues (RIGHT).

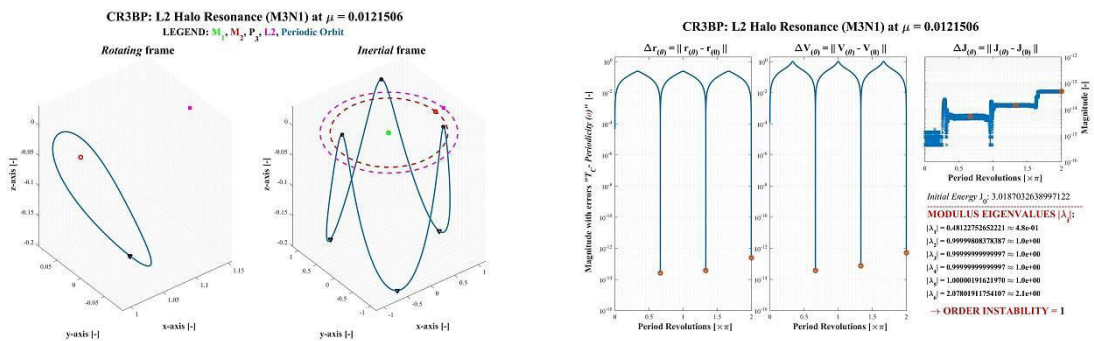


Figure 82: Starting resonance orbit (M3N1) for the Halo family at L1. It shows the 3D-plot in both co-rotating and inertial frames (LEFT) and the relative periodicity/eigenvalues (RIGHT).

As seen in Table 6, the Halo M3N1-resonance at L2 is very stable (linear stability), and with $M = 3$ the largest eigenvalue for the Elliptic problem is equal to ~ 10 . For what concerns the M2N1 case, we have a value for each revolution as ~ 150 , while the former solution, as evident in Section 3.6.1, is indeed really close to an existing “spectrally” stable zone. It is possible now to continue further analysing both aforementioned cases.

5.5.1 Comparison Left/Right families: the Halo “M2N1” at L2

In the following figure, in analogy with all previous results, we show the 3D-plot (TOP) of the resonance orbit propagated till the nominal value of eccentricity ($e_{EM} = 0.0549$), thus a periodicity validation (MIDDLE) follows with also the analysis on all eigenvalues (BOTTOM). Also to remember that since M is even, the e -bifurcation leads respectively to a Left-family and a Right-family, both closely compared in the Figure 83 below.

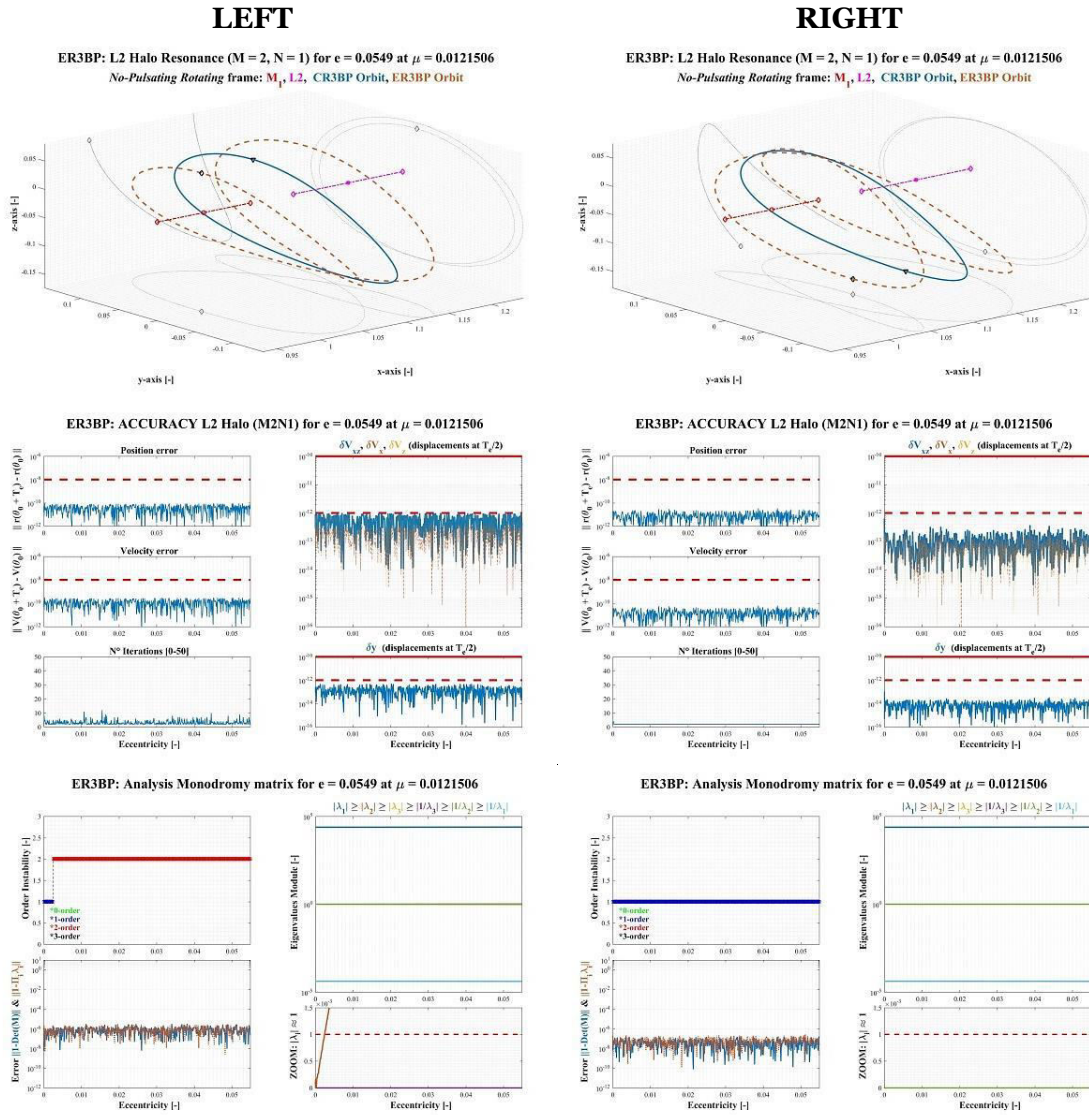


Figure 83: Illustration of the Left/Right-families bifurcating from the M2N1-resonance orbit of the Halo family at L2. The 3D-plot (TOP), the periodicity validation (MIDDLE) and the Eigenvalues analysis (BOTTOM) have been shown as well explained in the earlier results.

Both cases computed require only a small number of iterations to converge during the propagation, while few more iterations of the DC-algorithm for the Left-family are probably justified by the higher instability found (2-order). The largest eigenvalue is not very different, while for the Left-family at $e \approx 0.005$ we can trivially observe an additional stable/unstable manifold direction. In Section 5.5.3 the data relative to this “split” has been summarized with Table 9, as previously did in each previous section of this chapter. Let’s introduce at this point a second comparison, where for odd values of M (number of orbital revolutions) we arrive at the Apo- or the Peri-group of periodic solutions.

5.5.2 Comparison Apo/Peri groups: the Halo “M3N1” at L2

In the following figure, in analogy with all previous results, we show the 3D-plot (TOP) of the resonance orbit propagated till the nominal value of eccentricity ($e_{EM} = 0.0549$), thus a periodicity validation (MIDDLE) follows with also the analysis on all eigenvalues (BOTTOM). Note that since M is odd, we have a bifurcation into a Peri-group and an Apo-group, both closely compared in the next Figure 84.

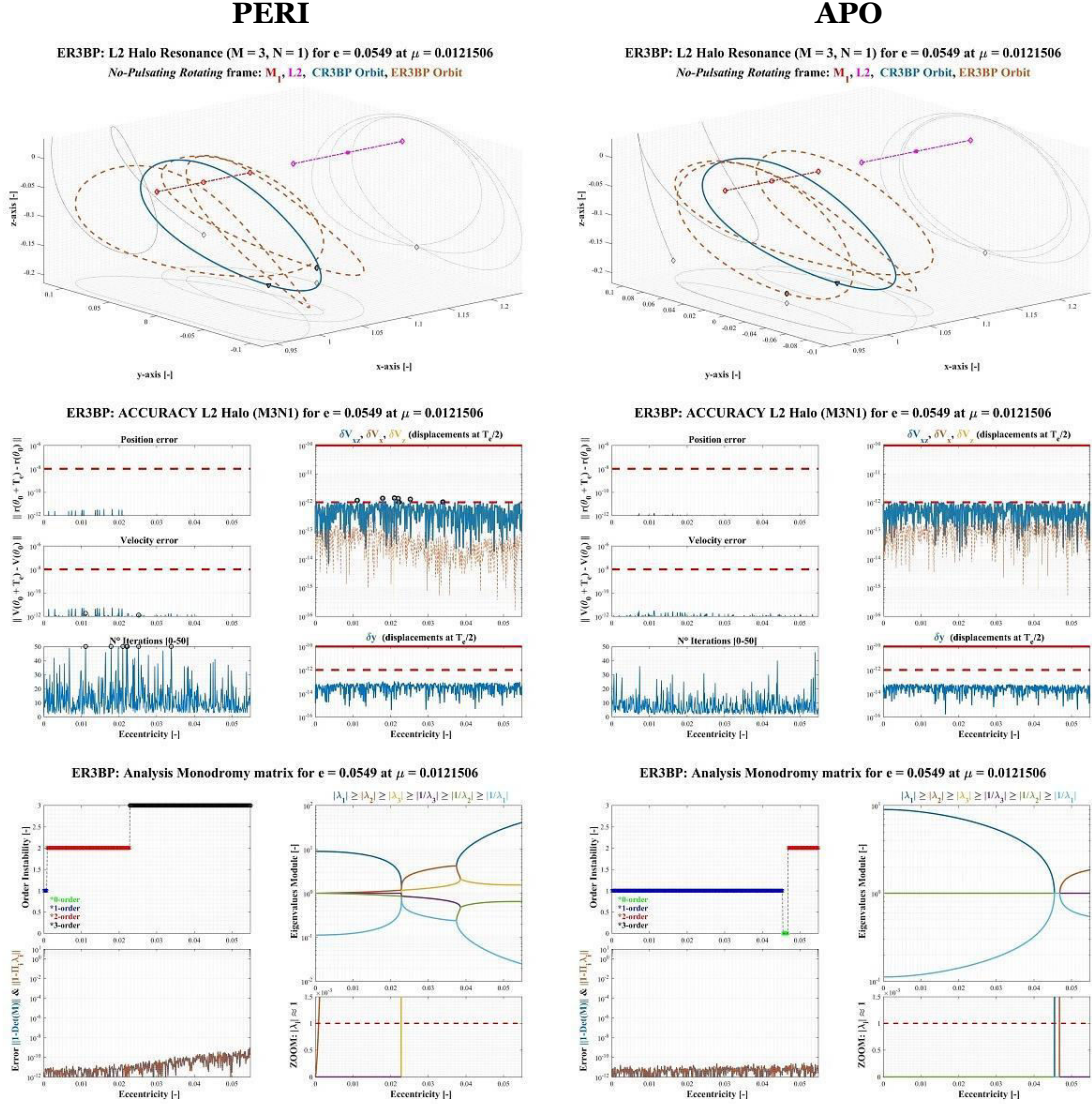


Figure 84: Illustration of the Peri/Apo-groups bifurcating from the M3N1-resonance orbit of the Halo family at L2. The 3D-plot (TOP), the periodicity validation (MIDDLE) and the Eigenvalues analysis (BOTTOM) have been shown as well explained in the earlier results.

This second comparison is really fascinating, requiring a very high number of iterations and in few cases non perfectly converging, with final displacements at around $2 \cdot 10^{-12}$. In the analysis on the Monodromy matrix, we are able to observe a very curious situation, where for the Apo-group there is actually an e -range where the M3N1-orbit is actually linearly stable, while concerning the Peri-group the order of instability only increases (with two bifurcations found). Nonetheless, at the nominal value e_{EM} both groups are actually linearly unstable, where largest eigenvalue is $|\lambda_{MAX}^{apo}| \approx 1.844$ for the Apo-group, so much smaller than the $|\lambda_{MAX}^{peri}| \approx 40.784$ found for the Peri-group.

5.5.3 Summary of e-bifurcations for the Halo family at L2

At this point, it seems reasonable to inquiry the effective meaning of all previous results, since the eccentricity of the Earth-Moon system is indeed well-known and almost fixed. De facto, we remind the reader that the latter has been selected only as a Test-Case, while similar methodologies can be applied for a more broad investigation, thus including different orbital eccentricities "e", along with other mass-ratios " μ " (e.g., binary systems). For time-limitations of this Master work, these possibilities have not been treated here, while some additional details are now discussed on what has been called "*e-bifurcation*".

5.5.3.1 Summary of e-bifurcations for the Halo M2N1-resonance at L2

The initial resonance orbit is I^o-order linear unstable, and it is possible to provide some data on all four eigenvalues initially lying on the unitary circle, as did for M1N1 and M2N1 cases of Horizontal Lyapunov orbits (both II^o-order). In next Table 9 these values have been shown, where eigenvalues related to the additional manifold have been highlighted in red, while in green same ones, but preserving their order of instability.

Table 9: Numerical values of the four unitary eigenvalues λ_i in the CR3BP for the M2N1 Halo resonance orbit, with their final values in the Elliptic problem computed at $e_{EM} = 0.0549$.

| M2N1 | Real Part | Imaginary Part | Module |
|---------------------|---------------------------|---------------------------|--------------------------|
| CR3BP | -0.899443094610471 | +0.437037892601167 | 1.000000000005865 |
| | -0.899443094610471 | -0.437037892601167 | 1.000000000005865 |
| | +0.999999997444340 | +0.000071857391491 | 1.000000000026083 |
| | +0.999999997444340 | -0.000071857391491 | 1.000000000026083 |
| Left-family | -0.904205910024912 | +0.427096794938111 | 0.99999999985193 |
| | -0.904205910024912 | -0.427096794938111 | 0.99999999985193 |
| | +0.977893773698392 | 0 | 0.977893773698392 |
| | +1.022605958621735 | 0 | 1.022605958621735 |
| Right-family | -0.903620115612936 | +0.428334783388860 | 1.00000000000558 |
| | -0.903620115612936 | -0.428334783388860 | 1.00000000000558 |
| | +0.999750008053436 | +0.022358922386245 | 1.00000000006560 |
| | +0.999750008053436 | -0.022358922386245 | 1.00000000006560 |

As expected, we see the additional order of instability arising within the Left-family, while for the Right-family we have a motion along the "unitary circle", with an absolute complex phase from $7.2 \cdot 10^{-5}$ (theoretically zero in the CR3BP) till $2.2 \cdot 10^{-2}$ at the e_{EM} . The previous bifurcation has been analysed in detail and summarized in the following Table 10, but taking into account only pairs of eigenvalue escaping from the unit circle.

Table 10: Numerical data of the e-bifurcation found within the Left-family, when starting from a M2N1-resonance orbit of the Halo family at L1. Main settings are given in Appendix-B.

| <i>Left-Family</i> | $e_{BIF}^- = 0.0024$ | \hat{e}_{BIF} | $e_{BIF}^+ = 0.0025$ |
|-----------------------|--|-----------------|--|
| Module | 0.999019468647137 1.000981493468671 | → | 0.998977975762686 1.001023069946239 |
| Real Part | +0.999019468647137 +1.000981493468671 | → | +0.998977975762686 +1.001023069946239 |
| Imaginary Part | 0 0 | → | 0 0 |

5.5.3.2 Summary of e-bifurcations for the Halo M3N1-resonance at L2

For this second comparison, the M3N1-resonance of Halo family has been considered. Initially we have four eigenvalues on the unitary circle, while for both groups (Peri and Apo) two bifurcations have been found in the propagation till a nominal value e_{EM} . Main data on eigenvalues at both $e \cong 0$ and $e = e_{EM}$ (for Peri/Apo-groups) is given below in Table 11, where all six eigenvalues have been considered due to the higher complexity of bifurcations found in this new comparison (for M odd).

Table 11: Numerical values of all the six eigenvalues λ_i for the M3N1 Halo resonance orbit, where their final values in the Elliptic problem have been computed at $e_{EM} = 0.0549$. In red, eigenvalues with a module larger or smaller than 1 (so lying outside the unitary circle)

| M3N1 | Real Part | Imaginary Part | Module |
|-------------------|--------------------|--------------------|--------------------|
| CR3BP | -0.111442638003795 | 0 | 0.111442638003795 |
| | 0.999995839315048 | 0 | 0.999995839315048 |
| | 0.046769220971739 | +0.998905721261439 | 0.99999999999569 |
| | 0.046769220971739 | -0.998905721261439 | 0.99999999999569 |
| | 1.000004160712827 | 0 | 1.000004160712827 |
| | -8.973226207746997 | 0 | 8.973226207746997 |
| Peri-group | 0.024519216502122 | 0 | 0.024519216502122 |
| | 0.587892983628985 | +0.267830791396652 | 0.646027470793888 |
| | 0.587892983628985 | -0.267830791396652 | 0.646027470793888 |
| | 1.408627963372916 | +0.641739147651266 | 1.547921791572269 |
| | 1.408627963372916 | -0.641739147651266 | 1.547921791572269 |
| | 40.784337464183267 | 0 | 40.784337464183267 |
| Apo-group | -0.056858122643957 | +0.539427770285132 | 0.542416044623851 |
| | -0.056858122643957 | -0.539427770285132 | 0.542416044623851 |
| | 0.616562343332575 | +0.787306088357874 | 0.999999999990567 |
| | 0.616562343332575 | -0.787306088357874 | 0.999999999990567 |
| | -0.193253541352812 | +1.833446516722492 | 1.843603281871466 |
| | -0.193253541352812 | -1.833446516722492 | 1.843603281871466 |

Once again we see a clear difference in final values, as also mentioned in Section 5.5.2, where for the Peri-group the linear stability assessment shows three stable/unstable manifolds against the only two of the Apo-group. In order to have a more coherent discussion we will now briefly review⁴⁰ the two bifurcations found for both cases, as previously illustrated with Figure 84 (BOTTOM).

Peri-group bifurcations:

- I. For $e_{B1}^{peri} \in (0.0454, 0.0455)$, with instability from I-order to 0-order.
- II. For $e_{B2}^{peri} \in (0.0468, 0.0469)$, with instability from 0-order to II-order.

Apo-group bifurcations:

- I. For $e_{B1}^{apo} \in (0.0008, 0.0009)$, with instability from I-order to 0-order.
- II. For $e_{B2}^{apo} \in (0.0228, 0.0229)$, with instability from 0-order to II-order.

⁴⁰ Data are here not provided in order to not overload this section with many tables, not really necessary for our qualitative discussion. Furthermore, one of the main objectives is here indeed to exploit differences and particular characteristics between groups/families, bifurcated once considering the dynamics of the Elliptic Restricted 3-Body Problem.

For the sake of completeness we provide in Figure 85 a graphic plot in the complex-plane of the full motion $\forall e: 0 \rightarrow e_{EM}$ for all previous six eigenvalues associated to the Peri/Apo-groups. We refer again to the M2N1-resonance solution in the Halo family at L2. With blue and magenta dots, respectively eigenvalues are shown for both Circular and Elliptic problems, thus the ‘asserted’ bifurcation points as black diamonds. Last, in red the full motion based on the eccentricity step-size adopted for $\Delta e = 10^{-4}$ (see Appendix-B).

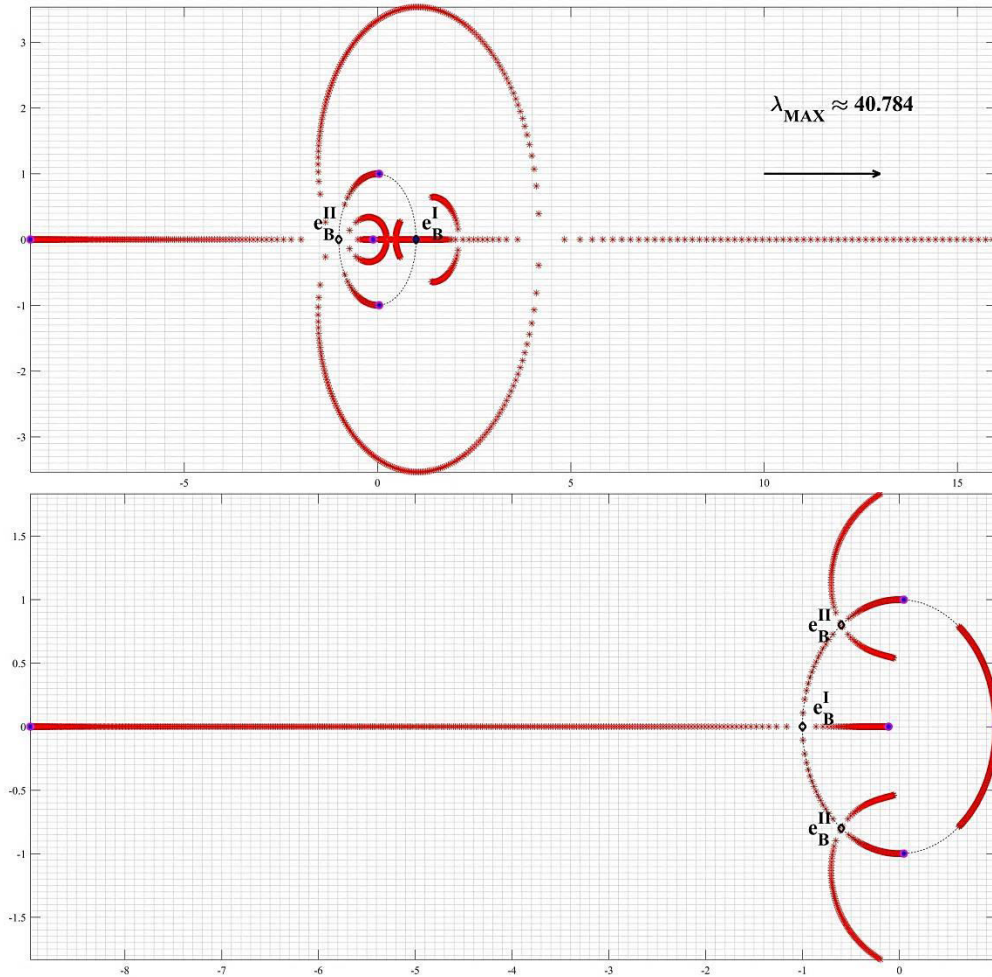


Figure 85: Illustration of the motion in the complex-plane of all six eigenvalues for the Peri-group (TOP) and the Apo-group (BOTTOM) bifurcated from the M3N1-resonance of the Halo family at L2. In blue/magenta the initial/final values, while in red the full “path” is shown.

Both previous plots show the motion of eigenvalues with both two bifurcations found during the propagation. A smaller step-size Δe allows having a better image of the real behaviour, thus leading to the possibility of evaluating also systems with a slightly different eccentricity. However, some additional bifurcations within this motion (without changes in the instability order) could be also interesting to be investigated, but here not treated. Moreover, even more important is the evident difference found, as previously demonstrated, with two distinct groups bifurcated from the exactly same Halo resonance orbit. The latter has been related to the specific initial phase adopted once propagating this reference orbit toward the Elliptic problem. More details on additional very similar e-bifurcations, also for no changes in the order of instability, has been well described in (H. Peng & Xu, 2015b). At this point, we proceed with the last very step of this chapter: an example for the numerical comparison between the Circular and the Elliptic model.

5.6 Linear stability comparison: Circular vs Elliptical

In this section we numerically test one among all the previous cases investigated. Main objective here is not to compute an effective periodic trajectory for the Earth-Moon system, but mostly to highlight the importance of considering the ER3BP as reference model for practical space mission planning and optimization. Again, we need to remind the reader that optimal transfer orbits, along with the characterization of stable/unstable manifolds, are not parts of this work, nonetheless we focus on two principal aspects:

- i. The consequence of adopting shooting conditions found from the Circular model into the full dynamics of the ER3BP, which better exemplify the real physical Earth-Moon system, as fully treated in Section 2.1.3.
- ii. At what extend it is possible to consider acceptable a small mismatch in the shooting-phase required by the **Elliptic Periodicity Condition**, while clearly that aspect does not affect at all the numerical integration within the CR3BP, since dealing with a *time-invariant differential system* (see Section 2.2.1).

For what concerns the first point “i”, we start considering the M3N1-resonance of the Southern Halo family at L2, previously treated in Section 5.5.2, while both two groups (Peri and Apo) bifurcated at $e \cong 0$ have been represented in Figure 84. At this point we consider again the Pulsating frame, where libration points have been found to be numerically the same for both models (Section 4.1.2). Thus, it is possible to consider initial conditions found from the CR3BP and the ER3BP, starting with $\theta_0 = 0$ or $\theta_0 = \pi$.

The resonance orbit shown in Figure 86 is very close to the Moon, perfect for observation missions of the gravity field, but with an apogee far enough for assuring communication and data transfer with the Earth. Under this perspective, an example is given where the trajectory is numerically integrated till divergence. This divergence is delineated by a boundary zone at $1.5 \times R_H$, where R_H is the Hill’s radius (here ~ 0.160) that ‘nominally’ define the so called Sphere-of-Influence of a single mass. ([Musielak & Quarles, 2014](#))

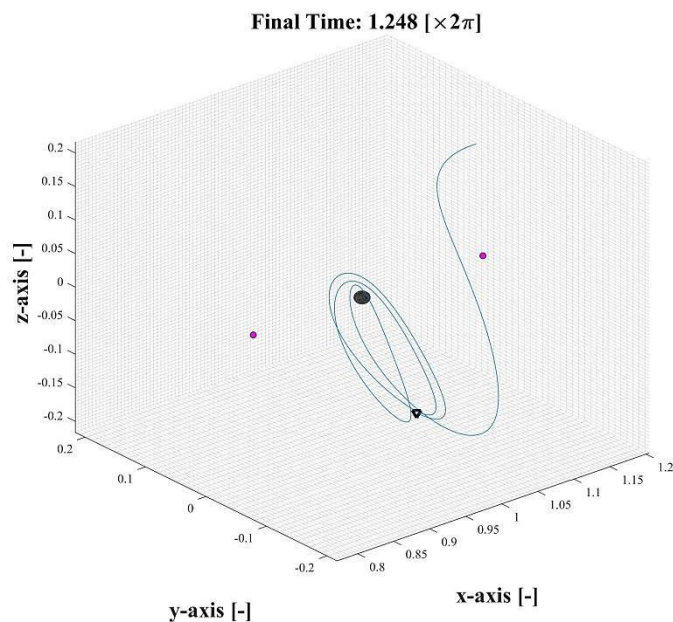


Figure 86: Illustration of the M3N1-resonance orbit integrated in the full dynamics of the Elliptic problem ($e_{EM} = 0.0549$), starting with the shooting condition previously found in the Circular model. In magenta both libration points have been shown.

In the previous Figure 86 we can clearly note that the “Circular shooting condition” is not able to well-propagate the resonance orbit within the full dynamics of the ER₃BP, which is supposed to be a much more correct approximation of the real EM-system. Clearly, the trajectory diverges in around one system revolution, so around three orbital rounds around the Moon. It follows that a mission based on such “design” is still possible but most-likely it involves higher costs for station-keeping and correcting manoeuvres.

5.6.1 Numerical stability of Peri/Apo-Halo M₃N₁-resonances at L₂

At this point, we can compare the previous result with a numerical propagation (in a very similar way) but starting with initial conditions found for the Peri and Apo groups bifurcated at $e \simeq 0$. Shooting conditions are given in Table 12, where we again stress the fact that this comparison has been placed within a Pulsating frame. Indeed, for this frame the location of masses and L-points is numerically the same for both models.

Table 12: Shooting conditions found in the Circular and Elliptic model for a M₃N₁-resonance Halo orbit at L₂ in the EM-system. Data refers to Pulsating coordinates (see Section 4.1.1.2).

| I.C. | CR ₃ BP | Peri-ER ₃ BP | Apo-ER ₃ BP |
|------------|---------------------|-------------------------|------------------------|
| X_0 | +1.063785954070617 | +1.061252432204949 | +1.063712371738405 |
| Z_0 | -0.200401559160425 | -0.177952611695976 | -0.212459411426779 |
| V_{Y0} | -0.177610250323491 | -0.206741611293892 | -0.163118549852345 |
| θ_0 | <i>Not relevant</i> | 0 | π |

Graphical results are shown in the figure below, where clearly both new simulations are able to exhibit a ‘longer’ stability. Considering an hypothetical DV-budget, it seems reasonable to assume that lower costs will be involve for these last two cases. More interesting is also the confirmation of what has been found in Section 5.5.2, with the M₃N₁ Apo-group much more stable than the Peri-group, due to the smaller $\|\lambda_{MAX}\|$ (see Table 11). In both cases, the trajectory is able to remain bounded near M_2 for a very long period, while additional manoeuvres are still necessary for much more accurate missions, in order to assure that the spacecraft correctly follows this “operative orbit”.

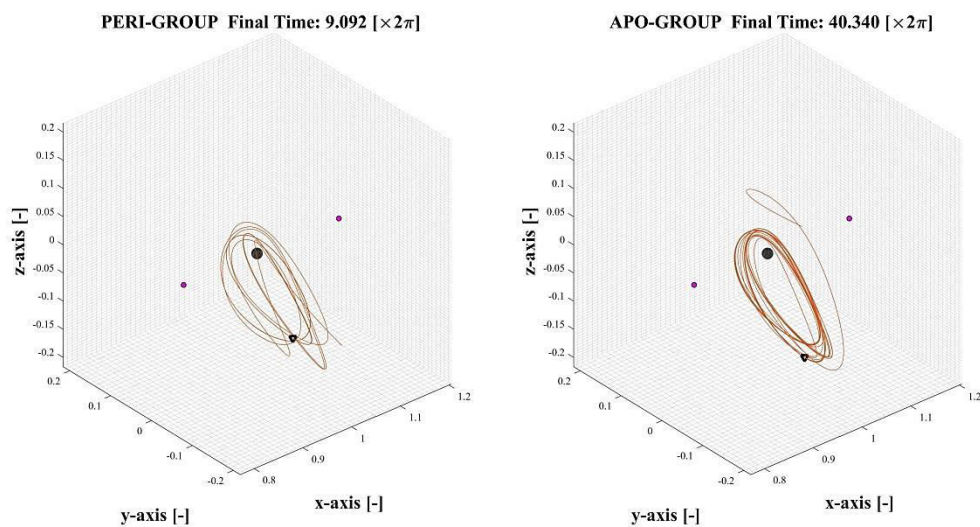


Figure 87: Numerical integration of the M₃N₁ Halo at L₂, using the full ER₃BP-dynamics and starting with shooting conditions found respectively for the Peri-group (LEFT) and for the Apo-group (RIGHT). In magenta both libration points have been shown.

For a clearer picture of such “assumed” higher accuracy, we show in Figure 88 both the Position and the Velocity displacement respect to each shooting condition previously given in Table 12. These two displacements are shown, still in Pulsating coordinates, with their “periodicity error” (given with red dots) being evaluated at $\theta = \theta_0 + k \cdot T_E, \forall k \geq 1$, thus considering both the Peri-group (TOP) and the Apo-group (BOTTOM).

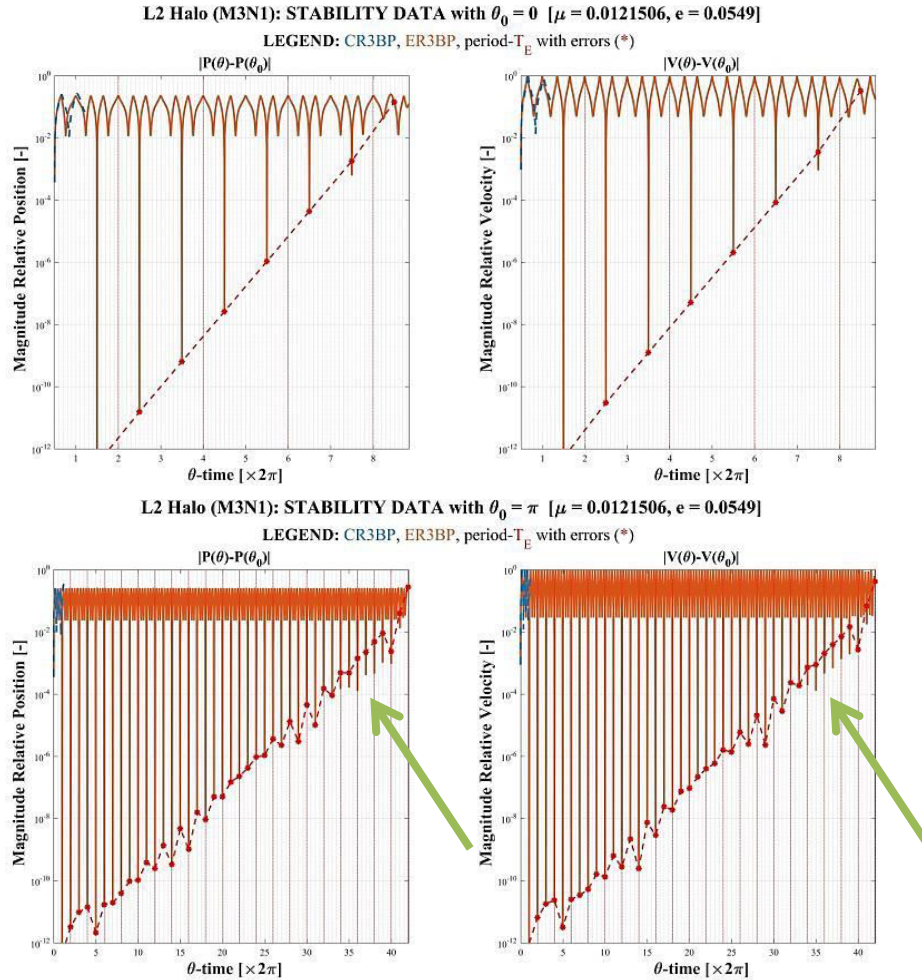


Figure 88: Numerical integration of the M3N1 Halo resonance orbit at L2 for the Peri-group (TOP) and the Apo-group (BOTTOM), where position and velocity displacements from respective initial conditions (in orange). All T_E -periodicity errors are shown (in red-dots).

An increasing trend is clearly observed, where errors grow at each revolution due to the linear instability. At the very end, we are able also to see that the phase synchronization has been lost, with red-dots not more related to the smaller displacement found at a specific n -revolution (green arrows). The displacement for the circular case is shown in blue, but related to very large errors order 10^{-2} (so thousands of km). The last example can be regarded as an additional confirmation of the necessity to take into account “ellipticity effects”, above the nominal dynamics given by the less accurate CR3BP model.

As stated in (H. Peng & Xu, 2015a, 2015b, 2015c), “In the Earth-Mon system, a reference orbit designed in the CR3BP requires frequent station-keeping manoeuvres to offset perturbations introduced by model errors. Energy cost can be reduced if a better nominal orbit in a more realistic model is adopted”. The latter very well summarizes what has been stated so far, in relation to all major advantages of using an ER3BP model.

5.6.2 Numerical stability due to shooting-phase errors

On the point “ii”, we briefly consider again the previous case, starting with an Apo-Halo M3N1-resonance at L2 and later numerically integrating it for 18 system revolutions (equivalent to 1.5 year integration in the Earth-Moon case). Furthermore, Position and Velocity displacements from the shooting-condition have been shown, but now only referring to the T_E -periodicity. Basically we are looking at the magnitude of red-dots, as found in Figure 88, but using shooting-phases slightly different from the nominal one.

We consider a maximum error in the initial shooting-phase as $\Delta\theta_0^{MAX} = \pm\pi/360$, so equal to around 3280 seconds (or around 50 minutes), while step chosen is 50 times smaller, thus equivalent to around 1 minutes in the Earth-Moon case. This serves just to show that errors can grow in multiple revolutions not only for the dynamical instability, but also due to an initial phase-shift (see the **Elliptic Periodicity Condition**). However, absolute errors have been shown here in a 2D-plot based on a log10 colour-scale, where in blue we have the simulation with a nominal shooting-phase (as in Figure 88). For this last case the periodicity error has been found to be initially smaller than 10^{-12} , as consequence of the threshold adopted by the DC-algorithm.

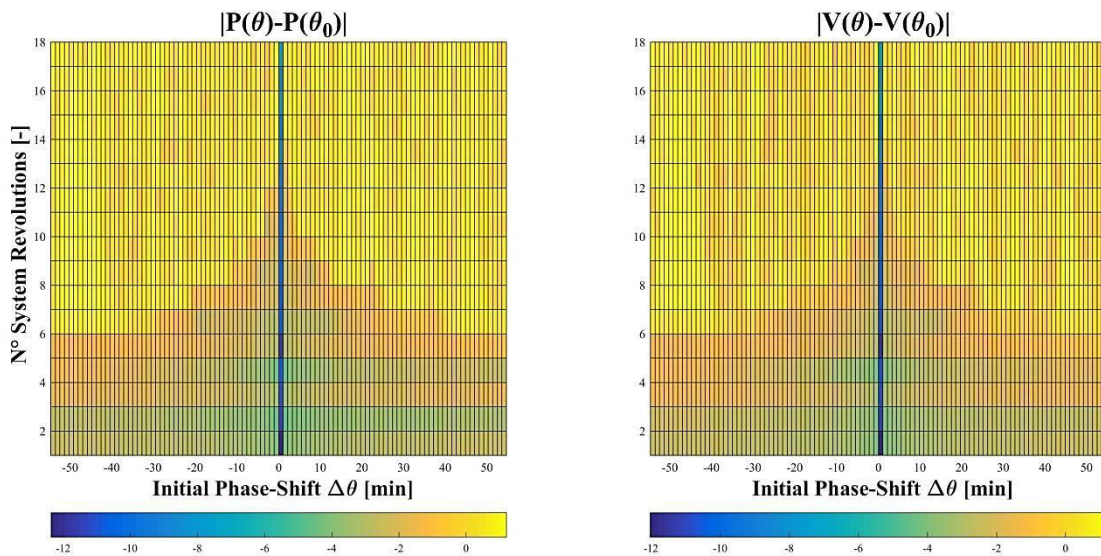


Figure 89: Illustration of position and velocity “periodicity errors” referring to 18 system revolutions and a range of phase-shift from the nominal shooting-time as $\pm\pi/360$. Absolute errors are given in a Log10 scale, while time-shift is based on minutes for the EM-system.

Very last observation, we underline that the darker area found in both previous plots is related to absolute errors still in an acceptable range below 10^{-4} (so dozens of km). Nonetheless, the smaller the errors, the smaller are corrections required and with it the overall maintenance costs of the mission (Koon et al., 2008). In addition, a generic phase-shift could also be combined with other shooting errors (but here not shown), thus further complicating the dynamical motion, already subjected to the highly unstable dynamics, as established during this investigation over the ER3BP.

6

Conclusions

In the last Chapter 6, the research journey of this Master thesis report comes to an end. Many aspects have been deeply investigated, many others have been only mentioned and several analyses also performed to provide the reader with an exhaustive overview on the celestial mechanics problem treated in this work. Primary effort has been devoted to well summarize the current state-of-the-art knowledge, involving most recent literature, so comparing it with our major results, along with a more general background ‘picture’ of what has been inspected here.

In Section 6.1, leading conclusions have been presented, based on what discussed so far, thus following the central workflow structure of this Master thesis project, as illustrated in Figure 1. Later, in Section 6.2, some recommendations on this research topic have been introduced, as well as for all main methodologies adopted. This last brief discussion serves to complete and to conclude this entire analysis, but most important aiming to establish a fundamental research’s step, as pivotal starting point for future investigations on very similar research topics.

6.1 Conclusions

The examination over some types of solutions has been the focal point of this Master thesis, when considering two dynamical models, first with the Circular Restricted 3-Body Problem (CR3BP) and later with the Elliptic problem (ER3BP). Main purpose has been the analysis and comparison between both models, while the Earth-Moon system has been test-case for all the numerical simulations. Particular solutions have been studied at two equilibrium points of the system, nominally L1 and L2, while three different families have been taken into account: both the Horizontal/Vertical Lyapunov families and a third one well-known as the Halo family.

With the use of the Dynamical System Theory, it has been possible to deeply observe main features of what we remind to be just part of the more complex real dynamics described by such models. Above all, periodic solutions have been examined, along with their linear stability and possible bifurcations in the continuous families found within the Circular problem. Next, specific members of these families (here *resonance orbits*) have been extended, under some particular assumptions, into the ER3BP model, while the named *eccentricity-bifurcation* has shown some additional peculiar characteristics to these solutions.

In the CR₃BP it has been shown that, for a particular co-rotating reference system (also defined as synodic), both main masses are fixed and they generate indeed a gravitation potential field, along with all the “fictitious forces” introduced when considering a non-inertial frame. Due to symmetries within the differential problem, some conditions arise on the existence of periodic orbits, while a closer analysis on their linear stability (based on characteristic multipliers of the Monodromy matrix) has been able to show how such solutions are actually embedded in continuous families. When extending periodic solutions from the Circular model to the Elliptic one, a dominant role is played by the time-like parameter of the system, here defined by the relative orbital phase θ between main masses. At this point, it should be possible to answer to the **Main Scientific Question** (as given in Section 1.3), in this way emphasizing some most critical aspects of the dynamics related to the Elliptic Restricted 3-Body Problem.

ANSWER TO THE MAIN SCIENTIFIC QUESTION:

The destruction of continuous families is here a very first critical element, where periodic solutions still exist but only at some resonance points, thus theoretically generating discrete families. Even under small “*elliptic perturbations*”, resonance effects remain predominant and can strongly influence costs of orbit maintenance and station-keeping manoeuvres. In addition to that, a second critical element arises due to the new time-constraint on shooting conditions, well summarized in the so-called **Elliptic Periodicity Condition**. The latter allows having distinct situations, where each solution actually bifurcates into two different branches, based on the specific shooting-time chosen. Main consequence is the possible very different behaviour, still referring to a linear stability, while periodic solutions in the ER₃BP seem to be in general much more unstable. In comparison with this model, other types of perturbations (as listed in Section 2.1.3) do not actually involve such time-dependence, but they are still able to well approximate the motion of a more complicate physical world. Practically, the major consequence of extending the standard Circular problem to the Elliptic one can be properly shortened in the new “direct” time-dependence found within the differential system, due to this elliptic bounded Kepler motion of both main masses.

ANSWER TO RELATIVE SUB-QUESTION:

Five main sub-questions have been given in Section 1.3, in order to better define what is the aim of this Master work, along with major focal points of the research here proposed. First of all, it has been necessary to comprehensively well define the Circular Restricted 3-Body Problem, in the limit of some choices made for the simulations (e.g., Lagrange points and families selected). In this first step (as shown in Figure 1), the linear stability has been assessed with the use of the Monodromy matrix, thus looking at the local dynamics around such trajectories. The latter has allowed discovering bifurcations within each family, where we remind that the bifurcation parameter is here the distance of each member from the nearest Lagrange point, as measured along the syzygy direction (connecting both M_1 and M_2). Type and location of all bifurcations is related to the selected μ -parameter, but here fixed to μ_{EM} for the Earth-Moon system. Moreover, the very fascinating aspect is here the birth of additional periodic families, starting from Tangent-bifurcations (Section 2.2.5), along with the existence of quasi-periodic ones.

Bifurcations treated here are connected to changes in the order of instability, where the linear stability of members within a family could be related to the \hat{x} -position of these “division points”. In Appendix-B, a further verification has been presented in relation to the unstable dynamics of the CR3BP (with numerical implications), as also for the importance of considering such bifurcation points. In fact, close members within the same family can have a very different behaviour, due to a different order of linear instability, and so involving a different number of stable/unstable manifolds.

The inspection of the Elliptic problem has shown many interesting characteristics. In first approximation, “elliptic perturbations” have been considered for a very small eccentricity value, principally based on an analytic approach. It has been possible to observe resonance effects related to this new dynamics, while the higher instability has been exploited later by the numerical computation of periodic orbits, in agreement with most recent literature. This type of trajectories still can exist for the general elliptic case, but subjected now to more strictly conditions, thus adding difficulties in their precise determination. Only solutions in resonance with the system can survive in this new model, while also indispensable is here the **Elliptic Periodicity Condition**. From this last condition it follows the existence of two different branches of the same solution, depending on the precise shooting-time for the third negligible mass.

Last, sub-question “V” is actually more generic and has not really a unique answer, where advantages of using a more complex dynamical model need often to be traded with other additional aspects. For example, the accuracy required by the model itself, depending also on what are the designed “mission objectives”, along main tolerances allowed for the nominal mission. For this reason, this entire research has been carefully described steps by steps within this report, providing all main settings and relative assumptions, in what can be regarded as a coherent and robust procedure.

COMMENT ON THE RESEARCH OBJECTIVES:

This Master work has introduced many methodologies, with the combination of both the analytic and the numeric approach for investigating principal features of these two models. The analysis, mostly based on the Dynamical System Theory, has presented an extensive survey of properties for the Circular model (in Chapter 2) and later for the Elliptic one (in Chapter 4). In this way it has been possible to delineate a systematic process, capable of leading to large insights in the dynamics. In addition to that, to be underlined that a similar scheme could have also been applied for any other 3-Body systems, as long as assumptions remain valid (or at least are acceptable).

Second objective has been to highlight distinctive elements of the ER3BP, for example related to resonance effects found under small “elliptical perturbations”, as well as for new constraints on the shooting-time suitable for such particular trajectories. Displacements from ideal conditions lead indeed to an unbounded drift, far away from the target orbit, while the non-existence of a First integral (the so-called Jacobi constant) complicates even more the situation. Moreover, the direct dependence on the time-like parameter has been designated as peculiar aspect of the Elliptic problem, while other perturbations, as oblateness or solar radiation, can be still characterized by an autonomous differential system (or by a time-independent potential function).

Last, not less important, we have seen in Section 5.6 some major outcomes when considering the more complete dynamics of the Elliptic problem. In particular, shooting-time becomes a very strict constraint, where also small shooting-phase displacements can have large effects on periodicity errors. Neglecting the ellipticity of main masses, the third small mass most-likely will deviate from its “operative trajectory”, with a clear consequence on the maintenance and station-keeping costs. However, most relevant is here the very different behaviour of bifurcated solutions, due to the fact that their stability proprieties (in a linear analysis) will now depend upon the shooting-time initially selected at the starting point of such periodic orbits.

6.2 Recommendations for future works

As discussed, the work represents a general investigation over different models, with an analysis limited to only certain families of periodic solutions, involving “Lagrange orbits” found in a neighbourhood of two equilibrium points of the system (here L1 and L2). Nonetheless, the reader should be aware that many parts of the discussion are still currently being investigated by many researchers and could be subjected to substantial modifications, thus reinforcing the necessity to always validate results with the most recent literature available. In the next list, some possible further developments for this Master thesis work are given, as summary of principal aspects already discussed inside this report. Here we have seven major bulleted points:

- The analysis of all the three families can be continued beyond the limits introduced and defined in Chapter 3 (see **ADDITIONAL SETTINGS**). In this way it is possible to look at additional bifurcations (here not shown), as well as for new resonances to be later propagated and analysed within the ER3BP.
- Considering very analogous analyses and procedures, the same investigation can be performed for different values of the μ -parameter, focusing also on some possible μ -bifurcations in all the six cases presented here.
- For a single μ -value, as the one here adopted for the Earth-Moon system, the analysis can be extended to higher values of the eccentricity, similarly to what has been briefly shown in Figure 79 (at page 113).
- For all previous points, it is also theoretically feasible to include other families of periodic solutions, so taking into account additional libration points or also *planetary orbits*, as briefly summarized in Appendix-C.
- The research can be also complete by including quasi-periodic solutions in this investigation. These lasts have been shown indeed to exist around each family studied in this Master thesis report (see Section 2.2.4).
- A more complete model can be considered, based on “additional perturbations”, as previously discussed in Section 2.1.3 (TEST-CASE: the Earth-Moon system), for example including the oblateness and solar radiation effects.
- As alternative research proposal, the entire discussion of this work can be enhanced by the analysis of stable/unstable manifolds, starting with some specific periodic solutions and later relating them to feasible “transfer problems”.

Appendices

A.

Constants and main parameters used

In this Appendix-A, we briefly summarize constants and main parameters used in our simulations, e.g. thresholds used in both the **Periodic L-Orbit Generator** and **Resonance L-Orbit Propagator** algorithms. First of all, we need to present some further details related to the Earth-Moon system, Test-Case adopted in all simulations.

Principal constants for the Earth-Moon system

An extensive description of the Earth-Moon system has been given in Section 2.1.3, so delineating the model adopted with all its major simplifications, as also for few main additional perturbations existing in the ‘real’ (or better approximated) dynamics. Moreover, in Table 1, Bulk and Orbital main characteristics have been listed, mostly with the objective of giving the reader a “more tangible measure” of the system. One remark, is that different Master theses, PhD theses and even articles provide usually different values for the μ -parameter (the mass-ratio). Clearly, a mathematically precise value is not very realistic, nonetheless we have pointed out many times that our analysis is not strictly designated for a particular real space mission design but theoretically applicable to any 3-Body systems. Under this perspective, first objective is to assure consistency in the procedure, while values for the parameters can change and this change itself could be analyse in future investigations, for example looking at bifurcations along the μ -value, as also performed in ([Doedel et al., 2003](#); [Doedel et al., 2007](#)).

We start with the value for Earth and Moon mass-ratio, so leading to

$$\mu_{EM} = \frac{M_M}{M_E + M_M} = \frac{1}{1 + \sigma^{-1}} = 0.012150584460351 \approx \hat{\mu}_{EM} = \mathbf{0.0121506} \quad (\text{A-1})$$

where the ratio $\sigma = M_M/M_E$ is equal to $0.0123000371 \pm 4 \cdot 10^{-10}$, as given in the “IAU 2009 System of Astronomical Constants” ([Luzum et al., 2011](#)). Adopted for all simulation is its approximation $\hat{\mu}_{EM}$ in Eq. (A-1), still in agreement with textbooks as ([Vallado & McClain, 1997](#)), or also used in ([Parker, 2007](#)). Furthermore, we have performed our analysis also on slightly different values rounded to 0.012150 and 0.012151 (here not given) without noting any substantial different behaviours at each family, while a very different situation can be observed for near binary systems ([Doedel et al., 2007](#)).

As seen in Section 2.1.2, in the Circular problem the system is fixed once given a μ -value, as also its main proprieties (e.g., location of the five Lagrange points). L-points can be calculated using both Eq. (2-7) and Eq. (2-8), with an analytic solution for triangular points $L_{4/5}$, as shown in Figure 4. For the three collinear points $L_{1/2/3}$, it is also possible to use and solve Eq. (2-9), quintic equation in $\gamma_L = \gamma_L$, scalar distance of each L-point from the nearest mass. Using the mass-ratio value $\hat{\mu}_{EM}$, we obtain

Table 13: Location of collinear Lagrange points (L-points) and their scalar distance γ_L from the nearest mass. All three found along the syzygy in a co-rotating frame for $\hat{\mu}_{EM} = 0.0121506$.

| Collinear L-point | x -position | γ_L -value |
|-------------------|--|--|
| L_1 | +0.836915054964205 $\approx +321710.147$ [km] | 0.150934345035795 ≈ 58019.162 [km] |
| L_2 | +1.155682220791537 $\approx +444244.245$ [km] | 0.167832820791537 ≈ 64514.936 [km] |
| L_3 | -1.005062651805919 ≈ -386346.083 [km] | 0.992912051805918 ≈ 381675.392 [km] |

Note that we have used the nominal semi-major axis, as $a_{EM} = 384400$ [km], in order to dimensionalize these coordinates (so using values in Table 1), but still referring to the origin of the reference frame (centre of mass of the co-rotating system).

Comment on the “non-dimensional” system

Almost the entire investigation has been performed adopting a non-dimensional reference system, where in Section 2.1.1 and Section 4.1.1 we have introduced the transformations for space, time and mass. In order to have more insights in the physical meaning of such analysis, here we can simply define each unit-value respect to the numerical ones found within this report, thus adopting the following transformations

$$\left\{ \begin{array}{l} 1 \text{ [meter]} \cong 2.6 \cdot 10^{-9} [-] \\ 1 \text{ [second]} \stackrel{\text{def}}{=} \frac{2\pi}{T_{EM}} \cong 2.662 \cdot 10^{-6} [-] \end{array} \right. \xrightarrow{\text{it follows}} 1 \text{ [Km/s]} \cong 0.97671 [-] \quad (\text{A-2})$$

$$1 \text{ [kg]} \cong 1.654 \cdot 10^{-25} [-] \xrightarrow{\text{it follows}} 1 \text{ [MJ]} \cong 0.15779 \cdot 10^{-24} [-] \quad (\text{A-3})$$

with the energy is defined in MJ (millions of Joule) and the Moon orbital period around the Earth has been approximated to $T_{EM} \cong 2360595$ [s]. (NASA, 2016)

PS: physical shooting velocity is not directly related to the previous relation, since the system adopted is synodic (so co-rotating), as also for the Pulsating frame, where the situation becomes even more complex. This work focuses mainly on the investigation of the general dynamical model, nonetheless such aspects needs to be taken into account for real space mission designs or in particular for the transfer trajectories’ optimization.

At this point, as conclusions, we present some main values used (e.g., thresholds) in the numerical computation, while others have been already discussed within the main text.

Parameters adopted for all main simulations

For what has been previously shown, we have decided to adopt specific thresholds in the numerical computation as trade between computational restrictions (e.g., the Matlab numerical precision) and limitations from the physical dynamics (e.g., physical units). We refer once again to (Vallado & McClain, 1997) for more accurate information, in particular on practical aspects related to common space missions, while here we simply list main values adopted, in comparison to similar simulations found in literature. Within the report the reader can find description and use of each one of these parameters, while their corresponding dimensional value can be computed using Eq. (A-2).

Table 14: Main parameters used for the numerical computation in both CR3BP and ER3BP are here shown, meanwhile their “dimensional values” can be computed using Eq. (A-2).

| | Parameter | Value at L ₁ [-] | Value at L ₂ [-] |
|---|------------------|-----------------------------|-----------------------------|
| Circular Problem: | | | |
| Distance members on $\hat{x}\hat{z}$ -plane | ΔX_{xz} | $\gamma_L \cdot 10^{-3}$ | $\gamma_L \cdot 10^{-3}$ |
| Displacement of velocity on $\hat{x}\hat{z}$ -plane | ΔV_{xz} | 10^{-12} | 10^{-12} |
| Displacement of position y | ΔY | 10^{-12} | 10^{-12} |
| Max number of iterations | N_{iter}^{MAX} | 20 | 20 |
| Elliptic Problem: | | | |
| Eccentricity step-size | Δe | 10^{-4} | 10^{-4} |
| Displacement of velocity on $\hat{x}\hat{z}$ -plane | ΔV_{xz} | 10^{-10} | 10^{-10} |
| Displacement of position y | ΔY | 10^{-10} | 10^{-10} |
| Max number of iterations | N_{iter}^{MAX} | 50 | 50 |

FINAL COMMENT:

In (Hao Peng & Xu, 2014) the accuracy condition involves at the same time both displacement terms, such that

$$\text{Total Displacement} = \sqrt{\Delta Y^2 + \Delta V_{xz}^2} \equiv \sqrt{\Delta Y^2 + \Delta V_x^2 + \Delta V_z^2} \quad (\text{A-4})$$

On the first crossing the threshold has been fixed at 10^{-9} , adopting a relative tolerance in the numerical integration (MATLAB function `ode45`) as $3 \cdot 10^{-14}$. Later, in (H. Peng & Xu, 2015a, 2015b, 2015c) this value has been reduced to 10^{-10} , in total agreement with the one used in this work for the elliptic case. Last remark is related to a much stricter threshold here used for the Circular problem, where the convergence of the DC-algorithm has been not so problematic, as discussed in Section 4.4.2. Unfortunately, in other literature cited (mostly related to periodic solutions for the ER3BP) there are not always enough data on main settings or methodologies, thus not very suitable for a comparison. A more detailed discussion on numerical integrations has been provided in Appendix-B.

B.

MATLAB Software Environment and Settings

In this Appendix-B, we provide a concise survey on numerical aspects of this work, in particular based on MATLAB software environment (version R2015b). Main critical element in our investigation is indeed related to the “integration accuracy”, and consequently the choice of an efficient numerical integrator is fundamental for all our purposes. All thresholds and physical aspects related have been analysed in Appendix-A, while for further technicalities the reader is referred to general literature on *numerical methods*. Example is ([Quarteroni, Sacco, & Saleri, 2000](#)) and above all, in ([Shampine & Reichelt, 1997](#)), an extensive comparison has been given about “*programs for solving ordinary differential equations in Matlab*”, reference point for the following discussion.

MATLAB (MATrix LABORatory) uses floating-point numbers, having a finite precision given by 16 significant decimal digits and an effective range between 10^{-308} and 10^{+308} , where the ϵ -Matlab⁴¹ is given as $\epsilon_1 \approx 2.22 \cdot 10^{-16}$ at 1 ([MathWorks, 2013](#)). In a physical world, in particular for real space missions, this value can be consider as completely ‘negligible’ (nanometre scale for the Earth-Moon CR3BP), while can be really important for integration on long periods, as also for stability assessment. A summary on numerical integrators schemes has been given in Chapter 6 of the Literature Study and is not the purpose here, thus we will only discuss some settings related to this “Matlab ode suite”.

MATLAB ode suite: the “ode113”.

Since considering orbits mostly near L-points and far from gravitational singularities, the numerical analysis has shown great robustness. Furthermore, for non-stiff problems Matlab ode suite allows using three functions as “ode23”, “ode45” and “ode 113”, respectively for a low, medium and high accuracy. In the very initial phase of this Master work, a choice has been made for using the ode113, which is a variable-step integrator, variable order (VSVO) Adams-Bashforth-Moulton PECE solver of orders from 1 to 12 ([Shampine & Reichelt, 1997](#)). As stated in their paper, “*compared to ode45, the ode113 solver is better at solving problems with stringent error tolerances. A common situation where ode113 excels is in orbital dynamics problems, where the solution curve is smooth and requires high accuracy*”.

⁴¹ Note that with ϵ -Matlab we refer to the “*Floating-point relative accuracy*”, meaning that the distance between $x = 1$ and the next larger double-precision number will be given as ϵ_1 . The latter for *single-precision* is given as $\epsilon_1^s = 2^{-23}$, while for *double-precision* is $\epsilon_1^d = 2^{-52}$.

The integrator selected is able indeed to define an error threshold, based on both the “Relative” and the “Absolute” tolerance, well described in ([MathWorks, 2013](#)) as

- I. Relative error-tolerance “**RelTol**”.
“It measures the error relative to the magnitude of each solution component. Roughly speaking, it controls the number of correct digits in all solution components, except those smaller than “AbsTol”.
- II. Absolute error-tolerance “**AbsTol**”.
“It is a threshold below which the value of the solution becomes unimportant. If the solution $|\mathbf{X}(t)|$ is smaller than “AbsTol”, then the solver does not need to obtain any correct digits in $|\mathbf{X}(t)|$ ”.

Thus, to be considered successful, each step t_i must have an acceptable error "err", so that

$$\|\text{err}(t_i)\| \leq \max(\text{RelTol} \cdot |\mathbf{X}(t_i)|, \text{AbsTol}(t_i)) \quad (\mathbf{B-1})$$

with $\mathbf{X} = \mathbf{X}(t_i)$ state-vector of the differential system integrated. Clearly conditions on AbsTol are taken into account only for very small values of $|\mathbf{X}(t_i)|$, thus final choice has been made in relation to non-dimensional units, such that

$$\begin{cases} \mathbf{RelTol} = 100 \cdot \epsilon_1 \\ \mathbf{AbsTol} = 10^{-24} \end{cases} \quad (\mathbf{B-2})$$

with ϵ_1 previously defined as epsilon-Matlab, where RelTol in Eq. (B-2) has been actually set to the lower boundary admitted by Matlab ode-functions. The latter is justified by the fact that the integration period T necessary for the Differential Correction algorithm (or the propagation of the STM) is relatively small (Chapter 3). In fact, the maximum T has been found for H-Lyapunov orbits at L1, approximately equal to 6.77 in non-dimensional time units. As consequence, such strict constraint is balanced by a short integration time, so leading to an overall efficient and precise computation. Moreover, the accurate numerical integration is an aspect fundamental for lowering the threshold used for the “periodicity conditions” described in Section 2.4.2.

NOTE: previous values has been based on a trial-and-error procedure, so balancing computational time with accuracy, thus defining most suitable thresholds and later comparing settings with a more general literature previously mentioned.

Unstable dynamics of the Restricted Three-Body Problem

Last step is to explain few major problematics relative to the integration and stability assessment of periodic (or quasi-periodic) solutions. In this work we have been focused principally on first-order stability (*linear stability*) and relative bifurcations, while in real space mission stability needs to be verified differently, for example based on Poincaré Mapping ([Teschl, 2012](#)), as also considering additional perturbations (Section 2.1.3.1). Moreover, there exists always a small error within the shooting conditions of periodic solutions, where the Differential Correction converges only once the threshold has been reached. When assuming very small uncertainties (in the limit of Matlab precision), the displacement initially follows the dynamics of the linearized system, in agreement with the entire discussion on stability given with Sections 2.2.2 (CR3BP) and 4.2.2 (ER3BP).

Clearly, once the error has grown too much, the first-order stability is no more a valid model and non-linear effects arise. In order to verify the validity of linear stability for our discussion, we have selected three member within the Halo family at L2 (Earth-Moon system), nominally 2-unstable, 1-unstable and 0-unstable, as shown in Table 15.

Table 15: Three periodic solutions selected from the Halo family at L2 (Earth-Moon system). Different orders-of-instability have been chosen and all shooting conditions $\{x_0, v_{y0}, z_0\}$ have been shown together with the largest eigenvalue's module $|\lambda_{MAX}|$ and the orbital period T.

| Member | #902 | #1041 | #1044 |
|-------------------|--------------------|-------------------|-------------------|
| <i>Order I.</i> | 2 | 1 | 0 |
| x_0 | 1.006913190189294 | 0.992588582490166 | 0.992377327198552 |
| v_{y0} | 0.541529474357983 | 0.684998059403458 | 0.689136385592912 |
| z_0 | 0.063314501881441 | 0.045194107092875 | 0.044737905101660 |
| $ \lambda_{MAX} $ | 22.138119542987397 | 1.353402273942142 | 1.000000000026339 |
| $T[\times 2\pi]$ | ~ 0.4390 | ~ 0.3798 | ~ 0.3783 |

Note that last two orbits have been taken really close (respectively member #1041 and #1044) having a relative distance on the $\hat{x}\hat{z}$ -plane as $[\Delta x_0, \Delta z_0] \approx [2.11, 4.56] \cdot 10^{-4}$ and consequently around [81, 175] km. These three orbits have been numerically integrated with similar setting for roughly 5 years, equivalent to around 60 system revolutions (Moon around the Earth) or respectively almost 137, 158, 159 orbital revolutions. In the following Figure 90, the graphical results have been shown with an evident trend, where the 0-unstable orbit seems to preserve its periodicity for the entire time-duration.

CR3BP: Comparison Linear Stability within the L2-Halo family.

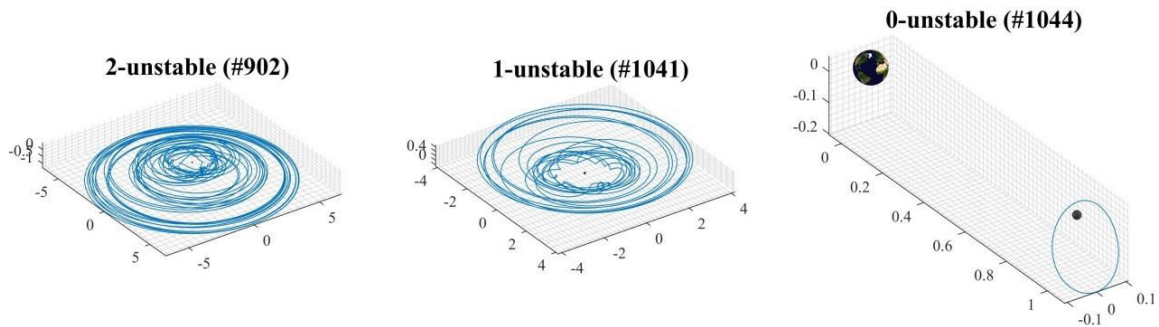


Figure 90: It shows graphical results based on the comparison among different orders of instability, thus numerically integrating for 60 system revolutions (corresponding to 5 years) the three members of the Halo family at L2 in the Earth-Moon system (synodic frame).

Obviously, it is necessary also to provide some data in addition to these qualitative plots, thus in Figure 91 for each solution the periodicity error of the position $P(t)$ and the velocity $V(t)$ has been shown, both defined as follows

$$\begin{aligned}
 P(t) &= [x(t), y(t), z(t)]^T \\
 V(t) &= [v_x(t), v_y(t), v_z(t)]^T
 \end{aligned}
 \tag{B-3}$$

In Figure 91, we can observe the absolute error after each revolution, where T is the orbital period of the solution, and the error is evaluated at $t = n \cdot T_c, \forall n > 0$ (integer). Trivial is to observe that for the 0-unstable case, errors at the 159th revolution are around $9.2 \cdot 10^{-8}$ and $8.1 \cdot 10^{-7}$, equivalent to ~ 35 m in position and ~ 0.1 mm/s in velocity. For what concerns the real world, initial displacements could also been larger for many physical reasons (e.g., additional perturbations), while only purpose of this example is to demonstrate the robustness of the selected numerical integrator itself.

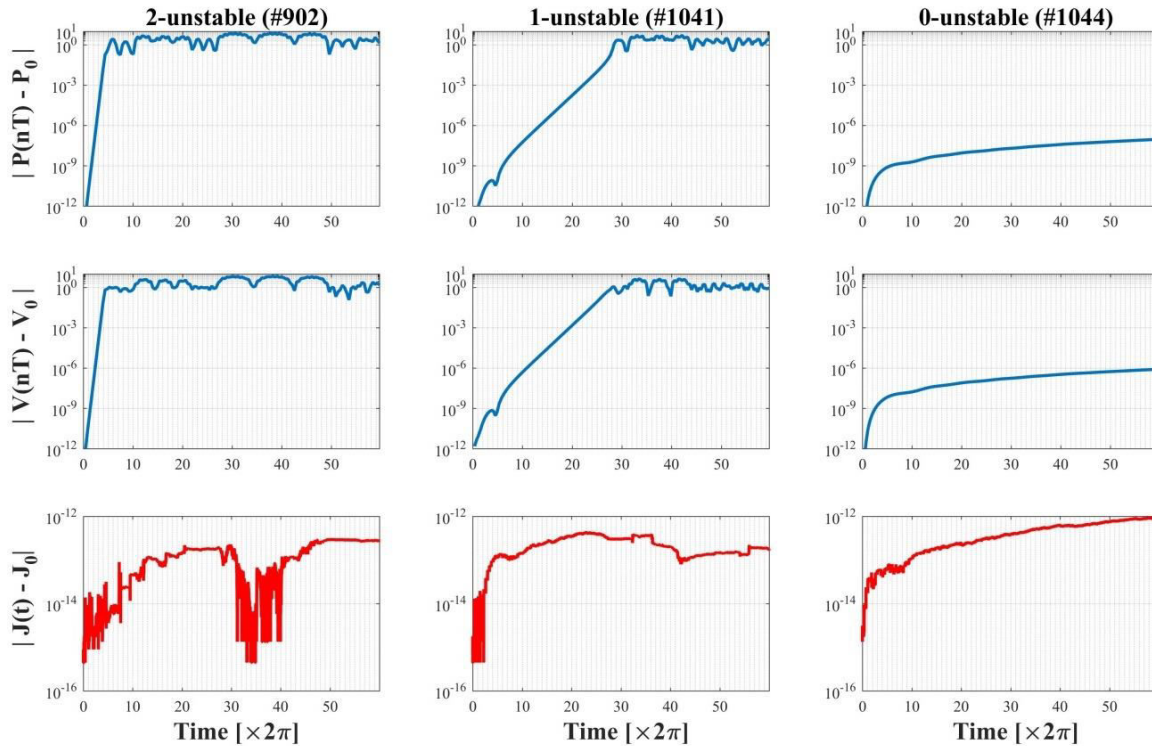


Figure 91: Plot of three periodic solutions (Halo family at L2 in the Earth-Moon system) with three different orders-of-instability. Displacement in position (TOP), velocity (MIDDLE) and energy (BOTTOM) is shown over around 60 systems revolutions, as described in the text.

From previous results, we can conclude that the divergence from a periodic behaviour is mostly influenced by the existence of unstable manifolds (see Section 2.2.4), and consequently related to the order of instability. Nonetheless, in the last two simulations, both members have been selected really close to each other and still outcome of the integration seems very different. It follows that also this linear stability plays a crucial role in the design of space observation missions, especially influencing station-keeping costs, while adjacent periodic solutions could have a very different behaviour, in response to the so-called “injection errors”. ([Utku, Hagen, & Palmer, 2015](#))

Indeed, in Figure 91 (Bottom), the energy displacement seems to be really small, where for first two cases it decreases when the trajectory jumps into particular solution, numerically more stable. This element can be seen as a confirmation of the fact that the numerical integration is very accurate, while the dynamics of both Circular/Elliptic restricted problems is highly unstable. As main consequence, such instability can leads to numerical complications, in particular when looking to specific closed trajectories.

FINAL NOTE:

In the last plot, an additional test has been performed, involving the only known Integral of Motion for the Circular problem (Jacobi constant). From the moment that its value (calculated at the initial time) is supposed to be nominally constant along the entire trajectory $\forall t \rightarrow \pm\infty$, it can be used to check the accuracy during the integration. Unfortunately, this necessary condition is also not sufficient, due to the fact that the expression given in Eq. (2-11) does not change when errors of different components cancel out reciprocally. Furthermore, in addition to both **Closing condition** and **Eigenvalue condition**, it is possible also to use this last **Energy condition** in order to assess the validity of results, only for what concerns the Circular Restricted 3-Body Problem. For the Elliptic Restricted 3-Body Problem it is not possible to adopt such additional verification to our results, even if a pseudo First Integral exists, as seen from Eq. (4-21). The latter has been applied indeed by (S. Campagnola et al., 2008) to define a sort of “*Sub-regions of Motion*” in opposition to forbidden regions existing within the circular case, divided by *Hill’s surfaces of zero velocity*. (Szebehely, 1967)

C.

Overview of main families at L1/L2 in the EM-system

In this Appendix-C, the overview of the overall Phase-space is given for both shooting conditions ($t_0 = 0, T/2$) and for all three families at L1/L2 in the Earth-Moon system, in addition with the respective order of instability (**0-yellow**, **1-normal line**, **2-thick line**). Main bifurcations (\diamond) are also given, while more details have been previously discussed in Chapter 3 and main theoretical concepts can be found in Section 2.2.

Overview families in the EM-CR3BP [$\mu = 0.0121506$]

LEGEND: M_2 , $L_{1/2}$, V-Lyapunov, H-Lyapunov, Halo, Bif. (\diamond)

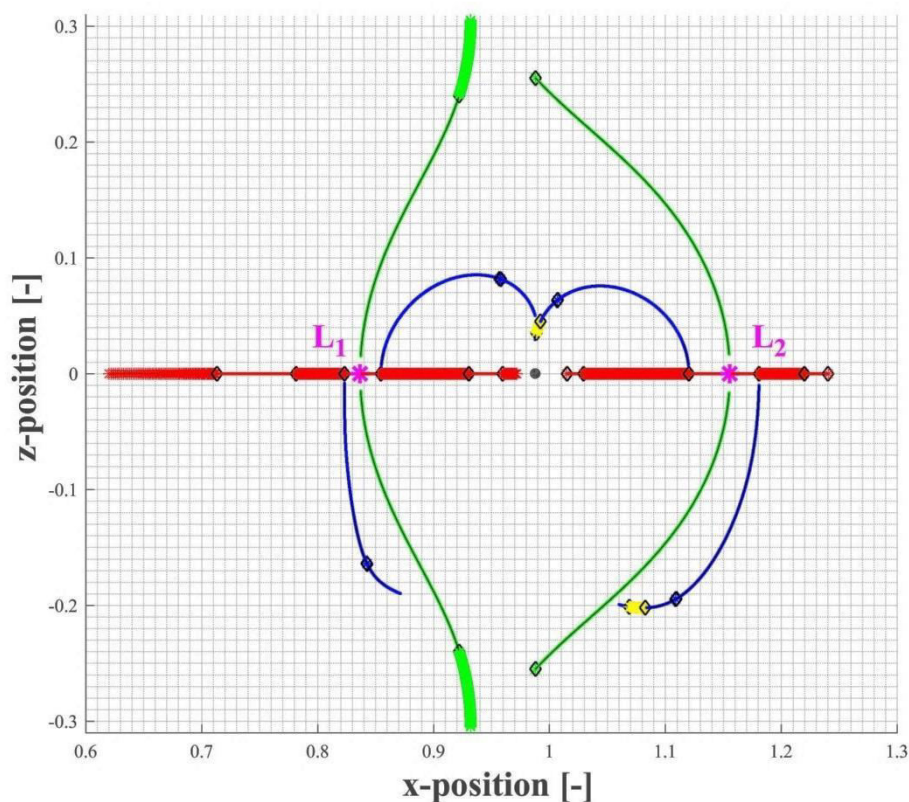


Figure 92: Illustration of the overall Phase-space of shooting conditions for all three families analysed in this work, referring to both L1 and L2 libration point of the Earth-Moon CR3BP. More details can be found in Chapter 3, while for the notation we refer to the LEGEND.

In the following Figure 93, two additional planes of the overall Phase-space have been shown (see LEGEND), while very interesting is here to observe the main phase-points where the Halo bifurcates from the H-Lyapunov one. The latter has been further examined in the following section of this Appendix-C.

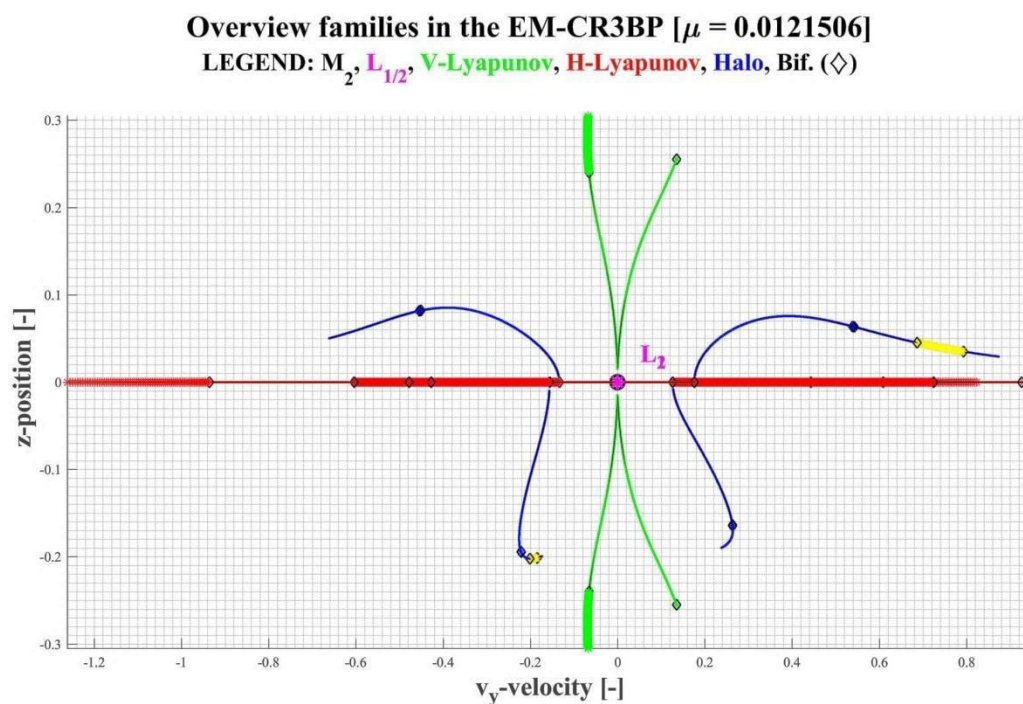
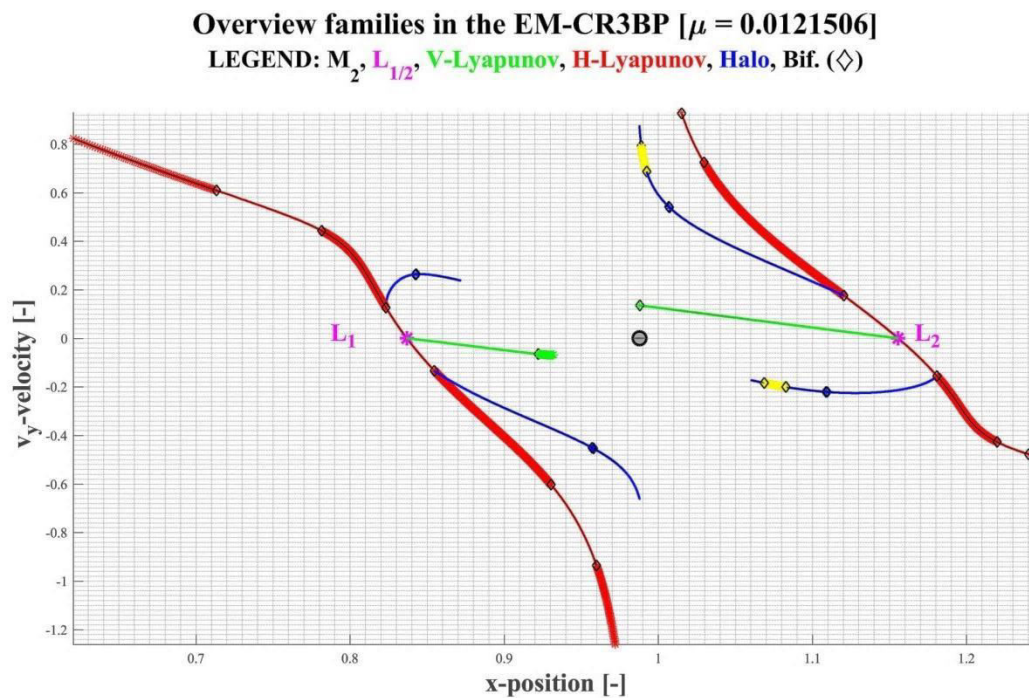


Figure 93: Additional plots for the Phase-space of shooting conditions for all three families analysed in this work, referring to L1 and L2 libration point of the Earth-Moon CR3BP. More details can be found in Chapter 3, while for the notation we refer to the LEGEND.

PS: for all three planes shown before, the uncertainty area of the Horizontal family at L2, as found in Figure 40, has been removed due to reasons provided within Section 3.4.

Primary Lyapunov-bifurcation: the Halo family

As shown in both Figure 92 and Figure 93, the Halo family arise from the first bifurcation in the Horizontal Lyapunov family. All discussion can be found in Chapter 3, while here we present at L1/L2 an analysis where the Numerical Continuation “jumps” from one family to another, so highlighting bifurcations in the main parameters of the analysis. The reader is referred again to Section 2.4 for the interpretation of all following results.

Bifurcation shown at L1

L1 Halo: PLOT at $\mu = 0.0121506$

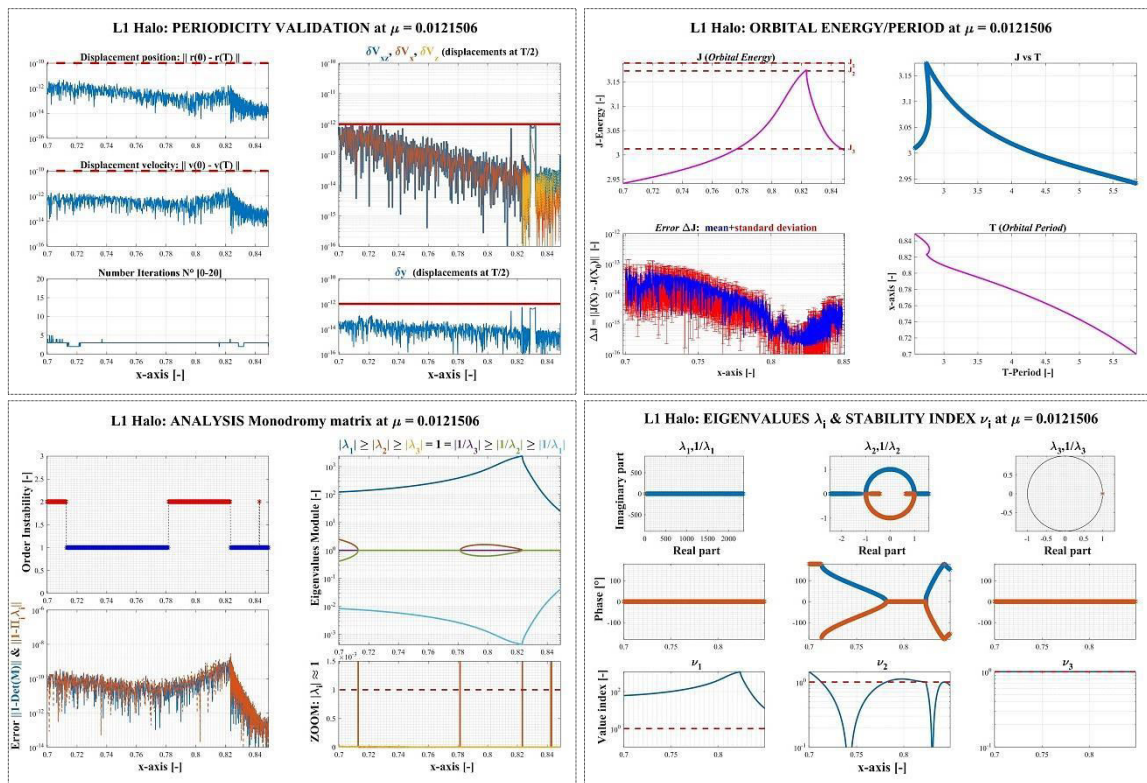
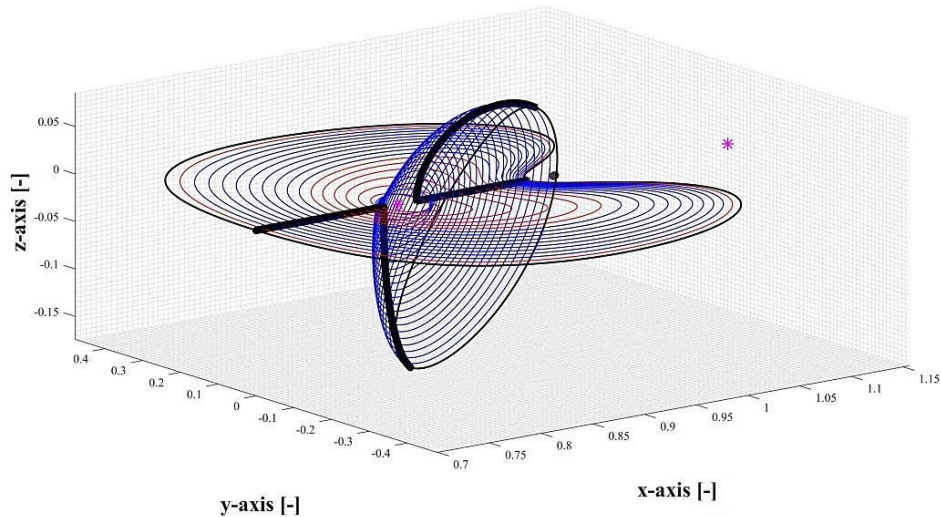


Figure 94: Illustration of Halo family bifurcations from the H-Lyapunov one at L1 (TOP) with main parameters considered in our analysis. For the interpretation we refer to Section 2.4.

Bifurcation shown at L2

L2 Halo: PLOT at $\mu = 0.0121506$

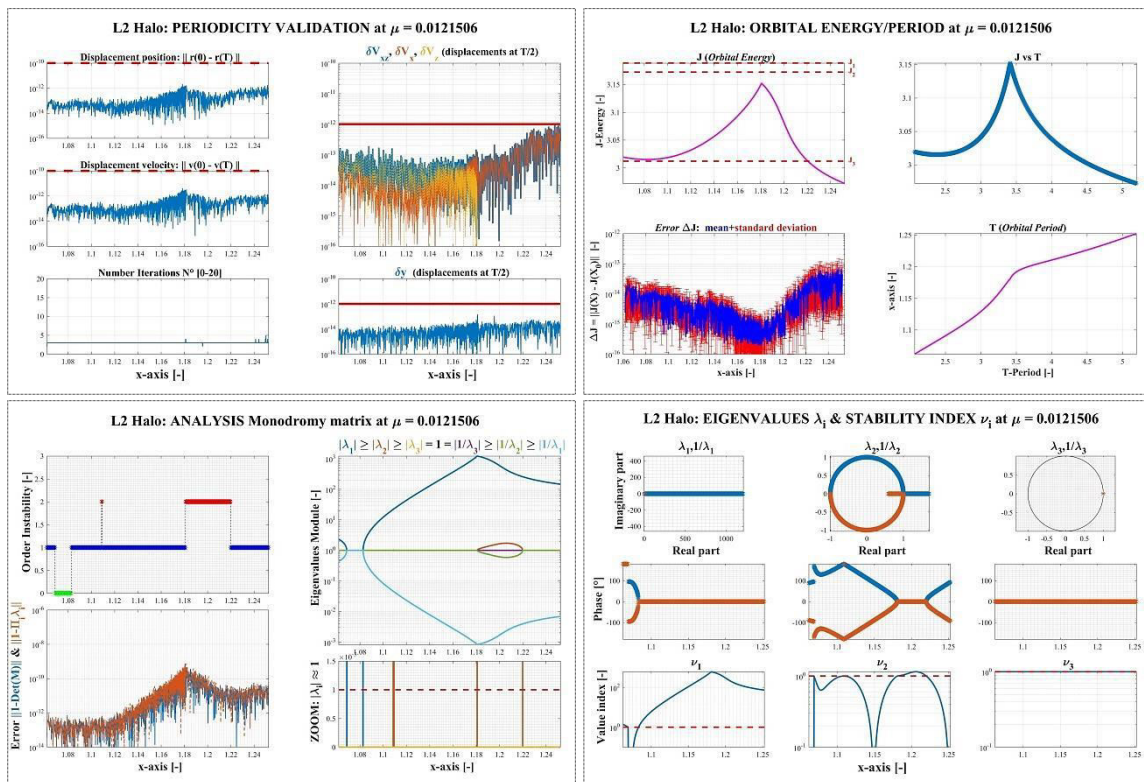
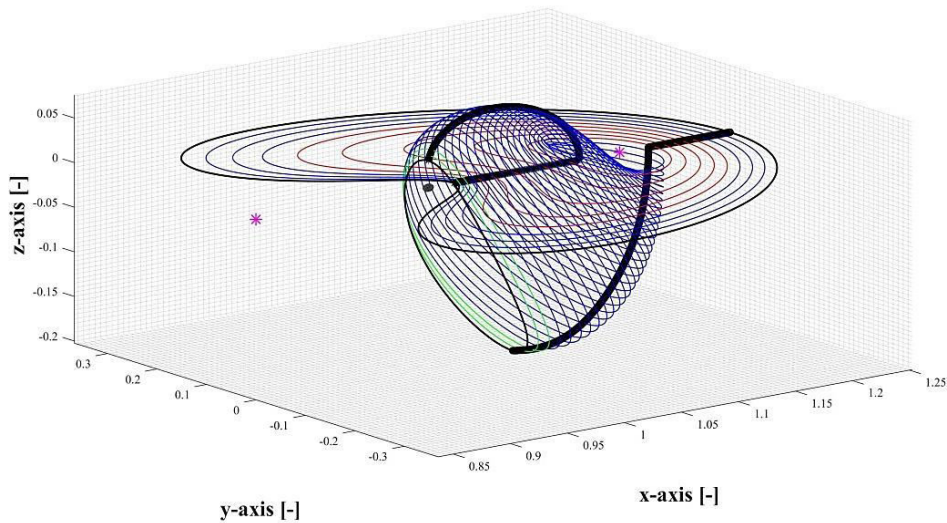


Figure 95: Illustration of Halo family bifurcations from the H-Lyapunov one at L2 (TOP) with main parameters considered in our analysis. For the interpretation we refer to Section 2.4.

So far, bifurcations seem evident in the interruption of the “natural continuity” for each parameter as the J-energy or T-period. Note also that for Southern/Northern families there is not a really difference, while both arise in similar way due to the “Mirrored symmetry” (Section 2.1.2.2) respect to the $\hat{x}\hat{y}$ -plane. At this point, for sake of completeness, we present a very brief discussion on the **Axial family**, generated from the additional bifurcation found within both Lyapunov families (Horizontal/Vertical).

Secondary Lyapunov-bifurcation: the Axial family

This secondary bifurcation found in both Lyapunov families is actually known in literature, and it is related to a new family of periodic solutions, called “Axial family”. The latter has been intensively studied in (Doedel et al., 2007), as also several other families not only restricted to L1/L2, and with many different mass-ratios up to binary systems ($\forall \mu \geq 0.1$). However, this family has been not considered here, due to time-constraints of the Master work, and consequently only resonance orbits of the three main families have been studied and later extended to the Elliptic problem. In order to provide the reader a more complete overview, in Figure 96 an example of *Axial orbits* is shown, arise from this second bifurcation in the Horizontal Lyapunov family. We refer to the aforementioned paper for more details and numerical simulations.

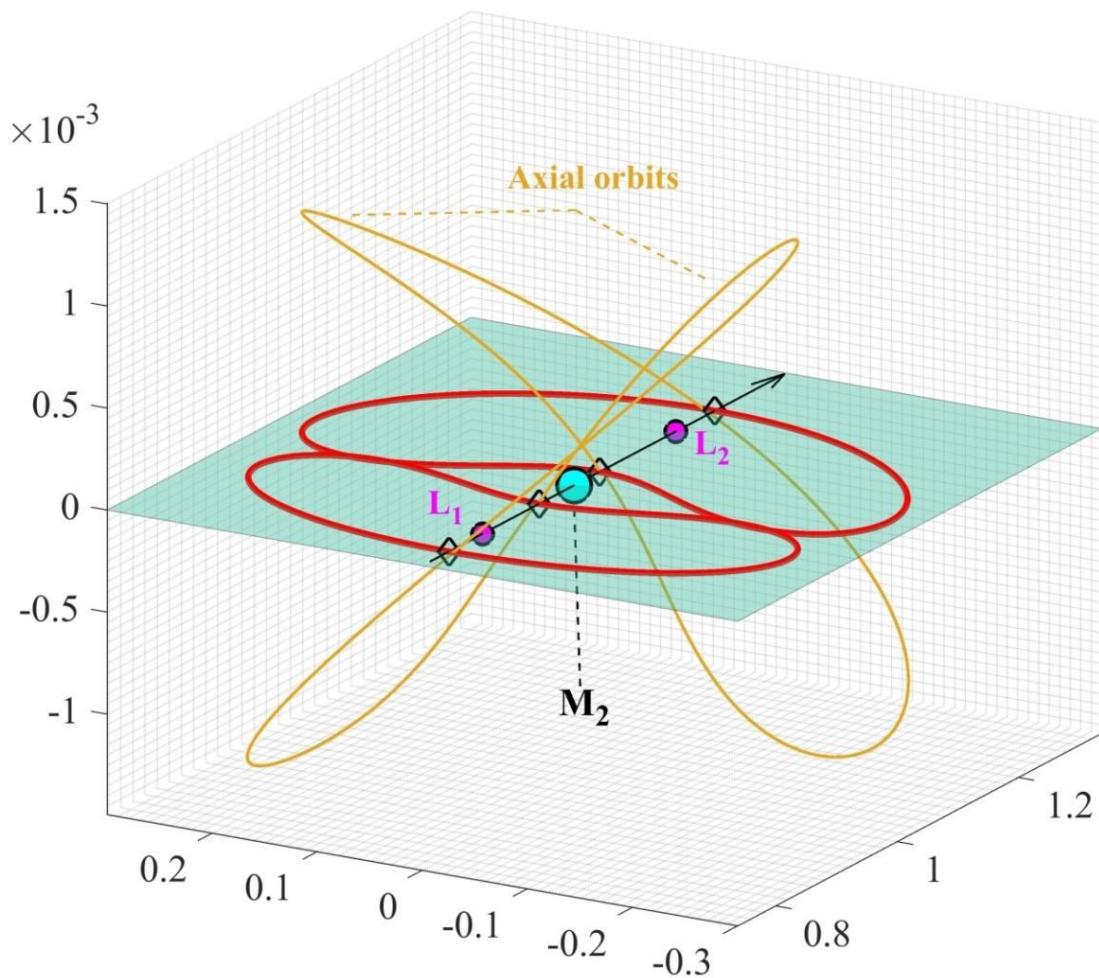


Figure 96: Illustration of the Axial family (in dark yellow) of periodic solution at L1/L2 (in magenta) for the Earth-Moon CR₃BP ($\mu = 0.0121506$). Note their intersection (\diamond) with the Horizontal family (in red) on the $\hat{x}\hat{z}$ -plane, due to the Tangent Bifurcation. See Section 3.7.

As seen in Section 3.7, this previous family has its origin in the Tangent-Bifurcation found within both H-Lyapunov and V-Lyapunov families, as for the Halo orbit arising from the first bifurcation in H-Lyapunov family. In a very similar way it is possible to study such new periodic solutions, thus exploiting all additional bifurcations connected to other families. In (Doedel et al., 2007) this has been extended indeed also to *Planetary orbits* revolving around the Primary M_1 or the Secondary M_2 , while also very distant orbits “surrounding” both masses have been indicated there as “**Circular family**”.

To conclude, in the next Table 16 an example of a possible classification of Lagrange orbits is given, similarly to what discussed in (Folta, Bosanac, Guzzetti, & Howell, 2015). Few classes has been defined, for example the Libration Point Orbits (here called *Lagrange orbits*), as also Resonance Orbits related to a motion bounded around the Secondary mass M_2 (here the Moon). These lasts can be found as prograde or retrograde depending on their direction of rotation (counter-clockwise or clockwise). Other possible classes that exist in the Circular Restricted 3-Body problem can be found and have been well described in their paper.

Table 16: Possible organization in different classes of some families within the dynamical model of the Earth-Moon system; note the connection between resonance orbit orbiting the Secondary mass M_2 (here the Moon), as also for the connection (due to bifurcations) of families existing around Lagrange points. More details can be found in (Folta et al., 2015).

| Libration Point Orbits | Resonance Orbits | Moon-Centred Orbits |
|--|---------------------------------|---------------------|
| H-Lyapunov: L_1, L_2, L_3 | 1: 1 (Interior and Exterior) | Conics |
| V-Lyapunov: L_1, L_2, L_3, L_4, L_5 | ... | Direct Retrograde |
| Halo: L_1, L_2, L_3 | N: 1 (Resonance) | Distant Prograde |
| Axial: L_1, L_2, L_3, L_4, L_5 | ... | Low Prograde |
| Butterfly: L_1, L_2 | 1: M (Exterior) | |
| Short Period: L_4, L_5 | ... | |
| Long Period: L_4, L_5 | N: M (Interior and Exterior) | |
| Horseshoe | | |

NOTE:

Further details have been treated in a more recent paper as (Guzzetti, Bosanac, Haapala, Howell, & Folta, 2016), “based upon a ‘dynamic’ catalogue of periodic and quasi-periodic orbits within the Earth–Moon system”. However, here the only scope has been to provide the reader with a more general overview of the state-of-art research on some possible periodic motions within the model of the Circular Restricted 3-Body Problem.

Bibliography

- Abraham, A. J. (2014). *Particle Swarm Optimization of Low-Thrust, Geocentric-to-Halo-Orbit Transfers*. (Doctor of Philosophy Dissertation), Lehigh University.
- Barrabés, E., Cors, J. M., & Ollé, M. (2015). Dynamics of the parabolic restricted three-body problem. *Communications in Nonlinear Science and Numerical Simulation*, 29(1-3), 400-415. doi:10.1016/j.cnsns.2015.05.025
- Barrabés, E., & Ollé, M. (2006). Invariant manifolds of L3 and horseshoe motion in the restricted three-body problem. *Nonlinearity*, 19(9), 2065-2089. doi:10.1088/0951-7715/19/9/004
- Barrow-Green, J. (1997). *Poincaré and the Three Body Problem*. London: London Mathematical Society, American Mathematical Society, Providence.
- Belbruno, E. A., & Miller, J. K. (1993). Sun-perturbed earth-to-moon transfers with ballistic capture. *Journal of Guidance, Control, and Dynamics*, 16(4), 770-775. doi:10.2514/3.21079
- Bennett, A. (1965). Characteristic exponents of the five equilibrium solutions in the elliptically restricted problem. *Icarus*, 4(2), 177-187.
- Bernelli, F., Topputo, F., & Massari, M. (2004). Assessment of Mission Design Including Utilization of Libration Points and Weak Stability Boundaries. *ESA ACT Report*.
- Bosanac, N. (2012). *Exploring the influence of a three-body interaction added to the gravitational potential function in the circular restricted three-body problem: A numerical frequency analysis*. (Master of Science), Purdue University.
- Bosanac, N., Howell, K. C., & Fischbach, E. (2015). Stability of orbits near large mass ratio binary systems. *Celestial Mechanics & Dynamical Astronomy*, 122(1), 27-52. doi:10.1007/s10569-015-9607-6
- Breakwell, J. V. B., & John V. (1979). The 'Halo' family of 3-dimensional periodic orbits in the Earth-Moon restricted 3-body problem. *Celestial Mechanics*, 20(4), 389-404. doi:10.1007/bf01230405
- Broucke, R. (1969). Stability of periodic orbits in the elliptic, restricted three-body problem. *AIAA Journal*, 7(6), 1003-1009. doi:10.2514/3.5267
- Broucke, R., Lass, H., & Boggs, D. (1976). A note on the solution of the variational equations of a class of dynamical systems. *Celestial Mechanics*, 14(3), 383-392. doi:10.1007/bf01228524
- Campagnola, S. (2010). *New techniques in astrodynamics for moon systems exploration*. (Doctor of Philosophy Dissertation), University of Southern California, Los Angeles, California.
- Campagnola, S., Lot, M., & Newton, P. (2008). *Subregions of motion and elliptic halo orbits in the elliptic restricted three-body problem*. Paper presented at the Advances in the Astronautical Sciences.
- Contopoulos, G. (1966). Adiabatic invariants and the "third" integral. *Journal of Mathematical Physics*, 7(5), 788-797.
- Crawford, J. D. (1991). Introduction to bifurcation theory. *Reviews of Modern Physics*, 63(4), 991-1037. doi:10.1103/RevModPhys.63.991
- Cronin, J., Richards, P. B., & Russell, L. H. (1964). Some periodic solutions of a four-body problem. *Icarus*, 3(5-6), 423-428.
- Cunningham, L. E. (1970). On the computation of the spherical harmonic terms needed during the numerical integration of the orbital motion of an artificial satellite. *Celestial Mechanics*, 2(2), 207-216. doi:10.1007/bf01229495

- Doedel, E. J., Paffenroth, R. C., Keller, H. B., Dichmann, D. J., Galán-Vioque, J., & Vanderbauwhede, A. (2003). Computation of periodic solutions of conservative systems with application to the 3-body problem. *International Journal of Bifurcation and Chaos in Applied Sciences and Engineering*, 13(6), 1353-1381. doi:10.1142/S0218127403007291
- Doedel, E. J., Romanov, V. A., Paffenroth, R. C., Keller, H. B., Dichmann, D. J., Galán-Vioque, J., & Vanderbauwhede, A. (2007). Elemental periodic orbits associated with the libration points in the Circular Restricted 3-Body Problem. *International Journal of Bifurcation and Chaos*, 17(8), 2625-2677. doi:10.1142/S0218127407018671
- Domingo, V., Fleck, B., & Poland, A. I. (1995). The SOHO mission: An overview. *Solar Physics*, 162(1-2), 1-37. doi:10.1007/BF00733425
- Dunham, D. W., & Roberts, C. E. (2001). Stationkeeping techniques for libration-point satellites. *Journal of the Astronautical Sciences*, 49(1), 127-144.
- Euler, L. (1744). *Methodus inveniendi lineas curvas maximi minimive proprietate gaudentes, sive Solutio problematis isoperimetrici latissimo sensu accepti*.
- Euler, L. (1767). De moto rectilineo trium corporum se mutuo attrahentium. *Novo Comm. Acad. Sci. Imp. Petrop.*
- Farquhar, R. W. (1968). *The control and use of libration-point satellites*. (Doctor of Philosophy).
- Farquhar, R. W. (1970). The Moon's influence on the location of the Sun-Earth exterior libration point. *Celestial Mechanics*, 2(2), 131-133. doi:10.1007/bf01229491
- Farquhar, R. W., & Kamel, A. A. (1973). Quasi-periodic orbits about the translunar libration point. *Celestial Mechanics*, 7(4), 458-473. doi:10.1007/bf01227511
- Feng, J., Noomen, R., Visser, P., & Yuan, J. (2016). Numerical analysis of orbital motion around a contact binary asteroid system. *Advances in Space Research*, 58(3), 387-401. doi:10.1016/j.asr.2016.04.032
- Feng, J., Noomen, R., & Yuan, J. (2015). Orbital Motion in the Vicinity of the Non-collinear Equilibrium Points of a Contact Binary Asteroid. *Planetary and Space Science*, 117, 1-14. doi:10.1016/j.pss.2015.04.008
- Feng, J., Noomen, R., Yuan, J., & Ambrosius, B. (2014). *Third-order analytical solutions around non-collinear equilibrium points of a contact binary asteroid*. Paper presented at the AIAA/AAS Astrodynamics Specialist Conference, SPACE Conferences and Exposition.
- Feng, J. L., Noomen, R., Visser, P. N. A. M., & Yuan, J. P. (2015). Modeling and analysis of periodic orbits around a contact binary asteroid. *Astrophysics and Space Science*, 357(2). doi:10.1007/s10509-015-2353-0
- Folta, D. C., Bosanac, N., Guzzetti, D., & Howell, K. C. (2015). An Earth–Moon system trajectory design reference catalog. *Acta Astronautica*, 110, 341-353. doi:10.1016/j.actaastro.2014.07.037
- Gauss, C. F., Davis, C. H., & Gauss, C. F. (1963). *Theory of the motion of the heavenly bodies moving about the sun in conic sections : a translation of Theoria motus*. New York: Dover Publications.
- Giorgilli, A., & Skokos, C. (1997). On the stability of the Trojan asteroids. *Astronomy and Astrophysics*, 317(1), 254-261.
- Goldstein, H., Poole, C. P., & Safko, J. L. (2002). *Classical Mechanics*: Addison Wesley.
- Gómez, G. (2001a). *Dynamics and mission design near libration points. the case of collinear libration points Vol. I*. Singapore; River Edge, NJ: World Scientific.
- Gómez, G. (2001b). *Dynamics and mission design near libration points. the case of triangular libration points Vol. II*. Singapore; River Edge, NJ: World Scientific.
- Gómez, G. (2001c). *Dynamics and mission design near libration points. Vol. III*. Singapore; River Edge, NJ: World Scientific.

- Gómez, G. (2001d). *Dynamics and mission design near libration points. Vol. IV*. Singapore; River Edge, NJ: World Scientific.
- Gómez, G., Jorba, A., Masdemont, J., & Simó, C. (1993). Study of the transfer from the Earth to a halo orbit around the equilibrium point L1. *Celestial Mechanics & Dynamical Astronomy*, 56(4), 541-562. doi:10.1007/BF00696185
- Gómez, G., Koon, W. S., Lo, M. W., Marsden, J. E., Masdemont, J., & Ross, S. D. (2002). *Invariant manifolds, the spatial three-body problem and space mission design*.
- Gómez, G., Koon, W. S., Lo, M. W., Marsden, J. E., Masdemont, J., & Ross, S. D. (2004). Connecting orbits and invariant manifolds in the spatial restricted three-body problem. *Nonlinearity*, 17(5), 1571-1606. doi:10.1088/0951-7715/17/5/002
- Gómez, G., Masdemont, J., & Simó, C. (1998). Quasihalo orbits associated with libration points. *Journal of the Astronautical Sciences*, 46(2), 135-176.
- Gómez, G., & Mondelo, J. M. (2001). The dynamics around the collinear equilibrium points of the RTBP. *Physica D: Nonlinear Phenomena*, 157(4), 283-321. doi:10.1016/S0167-2789(01)00312-8
- Gurfil, P., & Meltzer, D. (2007). Semi-analytical method for calculating the elliptic restricted three-body problem monodromy matrix. *Journal of Guidance, Control, and Dynamics*, 30(1), 266-271. doi:10.2514/1.22871
- Guzzetti, D., Bosanac, N., Haapala, A., Howell, K. C., & Folta, D. C. (2016). Rapid trajectory design in the Earth–Moon ephemeris system via an interactive catalog of periodic and quasi-periodic orbits. *Acta Astronautica*, 126, 439-455. doi:10.1016/j.actaastro.2016.06.029
- Hénon, M. (1974). Families of periodic orbits in the three-body problem. *Celestial Mechanics*, 10(3), 375-388. doi:10.1007/BF01586865
- Hill, G. W. (1886). On the part of the motion of the lunar perigee which is a function of the mean motions of the sun and moon. *Acta Mathematica*, 8(1), 1-36. doi:10.1007/bf02417081
- Hill, K., Lo, M. W., & Born, G. H. (2006, January). *Liaison navigation in the sun-earth-moon four-body problem*. Paper presented at the Proceedings of the AAS/AIAA 16th Spaceflight Mechanics Meetings.
- Hou, X., Liu, L., & Tang, J. (2011). Station-keeping of small amplitude motions around the collinear libration point in the real Earth-Moon system. *Advances in Space Research*, 47(7), 1127-1134. doi:10.1016/j.asr.2010.12.005
- Hou, X. Y., & Liu, L. (2009). On Lyapunov Families around Collinear Libration Points. *Astronomical Journal*, 137(6), 4577-4585. doi:10.1088/0004-6256/137/6/4577
- Howard, J. E., & MacKay, R. S. (1987). Linear stability of symplectic maps. *Journal of Mathematical Physics*, 28(5), 1036-1051. doi:10.1063/1.527544
- Howell, K. C. (1984). Three-dimensional, periodic, 'halo' orbits. *Celestial Mechanics*, 32(1), 53-71. doi:10.1007/BF01358403
- Howell, K. C., Barden, B. T., & Lo, M. W. (1997). Application of dynamical systems theory to trajectory design for a libration point mission. *Journal of the Astronautical Sciences*, 45(2), 161-178.
- Howell, K. C., & Campbell, E. T. (1999). Three-dimensional periodic solutions that bifurcate from halo families in the circular restricted three-body problem. *Spaceflight Mechanics 1999, Vol 102, Pts I and II*, 102, 891-910.
- Howell, K. C., & Pernicka, H. J. (1988). Numerical determination of Lissajous trajectories in the restricted three-body problem. *Celestial Mechanics*, 41(1-4), 107-124. doi:10.1007/BF01238756
- Jacobi, C. G. J. (1836). Sur le mouvement d'un point et sur un cas particulier du problème des trois corps. *Comptes Rendus de l'Académie des Sciences de Paris*.

- James, R. C. (1966). *Advanced calculus*: Wadsworth Pub. Co.
- Jorba, A., & Masdemont, J. (1999). Dynamics in the center manifold of the collinear points of the restricted three body problem. *Physica D: Nonlinear Phenomena*, 132(1-2), 189-213.
- Jordan, D. W., & Smith, P. (2002). *Mathematical techniques : an introduction for the engineering, physical, and mathematical sciences*. Oxford; New York: Oxford University Press.
- Kevorkian, J., & Cole, J. D. (1996). *Multiple scale and singular perturbation methods*. New York: Springer.
- Koon, W. S., Lo, M. W., Marsden, J. E., & Ross, S. D. (2008). Dynamical systems, the three-body problem and space mission design. *Free online Copy: Marsden Books*.
- Landau, E. (1974). *Handbook of the theory of distribution of prime numbers*. New York: Chelsea Pub. Co.
- Legendre, A. M. (1806). Nouvelles méthodes pour la détermination des orbites des comètes avec un supplément contenant divers perfectionnemens de ces méthodes et leur application aux deux comètes de 1805.
- Lei, H. L., Xu, B., Hou, X. Y., & Sun, Y. S. (2013). High-order solutions of invariant manifolds associated with libration point orbits in the elliptic restricted three-body system. *Celestial Mechanics & Dynamical Astronomy*, 117(4), 349-384. doi:10.1007/s10569-013-9515-6
- Lo, M. W., & Ross, S. D. (1998). Low Energy Interplanetary Transfers Using the Invariant Manifolds of L1, L2, and Halo Orbits (AAS 98-136). *Advances in astronomical sciences.*, 99(1), 551.
- Lo, M. W., Williams, B. G., Bollman, W. E., Han, D. S., Hahn, Y. S., Bell, J. L., . . . Wilson, R. (2001). Genesis mission design. *Journal of the Astronautical Sciences*, 49(1), 169-184.
- Luzum, B., Capitaine, N., Fienga, A., Folkner, W., Fukushima, T., Hilton, J., . . . Wallace, P. (2011). The IAU 2009 system of astronomical constants: the report of the IAU working group on numerical standards for Fundamental Astronomy. *Celestial Mechanics & Dynamical Astronomy*, 110(4), 293-304. doi:10.1007/s10569-011-9352-4
- Lynch, J. P. (2001, 2001). *Flight Mechanics Symposium proceedings of a conference sponsored and held at NASA Goddard Space Flight Center, Greenbelt, Maryland, June 19-21, 2001*, Greenbelt, Md.; Hanover, MD.
- Marchal, C. (1990). *The Three-body Problem (Studies in Astronautics)*. New York: Elsevier Science Ltd.
- Masdemont, J. J. (2005). High-order expansions of invariant manifolds of libration point orbits with applications to mission design. *Dynamical Systems-an International Journal*, 20(1), 59-113. doi:10.1080/14689360412331304291
- Massarweh, L. (2015). *An Analytic approach to find periodic and quasi-periodic Lagrange orbits*. Literature Study performed at Delft University of technology, Aerospace Engineering, Space Flight track.
- MathWorks, I. (2013). *MATLAB & Simulink Student Version 2013a*. Upper Saddle River: Pearson Education (US).
- McInnes, A. I. (2000). *Strategies for solar sail mission design in the circular restricted three-body problem*. Purdue University.
- Miele, A. (1960). Theorem of image trajectories in the earth-moon space. *Astronautica Acta*, 6(5), 225-232.
- Miele, A. (2010). Revisit of the Theorem of Image Trajectories in the Earth-Moon Space. *Journal of Optimization Theory and Applications*, 147(3), 483-490. doi:10.1007/s10957-010-9734-x
- Moulton, F. R., Buchanan, D., Buck, T., Griffin, F. L., Longley, W. R., & MacMillan, W. D. (1920). *Periodic orbits*. Washington: Carnegie Institution of Washington.
- Mueller, G. (2014). Prospects for a space-based gravitational-wave observatory. *SPIE Newsroom*. doi:10.1117/2.1201408.005573

- Murray, C. D. D., Stanley F. (1999). *Solar system dynamics*. Cambridge Cambridge university press.
- Musielak, Z. E., & Quarles, B. (2014). The three-body problem. *Reports on Progress in Physics*, 77(6), 065901. doi:10.1088/0034-4885/77/6/065901
- Nagata, K., Sakamoto, N., & Habaguchi, Y. (2016). *Center manifold method for the orbit design of the restricted three body problem*.
- NASA, N. S. S. D. C. (2016). *Planetary Fact Sheets*. Retrieved from: <http://nssdc.gsfc.nasa.gov/planetary/planetfact.html>
- Nayfeh, A. H. (2007). *Perturbation methods*. Weinheim: Wiley.
- Ott, E. (2002). *Chaos in Dynamical Systems*: Cambridge University Press.
- Palacián, J. F. Y., Patricia ; Fernández, Silvia ; Nicotra, Mariano A. (2006). Searching for periodic orbits of the spatial elliptic restricted three-body problem by double averaging. *Physica D: Nonlinear Phenomena*, 213(1), 15-24. doi:10.1016/j.physd.2005.10.009
- Parker, J. S. (2007). *Low-Energy ballistic Lunar Transfers*. (Doctor of Philosophy PhD), University of Colorado.
- Peng, H., & Xu, S. (2014). *Numerical stability study of multi-circle elliptic halo orbit in the elliptic restricted three-body problem*. Paper presented at the Proceedings 24th International Symposium on Space Flight Dynamics—24th ISSFD. Luarel, United States.
- Peng, H., & Xu, S. (2015a). Low-energy transfers to a Lunar multi-revolution elliptic halo orbit. *Astrophysics and Space Science*, 357(1), 1-15. doi:10.1007/s10509-015-2236-4
- Peng, H., & Xu, S. (2015b). Stability of two groups of multi-revolution elliptic halo orbits in the elliptic restricted three-body problem. *Celestial Mechanics & Dynamical Astronomy*, 123(3), 279-303. doi:10.1007/s10569-015-9635-2
- Peng, H., & Xu, S. (2015c). Transfer to a Multi-revolution Elliptic Halo orbit in Earth-Moon Elliptic Restricted Three-Body Problem using stable manifold. *Advances in Space Research*, 55(4), 1015-1027. doi:10.1016/j.asr.2014.11.013
- Perko, L. (2001). *Differential equations and dynamical systems*. New York: Springer.
- Poincaré, H. (1885). Sur l'équilibre d'une masse fluide animée d'un mouvement de rotation. *Acta Math. Acta Mathematica*, 7(1), 259-380.
- Quarteroni, A., Sacco, R., & Saleri, F. (2000). *Numerical mathematics*. New York: Springer-Verlag New York.
- Richardson, D. L. (1980a). Analytic construction of periodic orbits about the collinear points. *Celestial Mechanics*, 22(3), 241-253. doi:10.1007/BF01229511
- Richardson, D. L. (1980b). A note on a Lagrangian formulation for motion about the collinear points. *Celestial Mechanics*, 22(3), 231-236. doi:10.1007/BF01229509
- Rohner, J. (2014). *To the Far Side of the Moon*. (Master of Science), Delft University of Technology, Delft.
- Sarris, E. (1982). Integrals of motion in the elliptic three-dimensional restricted three-body problem. *Celestial Mechanics*, 26(4), 353-360. doi:10.1007/bf01230416
- Sarris, E. (1989). Families of symmetric-periodic orbits in the elliptic three-dimensional restricted three-body problem. *Astrophysics and Space Science*, 162(1), 107-122. doi:10.1007/BF00653348
- Schuerman, D. W. (1980). The restricted three-body problem including radiation pressure. *The Astrophysical Journal*, 238, 337. doi:10.1086/157989
- Shampine, L. F., & Reichelt, M. W. (1997). The MATLAB ode suite. *SIAM Journal on Scientific Computing*, 18(1), 1-22.

- Sharma, R. K. (1987). The linear stability of libration points of the photogravitational restricted three-body problem when the smaller primary is an oblate spheroid. *Astrophysics and Space Science*, 135(2), 271-281. doi:10.1007/BF00641562
- Shirobokov, M. G. (2014). Libration point orbits and manifolds: design and station-keeping. *Keldysh Institute*(0), 90-31.
- Sicardy, B. (2010). Stability of the triangular Lagrange points beyond Gascheau's value. *Celestial Mechanics & Dynamical Astronomy*, 107(1-2), 145-155. doi:10.1007/s10569-010-9259-5
- Simo, J., & McInnes, C. R. (2009). Solar sail orbits at the Earth-Moon libration points. *Communications in Nonlinear Science and Numerical Simulation*, 14(12), 4191-4196. doi:10.1016/j.cnsns.2009.03.032
- Szebehely, V. G. (1967). *Theory of orbits, the restricted problem of three bodies*. New York: Academic Press.
- Tantardini, M., Fantino, E., Ren, Y., Pergola, P., Gómez, G., & Masdemont, J. J. (2010). Spacecraft trajectories to the L3 point of the Sun-Earth three-body problem. *CELESTIAL MECHANICS AND DYNAMICAL ASTRONOMY*, 108(3), 215-232. doi:10.1007/s10569-010-9299-x
- Teschl, G. (2012). *Ordinary differential equations and dynamical systems*: American Mathematical Society Providence, RI.
- Thurman, R., & Worfolk, P. A. (1996). *Technical report, The Geometry of Halo Orbits in the Circular Restricted Three-Body Problem*.
- Tiwary, R. D., & Kushvah, B. S. (2015). Computation of halo orbits in the photogravitational Sun-Earth system with oblateness. *Astrophysics and Space Science*, 357(1), 1-16. doi:10.1007/s10509-015-2243-5
- Utku, A., Hagen, L., & Palmer, P. (2015). Initial condition maps of subsets of the circular restricted three-body problem phase space. *Celestial Mechanics & Dynamical Astronomy*, 123(4), 387-410. doi:10.1007/s10569-015-9641-4
- Vallado, D. A., & McClain, W. D. (1997). *Fundamentals of Astrodynamics and Applications*: McGraw-Hill.
- Van der Ham, L. (2012). *Interplanetary Trajectory Design using Dynamical Systems Theory*. (Master of Science), Delft University of Technology. Retrieved from uuid:98c55fe3-cd59-4c61-817e-9caa6ac835b6
- Vaquero, M., & Howell, K. C. (2014). Design of transfer trajectories between resonant orbits in the Earth-Moon restricted problem. *Acta Astronautica*, 94(1), 302-317. doi:10.1016/j.actaastro.2013.05.006
- Vázquez, M., Pallé, E., & Rodríguez, P. M. (2010). Extrasolar Planetary Systems *The Earth as a Distant Planet: A Rosetta Stone for the Search of Earth-Like Worlds* (pp. 337-390). New York, NY: Springer New York.
- Verhulst, F. (2000). *Nonlinear differential equations and dynamical systems*. Berlin: Springer.
- Vermeiden, H. (2014). *Optimal Translunar Lagrange Point Orbits for OLFAR*. (Master of Science), Delft University of Technology. Retrieved from uuid:780071cb-c856-4e8a-8783-915c2dfid8ea
- Vladimir, I. A. d. (1972). LECTURES ON BIFURCATIONS IN VERSAL FAMILIES. *Russian Mathematical Surveys*, 27(5), 54-123.
- Waters, T. J., & McInnes, C. R. (2007). Periodic orbits above the ecliptic in the solar-sail restricted three-body problem. *Journal of Guidance, Control, and Dynamics*, 30(3), 687-693. doi:10.2514/1.26232
- Wilson, A., European Space, A., European Space, R., & Technology, C. (2005). *Cosmic vision : space science for Europe 2015-2025*. Noordwijk, the Netherlands: ESA Publications Division, ESTEC.
- Wintner, A. (1941). *The analytical foundations of celestial mechanics*: Princeton University Press.